THE DEVELOPMENT OF MULTIFUNCTIONAL NANOPLATFORMS FOR TARGETED DUAL DRUG DELIVERY

A DISSERTATION SUBMITTED TO
THE GRADUATE SCHOOL OF
ENGINEERING AND NATURAL SCIENCES
OF ISTANBUL MEDIPOL UNIVERSITY
IN PARTIAL FULFILLMENT OF THE REQUIREMENTS FOR
THE DEGREE OF
DOCTOR OF PHILOSOPHY
IN
BIOMEDICAL ENGINEERING AND BIOINFORMATICS

By

Erhan Demirel

September, 2022

THE DEVELOPMENT OF MULTIFUNCTIONAL NANOPLATFORMS FOR TARGETED DUAL DRUG DELIVERY

By Erhan Demirel

15 September 2022

We certify that we have read this dissertation and that in our opinion it is fully adequate, in scope and in quality, as a dissertation for the degree of Doctor of Philosophy.

_____

Prof. Dr. Yasemin Yüksel Durmaz (Advisor)

_____

Assoc. Prof. Dr. Sultan Sibel Erdem

_____

Assist. Prof. Dr. Mehmet Hikmet Üçışık

_____

Assist. Prof. Dr. Özge Şensoy

_____

Assoc. Prof. Dr. Muhammet U. Kahveci

Approved by the Graduate School of Engineering and Natural Sciences:

_____

Prof. Dr. Yasemin Yüksel Durmaz

Director of the Graduate School of Engineering and Natural Sciences

I hereby declare that all information in this document has been obtained and presented in accordance with the academic rules and ethical conduct. I also declare that, as required by these rules and conduct, I have fully cited and referenced all material and results that are not original to this work.

Signature :

Name, Surname: ERHAN DEMİREL

ACKNOWLEDGEMENT

First and foremost, I would like to express my gratitude to my advisor Prof. Dr. Yasemin Yüksel Durmaz for guiding me throughout a complex research project and teaching me how to conduct high-quality research. This work would not have been possible without her immense knowledge, advice, and support. Apart from my supervisor, I would like to extend my sincere thanks to the committee members: Assoc. Prof. Dr. Sultan Sibel Erdem and Assist. Prof. Dr. Mehmet Hikmet Üçışık for sharing insightful suggestions and their help whenever needed.

I am also pleased to thank my fellow IPONT lab members Cemran Toydemir, Waleed Mustafa, Merve Ercan Ayra, Betül Kaymaz, and Tanzeel Ur Rehman, and an old friend and colleague Ceyda Şimşek for their help, support, and the time we spent together while working in the laboratory. I would like to thank all researchers and personnel of the Research Institute for Health Sciences and Technologies (SABITA), Graduate School of Engineering and Natural Sciences of Medipol University, and Center for Medical Research (MEDITAM), but specially Burcu Kurt Vatandaşlar, Emre Vatandaşlar, Fatmagül İlayda Aydınlı, Olgu Enis Tok, Dr. Mehmet Şerif Aydın, Dr. Esra Nur Yiğit, Safiye Serdengeçti, and Volkan Bülbül for their unconditional support and assistance.

In the end, I would like to offer the most gratitude to my mother Fatoş, my father Abdullah and my brothers Ali Serkan and Barış, and my beloved sister-in-law Fulya Çavuoğlu for their patience, understanding, and love. Lastly, I want to express my heartfelt appreciation to my fiancé Zeynep Günal, throughout this seven-year-old journey she was and will be the reason for me to move forward just by standing next to me and making the world worth living with her heartwarming love.

Finally, I would like to thank The Scientific & Technological Research Council of Turkey (TUBITAK, Project No:15Z845 and Project No:116Z534) for the financial support of this project.

Erhan Demirel

September, 2022

CONTENTS

Page

ACKNOWLEDGEMENT ..... **iv**
CONTENTS ..... **v**
LIST OF FIGURES ..... **viii**
LIST OF TABLES ..... **xii**
LIST OF SYMBOLS ..... **xiii**
ABBREVIATIONS ..... **xiv**
ÖZET ..... **xv**
ABSTRACT ..... **xvii**
1. INTRODUCTION **1**
2. THEORETICAL PART **4**
2.1. Cancer Statistics and Current Treatment Approaches 4
2.2. Drug Delivery Systems 6
2.3. Chemical and Physical Properties of Graphene, Graphene Oxide, and Reduced Graphene Oxide 9
2.4. Biomedical Applications of Graphene Derivatives, Concerns on Cytotoxicity, and Strategies to Improve Biocompatibility 13
2.5. Use of Graphene, GO, and rGO as Gene and Drug Delivery Platforms 18
2.6. Aim and Methodology of The Study 21
2.6.1. Effective PEGylation method to improve the biocompatibility of graphene derivatives 21
2.6.2. PEGylated reduced graphene oxide as nanoplatform for targeted gene and drug delivery 23
3. EXPERIMENTAL PART **25**
3.1. Materials 25
3.2. Characterization 26
3.3. Synthesis of Poly[(poly(ethylene glycol) methyl ether methacrylate)-*co*-(3-azidopropyl methacrylate)-*co*-(methyl methacrylate)-*co*-(1-pyrenemethyl methacrylate)-*g*-Poly(hexyl methacrylate-*co*-2-(dimethylamino)ethyl methacrylate-*co*-*N*,*N*,*N*-trimethylaminoethyl methacrylate iodide) 27
3.3.1. General procedure for functional ATRP initiators 27
3.3.2. Synthesis of 2,5-dioxopyrrolidin-1-yl pent-4-ynoate 29
3.3.3. Synthesis of pent-4-ynehydrazide 29
3.3.4. Synthesis of 4-((2-(pent-4-ynoyl)hydrazineylidene)methyl)phenyl 2-bromo-2-methylpropanoate 30
3.3.5. Synthesis of 3-azido-1-propanol 30
3.3.6. Synthesis of 3-azidopropyl methacrylate 30
3.3.7. General procedure for the synthesis of poly[(poly(ethylene glycol) methyl ether methacrylate)-*co*-(methyl methacrylate)-*co*-(1-pyrenemethyl methacrylate)] (P(PEGMA-*co*-MMA-*co*-PMA)) or poly[(poly(ethylene glycol) methyl ether methacrylate)-*co*-(3-azidopropyl methacrylate)-*co*-(methyl methacrylate)-*co*-(1-pyrenemethyl methacrylate)] (P(PEGMA-*co*-AzPMA-*co*-MMA-*co*-PMA)) 31
3.3.8. Synthesis of poly(hexyl methacrylate-*co*-2-(dimethylamino)ethyl methacrylate (P(HMA-*co*-DMAEMA)) by ATRP 32
3.3.9. Synthesis of poly(hexyl methacrylate-*co*-2-(dimethylamino)ethyl methacrylate-*co*-N,N,N-trimethylaminoethyl methacrylate iodide) (P(HMA-*co*-DMAEMA-*co*-TMAEMA)) 32

3.3.10. Synthesis of poly[(poly(ethylene glycol) methyl ether methacrylate)-*co*-(3-azidopropyl methacrylate)-*co*-(methyl methacrylate)-*co*-(1-pyrenemethyl methacrylate)]-*g*-poly(hexyl methacrylate-*co*-2-(dimethylamino)ethyl methacrylate-*co*-*N*,*N*,*N*-trimethylaminoethyl methacrylate iodide) by CuAAC of P(HMA-*co*-DMAEMA-*co*-TMAEMA) and P(PEGMA-*co*-AzPMA-*co*-MMA-*co*-PMA) (PAMP-*g*-CP) 33
3.4. Preparation of PEGylated rGO Derivatives 34
3.4.1. PEGylation of GO and simultaneous reduction 34
3.4.2. Synthesis of alkyne-PEG-EPPT1 35
3.4.3. Conjugation of EPPT1 on PAMP-CP-rGO 36
3.4.4. Doxorubicin loading on PEGylated rGO and determination of drug release profile and release kinetics 37
3.5. Agarose Gel Retardation Assay 38
3.6. Zeta Potential and Size Measurements 39
3.7. Coomassie (Bradford) Protein Assay Protocol 39
3.9. *In Vitro* Studies 40
3.9.1. Cell culture procedure 40
3.9.2. Hemocompatibility of PMP-rGO derivatives 40
3.9.3. MTS assay 41
3.9.4. Resazurin assay 41
3.9.5. Clonogenic assay 42
3.9.6. LDH release assay 42
3.9.7. Detection of induced reactive oxygen species (ROS) 43
3.9.8. Determination of cellular uptake of rGO derivatives by confocal fluorescence microscopy 43
3.9.9. Determination of cellular uptake of Dox carrying PAMP-rGO and PAMP-CP-rGO derivatives by fluorescence-activated cell sorting technique 44
3.9.10. Determination of cell apoptosis levels induced by the combination of Dox and siRNA through APC-Annexin-V/Helix NP Blue double staining 44
3.9.11. Determination of change in GAPDH levels by KDalert™ assay kit 45
3.9.12. Determination of change in gene expression levels by real-time polymerase chain reaction 45
3.9.12.1. RNA isolation 46
3.9.12.2. Reverse transcription 46
3.9.12.3. Determination of quantitative gene expression 46
3.9.13. SDS-Page and Western-Blot analysis for determination of Bcl-2 protein expression 47
3.10. *In vivo* Therapeutic Effect of Nanoplatforms 48
3.10.1. Animal care 48
3.10.2. Murine breast cancer model 48
3.10.3. *In vivo* examination of anticancer effect 49
3.11. Statistical Analysis 49
4. RESULTS AND DISCUSSION 50
4.1. Development of an Effective PEGylation Method to Improve Biocompatibility of Graphene Derivatives 50
4.1.1. Synthesis and characterization of P(PEGMA-*co*-MMA-*co*-PMA) coated rGO derivatives 50
4.1.2. Biocompatibility and cytotoxicity evaluation of P(PEGMA-*co*-MMA-*co*-PMA) coated rGO derivatives (PMP-rGO) 64

4.2. Preparation of PEGylated Reduced Graphene Oxide as Nanoplatform for Targeted Gene and Drug Delivery 73
4.2.1. Synthesis of 3-azidopropyl methacrylate 74
4.2.2. Synthesis of 2-bromo-2-methyl propanoate (benzyl initiator) 75
4.2.3. Synthesis, and characterization of PAMP-*g*-CP 76
4.2.4. Synthesis of alkyne-PEG-EPPT1 83
4.2.5. Preparation of EPPT1-PAMP-CP-rGO-Dox-siRNA and derivatives 85
4.3. *In Vitro* Evaluation of PAMP-CP-rGO Nanoplatforms 95
4.3.1. Determination of induced cytotoxicity by PAMP-CP-rGO nanoplatforms using resazurin assay 95
4.3.2. Determination of induced cytotoxicity by PAMP-CP-rGO nanoplatforms using the clonogenic assay 100
4.3.3. Determination of cellular uptake of nanoplatforms by confocal fluorescence microscopy 102
4.3.4. Localization of EPPT1-PAMP-CP-rGO-Dox-siRNA in MCF-7 cells 109
4.3.5. Determination of cellular uptake of nanoplatforms by fluorescence-activated cell sorting (FACS) 110
4.3.6. Detection of cell apoptosis induced by the combination of Dox and siRNA through APC-Annexin-V/Helix NP Blue double staining 112
4.3.7. Comparative transfection efficiency of anti-GAPDH and anti-Bcl-2 siRNA carrying nanoplatforms 118
4.3.7.1. Effect of anti-GAPDH-siRNA carrying nanoplatforms on GPADH protein expression levels 118
4.3.7.2. Determination of change in Bcl-2 gene expression levels by the real-time polymerase chain reaction 119
4.3.7.3. SDS-Page and Western-Blot Analysis for determination of Bcl-2 protein expression 122
4.4. *In vivo* Studies 125
4.4.1. Anticancer activity of nanoplatforms 125
4.5. Final Evaluation of Nanoplatforms, Promise, and Achievements 127
5. CONCLUSIONS AND FUTURE WORK 144
BIBLIOGRAPHY 147
CURRICULUM VITAE 172

LIST OF FIGURES

Figure 1.1: Schematic representation of cellular uptake, endosomal escape, Dox and siRNA release and induced cell death by EPPT1-PAMP-CP-rGO-Dox-siRNA.....3
Figure 2.1: Number of deaths by major types of cancers **a)** all sexes and **b)** females [15]. 4
Figure 2.2: a) Number of cancer death by 5 major cancer types by year in Turkey, **b)** the number of cancer death by major type of cancer in 2019 [17]. 5
Figure 2.3: Milestones of nano-sized drug delivery. (Adapted from: [35]) 7
Figure 2.4: A collection of illustrations demonstrating the many forms of nanoparticles. (Adapted from: [42]).....9
Figure 2.5: Use of graphene to form buckyballs, nanotubes, and graphite (Adapted from: [49]).....10
Figure 2.6: a) TEM images of bi and multi-layered graphene sheets (Adapted from: [52]), **b)** image of a single-layered graphene sheet acquired by high-resolution TEM (Adapted from: [53]). 11
Figure 2.7: Based on particular requirements and uses, alternative manufacturing techniques for graphene and its derivatives are used (Adapted from: [60]).....12
Figure 2.8: Structures of graphene, GO, and rGO and path for rGO production. (Adapted from: [65]). 13
Figure 2.9: a) Key and **b)** biomedical applications of graphene and its derivatives. (Adapted from:[78] and [79]) 14
Figure 2.10: A schematic illustration showing covalent and non-covalent modifications applied to carbon nanomaterials to improve their therapeutic effectiveness (Adapted from: [29]). 16
Figure 2.11: Diagram depicting the extracellular obstacles in siRNA delivery. (Adapted from:[160]) 19
Figure 3.1: Synthesis of benzyl 2-bromo-2-methyl propanoate. 28
Figure 3.2: Synthesis of pyren-1-ylmethyl 2-bromo-2-methyl propanoate.....28
Figure 3.3: Synthesis of 4-formylphenyl 2-bromo-2-methyl propanoate. 29
Figure 3.4: Synthesis of 2,5-dioxopyrrolidin-1-yl pent-4-ynoate. 29
Figure 3.5: Synthesis of pent-4-ynehydrazide. 29
Figure 3.6: Synthesis of 4-((2-(pent-4-ynoyl)hydrazineylidene)methyl)phenyl 2-bromo-2-methylpropanoate. 30
Figure 3.7: Synthesis of 3-azido-1-propanol. 30
Figure 3.8: Synthesis of 3-azidopropyl methacrylate.....31
Figure 3.9: Synthesis of P(HMA-*co*-DMAEMA).....32
Figure 3.10: Synthesis of P(HMA-*co*-DMAEMA-*co*-TMAEMA). 33
Figure 3.11: Synthesis of PAMP-*g*-CP. 34
Figure 3.12: Coating of **a)** PMP and **b)** PAMP-*g*-CP on GO and simultaneous reduction to obtain PMP-rGO and PAMP-CP-rGO respectively. 35
Figure 3.13: Synthesis of alkyne-PEG-EPPT1. 36
Figure 3.14: Synthesis of targeted EPPT1-PAMP-CP-rGO. 36
Figure 3.15: Doxorubicin loading on EPPT1-PAMP-CP-rGO. 37
Figure 3.16: Complexation of EPPT1-PAMP-CP-rGO-Dox and siRNA (anti-GAPDH or anti-Bcl-2). 38
Figure 4.1: Reaction scheme of P(PEGMA-*co*-MMA-*co*-PMA) synthesis. 51
Figure 4.2: ^{1}H NMR spectra of P(PEGMA-*co*-MMA-*co*-PMA) (PMP1). 51
Figure 4.3: Calibration curve of pyrene at 344.5 nm in DCM.....52
Figure 4.4: Schematic representation of possible paths for PEGylation of graphene derivatives. 53

Figure 4.5: ^{1}H NMR spectrum of PMP1 coated rGO (PMP_{500}-rGO1). 54
Figure 4.6: a) UV-Vis and **b)** Fluorescence spectrum of GO, PMP3, and related PMP_{500}-rGO1. 54
Figure 4.7: FTIR spectra of GO, PMP1, and PMP_{500}-rGO1. 55
Figure 4.8: Raman spectra of GO, rGO, PMP_{500}-rGO3, and PMP_{2000}-rGO5. 56
Figure 4.9: Thermogravimetric analysis of GO, rGO, PMP1, PMP5, PMP_{500}-rGO3, and PMP_{2000}-rGO5. 57
Figure 4.10: a) PEGylation and reduction of GO by using P(PEGMA-*co*-MMA) (no pyrene) and **b)** simultaneous PEGylation and reduction of GO in DMF. 58
Figure 4.11: Thermogravimetric analysis of GO-PMP3, rGO-PMP1, PMP_{500}-rGO7, and PMP_{500}-rGO8.....59
Figure 4.12: XPS spectra of **a)** GO, **b)** rGO, **c)** PMP_{500}-rGO3 and **d)** PMP_{2000}-rGO5..61
Figure 4.13: AFM images of **a)** GO, **b)** rGO, **c)** PMP_{500}-rGO3, **d)** PMP_{2000}-rGO5, and **e)** GO and PMP5 physical mixture. 62
Figure 4.14: Size and Zeta Potential of copolymers and rGO conjugates, where rGO has a size of 27878 ±528.2 nm and ζ Potential -27.6 mV. 63
Figure 4.15: TEM images of **a)** GO, **b)** PMP_{500}-rGO3, **c)** PMP_{2000}-rGO5, and **d)** GO coating product of PMP5 in DMF at 100,000 magnification (Scale bar: 100 nm). 64
Figure 4.16: Hemolytic activity of GO, PMP2, PMP5, and PMP-rGO derivatives. 66
Figure 4.17: a) Stability of GO, PMP_{500}-rGO, and PMP_{2000}-rGO derivatives in 10% FBS containing DMEM and **b)** stability and dispersibility of PMP_{2000}-rGO5 in common organic solvents. 67
Figure 4.18: a) MRC-5 and **b)** HEK-293T cell viability results detected by MTS assay after PMP-rGO treatment for 24 hours. 68
Figure 4.19: LDH release rate of PMP-rGO compositions on **a)** MRC-5 and **b)** HEK-293T cells.....70
Figure 4.20: Confocal fluorescent images showing the internalization of **a)** PMP_{500}-rGO3 and **b)** PMP_{2000}-rGO5 into MRC-5 cells after 2, 6, and 24 hours of incubation. The green fluorescent originates from Alexa Fluor™ 488 stained PMP-rGO derivatives where Hoechst dyed nucleus shows blue fluorescence. (Scale bar: 50 μm).71
Figure 4.21: Effect of PMP-rGO derivatives on ROS generation rate on HEK-293T cells. 72
Figure 4.22: a) Synthesis of P(PEGMA-*co*-AzPMA-*co*-MMA-*co*-PMA), **b)** Schematic representation of P(PEGMA-*co*-AzPMA-*co*-MMA-*co*-PMA)-*g*-P(HMA-*co*-DMAEMA-*co*-TMAEMA), synthesis of **c)** functional ATRP initiator, **d)** P(HMA-*co*-DMAEMA) and P(HMA-*co*-DMAEMA-*co*-TMAEMA). 74
Figure 4.23: ^{1}H NMR spectrum of **a)** 3-azido-1-propanol and **b)** 3-azidopropyl methacrylate. 75
Figure 4.24: ^{1}H NMR spectrum of 2-bromo-2-methyl propanoate. 75
Figure 4.25: ^{1}H NMR spectrum of P(PEGMA-*co*-AzPMA-*co*-MMA-*co*-PMA). 77
Figure 4.26: FTIR spectrum of P(HMA-*co*-DMAEMA), P(HMA-*co*-DMAEMA-*co*-TMAEMA), 3-azido-1-propanol, P(PEGMA-*co*-AzPMA-*co*-MMA-*co*-PMA) and P(PEGMA-*co*-AzPMA-*co*-MMA-*co*-PMA)-*g*-P(HMA-*co*-DMAEMA-*co*-TMAEMA). 78
Figure 4.27: ^{1}H NMR spectrum of **a)** 2,5-dioxopyrrolidin-1-yl pent-4-ynoate, **b)** pent-4-ynehydrazide and **c)** 4-formylphenyl 2-bromo-2-methylpropanoate. 79
Figure 4.28: ^{1}H NMR spectrum of 4-((2-(pent-4-ynoyl) hydrazineylidene) methyl) phenyl 2-bromo-2-methylpropanoate. 80
Figure 4.29: Ion mass spectra of 4-((2-(pent-4-ynoyl) hydrazineylidene) methyl) phenyl 2-bromo-2-methyl propanoate. 81

Figure 4.30: ^{1}H NMR spectrum of **a)** P(HMA-*co*-DMAEMA) and **b)** P(HMA-*co*-DMAEMA-*co*-TMAEMA).....82
Figure 4.31: ^{1}H NMR spectrum of PAMP-*g*-CP. 83
Figure 4.32: ^{1}H NMR spectrum of **a)** alkyne-PEG-NHS, **b)** EPPT1, and **c)** alkyne-PEG-EPPT1. 85
Figure 4.33: Preparation steps of pH sensitive, targeted, siRNA and chemotherapeutic agent carrying drug delivery agent.....86
Figure 4.34: TGA thermogram of GO, rGO, PAMP-*g*-CP and PAMP-CP-rGO. 87
Figure 4.35: Bradford calibration curve prepared at various bovine serum albumin (BSA) concentrations. 87
Figure 4.36: Scanning electron microscopy images of GO, rGO, PAMP-CP-rGO, EPPT1-PAMP-CP-rGO, PAMP-CP-rGO-Dox, and EPPT1-PAMP-CP-rGO-Dox 89
Figure 4.37: Change in absorption based on Dox concentration at different pH levels in PBS.....90
Figure 4.38: a) Dox release profile by time, **b)** Weibull Model and **c)** zero-order linear regression graphs of EPPT1-PAMP-CP-rGO-Dox and PAMP-CP-rGO-Dox at pH 7.4 and pH 5.5.....92
Figure 4.39: Protein adsorption by GO, rGO, and PAMP-CP-rGO at physiological conditions.....93
Figure 4.40: Agarose gel electrophoresis assays performed by using **a)** anti-GAPDH-siRNA and **b)** anti-Bcl-2-siRNA (DNA ladder and free siRNA were used as the control for gel retardation).....94
Figure 4.41: Size and zeta potential results of GO, PAMP-CP-rGO, PAMP-CP-rGO-Dox, EPPT1-PAMP-CP-rGO, and EPPT1-PAMP-CP-rGO-Dox at various mass ratios. 95
Figure 4.42: a) UV absorbance of Dox and resorufin, **b)** fluorescence spectrum of resorufin.....96
Figure 4.43: Cell viability results of anti-GAPDH-siRNA complexed nanoplatform derivatives with MCF-7 after 24 hours of incubation. 97
Figure 4.44: Cell viability results of anti-Bcl-2-siRNA complexed nanoplatform derivatives with MCF-7 after **a)** 24 and **b)** 48 hours of incubation. 98
Figure 4.45: Cell viability results of anti-Bcl-2-siRNA complexed targeted carrier and derivatives with MDA-MB-231 after **a)** 24 and **b)** 48 hours of incubation. 100
Figure 4.46: Step-by-step colony counting process. 101
Figure 4.47: Colony formation rates of MCF-7 cells after incubation with nanocarriers.....102
Figure 4.48: Confocal microscope images of Dox-loaded nanoplatforms with MCF-7 cancer cells after 4 hours of incubation. (Scale bar: 20 µm) 104
Figure 4.49: Confocal microscope images of FAM-labeled siRNA-loaded nanoplatforms with MCF-7 cancer cells after 4 hours of incubation. (Scale bar: 20 µm) 105
Figure 4.50: Comparison of **a)** Dox and **b)** FAM fluorescent intensities normalized against Hoechst intensity. (n=7, ****p<0.0001, ***p<0.001, **p<0.01) 106
Figure 4.51: Confocal microscope images of Dox-loaded nanoplatforms with MCF-10A cancer cells after 4 hours of incubation. (Scale bar: 20 µm).....107
Figure 4.52: Confocal microscope images of FAM-siRNA-loaded nanoplatforms with MCF-10A cancer cells after 4 hours of incubation. (Scale bar: 20 µm) 108
Figure 4.53: Comparison of **a)** Dox and **b)** FAM fluorescent intensities normalized against Hoechst intensity. (n=7, ****p<0.0001, ***p<0.001, **p<0.01) 108

Figure 4.54: Colocalization of EPPT1-PAMP-CP-rGO-Dox-siRNA with LysoTracker Green DND-26 in MCF-7 cells. (Scale bar: 20 μm) 110
Figure 4.55: Flow cytometric Dox fluorescence measurements of MDA-MB-231 cells after treatment of 2 hours with free Dox and anti-Bcl-2-siRNA complexed nanoplatforms against non-treated cells. 111
Figure 4.56: Flow cytometric Dox fluorescence measurements of MCF-7 cells after treatment of 2 hours with free Dox and anti-Bcl-2-siRNA complexed nanoplatforms against non-treated cells. 112
Figure 4.57: Normal, early apoptotic, late apoptotic, and necrotic cell populations of MCF-7 determined by flow cytometry analysis after incubating 4 hours with nanoplatforms and 48 hours with fresh medium.....115
Figure 4.58: Normal, early apoptotic, late apoptotic, and necrotic cell populations of MDA-MB-231 determined by flow cytometry analysis after incubating 4 hours with nanoplatforms and 48 hours with fresh medium.....116
Figure 4.59: Normal, early apoptotic, late apoptotic, and necrotic cell populations of MDA-MB-231 determined by flow cytometry analysis after 24 hours of incubation with nanoplatforms.....117
Figure 4.60: The effect of anti-GAPDH siRNA and scrambled siRNA loaded nanoplatforms on GAPDH protein expression levels, after 2 hours of incubation with nanoplatforms and 48 hours in fresh medium relative to the untreated cells. (*p≤0.05, **p≤0.01, ***p≤0.001 and ****p≤0.0001).....119
Figure 4.61: Detected mean fold change in Bcl-2 mRNA expression levels of MDA-MB-231 cells after incubating 4 hours with nanoplatforms and **a)** 48 and **b)** 72 hours post-incubation in fresh medium. (*p≤0.05, **p≤0.01 and ***p≤0.001).....121
Figure 4.62: Detected mean fold change in Bcl-2 mRNA expression levels of MCF-7 cells after incubating 4 hours with nanoplatforms and **a)** 48 and **b)** 72 hours post-incubation in fresh medium. (**p≤0.01) 122
Figure 4.63: Western blot analysis of β-Actin and Bcl-2 expressions detected from **a)** MCF-7 and **b)** MDA-MB-231 cell lysates after treatment with free siRNA, free Dox, and nanoplatforms, following 4 hours with materials and 48 hours of incubation in fresh medium against untreated control cells. 124
Figure 4.64: Percent Bcl-2 expression normalized against the housekeeping protein and untreated control **a)** MCF-7 and **b)** MDA-MB-23 cell lines.....125
Figure 4.65: a) Relative tumor volume **b)** body weight changes in the subcutaneous MDA-MB-231 tumor-bearing mice over 21 days after 3 drug injections on days 0, 3, and 6 (n=4, *p<0.05). 126
Figure 4.66: Images of tumor-bearing mice before and after treatment. 127

LIST OF TABLES

Table 2.1: List of selected properties of graphene [59]. 11
Table 4.1: Features of chosen copolymers for PEGylation. 52
Table 4.2: Features of copolymers used for PEGylation, %PEG content, and coating efficiency of PMP-rGO derivatives. 57
Table 4.3: Features of copolymers used for control of PEGylation, coating efficiency, and %PEG content of PMP-rGO derivatives. 60
Table 4.4: Atomic percentage, which is determined by XPS survey scan of GO, rGO, PMP_{500}-rGO3, and PMP_{2000}-rGO5. 61
Table 4.5: Mol percent distribution of monomers during copolymer synthesis. 76
Table 4.6: Characteristics of synthesized PAMP copolymers. 77
Table 4.7: Characteristics of synthesized copolymers. 82
Table 4.8: Elemental composition of rGO derivatives determined by SEM-EDAX scan. 89
Table 4.9: Regression modules (R^2) of tested mathematical models. 91
Table 4.10: Wavelength settings for confocal microscopy studies. 103
Table 4.11: Wavelength settings for LysoTracker Green DND-26 and Dox loaded nanoplatform detection. 109
Table 4.12: List of excitation and emission wavelengths of the designed experiment. 113
Table 4.13: Calculated and standard molecular weight of β-actin and Bcl-2 proteins. 124

LIST OF SYMBOLS

ζ	:Zeta Potential
±	:Represent Standard Deviation
°C	:Celsius Degrees
µL	:Microliter
µg	:Microgram
λ	:Wavelength

ABBREVIATIONS

^{1}H-NMR :Hydrogen Nuclear Magnetic Resonance
AFM :Atomic Force Microscopy
ATRP :Atom transfer radical polymerization
Bcl-2 :B cell CLL/lymphoma-2
CuAAC :Copper Catalyzed Azide Alkyne Cycloaddition
CVD :Chemical Vapor Deposition
DDS :Drug Delivery System
DLS :Dynamic Light Scattering
DNA :Deoxyribonucleic acid
DOX :Doxorubicin
ER :Estrogen Receptor
FACS :Fluorescence-Activated Cell Sorting
FC :Flow Cytometry
FDA :U.S. Food and Drug Administration
FPT :Freeze-Pump-Thaw
FTIR :Fourier Transformation Infrared Spectroscopy
GAPDH :Glyceraldehyde 3-phosphate Dehydrogenase
GO :Graphene Oxide
GPC :Gel Permeation Chromatography
HER2 :Human Epidermal Growth Receptor 2
IC_{50} :Half Maximal Inhibitory Concentration
LDH :Lactate Dehydrogenase
MALS :Multi-Angle Light Scattering
MS :Mass Spectrometry
PCR :Polymerase chain reaction
PR :Progesterone Receptor
RBC :Red Blood Cells
RES :Reticuloendothelial System
rGO :Reduced Graphene Oxide
RNA :Ribonucleic Acid
ROS :Reactive Oxygen Species
SEM :Scanning Electron Microscopy
siRNA :Small Interfering RNA
TEM :Transmission Electron Microscopy
TGA :Thermal Gravimetric Analysis
UV-Vis :Ultraviolet–Visible Spectroscopy
XPS :X-ray Photoelectron Spectroscopy

HEDEFLİ, İKİLİ İLAÇ TAŞIMA SİSTEMLERİ İÇİN FONKSİYONEL NANO-PLATFORMLARIN GELİŞTİRİLMESİ

ÖZET

Erhan Demirel

Biyomedikal Mühendisliği ve Biyoenformatik, Doktora

Tez Danışmanı: Prof. Dr. Yasemin Yüksel Durmaz

Eylül, 2022

Biyolojik uygulamalarda ilaç ve gen taşıyıcı olarak grafenin (G) kullanımına ilişkin araştırmalar, nanomalzeme olarak üstün özelliklerinin öne çıkması neticesinde katlanarak artmıştır. Öte yandan, birçok araştırma grafen ve türevleri olan grafen oksitin (GO) ve indirgenmiş grafen oksitin (rGO) farklı mekanizmalarla hücreler üzerinde sitotoksik etki gösterdiğini belirlemiş ve biyolojik uygulamalarda kullanımlarıyla ilgili endişeler ortaya çıkarmıştır. Çözüm olarak yüzeyin biyouyumlu polimerlerle modifikasyonu yaygın olarak kullanılmakta olup grafen türevlerinin su ortamındaki zayıf çözünürlüğü veya yüzey kimyasından kaynaklanan dezavantajlarının üstesinden gelmek için poli(etilen glikol) (PEG)'nin kullanımı umut verici bir yaklaşımdır. Bu doktora projesinde, biyomedikal uygulamalar için iki boyutlu grafen tabanlı nanomalzeme kullanımı için bir platform olarak rGO'in potansiyel kullanımı değerlendirilerek deneysel çalışmalara başlanmıştır, bu amaçla farklı PEG uzunluğuna ve polimer bileşimine sahip poli[(poli(etilen glikol) metil eter metakrilat)-*ko*-(metil metakrilat)-*ko*-(piren metakrilat)] (P(PEGMA-*ko*-MMA-*ko*-PMA), PMP) kopolimerleri ATRP kullanılarak hazırlanmış, GO yüzeyine π-π etkileşimleri ile yapıdaki piren birimleri aracılığıyla tanıtılmıştır. PMP-rGO türevi nanoplatformların fizikokimyasal özelliklerini anlamak için birçok açıdan kimyasal olarak karakterize edilmiş ve en uygun sonucu seçmek için su ortamındaki kararlılıkları ve biyouyumlulukları açısından birbirleriyle karşılaştırılmıştır. Çalışmanın bu ilk aşamasında PEG'leme yöntemi mükemmelleştirilmiş, üretilen nanomalzemelerin kararlılığı, hemolitik aktivitesi, sitotoksisitesi ve hücreye alımı test edilmiş ve en uygun sonuçlar %71,2 kaplama verimi ile üretilen, 3 piren ünitesi ve kütlece %86 PEG içeren kopolimer kaplı rGO'in kullanımı ile elde edilmiştir.

Başarı ile sonuçlanan ilk aşamanın ardından ikinci aşamada kopolimer kompozisyonuna azit uç gurubu taşıyan bir monomer eklenerek kullanımı kolay bir metot olan CuAAC reaksiyonu ile hedefleme ajanları ve çok yönlü polimerler gibi yeni fonksiyonların eklenmesinin önü açılmıştır. Literatüre ilk kez bildirilen, yapısında alkin ve hidrazon bağı bulunduran bir ATRP başlatıcısı kullanılarak katyonik yük taşıyan bir kopolimer sentezlenmiş ve PAMP kopolimeri üzerine aşılanarak poli[(poli(etilen glikol)metil eter metakrilat)-*ko*-(3-azidopropil metakrilat)-*ko*-(metil metakrilat)-*ko*-(1-pirenmetil metakrilat)]-*g*-poli(heksil metakrilat-*ko*-2-(dimetilamino)etil metakrilat-*ko*-N,N,N-trimetilaminoetil metakrilat iyodür) (PAMP-g-CP) yapısı elde edilmiştir. Bu çalışma sırasında kullanılan modüler fonksiyonlandırma tekniklerinden yararlanılarak hedefli, ikili gen ve ilaç taşıma nanoplatformu oluşturulmuş, GO, PAMP-g-CP ile kaplanıp, ardından EPPT1 konjugasyonu, Dox yüklemesi ve siRNA kompleksleşmesi yapılarak

EPPT1-PAMP-CP-rGO-Dox-siRNA elde edilmiştir. Nihai nanoplatform ve türevlerinin fizikokimyasal özellikleri kapsamlı bir şekilde karakterize edilip, *in vitro* ve *in vivo* uygulamaları ve etkinliği araştırılmıştır. Elde edilen grafen türevi, yüksek oranlarda Dox yüklerken başarılı bir şekilde anti-GAPDH ve anti-Bcl-2 siRNA'ları ile komplekslerini oluşturmuş ve pH değişikliği ile salım kinetiği profili arasında geçiş yaparak kontrollü bir ilaç salımın profili göstermiştir. Ayrıca, PAMP-CP-rGO'in Dox yüklü ve hedefli türevlerinin *in vitro* sitotoksisite testi sonuçlarına göre, hedeflenmemiş versiyonlara göre konsantrasyona bağlı olarak değişen seçici hücresel toksisite gösterdiği tespit edilmiştir. Nanoplatformların EPPT1 ile kanser hücrelerini hedeflenmesindeki etkinliği, konfokal mikroskobu ve akış sitometrisi analizi kullanılarak hücre içine alım oranları gözlemlenerek test edilmiş ve nanoplatformların kanser hücreleri tarafından yüksek oranda hücre içine alındığı tespit edilmiştir, ayrıca Lyso Tracker® Green DND-26 boyaması ile MCF-7 hücrelerinin asidik bölümlerinde EPPT1-PAMP-CP-rGO-Dox-siRNA varlığı gösterilmiştir. Nihai nanoplatformun, hedeflenen GAPDH ve Bcl-2 protein seviyelerinin yanı sıra Bcl-2 kodlayan mRNA ifadesinde düşüşe neden olduğu tespit edilmiştir. Nanoplatformların anti-kanser etkisi, atimik nude fareler üzerinde bir kanser modeli ile incelenmiş ve yüksek oranda tümör büyümesinin baskılandığı tespit edilmiştir. Bu bulguların ışığında, PAMP-CP-rGO nanoparçacıkları, hidrofobik ilaç moleküllerinin ve genetik materyalin hedeflenen tümör bölgesine taşınmasında yüksek verimlilik göstermekte olup, kanser hücrelerini iki ayrı strateji ile tedavi ediyor olması yenilikçi kanser tedavi yöntemlerine uyarlanabilir bir yaklaşım sağlamıştır.

Anahtar sözcükler: İlaç taşıma, gen taşıma, grafen oksit, indirgenmiş grafen oksit, polietilen glikol, Doksorubisin, Dox, siRNA, GAPDH, Bcl-2, EPPT1, nude fare, ksenograft model.

THE DEVELOPMENT OF MULTIFUNCTIONAL NANOPLATFORMS FOR TARGETED DUAL DRUG DELIVERY

ABSTRACT

Erhan Demirel

Ph.D. in Biomedical Engineering and Bioinformatics

Advisor: Prof. Dr. Yasemin Yüksel Durmaz

September, 2022

The research on the use of graphene (G) in biological applications as a drug and gene carrier has increased exponentially simply due to its superior properties as a nanomaterial. On the other hand, many research studies have shown graphene and its derivatives graphene oxide (GO) and reduced graphene oxide (rGO) show cellular cytotoxicity with different mechanisms and emerge concerns regarding their use in biological applications. The modification of the surface with biocompatible polymers is a promising approach to overcome drawbacks that come from poor solubility or surface chemistry of graphene derivatives, where poly(ethylene glycol) (PEG) has been extensively used. In this PhD study, experimental studies were initiated by assessing the potential use of rGO as a platform for the use of 2D graphene-based nanomaterial for biomedical applications, with this goal poly[(poly(ethylene glycol) methyl ether methacrylate)-*co*-(methyl methacrylate)-*co*-(pyrene methacrylate)] (P(PEGMA-*co*-MMA-*co*-PMA), PMP) copolymer with different PEG length and polymer composition were prepared by using ATRP, introduced to GO surface via π-π interactions through multiple pyrene units on the copolymer. PMP-rGO nanoplatforms were characterized chemically in many respects to understand the physicochemical properties of the composites, and they were compared to each other based on their stability in aqueous environments and their biocompatibility to select the most favorable outcome. In the first stage of the study, PEGylation method was perfected, produced nanomaterials were tested for their stability, hemolytic activity, cellular cytotoxicity and uptake, and the most favorable results were obtained from 3 pyrene units and 86% PEG containing copolymer coated rGO with a 71.2% coating efficiency.

Taking into account the successful initiation, in the second phase of the study selected copolymer composition was enriched with the incorporation of an azide functional monomer on the side chain to enable easily conducted modifications by CuAAC reaction to introduce new functionalities to the system such as active targeting agents or versatile copolymers. A cationic charge carrying copolymer was synthesized by ATRP using a first-time reported ATRP initiator that has alkyne and hydrazone bond on its structure and grafted onto PAMP copolymer via CuAAC to produce poly[(poly(ethylene glycol) methyl ether methacrylate)-*co*-(3-azidopropyl methacrylate)-*co*-(methyl methacrylate)-*co*-(1-pyrenemethyl methacrylate)]-*g*-poly(hexyl methacrylate-*co*-2-(dimethylamino) ethyl methacrylate-*co*-N,N,N-trimethylaminoethyl methacrylate iodide) (PAMP-g-CP). Targeted, dual gene and drug delivery nano-platform was constructed by taking advantage of modular functionalization techniques that were utilized during this study,

GO was coated with PAMP-g-CP, followed by EPPT1 conjugation, Dox loading, and siRNA complexation resulting in EPPT1-PAMP-CP-rGO-Dox-siRNA. The final nanoplatform and its derivative's physicochemical properties were thoroughly characterized, and its *in vitro* and *in vivo* applications and effectiveness were studied. The resulting graphene derivative could load high rates of doxorubicin and successfully conjugated anti-GAPDH and anti-Bcl-2 siRNA, consequently showing a controlled drug release that switches between release kinetics by the change of pH. Moreover, the *in vitro* cytotoxicity test of PAMP-CP-rGO's Dox loaded and targeted derivatives show concentration-dependent, selective cellular toxicity than non-targeted versions. Efficacy of EPPT1 targeting was tested by cellular uptake experiments using confocal microscopy and flow cytometric analysis and high uptake rates were detected, additionally, EPPT1-PAMP-CP-rGO-Dox-siRNA was located in the acidic compartments of MCF-7 cells by Lyso Tracker® Green DND-26 staining. The final nanoplatform induced high transfection and knockdown efficiency regarding targeted GAPDH protein and Bcl-2 protein levels as well as Bcl-2 coding mRNA levels. Anti-cancer effect of the nanoplatforms was studied by a xenograft model on athymic nude mice and significant tumor progress suppression was detected. In the light of these findings, PAMP-CP-rGO nanoparticles show high efficiency in transporting hydrophobic drug molecules and genetic material to the targeted tumor site, and the fact that they treat cancer cells with the combination of two different strategies has provided a modular approach to innovative cancer treatment methods.

Keywords: Drug delivery, gene delivery, graphene oxide, reduced graphene oxide, polyethylene glycol, Doxorubicin, Dox, siRNA, GAPDH, Bcl-2, EPPT1, nude mice, xenograft model.

CHAPTER 1

1. INTRODUCTION

The key objective of recent research and technological advancement has been nanotechnology and associated implementations. Due to their unique properties including biological, physical, chemical, electronic, and optical features their applications in electronics and other disciplines are currently available for the development and use of materials and devices at the nanoscale [1]. Particularly, the greatest expectations are placed on its use in biotechnology and medicine, with the potential to significantly improve the detection and treatment of various diseases in the future. An increasing number of nano-sized drug delivery systems are being developed for different treatment and diagnosis approaches including molecular imaging and early detection, hydrophobic anticancer drugs, therapeutic oligonucleotides, and imaging probes are being incorporated with nano-sized trailers to improve their effectiveness against the targeted disease separately or in combination [2]. The *in vitro* and *in vivo* activities of these drug delivery systems together with the experimental and clinical studies regarding their biocompatibility, stability, control over drug release, targetability, and response to internal and external triggers have been demonstrated by many studies in the literature [3].

Nanoparticles with various properties were developed with different techniques for use in diagnosis and treatment, designed to allow early detection of the disease and determination of the stage of the disease and controlled release of the drug and minimize the dosage level, reduce side effects, and increase the effectiveness of treatment [4], [5]. Different approaches have been studied for the advancement of ideal drug delivery systems including, natural biopolymers such as chitosan, dextran, and alginate, dendrimers consisting of branched polymers, nanoparticles made of inorganic materials such as iron oxide, titanium dioxide, and gold, lipid-based liposomes, micelles and nano-

emulsions, polymeric nanoparticles prepared by synthetic poly(lactic-*co*-glycolic acid), polycaprolactone, poly(ethylene glycol) polymers, and carbon-based materials such as carbon nanotube, graphene, and quantum dots [6]. Each type of nanoparticle has its advantages and disadvantages; even so, carbon nanomaterials (carbon nanotubes, fullerenes, nanodiamonds, quantum dots, and graphene) with their distinct physicochemical properties stand out as one of the most appealing candidates in cancer theranostics [7]. With the main benefit of excessive surface area, sp^2 and sp^3 hybrid carbon atoms get easily functionalized either with covalent or non-covalent strategies [7], [8]. Carbon nanoparticles can be easily conjugated with imaging agents for the emergence of contrast agents, loaded with a broad variety of anti-cancer drugs and targeting ligands for improved drug delivery systems with tunable release profiles, and customized to carry gene treatment agents [9].

The discovery of a single-layered, two-dimensional carbon allotrope with a honeycomb lattice structure arrangement of graphene in 2004 has attracted considerable interest for its potential in biomedical applications, since it has remarkable physicochemical properties, for instance, high specific surface and drug loading capacity and excellent thermal conductivity [10]. Numerous nano-sized graphene-based drug carriers have been developed since their discovery and their activities have been tested *in vivo* and *in vitro,* showing promising results, however, there are still many limitations with graphene-based nanocarriers, such as instability in aqueous mediums, premature drug release during systemic circulation, nonspecific accumulation in RES organs, inadequate tumor diffusion capacity, and uncontrolled drug release at the tumor site [11] - [13]. Building stimulus-responsive drug delivery systems that are susceptible to endogenous or exogenous stimuli is an effective technique to get around these restrictions which improve therapeutic effects on the target location. Evidently, graphene-based drug delivery systems have shifted toward the tumor microenvironment and/or intracellular stimuli responsive carrier, in particular enzymatic activity, redox potential, and pH. This will ultimately improve therapeutic efficacies and minimize potential side effects [11], [12].

The development of multifunctional nanoplatforms for targeted dual drug delivery has been achieved in two stages, in the first stage, unique copolymers composed of poly(ethylene glycol methyl ether methacrylate) (PEGMA 500 or 2000 g/mol), methyl methacrylate (MMA) and 1-pyrenemethyl methacrylate (PMA) in short P(PEGMA-*co*-MMA-*co*-PMA) were synthesized at different monomer ratios for PEGylation of GO by

employing π-π stacking between pyrene units on the copolymer sidechain and conjugated graphene oxide surface. GO was reduced *in-situ* during PEGylation to achieve similar properties to pristine graphene and from the comparison of their dispersibility and stability in water environment, hemolytic activity, cytotoxicity (by testing cell viability, ROS generation, and LDH release), and cellular uptake a successful copolymer composition was selected containing a certain number of PEG and pyrene repeating units.

After overcoming dispersibility and stability problems of PEGylated rGO most biocompatible composition was selected, P(PEGMA-*co*-MMA-*co*-PMA) expanded with an azide methacrylate for adding new features by copper catalyzed azide alkyne cycloaddition (CuAAC) reaction. In parallel, a second copolymer consisting of hexyl methacrylate (HMA), 2-(dimethylamino)ethyl methacrylate (DMAEMA), and cationic N,N,N-trimethyl amino ethyl methacrylate (TMAEMA) (P(HMA-*co*-DMAEMA-*co*-TMAEMA)) was synthesized with a custom made multifunctional ATRP initiator. The cationic charge-carrying copolymer was grafted onto the PEG-bearing frame enabling oligonucleotide complexation, conjugated with EPPT1 peptide for targeting the tumor site, and loaded with an anticancer drug (**Figure 1.1**). The resulting "smart" nanocarrier was prepared in combinations to test their *in vitro* drug release kinetics, anticancer effectiveness, gene and protein knockdown abilities, cellular uptake performance, the synergistic effect of siRNA and Dox, and *in vivo* tumor inhibition on a carcinoma model using tumor-bearing mice.

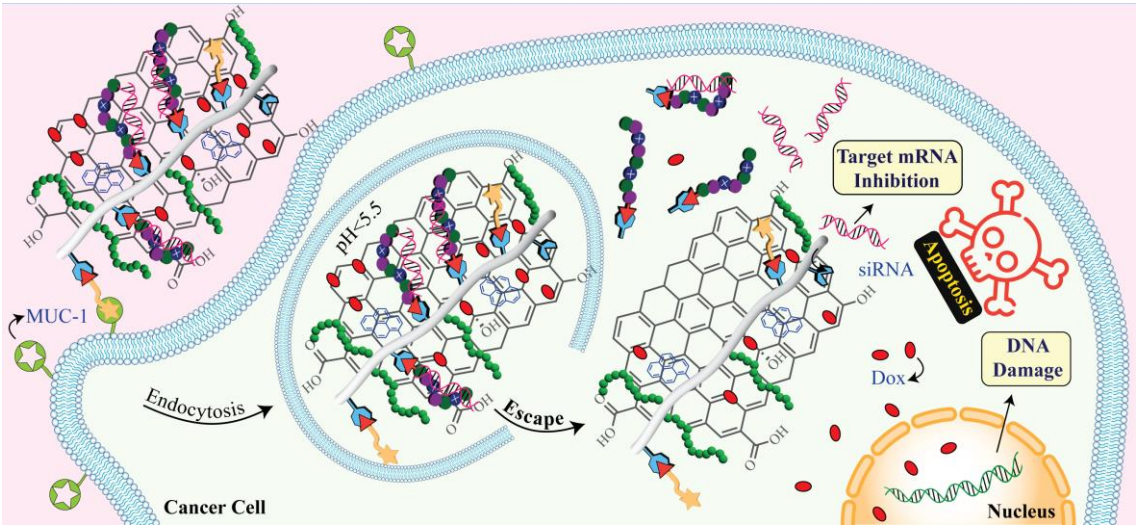


Figure 1.1: Schematic representation of cellular uptake, endosomal escape, Dox and siRNA release and induced cell death by EPPT1-PAMP-CP-rGO-Dox-siRNA.

CHAPTER 2

2. THEORETICAL PART

2.1. Cancer Statistics and Current Treatment Approaches

Cancer is the primary or second major cause of death before the age of 70 in 112 of 183 countries, according to estimates from the World Health Organization (WHO) in 2019 and ranking cancer as a primary cause of mortality that significantly reduces the chances of improving life expectancy in every country of the world [13], [14]. In 2020, there were an estimated 2.3 million new cases of female breast cancer, which overtook lung cancer as the most common cancer diagnosed in the female population. Lung and colorectal cancers were the next most common cancers, with an estimated total of 19.3 million new cases and almost 10 million cancer deaths worldwide. Together with an anticipated 1.8 million casualties, lung cancer continued to be the most common kind of cancer, followed by colorectal and liver cancers in both sexes. From the point of view of incidence and mortality colorectal cancer and lung cancer are the second most frequently diagnosed cancer in women, after breast cancer [14].

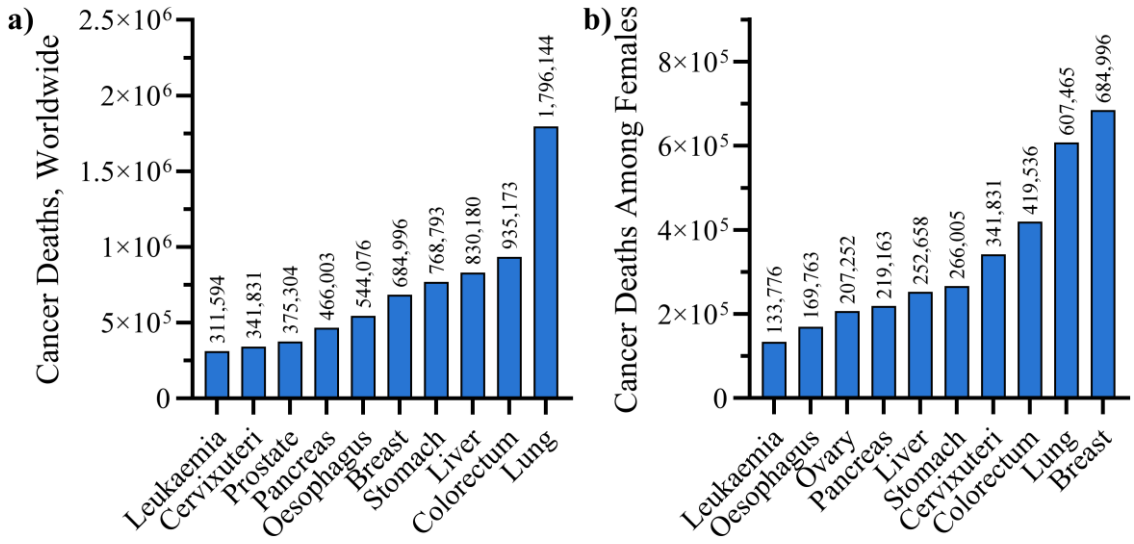


Figure 2.1: Number of deaths by major types of cancers **a)** all sexes and **b)** females [15].

When focused on isolated cancer death numbers for Turkey, it can be seen cancer rates have a parallel trend with the world, there is an acceleration in lung cancer after the 2000s (**Figure 2.2a**), which can be seen as a factor in the world's second fastest growing cigarette market in this period [16]. As of 2019, death by lung cancer leads to death by cancer in the country, while the colorectum, stomach, pancreas, and breast follow it [17].

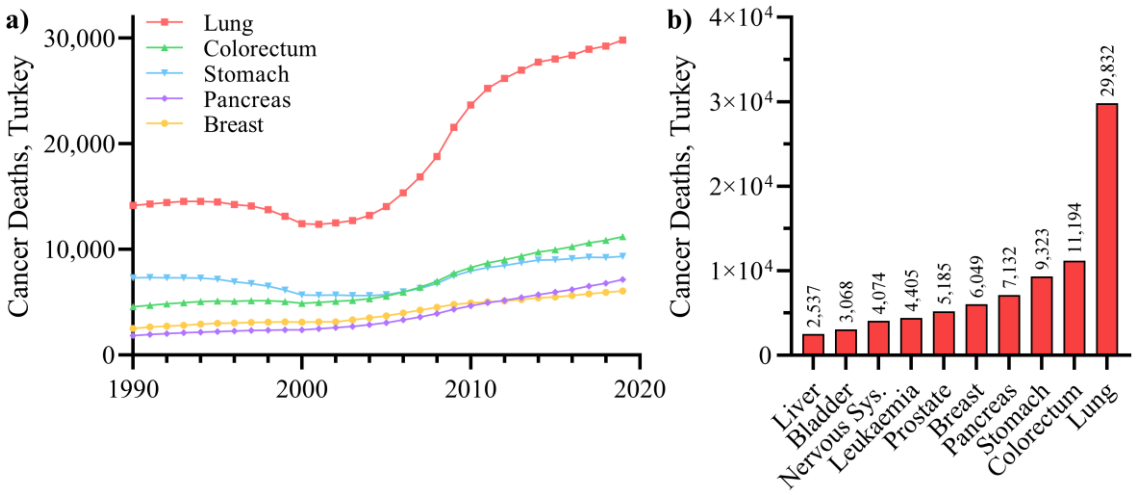


Figure 2.2: a) Number of cancer death by 5 major cancer types by year in Turkey, **b)** the number of cancer death by major type of cancer in 2019 [17].

The plague of the 21st century, cancer develops when healthy cells in a particular part of the body fail in controlled cell death when after DNA damage, they begin to grow out of control, developing locally in the tissue is followed by spreading to the lymph nodes and other tissues and organs [18]. When focusing on breast cancer, has been proven to be a difficult disease to treat due to the heterogenicity of the disease as there are different subtypes, each exhibiting different but specific characteristics [19]. When the diagnosis of breast cancer is made pathologically, following the work of Perou and coworkers in 2000 breast cancer is divided into 4 major subgroups by detecting estrogen receptor (ER), progesterone receptor (PR), and human epidermal growth receptor 2 (HER2) expressions ([ER+|PR+] HER2-, [ER+|PR+] HER2+, ER-PR-HER2+, ER-PR-HER2-), in addition to tumor size, class and node involvement variables, cancer subtype is used for prognosis and treatment of the patient [20]–[22]. Different than triple-negative breast cancer (ER-PR-HER2-), hormone receptor-positive breast cancer types usually respond well to hormone therapy. Although triple-negative breast cancer has a very small proportion of all breast cancers, this group of patients is drawing attention due to the very high mortality rate, the aggressive progress of the tumor, and the lack of individually targeted treatment [23]–[26].

There are several methods and medications for treating cancer depending on the type of cancer, its stage, and the overall strategy of the treatment goal. Some therapies are performed "locally," like surgery and radiation therapy, to treat a particular tumor or region of the body, and some therapies are called “systemic” treatments because of their impact on the entire body, such as chemotherapy [27]. Traditional breast cancer treatment consists of surgical intervention, chemotherapy, radiotherapy, and immunotherapy options. Chemotherapeutic agents are usually small-structured molecules, during the treatment they can be used singly or in combination, and they are classified as cytostatic antibiotics (doxorubicin, idarubicin), alkylating agents (cyclophosphamide, ifosfamide), antimetabolites (fluorouracil, cytarabine) and anti-microtubule agents (paclitaxel, etoposide) [28]. Different emerging therapeutic approaches for instance immunotherapy, gene therapy, and phototherapy have been shown to overcome drawbacks of the traditional approach by reducing unwanted effects on the patient’s body. By using an extensive toolkit that is provided by nanotechnology many scientists focus on the development of ideal cancer nano-sized theranostics [29].

2.2. Drug Delivery Systems

Delivering therapeutic compounds for the treatment of many diseases has been accomplished in pre-clinical and clinical settings using a drug delivery system (DDS). Standard drugs, which are often taken orally or intravenously, have numerous benefits, including simplicity of administration and patient acceptance, but it also has significant drawbacks. When taken orally, many medications have varying rates of uptake, also the low pH environment and digestive enzymes may cause certain medications to break down before they reach the bloodstream, reducing their efficacy. Due to its poor biodistribution and lack of selectivity, oral drug administration is not recommended for medications that need to target certain organs; instead, they may end up in the liver or kidney, causing toxicity due to drug absorption [30], [31]. Many of the drawbacks that traditional drug delivery methods have can be solved by using controlled drug delivery systems; these modern technologies improve drug pharmacokinetics, increase systemic circulation, and decrease the appearance of pharmacological side effects different from conventional chemotherapy that affect both healthy and cancerous cells, since it is administered nonspecifically, resulting in poor efficacy and significant toxicities throughout the body [32]. Controlled DDSs also prevent cargo from being cleared or degraded on its way to

the target site, helping with nonspecific protein distribution, enabling the development of novel therapeutics such as oligonucleotides used for gene therapy, and preventing their absorption by the reticuloendothelial system and enzyme degradation in the bloodstream [33].

Following scientific developments in nanotechnology, nanoparticles with a diameter of around 10-1000 nm are now a potential choice for regulated DDS, they can be applied to the prevention, detection, and treatment of disease [34]. On top of the protection of the drug from environmental effects, by improving the half-life of the medication, enhancing the solubility of certain hydrophobic pharmaceuticals, and releasing the drug in a controlled or sustained manner, nanoparticles will enhance the effectiveness of the treatment. Additionally, the introduction of active targeting next to readily available enhanced permeability and retention (EPR) effect and stimuli-responsivity, nanoparticles would aid in reducing the toxicity and managing the biodistribution of medications with high efficiency [35].

In the 1960s, liposomes the first nano-sized DDS discovered were utilized as protein and drug carriers based mainly on liposomes, followed by dendrimers, microneedles, and carbon-based nanoparticles (**Figure 2.3**). Since then, an ever-increasing variety of materials has been converted into nanoparticles, and the FDA has authorized over 20 nanosized therapeutics, and even more undergoing clinical trials [35].

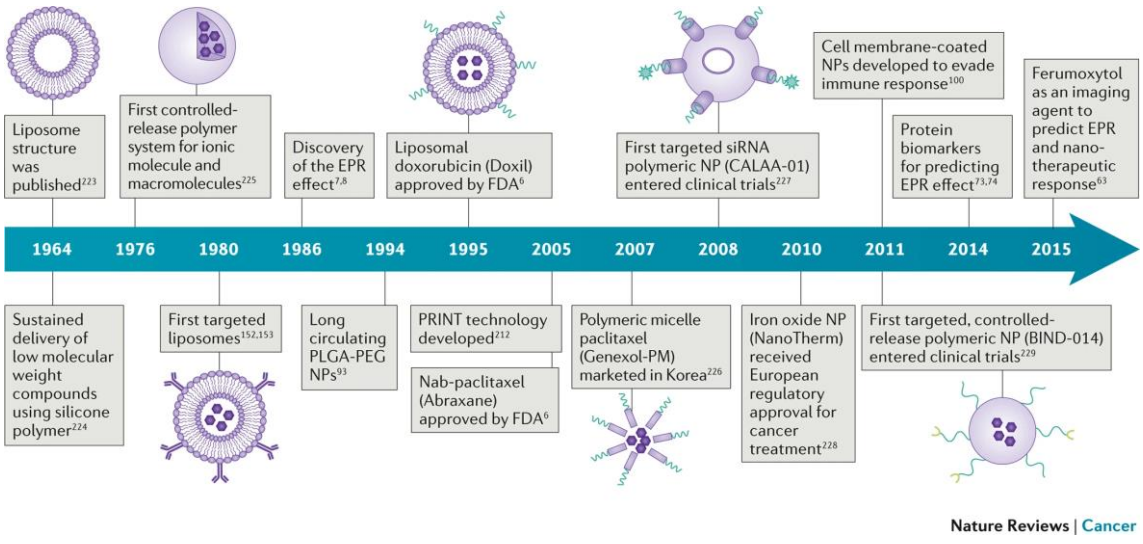


Figure 2.3: Milestones of nano-sized drug delivery. (Adapted from: [35])

Organic and inorganic nanomaterials developed since the 1960s have been researched and characterized in countless ways for use as drug delivery systems aiming at various

diseases not only for treatment but also for diagnosis [36]. From a recent literature review, various examples can be seen that utilizing nanomaterials prepared by using natural or synthetic polymers, viruses, metal oxides, and carbon derivatives have been intensively investigated on their own or with surface modifications (**Figure 2.4**) [37]. Even though polymer-based nanomaterials employed for gene and drug delivery received approval for their commercial use most of the inorganic nanoparticles are still being preclinically examined for their safe and effective use as nanocarriers [38]. Even though they are still underdevelopment inorganic nanoparticles have shown great potential in drug delivery systems [39]. Carbon-based inorganic nanocarriers serve as skeletons for drug delivery systems allowing drug loading with high efficiency and controlled release, maintaining structural integrity during blood circulation, and high cellular uptake, while enabling different modification methods and resulting in biocompatible nanocarriers [40]. The diverse carbon nanostructures and the distinctive chemical characteristics of carbon are factors in the wide-ranging commercial and therapeutic applications of carbon nanomaterials. Carbon nanostructures including fullerenes, carbon nanotubes, and graphene share the hexagonal arrangement owing to sp^2 hybridized carbon atoms in their structure has undiscovered potential for use in biomedical applications [41].

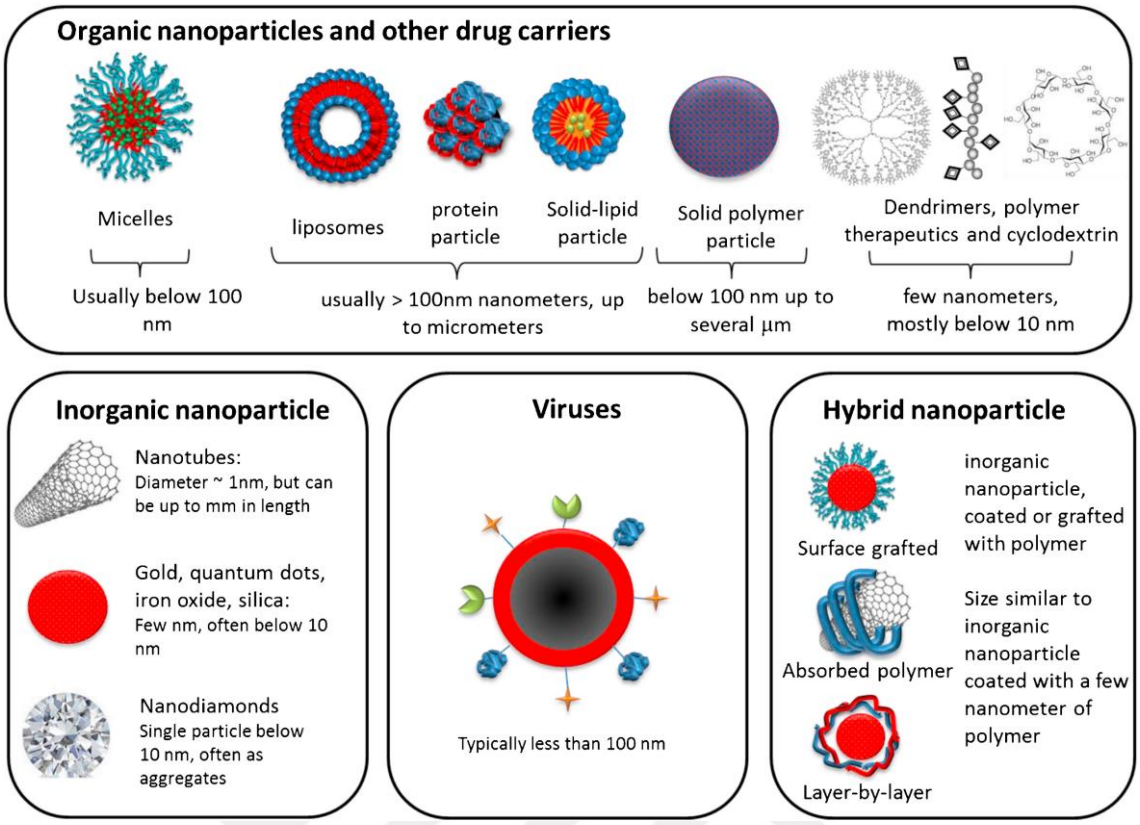


Figure 2.4: A collection of illustrations demonstrating the many forms of nanoparticles. (Adapted from: [42])

2.3. Chemical and Physical Properties of Graphene, Graphene Oxide, and Reduced Graphene Oxide

One of the most abundant elements in nature, carbon, is the first element in group 4A on the periodic table capable of forming 4 bonds. As a building block, it unlocks an infinite number of combinations to produce unique compounds, this ability of carbon has placed it at the core of life for carbon-based organisms. Aside from compounds produces in combination with other elements, the carbon atom has two naturally accruing allotropes, namely diamond, and graphite but many synthetic allotropes were reported ranging from zero-dimensional (0-D) to three-dimensional (3-D) structures, and each has its own set of physical and chemical characteristics, including varying degrees of hardness and electrical and thermal conductivity [43]–[45].

The discovery of fullerenes in 1985 by Kroto *et al.* [46], followed by the synthesis of carbon nano-tubes in 1991 by Iijima [47] revolutionized carbon chemistry and their use. Since its re-discovery by Geim, Novoselov, and colleagues in 2004, graphene has attracted the most attention among all the carbon allotropes due to its remarkable surface

area, high electrical conductivity, outstanding thermal stability, and excellent mechanical strength. [48]. Single-layered graphene sheets can be used to create all graphitic forms, such as 0-D fullerenes, 1-D nanotubes, and 3-D graphite [49].

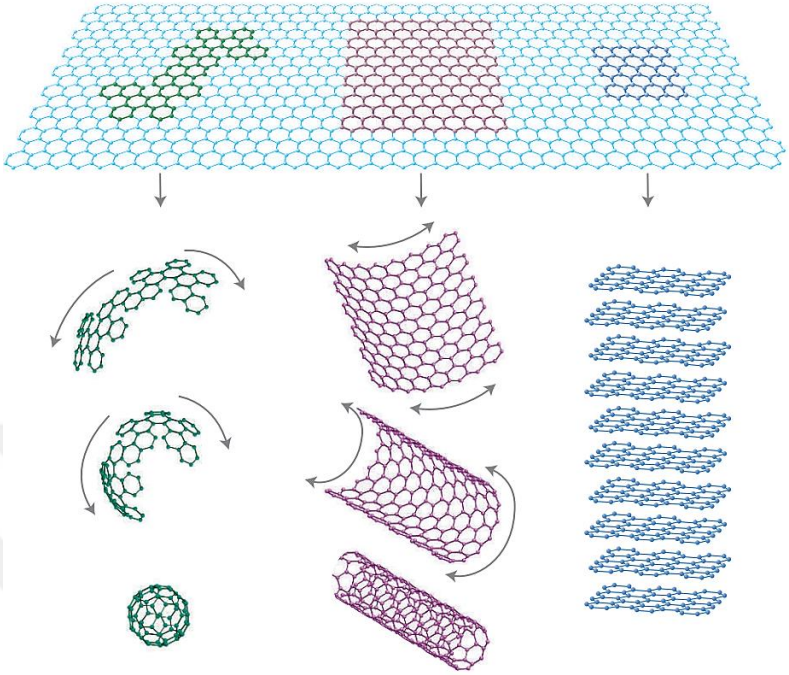


Figure 2.5: Use of graphene to form buckyballs, nanotubes, and graphite (Adapted from: [49]).

One atom thick crystals of carbon in a honeycomb lattice are made up of six-membered rings of sp^2 hybridized carbon atoms and the distance between carbon atoms ranges from 1.42 to 1.47 Å in an ideal structure [50]. Graphene can be found as single-layer or bilayer and few-layer, which have 2 and 3 to 10 layers, respectively as seen in **Figure 2.6**. The bonds between carbon atoms are 3 in plane σ bonds/atom and π orbitals perpendicular to the plane, while the strong s bonds are responsible for the rigid backbone of the honeycomb structure, the π bonds control intermolecular interactions, such as between different graphene layers and conjugated molecules. [51]

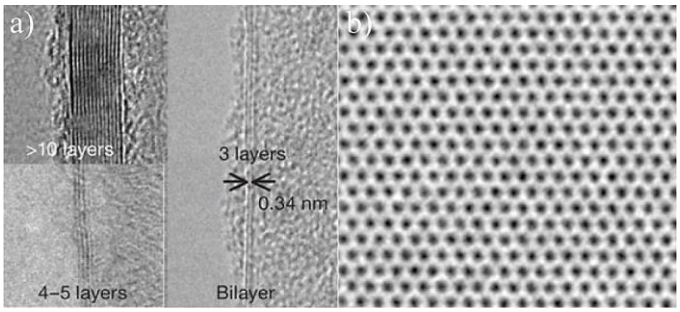


Figure 2.6: a) TEM images of bi and multi-layered graphene sheets (Adapted from: [52]), **b)** image of a single-layered graphene sheet acquired by high-resolution TEM (Adapted from: [53]).

The wonder material graphene has a high in-plane electrical ($\sim 10^4\ \Omega^{-1}\ cm^{-1}$) conductivity and similarly thermal conductivity (~3000 W/mK) [54]. These properties enable its allotrope graphite to be used in electrodes and as heating elements for industrial blast furnaces [55], [56], where taking advantage of the high mechanical stiffness of the hexagonal network (~1060 GPa) and tensile modulus (~400 GPa) graphene is also utilized in carbon fiber reinforced composites [57]. The summary of the properties of graphene can be seen in **Table 2.1**. These superior properties of graphene and derivatives generate an annual demand of more than 1 million tons of graphite worldwide [58].

Table 2.1: List of selected properties of graphene [59].

Properties	Value	Observations
Surface area	$2600\ m^2\ g^{-1}$	Theoretical prediction
Thermal Conductivity	$(5.3 \pm 0.48) \times 10^3\ W\ m^{-1}\ K^{-1}$	Better thermal conductivity than in most crystals
Breaking strength	$40\ N\ m^{-1}$	Reaching theoretical limit
Young's modulus	1.0 TPa	Ten times greater than in steel
Opacity	2.3%	Visible light
Optical transparency	97.9%	Visible light

A variety of production methods have been developed to meet the demands of various needs such as chemical vapor deposition (CVD) have been used for surface or molecular assembly for the production of nanoelectronics or mechanical exfoliation for prototyping and research (**Figure 2.7**) [60]. The mechanical exfoliation, often known as the "Scotch-tape" approach, of bulk graphite and epitaxial chemical vapor deposition were the first methods used to create few- and single-layer graphene nanosheets. Even if they may be favored for their simplistic approach, these methods can not be employed for manufacturing on a wide scale. The obstacle for single or few-layer graphene would be overcoming van der Waals forces binding the layers of graphite, due to its low yield in

terms of preparation researchers replaced the use of pristine graphene with its derivatives like graphene oxide (GO) and reduced graphene oxide (rGO) showing similar properties [61].

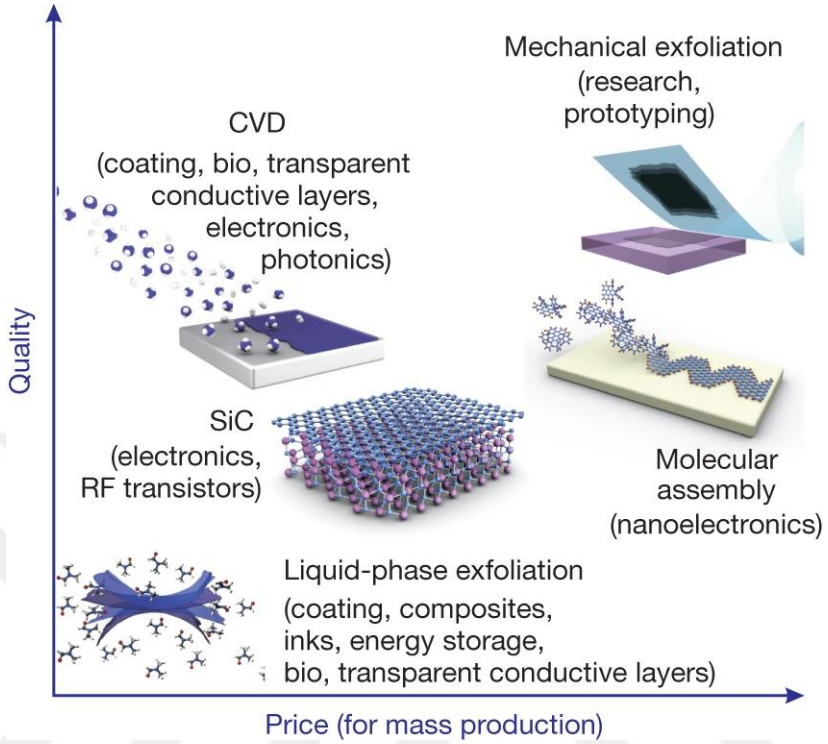


Figure 2.7: Based on particular requirements and uses, alternative manufacturing techniques for graphene and its derivatives are used (Adapted from: [60]).

The production need can be addressed by following chemical methods including chemical derivatization, oxidation-reduction, or the use of surfactants that have been used to exfoliate graphite. GO can be produced rapidly utilizing powerful oxidizing chemicals to exfoliate graphite at a low cost. Historically GO has been prepared with different approaches but the most commonly used approach was reported by Hummers and Offeman in 1958 [62]. This approach utilizes oxidation of graphite by potassium permanganate and sodium nitrate in concentrated sulfuric acid, produced GO can be dispersed in water due to the introduced oxygen functionalities like hydroxyl, epoxide, carboxyl, and carbonyl (**Figure 2.8**) [63].

Even while GO and rGO have weakened characteristics than graphene, they can still be enhanced by introducing additional functionalization using surface modifications. GO is better suited to be functionalized covalently just because its reactivity of it increases since there are more oxygen groups present in GO, especially when compared to rGO. However, rGO is suitable for non-covalent functionalization even when some of its

oxygen sites are retained due to reduced defects on the surface and heals imperfections to act like a graphitic surface [64].

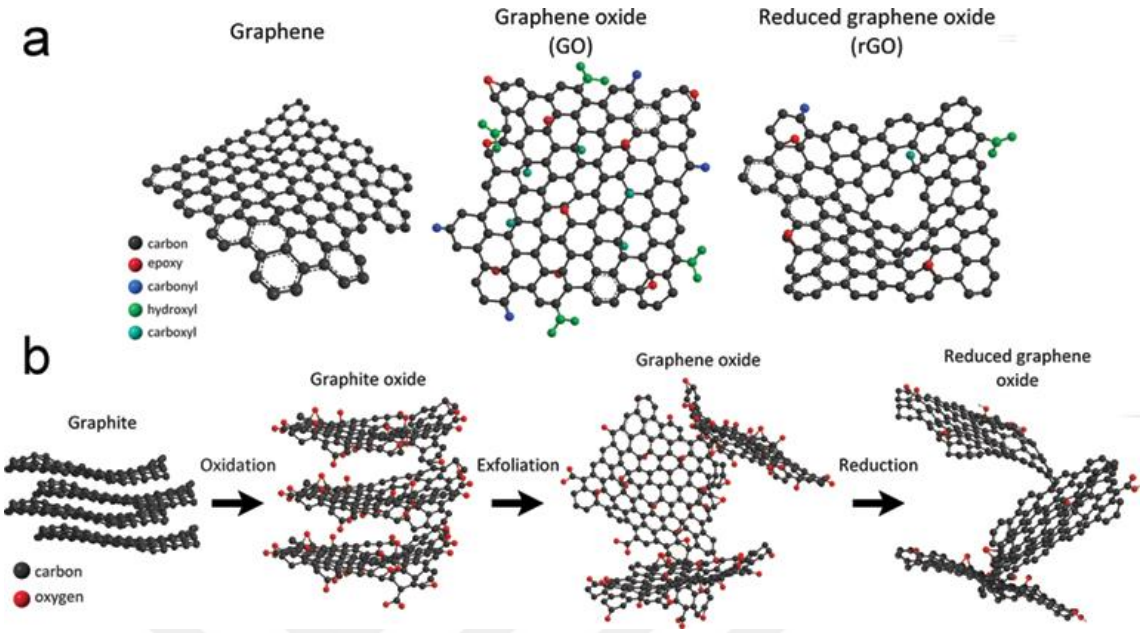


Figure 2.8: Structures of graphene, GO, and rGO and path for rGO production. (Adapted from: [65]).

There have been several different reduction techniques discovered, most of which belong to the categories of chemical, thermal, photo-mediated, and solvothermal reduction. One of the most frequently used is the chemical reduction of GO to rGO. Most of the oxygen-containing functional groups in GO are removed during the reduction processes, and the majority of the π-electron conjugation within the aromatic structure of graphite is recovered, resulting in rGO properties being very similar to graphene [66].

2.4. Biomedical Applications of Graphene Derivatives, Concerns on Cytotoxicity, and Strategies to Improve Biocompatibility

Use of graphene and its derivatives such as GO, rGO and nano-graphene (nGO) have an extent from electronics and optoelectronics [67], energy conversion [68], catalysis [69], 3-D printing [70] to environmental [71] and biological applications especially in the field of bio-imaging [72], gene delivery [73], tissue engineering [74], bio-sensing [75], and drug delivery [76], [77].

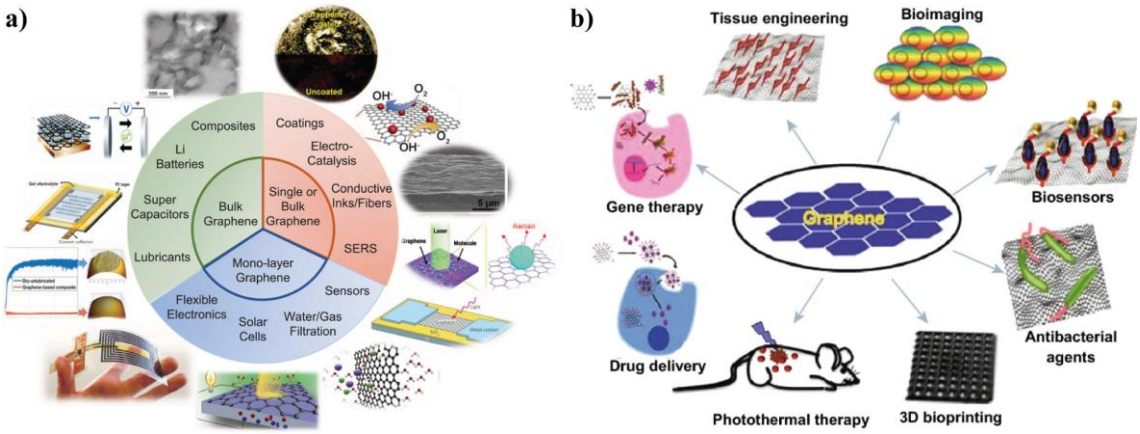


Figure 2.9: a) Key and **b)** biomedical applications of graphene and its derivatives. (Adapted from:[78] and [79])

Among different approaches for gene and drug delivery, such as polymeric [80], lipid [81], carbon [82], and inorganic (silica [83], gold [84], iron oxide [85]) nanoparticles, the use of graphene and its derivatives as gene and drug delivery vehicles have been gaining attention since their discovery. This growing interest in graphene's biological applications has triggered more research to improve its biocompatibility, solubility, and stability in aqueous media to be able to use its superior properties [86]. Recent studies about the cytotoxicity of graphene-based materials revealed that it depends on the shape, layer thickness, size, concentration, dose, surface properties, and surface chemistry of graphene and takes place through different mechanisms [87]–[89]. Graphene derivatives can directly interact with the cell membrane resulting in accumulation on the cell surface and destabilization of the lipid bilayer resulting in leakage of cytoplasm content [87], [90]. They can also cause intracellular generation of reactive oxygen species (ROS), which leads to oxidative stress-mediated apoptosis of the cell [91], [92] and affects DNA directly thereby resulting in genotoxicity[93]. Moreover, wide surface area and charged functional groups enhance the interaction and absorption of proteins and other cell nutrition to the surface of graphene derivatives which leads cells to starvation as shown by Hu and coworkers [94].

The production of ROS which has the potential of downregulation of protective mechanisms, leading to disruption of the structure and function of normal cells has been regarded as the fundamental cause of nanoparticle toxicity. Proteins, DNA, and lipids are potentially damaged by ROS evidently leading to the production of inflammatory cytokines and chemokines. As mentioned before cytotoxicity of graphene derivatives depends on not only shape and size, particle surface chemistry, and surface charges but

also on solubility, stability, and aggregation, photo-activation, mode of interaction with cells, and pH of the system in contact, comprising the duration of exposure, the dosage, and the cell type. Graphene can induce an inflammatory response that generates relatively high levels of hydroxyl radicals and other free radicals [95], [96]. At elevated concentrations such as 200 μg/mL of graphene quantum dots induced reduction in the mitochondrial membrane potential of THP-1 macrophages through increased ROS production, in conjunction with apoptotic and autophagic cell death, accompanied by a rise in the expression of caspase 3, caspase 9, and beclin 1 [97].

In another study, Zhang and colleagues evaluated the cytotoxicity and cellular uptake of carbon nanotubes, nano diamonds, and graphene oxide on HeLa cells. Despite the fact that nano diamond has higher cellular uptake than GO and carbon nanotubes, GO has demonstrated lower cytotoxicity [98]. In another study by using the radiotracer technique biocompatibility and bio-distribution of GO on mice were investigated, and no pathological changes in organs were detected when mice are exposed to a 1 mg kg^{-1} dosage of GO. However, significant pathological changes, including inflammation cell infiltration, pulmonary edema, and granuloma formation at the GO dosage of 10 mg kg^{-1} body weight, conclude that concentration-dependent cytotoxicity caused by GO, as the authors of the paper suggested, greater emphasis should be paid to GO's cytotoxicity [99].

To address the mentioned drawbacks of graphene and its derivatives, several attempts have been made to investigate its behaviors and toxicological processes in order to better understand nanomaterials' behavior for the purpose of preparing safer biomedical applications. A reasonable approach to tackle these issues was found to reduce oxygen functionalities on the GO surface by chemical or thermal reduction, and improve the sp^2 conjugated surface, enhancing the electrical [100], thermal conductivity [101] hydrophobic drug loading capacity [102] and more importantly the *in vitro* [103], [104] and *in vivo* [105], [106] biocompatibility.

Different approaches to improve the stability of graphene derivatives in aqueous environments, reduce accumulation in the reticuloendothelial system (RES) and prolong circulation time in the bloodstream have been employed to eliminate the undesired cytotoxic effect. Concerning the superior properties of graphene, surface treatment is a widely used tool for improving the biocompatibility of nanomaterials for optimal biomedical applications [107]. Hydrophilic coatings such as poly(ethylene glycol) (PEG) [108], [109], poly(vinyl alcohol) [110], polyethyleneimine (PEI) [111], hyaluronic acid

(HA) [112], chitosan [113], starch [114] and proteins [115] administrated either covalent or noncovalent methodologies were promising strategies, a short list of different functionalization methods applied on carbon nanomaterials can be seen in **Figure 2.10** [29]. Nature-inspired smart materials like polydopamine and melanin-like materials have also been used for the coating of carbon-based surfaces to increase biocompatibility [116]–[120]. Among all different polymeric structures, PEG has gained excessive attention since it is US Food and Drug Administration (FDA) approved material, non-toxic, non-immunogenic, non-antigenic polymer with high water solubility [121] and PEGylation reduces reticuloendothelial clearance, prolong circulation time and improve stability of the material [122]. Current literature supports that PEGylation reduces the cytotoxicity of different graphene derivatives and improves physiological stability, and pharmacokinetic properties [108], [109], [123]–[125].

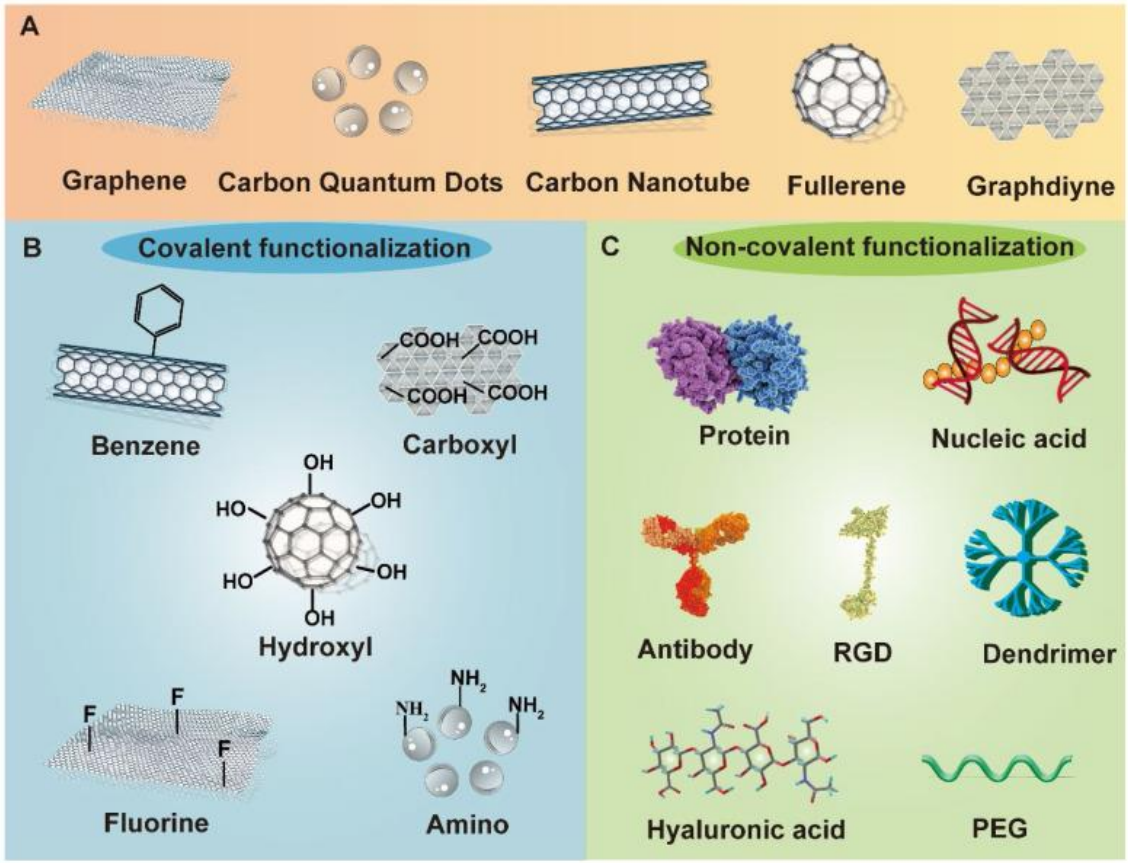


Figure 2.10: A schematic illustration showing covalent and non-covalent modifications applied to carbon nanomaterials to improve their therapeutic effectiveness (Adapted from: [29]).

The first PEGylation application is done by Liu et al. on GO resulting in highly aqueous soluble and physiological fluid stable particles [126]. This example has been followed by

many different researchers; Yang and coworkers have shown the significant passive tumor-targeting ability of non-covalently PEGylated nano-rGO [127], and Yang et. al. found decreased levels of accumulation of PEG-coated graphene in the reticuloendothelial system [128]. Another study has been published by Li and coworkers found that PEGylation of graphene reduces retention and promotes the clearance of graphene from RES organs [129]. *In vivo* biodistribution study by Yang and colleagues in 4T1 tumor-bearing mice showed PEGylated nGO which is administrated intravenously, reduced accumulation in RES organs and demonstrated gradual clearance by renal and fecal excretion, in contrast, over 40 days 20 mg/kg PEGylated nGO administration evidently did not cause appreciable toxicity, as well as high accumulation in the tumor site, was followed by NIR laser irradiation which resulted in a decrease of the tumor volume [130]. In another study, graphene, carboxylated graphene, and PEGylated graphene have been administrated intravenously over 3 months into mice by Sasidharan et al., and they found large aggregates of graphene and carboxylated graphene in the lungs, liver, spleen, and kidney where only a trace amount of PEGylated graphene have been detected in the liver and spleen [131]. As a result, PEGylation is found to be the key to improving the use of graphene derivatives for biological applications. Carboxylic acids on the edge of GO are commonly used for covalent functionalization of hydroxyl functional PEG via esterification reactions that occur with a low yield and leave the vast surface untouched [132] can contribute to cytotoxicity causing starvation of the cell as mentioned above.

Oxygen-containing functional groups like hydroxyl and epoxy on the basal surface are another source of cytotoxic effect of graphene derivatives, promote aggregate formation in the cell medium if they are not specifically used for functionalization [133]–[137] and they create defects on the conjugated honeycomb-like structure of graphene sheets. The reduction of GO not only removes the oxygen-containing functional groups and lattice defects it also recovers the conjugated network of graphene which results in better physical and optical properties and higher surface area for non-covalent modifications [138], [139]. Chemical reduction of GO has been studied intensively to determine the most suitable method for different applications, including reduction with strong alkaline solutions of KOH and NaOH, $NaBH_4$, ascorbic acid, amino acids, glucose, hydrazine hydrate, and hydrohalic acid [140]. Due to its capacity to accomplish a high degree of GO reduction, hydrazine has been one of the most often employed reducing agents. Studies

have shown that this reduction can increase the thermal stability of graphene and restore its π-conjugated structure [138], [141], [142].

2.5. Use of Graphene, GO, and rGO as Gene and Drug Delivery Platforms

A single layer, the two-dimensional structure of graphene is an extreme instance in which every atom on the surface is exposed to the environment, increasing surface area and leading to high drug loading capacity [143]. Alteration of graphene derivatives, in particular for drug delivery applications can be achieved by utilizing functional groups and covalently binding onto the surface but mostly edges of the plane or else taking advantage of van der Waals and π-π interactions of sp^2 hybridized carbon atoms for non-covalent modifications, making graphene an ideal carrier for hydrophobic drug molecules, nucleic acids and proteins [107], [144]. Non-covalent functionalization methods have been utilized for both surface engineering and non-polar drug conjugation on the graphene surface, π-π stacking, Van der Waals forces, electrostatic interactions, and hydrogen bonding are commonly employed forces, in contrast, π-π stacking is the most efficient method to perform non-covalent modifications, especially by the use of pyrene groups on organic molecules and polymers [145]–[147]. Binding force between GO and pyrene group has been measured by Zhang and coworkers by conjugating graphene with a modified AFM tip which consists of pyrene bearing PEG and pull-out force has been measured to be ~55pN indicating a strong interaction between pyrene and graphene surface [148].

Having superior properties does not straightforwardly enable the biological use of graphene derivatives, although they should be treated such as by polymers to reduce their cytotoxicity and if needed provide cationic surface characteristics to allow electrostatic interactions with negatively charged oligonucleotides. Surface modifications have been summarized in the previous section, following the promising results mentioned earlier, many drug carriers prepared by PEGylation of the graphene surface have been studied either through covalent interactions or non-covalent interactions to carry hydrophobic anticancer drugs such as paclitaxel [149], doxorubicin [150] and camptothecin [151].

A natural defense against the invasion of external genes is RNA interference (RNAi) based on short double-stranded RNAs [152]. siRNA treatments have gone through several ups and downs since the RNAi idea was first introduced in 1998 by Fire and Mello which led them to the Nobel Prize in Physiology or Medicine in 2006 [153], [154]. By

introducing artificially produced siRNA into mammalian cells in 2001, Tuschl et al. were able to successfully suppress the expression of a particular gene, which resulted in an increase in the developmental activity of new siRNAs and applications [155]. As a result of this initiative in 2018, the European Commission (EC) and the US-FDA mutually authorized ONPATTRO® (patisiran, ALN-TTR02) as the first commercial RNAi-based therapy for the treatment of polyneuropathy associated with hereditary trans-thyretin-mediated amyloidosis [156]. In parallel with anticancer drug delivery with an increasing understanding of the molecular mechanisms of endogenous RNA interference, researchers are focusing on the use of siRNA as a new nucleic acid therapy for cancer treatment, where siRNAs can be used for down-regulation of the genes involved in disease progression or for improvement of chemosensitivity of cancer cells [157].

Several intracellular and extracellular barriers prevent siRNA from being used extensively in clinical settings, limiting its potential for drug development. Using naked or unmodified siRNA exhibits unsatisfactory stability, poor pharmacokinetic behavior, and the potential to induce off-target effects. When siRNA is systematically administered into circulation, the phosphodiester bond is sensitive to RNases and phosphatases, which causes rapid fragmentation by endonucleases or exonucleases throughout the body. This prevents the accumulation of intact therapeutic siRNA in the targeted tissue (**Figure 2.11**) [158]–[160].

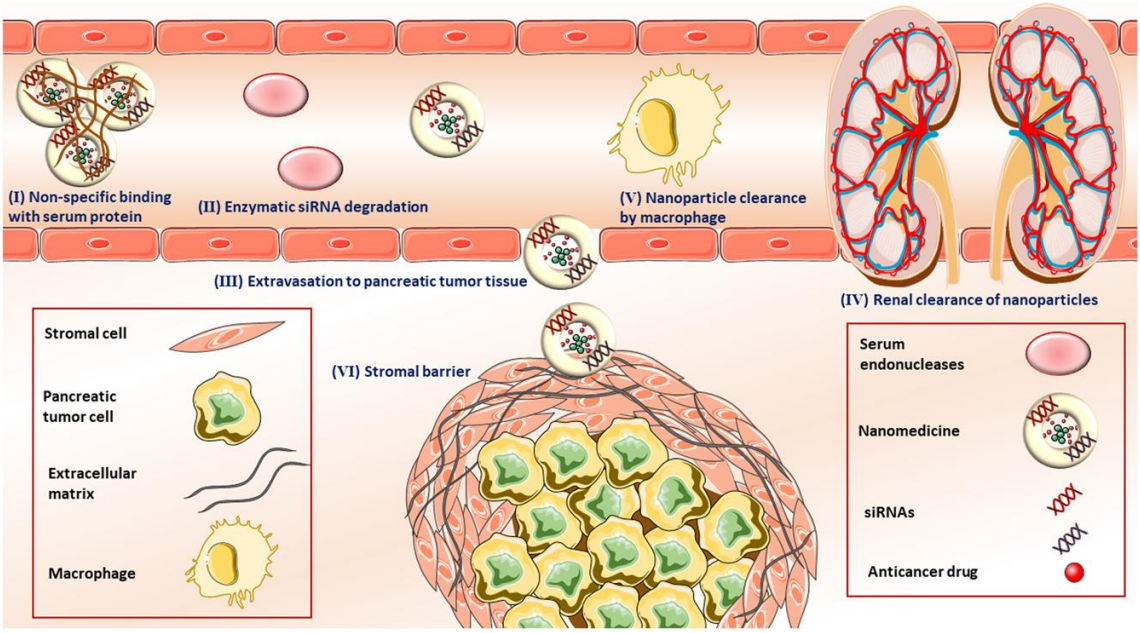


Figure 2.11: Diagram depicting the extracellular obstacles in siRNA delivery. (Adapted from:[160])

Despite the progress made in clinical RNAi treatment improvement, there is still a fair bit of potential for advancement by resolving the remaining obstacles. In this regard, there have been continuous advancements in well-established technologies, such as the use of viral or non-viral carriers to transport oligonucleotides.

Viruses were the ancestors of siRNA delivery; despite their great gene transport efficiency, there are grave safety issues regarding their use due to the immune response against viral sheath and mutagenic risks, the alternative synthetic vectors are intensively studied [161], [162].Conveniently natural and synthetic cationic polymers have been adopted intensively including polyethyleneimine (PEI) [163], [164], chitosan [165], [166], polyamidoamine (PAMAM) [167], polypropylenimine (PPI) [168] and poly(dimethylamino ethyl methacrylate (PDMAEMA) [169]. 2-(dimethylamino)ethyl methacrylate derivatives have been heavily studied in the literature as gene carriers since this monomer can be easily prepared with radical polymerization in different architectures. The use of DMAEMA polymers shows high transfection efficiency and low N/P ratios along with the endosomal escape mechanism “proton sponge effect” [170]. Endosomal escape can be enhanced by the addition of membrane disruptive units onto the structure, as shown by Durmaz and co-workers with the combination of hydrophobic hexyl methacrylate (HMA), DMAEMA, and cationic N,N,N-trimethyl aminoethyl methacrylate (TMAEMA) units efficiently deliver anti-GAPDH siRNA to knockdown GAPDH protein levels on targeted cells [171].

Cancer patients frequently acquire multidrug resistance (MDR), despite earnest efforts to discover novel chemotherapeutic drugs, biological treatments, and drug delivery technologies and as a result, substantially higher dosages and combinations of chemotherapeutics are required to provide significant clinical outcomes despite increasing side effects [172]. Combination therapy techniques involving chemotherapeutic medicines and other drug resistance inhibitor gene therapy agents have attracted attention over the past several years for treating acquired drug-resistant cancers [173]–[175]. Pump and non-pump resistances are two separate subtypes of MDR, where pump resistance actively lowers the concentration of the drug in the cell while non-pump resistance is based on antiapoptotic defense built by overexpressed proteins [176]. The B-cell lymphoma-2 (Bcl-2) protein was discovered to be inhibiting the cell from triggering the caspase cascade initiating apoptosis, according to the findings from several studies on cell apoptosis [177]. Overcoming underlying mechanisms of MDR requires a

combination of different methods, Zhen et. al. employed chemo-photothermal therapy by using Cu-Se/rGO nanocomposites [178], in another study to minimize the negative effects of the high concentration of Dox, Yang et.al. manufactured a GO carrier for the transport of Dox and two nucleic acids into cancer cells and reduced effective dosage by half [179]. Similarly, Izadi and co-workers used carboxylated graphene oxide for the codelivery of HIF-1α siRNA and Dinaciclib demonstrated enhanced growth inhibition of cancer cells [180].

2.6. Aim and Methodology of The Study

The purpose of this study is to develop a simple, efficient, and tunable method to overcome the solubility and cytotoxicity drawbacks of GO and its derivatives to be used in biological applications and employ this method to prepare a smart, targeted dual drug delivery nanoplatform to enhance treatment effectiveness on focused cancer. The development of multifunctional graphene nanoplatform has been achieved in two stages, in the first stage, biological properties of reduced graphene oxide were improved with PEGylation, and among 6 candidates most stable and biocompatible composition was selected to be used as drug delivery agents. In the second stage, rGO was further functionalized by cancer cells targeting EPPT1 peptide and a cationic copolymer to carry anti-Bcl-2-siRNA along with the chemotherapeutic agent Doxorubicin.

2.6.1. Effective PEGylation method to improve the biocompatibility of graphene derivatives

A highly efficient and straightforward PEGylation method is employed that uses multiple pyrene units and PEG-containing copolymer to coat the GO surface, as a water-soluble derivative of graphene, through π-π stacking while simultaneous reduction of GO to rGO takes place to obtain more biocompatible graphene nanoplatform with restored graphene properties and reduced functional groups. It was hypothesized that using multiple pyrenes will enhance the coating efficiency and result in more surface distributed functionalization compared to covalent edge functionalization which might decrease the nutrition absorption. Using this method, the graphene's superior properties for further application can be restored and the potential toxicity associated with functional groups can be eliminated via reduction of GO, while better aqueous solubility and stability in cell medium can be achieved via distributed PEG brushes on the surface. The length of the

PEG brush and the percentage of PEG content can be easily tuned with different copolymer compositions as well as incorporating new functionality that might allow combining different treatment techniques on the graphene surface for different applications.

In this work, PEGylation of GO has been achieved with a higher efficiency using multiple pyrene groups of a unique copolymer composed of poly(ethylene glycol methyl ether methacrylate) (PEGMA), methyl methacrylate (MMA) and 1-pyrenemethyl methacrylate (PMA) P(PEGMA-*co*-MMA-*co*-PMA). There are two recent examples in the literature about using multiple pyrene groups in the polymer for the non-covalent functionalization of carbon allotropes. The first one is about the functionalization of single-wall carbon nanotubes with MMA and PMA copolymer to increase solubility in organic solvents and the second uses pyrene functional ionic copolymer to obtain ultra-fine Pd catalyst doped rGO [181], [182]. To the best of our knowledge, our work is the first example that employs a PEG copolymer with multiple pyrenes to coat the graphene's surface to obtain better biocompatibility and solubility. Moreover, this method has the potential to be a practical way to incorporate different functionalities or treatments onto the surface of graphene for future applications while maintaining its biocompatibility. The P(PEGMA-*co*-MMA-*co*-PMA) (PMP) copolymer was synthesized via atom transfer radical polymerization (ATRP) to obtain a well-defined structure to optimize the number of PEG and the number of pyrene in the copolymer to ensure biocompatibility and solubility in aqueous environments such as the cell medium. The copolymers were tailored with two different PEG brush lengths (500 and 2000 g/mol) to be able to tune the PEG density with different brush numbers. Taking advantage of both dispersibility of GO and solubility of the copolymer in water, PEGylation was conducted in an aqueous environment with prepared copolymers via π-π stacking by using pendant pyrene groups, and simultaneously GO was reduced by hydrazine to obtain rGO with a more conjugated and defect-free surface with less functional groups. The effect of copolymer composition, number of brushes, length of brush on solubility/biocompatibility, and number of pyrenes on coating efficiency were investigated. Biocompatibility of obtained PMP-rGO derivatives was tested using MTS, LDH, and ROS assays to show how the suggested method addresses the different toxicity mechanisms using both healthy human embryonic kidney cells, HEK-293T, and human fibroblast lung cells, MRC-5, as they are potentially most affected organs by the cytotoxicity of graphene derivatives.

2.6.2. PEGylated reduced graphene oxide as nanoplatform for targeted gene and drug delivery

Research on the delivery of aromatic anticancer drugs (doxorubicin, paclitaxel, lucanthone, etc.) has shown that when hydrophobic drugs were loaded onto PEGylated graphene noncovalently better results have been obtained than the drug itself [183]–[186]. Following this lead, in the second step, an ideal gene and drug delivery system was designed to address the previously listed specifications. A novel reduced graphene oxide nano-carrier has been prepared to take advantage of hydrophobic anticancer drugs and oligonucleotides' simultaneous delivery while targeting a wide range of cancer types with modular units that are open for further modifications. P(PEGMA-*co*-MMA-*co*-PMA) was redesigned by the addition of an azide carrying methacrylate monomer to prepare poly[(poly(ethylene glycol) methyl ether methacrylate)-*co*-(3-azidopropyl methacrylate)-*co*-(methyl methacrylate)-*co*-(1-pyrenemethyl methacrylate)] enabling grafting onto the copolymer backbone with copper catalyzed azide alkyne cyclo-addition (CuAAC) not only for targeting agent EPPT1 and cationic copolymer with the responsibility of endosomal escape by proton sponge and membrane disruption and siRNA complexation but also any alkyne containing group. The cationic copolymer was synthesized by a first-time reported multifunctional ATRP initiator carrying an alkyne group, acid-labile hydrazone link, and initiator unit.

Previously published work on the selective treatment of breast cancer tumor cells has targeted various molecular recognition biomarkers, including estrogen receptor, progesterone receptor, human epidermal growth factor, vascular endothelial growth factor, and glycoproteins such as cell surface adhesion receptor CD44 or cell surface-associated mucin-1 [187]–[189]. Since MUC1 protein was found to be expressed in a variety of human epithelial cell adenocarcinomas, including 90% of breast cancer [190], [191], studies on targeting this transmembrane glycoprotein have accelerated and a synthetic peptide nonimmunogenic, MUC1 tumor antigen EPPT1 (YCAREPPTRTFAYWG) was created [160], [192]–[194] and selected as a targeting moiety for the modifications of nanoplatforms in this study.

Doxorubicin, a hydrophobic chemotherapeutic agent, is widely used with nanoparticles, anti-cancer effectiveness of Dox is primarily mediated through DNA intercalation and topoisomerase II inhibition in rapidly growing cancer cells [187] and when used alone or in conjunction with other cytotoxic antitumor medications, it is found to be a successful

cytotoxic agent for the elimination of tumors [195]. Dose-dependent, long-term, and possibly fatal cardiovascular damage caused by prolonged Dox usage can even surface many years after the completion of chemotherapy [196]–[198]. Innovative approaches in the current literature use gene therapy in combination with Dox to improve the efficacy of the drug in the elimination of tumors by single administrations, overcome multidrug resistance and decrease the mentioned side effects. The B-cell lymphoma-2 (Bcl-2) protein was discovered to be inhibiting the cell from triggering the caspase cascade initiating apoptosis and associated with multi-drug resistance since then its use is highly considered in combination therapy [177], [199]–[202].

Consecutively the carrier was completed by loading selected chemotherapeutic doxorubicin, oligonucleotide such as anti-GAPDH-siRNA as a model and anti-Bcl-2-siRNA as the target. The final platform and its variations were tested for their physicochemical properties, *in vitro* for drug release by time, release kinetics, siRNA complexation, cytotoxicity, cellular uptake, GAPDH, and Bcl-2 protein knockdown, Bcl-2 gene expression knockdown, cellular uptake, and *in vivo* for anticancer effect.

CHAPTER 3

3. EXPERIMENTAL PART

3.1. Materials

Methyl methacrylate (MMA, Sigma-Aldrich, 99%), poly(ethylene glycol) methacrylate 500 Da and 2000 Da (PEGMA, Sigma-Aldrich), hexyl methacrylate (HMA, Sigma-Aldrich, 98%), 2-(dimethylamino)ethyl methacrylate (DMAEMA, Sigma-Aldrich, 98%) were passed through a basic alumina column to remove inhibitor prior to use.

Copper (I) bromide (CuBr, Sigma-Aldrich, 98%), copper(I) chloride (CuCl, Sigma-Aldrich ≥97.0%), copper(II) chloride ($CuCl_2$, Sigma-Aldrich, 99%), N,N,N',N''',N''-pentamethyldiethylenetriamine (PMDETA, Sigma-Aldrich, 99%), 1,1,4,7,10,10-hexamethyltriethylenetetramine (HMTETA, Sigma-Aldrich, 97%), ethyl 2-bromo-2-methylpropionate (EiBr, Sigma-Aldrich, 98%), graphene oxide (GO, Sigma-Aldrich, 4 mg/mL, dispersion in H_2O), doxorubicin hydrochloride (Dox, Cayman Chemical, ≥98%), EPPT1 (YCAREPPTRTFAYWG, C terminus capped, N terminus free >95%, Metabion International AG, Germany), alkyne-PEG-NHS 3000 Da (133000-35-70, Rapp Polymere), Cyanine7-Alkyme (Cy7-Alkyne, BP-23920, Broadpharm) used without further purification.

Anti Bcl-2 siRNA (Sense: 5'-[GCCCUGAUUGUGUAUAUUCA], Antisense:5'-[UGAAUAUACACAAUCAGGGC], Eurofins Genomics), Silencer® FAM™- FAM-labelled negative control siRNA (AM4620, Invitrogen™), Silencer™ GAPDH siRNA, Positive Control (human) (AM4633, Invitrogen), Silencer™ Negative Control siRNA (AM4635, Invitrogen), 7-Hydroxy-3H-phenoxazin-3-one-10-oxide sodium salt (Resazurin Sodium Salt, Sigma Aldrich), MTS ([3-(4,5-dimethylthiazol-2-yl)-5-(3carboxymethoxyphenyl)-2-(4- sulfophenyl)-2H-tetrazolium]), CellTiter 96® AQueous one solution cell proliferation assay (MTS, Promega Corporation), Pierce™ Coomassie (Bradford) Protein Assay Kit, 23200, Thermo Scientific™), Pierce™ LDH Cytotoxicity

Assay Kit (88954, Thermo Scientific™), Cellular Reactive Oxygen Species Detection Assay Kit (Deep Red Fluorescence, ab186029, ABCAM), KDalert™ GAPDH Assay Kit (AM1639, Invitrogen), Hoechst (33342, Thermo Scientific™), LysoTracker Green DND-26 (7525, Setareh Biotec), RIPA lysis buffer system (sc-24948, Santa Cruz), TGX Stain-Free™ FastCast™ acrylamide starter kit (10%, 1610182, Bio-Rad), TEMED (BP150-20, Fisher Scientific), APS (BP179-100, Fisher Scientific), Laemmli sample buffer (4X, 1610747, Bio-Rad), pre-stained protein ladder (10-180 kDa, ab116027,ABCAM), β-Actin antibody (C4) (sc47778, Santa Cruz), Bcl-2 Antibody (C2) (sc-7382, Santa Cruz), m-IgGκ BP-HRP secondary antibody (sc-516102, Santa Cruz), Clarity™ Western ECL substrate (170-5060, Bio-Rad), total RNA isolation kit (TR01, Gene Mark), QIAshredders (79654, Qiagen), Omniscript Reverse Transcriptase (205111, Qiagen), Random Hexamers (6N, 1.0 OD, 500 µL, 10 µM, G139, ABM), TaqMan™ universal PCR master mix (4304437, Applied Biosystems™), TaqMan™ Bcl-2 gene expression assay (FAM/MGB Human Bcl-2: 4331182, Applied Biosystems, Assay ID:Hs04986394_s1), eukaryotic 18S rRNA endogenous control (FAM/MGB, 4333760, Applied Biosystems), Helix NP Blue (5 nM, 425305, Biolegend) and APC Annexin V (640941, Biolegend) were used according to the manufacturer's protocol.

Dulbecco's Modified Eagle's Medium (DMEM, high glucose, Gibco™), MEBM™ mammary epithelial cell growth basal medium (CC-3151, Lonza), MEGMTM mammary epithelial cell growth medium SingleQuots™ Kit (CC-4136, Lonza), fetal bovine serum advanced, heat-inactivated (FBS, Capricorn Scientific GmbH), L-Glutamine (200 mM, Gibco™), penicillin/streptomycin solution (10,000 U/mL, Gibco™), MEM non-essential amino acids solution (100X, Gibco™), Trypsin/EDTA (0.25%, Gibco™), trypan blue solution, (0.4%, Sigma-Aldrich), Corning® Matrigel® Basement Membrane Matrix, LDEV-free (356234, Corning®), Spectra/Por 7 standard regenerated cellulose dialysis tubing (MWCO: 3.5 kD & 1 kD, Repligen) and phosphate buffered saline tablets (reconstitution: 100 mL, VWR Life Sciences) were used as received. Non-listed reagents were purchased from Sigma-Aldrich or Thermo Fisher Scientific and used as received without further purification.

3.2. Characterization

^{1}H nuclear magnetic resonance (NMR) spectra were recorded using an Agilent VNMRS 500 MHz instrument in $CDCl_3$ and D_2O. Using a TOSOH Ecosec GPC system (HLC-

8320) with a Wyatt miniDAWN Treos II multi-angle light scattering (MALS) detector (λ= 660 nm, Detection Angles = 45°, 90°, and 135°), GPC analysis were performed. THF or water was used as eluent at a flow rate of 1.0 mL/min at 35 °C. A Cary 630 FTIR instrument (Agilent Technologies Inc., USA), with attenuated total reflectance (ATR) sampling module, was used to record Fourier transform infrared (FTIR) spectra over the range 4000-400 cm^{-1}. The particle size and zeta potential of graphene derivatives were determined in distilled water by dynamic light scattering (DLS) using Malvern Zetasizer Ultra (Laser: 10 mW, 632,8 nm). Thermogravimetric studies (TGA) were conducted by using TGA 8000TM, PerkinElmer instruments, under the N_2 atmosphere with a 10 °C per minute heating rate, between 30-800 °C. UV-Vis absorption and fluorescent measurements of 96-well plates were recorded using the SpectraMax i3 spectrophotometer and UV-Vis absorption measurements of polymers were recorded using Shimadzu UV-1800 spectrophotometer in CH_2Cl_2 where fluorescence spectroscopy study was done by HITACHI F-4500 in CH_2Cl_2. Atomic Force Microscope (AFM) scans were recorded by High-Performance AFM/MFM (hpAFM), NanoMagnetics Instruments, samples were dispersed in distilled water and prepared for AFM analysis by drop casting. Renishaw inVia™ Raman microscope was used for Raman spectroscopy analysis and K-Alpha X-ray Photoelectron Spectrometer (XPS) System Thermo Scientific™ was used for XPS analysis. Particles were dispersed in water and then applied on the grid by drop casting method and Transmission Electron Microscope (TEM) scans were recorded using JEM 1220, JEOL instrument. The mass spectra were obtained using a Shimadzu LC-MS 2040 C mass spectrometry system equipped with an Electrospray Ionization (ESI) source operating in positive mode (Kyoto, Japan). Zeiss LSM800 and LSM780 (Carl Zeiss AG) confocal laser scanning microscope equipped with Airyscan module was used for image acquisition and evaluation.

3.3. Synthesis of Poly[(poly(ethylene glycol) methyl ether methacrylate)-*co*-(3-azidopropyl methacrylate)-*co*-(methyl methacrylate)-*co*-(1-pyrenemethyl methacrylate)-*g*-Poly(hexyl methacrylate-*co*-2-(dimethylamino)ethyl methacrylate-*co*-*N,N,N*-trimethylaminoethyl methacrylate iodide)

3.3.1. General procedure for functional ATRP initiators

Hydroxyl functional compound (benzyl alcohol (**Figure 3.1**), 1-pyrene methanol (**Figure 3.2**) or 4-hydroxybenzaldehyde (**Figure 3.2**), 1 eq), triethylamine (2 eq), and 4-

(dimethylamino)pyridine (DMAP) (0.2 eq) were dissolved in tetrahydrofuran (THF) in a two-neck round bottom flask and the flask was placed in an ice bath. 2-bromo-2-methylpropanoyl bromide (1.2 eq) was diluted with THF and added dropwise into the flask under a nitrogen atmosphere. The reaction mixture was stirred for 2 hours in an ice bath and stirred overnight at room temperature in dark [203], [204]. The following day precipitates were filtered and THF was removed by vacuum. The reaction mixture was dissolved in dichloromethane (DCM) and extracted with 10% HCl solution then with distilled water, dried over sodium sulfate, and the solvent removed by using a rotary evaporator. The product was purified by silica gel column chromatography using 1:9 ethyl acetate-hexane as a mobile phase and characterized by ^{1}H NMR spectroscopy.

Benzyl 2-bromo-2-methylpropanoate: Yield: 88.3%. ^{1}H NMR (500 MHz, $CDCl_3$) δ (ppm)= 7.40-7.31 (m, 5H, Ar*H*), 5.21 (s, 2H), 1.96 (s, 6H).

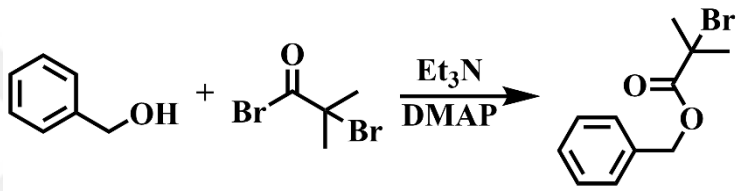


Figure 3.1: Synthesis of benzyl 2-bromo-2-methyl propanoate.

Pyren-1-ylmethyl 2-bromo-2-methylpropanoate: Yield: 81.2%. ^{1}H NMR (500 MHz, $CDCl_3$) δ (ppm)= 8.32-8.09 (m, 9H, Ar*H* pyrene), 8.08-8.02 (m, 1H), 5.94 (s, 2H), 1.95 (s, 6H).

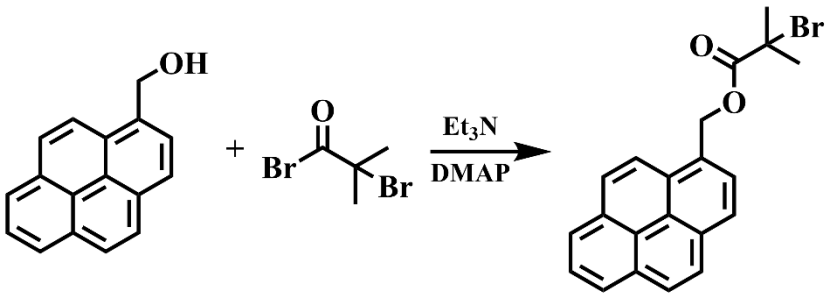


Figure 3.2: Synthesis of pyren-1-ylmethyl 2-bromo-2-methyl propanoate.

4-formylphenyl 2-bromo-2-methylpropanoate: Yield: 73.0%. ^{1}H NMR (500 MHz, $CDCl_3$) δ (ppm) = 10.01 (s, 1H), 7.96 (d, J = 8.6 Hz, 2H), 7.33 (d, J = 8.6 Hz, 2H), 2.08 (s, 6H).

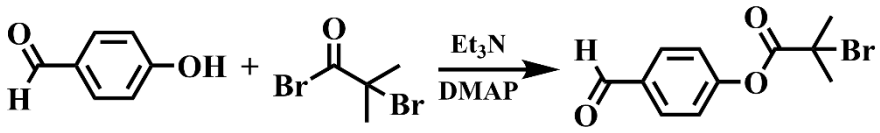


Figure 3.3: Synthesis of 4-formylphenyl 2-bromo-2-methyl propanoate.

3.3.2. Synthesis of 2,5-dioxopyrrolidin-1-yl pent-4-ynoate

4-pentynoic acid (1 eq), N-hydroxysuccinimide (1.1 eq), and 4-(dimethylamino)pyridine (DMAP, 0.1 eq) were dissolved in dichloromethane (DCM) and in a separate flask N,N′-dicyclohexylcarbodiimide (DCC, 1.05 eq) was dissolved in DCM and transferred to the reaction mixture (**Figure 3.4**). After stirring overnight at room temperature, the precipitated solid was removed by filtration, concentrated, and crystallized in a 1:1 ethyl acetate-hexane mixture. Obtained crystals were characterized by ^{1}H NMR spectroscopy [205] (Yield: 76.3%). ^{1}H NMR (500 MHz, $CDCl_3$) δ (ppm) = 2.91 – 2.79 (m, 6H), 2.62 (td, J = 7.5, 2.6 Hz, 2H), 2.05 (t, J = 2.6 Hz, 1H).

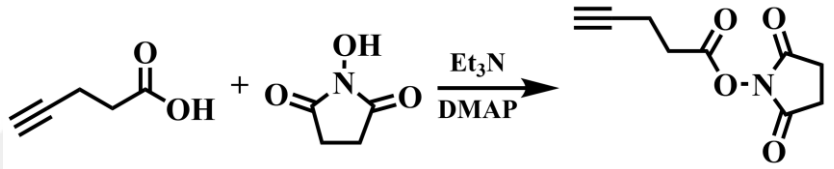


Figure 3.4: Synthesis of 2,5-dioxopyrrolidin-1-yl pent-4-ynoate.

3.3.3. Synthesis of pent-4-ynehydrazide

2,5-dioxopyrrolidin-1-yl pent-4-ynoate (1 eq) was dissolved in THF and the solvent was degassed for 10 minutes before hydrazine hydrate addition. Hydrazine hydrate (10 eq) was then added to the flask and the reaction mixture was refluxed for 24 hours at 65 °C under a nitrogen atmosphere (**Figure 3.5**) [206]. The immiscible hydrazine phase was separated from the organic phase and THF was evaporated. The partly solidified product was not purified further and characterized via ^{1}H NMR spectroscopy (Yield: 64.1%). ^{1}H NMR (500 MHz, $CDCl_3$) δ (ppm) = 6.96 (s, 1H), 3.93 (s, 2H), 2.54 (td, J = 7.2, 2.6 Hz, 2H), 2.38 (t, J = 7.1 Hz, 2H), 2.01 (t, J = 2.7 Hz, 1H).

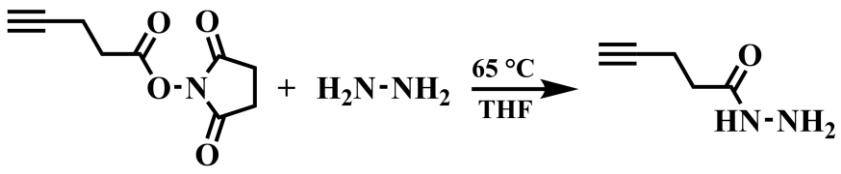


Figure 3.5: Synthesis of pent-4-ynehydrazide.

3.3.4. Synthesis of 4-((2-(pent-4-ynoyl)hydrazineylidene)methyl)phenyl 2-bromo-2-methylpropanoate

4-formylphenyl 2-bromo-2-methylpropanoate (1 eq) and pent-4-ynehydrazide (1.4 eq) were dissolved in THF and refluxed at 65 °C for 24 hours under an inert atmosphere (**Figure 3.6**). After treatment solvent was evaporated and impurities were removed by silica gel column chromatography where 1:9 ethyl acetate-hexane was used as the mobile phase. The collected yellowish product was further crystallized in methanol and the resulting white solid hydrazone was characterized by ^{1}H NMR spectroscopy and MS spectrometry [207] (Yield: 32.6%). ^{1}H NMR (500 MHz, $CDCl_3$) δ 9.33 (s, 1H), 7.77 (s, 1H), 7.71 (d, J = 8.6 Hz, 2H), 7.19 (d, J = 8.7 Hz, 2H), 3.03 (dd, J = 8.3, 6.7 Hz, 2H), 2.63 (td, J = 7.5, 2.6 Hz, 2H), 2.08 (s, 6H), 2.00 (t, J = 2.7 Hz, 1H). HRMS m/z: $[M+H]^+$ calculated for $C_{16}H_{18}BrN_2O_3$ 365.04; found 365.

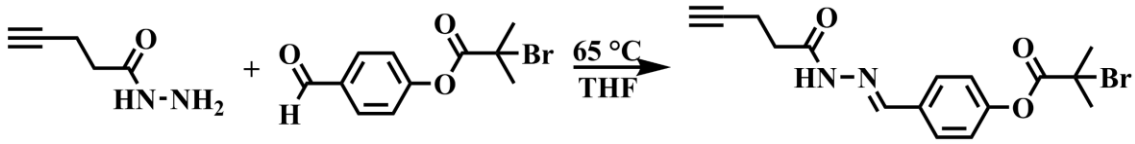


Figure 3.6: Synthesis of 4-((2-(pent-4-ynoyl)hydrazineylidene)methyl)phenyl 2-bromo-2-methylpropanoate.

3.3.5. Synthesis of 3-azido-1-propanol

3-chloro-1-propanol (1 eq), sodium azide (2 eq), and tetrabutylammonium persulfate (0.01 eq) were dissolved in water in a round bottom flask and stirred for 24 hours at 80 °C (**Figure 3.7**). After the reaction time, undissolved sodium azide was filtered, and the water phase was extracted with diethyl ether 3 times. The organic phase was dried over sodium sulfate and the solvent was removed by a rotary evaporator under vacuum. The crude product was purified by vacuum distillation. ^{1}H NMR and FTIR were employed for the characterization of the product. (Yield: 75.0%) ^{1}H NMR (500 MHz, $CDCl_3$) δ (ppm)= 3.72 (t, J = 6.0 Hz, 2H), 3.42 (t, J = 6.6 Hz, 2H), 1.81 (p, J = 6.3 Hz, 2H).

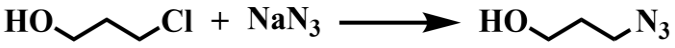


Figure 3.7: Synthesis of 3-azido-1-propanol.

3.3.6. Synthesis of 3-azidopropyl methacrylate

3-azido-1-propanol (1 eq) and triethylamine (2 eq) were transferred into a round bottom flask, dissolved in DCM, and placed in an ice bath. Methacryloyl chloride (1.5 eq) was

diluted with DCM and added dropwise to the reaction mixture under a nitrogen atmosphere. The reaction was stirred for 2 hours in an ice bath and stirred overnight at room temperature (**Figure 3.8**). The following day precipitate was filtered out and the remaining reaction mixture was extracted 2 times with 10% HCl solution and distilled water. The extract was dried over sodium sulfate and concentrated via the rotary evaporator. The product was purified by vacuum distillation using Bredt distributor by hydroquinone addition and characterized by ^{1}H NMR spectroscopy. (Yield: 46.6%) ^{1}H NMR (500 MHz, $CDCl_3$) δ (ppm)= 6.10 (s, J = 2.0, 1.0 Hz, 1H), 5.57 (s, J = 1.6 Hz, 1H), 4.29 – 4.19 (t, 2H), 3.40 (t, J = 6.7 Hz, 2H), 2.01 – 1.90 (m, 5H).

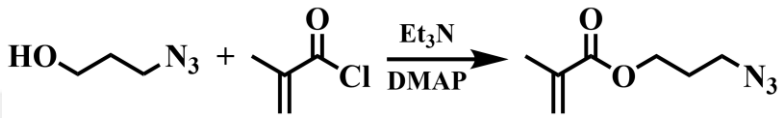


Figure 3.8: Synthesis of 3-azidopropyl methacrylate.

3.3.7. General procedure for the synthesis of poly[(poly(ethylene glycol) methyl ether methacrylate)-*co*-(methyl methacrylate)-*co*-(1-pyrenemethyl methacrylate)] (P(PEGMA-*co*-MMA-*co*-PMA)) or poly[(poly(ethylene glycol) methyl ether methacrylate)-*co*-(3-azidopropyl methacrylate)-*co*-(methyl methacrylate)-*co*-(1-pyrenemethyl methacrylate)] (P(PEGMA-*co*-AzPMA-*co*-MMA-*co*-PMA))

The methacrylate copolymers have been synthesized via atom transfer radical polymerization (ATRP) by using different molar ratios between monomers according to literature with minor modifications [208], [209]. In a typical experiment monomers, including poly(ethylene glycol) methyl ether methacrylate (PEGMA) with different molecular weights (500 or 2000 g/mol), 1-pyrenylmethyl methacrylate (PMA), methyl methacrylate (MMA), and 3-azidopropyl methacrylate (AzPMA) at certain feeding ratio were dissolved in toluene and N,N,N',N'",N"-pentamethyldiethylenetriamine (PMDETA), copper (I) bromide (CuBr) and lastly initiator (ethyl 2-bromo-2-methylpropionate, benzyl 2-bromo-2-methylpropanoate or pyren-1-ylmethyl 2-bromo-2-methylpropanoate) were added to the reaction flask, sealed and submerged into liquid nitrogen followed by 3 freeze-pump-thaw (FPT) cycles. The reaction mixture was subsequently heated to 90 °C or 60 °C, reacted for predetermined times and after removal of the catalyst, copolymers were precipitated in cold ether or hexane, and characterized by ^{1}H NMR, UV-Vis, FTIR spectroscopies, and GPC.

3.3.8. Synthesis of poly(hexyl methacrylate-*co*-2-(dimethylamino)ethyl methacrylate (P(HMA-*co*-DMAEMA)) by ATRP

P(HMA-*co*-DMAEMA) copolymer has been synthesized by ATRP, in a Schlenk tube hexyl methacrylate (HMA), 2-(dimethylamino)ethyl methacrylate (DMAEMA) was dissolved in a THF and degassed by three FPT cycles. In a second tube 4-((2-(pent-4-ynoyl)hydrazineylidene)methyl)phenyl 2-bromo-2-methylpropanoate, 1,1,4,7,10,10-hexamethyltriethylenetetramine (HMTETA), copper (II) chloride and copper (I) chloride was dissolved in THF (HMA:DMAEMA=1:1, $[M_{T,0}]/[I_0]$=600, [I]:[CuCl]:[$CuCl_2$]:[HMTETA] = 1:0.8:0.2:1) and degassed similarly. The initiator solution was transferred to the first tube with a syringe under nitrogen, sealed, and placed in a preheated oil bath at 60 °C (**Figure 3.9**). Once reaction time was completed Schlenk tube was cooled immediately, diluted with THF, and passed through neutral alumina to remove copper chlorides, concentrated by rotary-evaporator and precipitated in cold hexane twice, dried at room temperature under vacuum, and characterized by ^{1}H NMR spectroscopy. ^{1}H NMR (500 MHz, $CDCl_3$) δ (ppm) = 7.79 – 7.60 (m, 3H), 7.11 (s, 2H), 4.13 – 3.84 (m, -COO-C*H*$_2$-), 3.02 (t, 1H), 2.56 (t, HC-C*H*$_2$- & $(CH_3)_2$-N-C*H*$_2$-), 2.33 – 2.26 (m, $(CH_3)_2$-N-), 1.62 (s, -COO-CH_2-C*H*$_2$-CH_2).

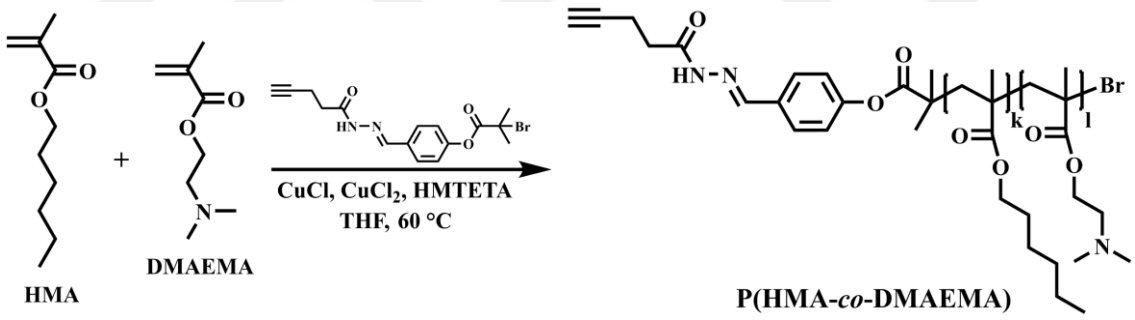


Figure 3.9: Synthesis of P(HMA-*co*-DMAEMA).

3.3.9. Synthesis of poly(hexyl methacrylate-*co*-2-(dimethylamino)ethyl methacrylate-*co*-N,N,N-trimethylaminoethyl methacrylate iodide) (P(HMA-*co*-DMAEMA-*co*-TMAEMA))

P(HMA-*co*-DMAEMA) (1 eq of DMAEMA monomer) was dissolved in THF, and methyl iodide (0.5 eq) was added dropwise to the solution and stirred overnight at room temperature in dark (**Figure 3.10**). The following day reaction mixture was concentrated and precipitated in cold hexane. The product was vacuum dried and characterized by ^{1}H NMR. ^{1}H NMR (500 MHz, $CDCl_3$) δ (ppm) = 7.76 – 7.55 (m, 3H), 7.11 (s, 2H), 4.84 –

3.80 (m, -COO-CH_2- & $(CH_3)_3$-N-CH_2-), 3.80-3.49 (m, (CH_3)$_3$-N-), 3.01 (t, 1H), 2.56 (t, HC-CH_2- & $(CH_3)_2$-N-CH_2-), 2.47 – 2.18 (m, (CH_3)$_2$-N-), 1.61 (s, -COO-CH_2-CH_2-CH_2).

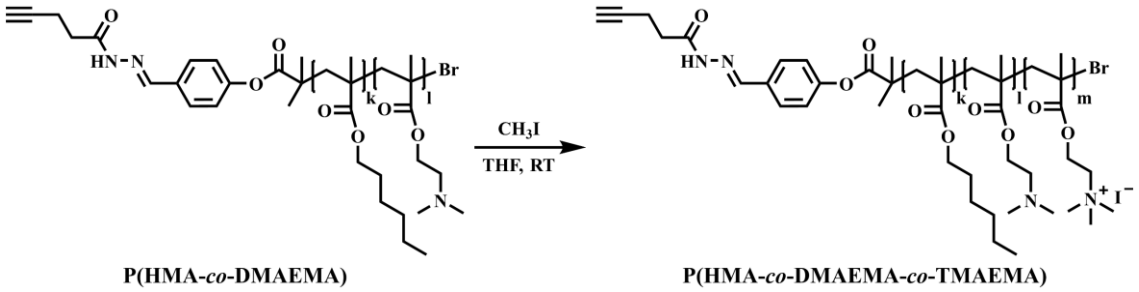


Figure 3.10: Synthesis of P(HMA-*co*-DMAEMA-*co*-TMAEMA).

3.3.10. Synthesis of poly[(poly(ethylene glycol) methyl ether methacrylate)-*co*-(3-azidopropyl methacrylate)-*co*-(methyl methacrylate)-*co*-(1-pyrenemethyl methacrylate)]-*g*-poly(hexyl methacrylate-*co*-2-(dimethylamino)ethyl methacrylate-*co*-*N,N,N*-trimethylaminoethyl methacrylate iodide) by CuAAC of P(HMA-*co*-DMAEMA-*co*-TMAEMA) and P(PEGMA-*co*-AzPMA-*co*-MMA-*co*-PMA) (PAMP-*g*-CP)

In a Schlenk tube P(PEGMA-*co*-AzPMA-*co*-MMA-*co*-PMA) (1 eq copolymer / 9.54 eq AzPMA) and P(HMA-*co*-DMAEMA-*co*-TMAEMA) (7 eq) were dissolved in pH 7.4 PBS, copper sulfate (3.5 eq) and sodium ascorbate (10.5 eq) were added sequentially to the tube after 3 FPT cycles reaction mixture was placed in a preheated oil bath at 35 °C (**Figure 3.11**). Following 36 hours of reaction time mixture was transferred to a 3.5 kDa molecular weight cut-off dialysis membrane, dialyzed against pH 7.4 PBS, and later against double distilled water. Following removal of catalytic system crude product lyophilized and obtained solid was precipitated in cold hexane. Vacuum dried product was characterized by ^{1}H NMR and FTIR spectroscopy.

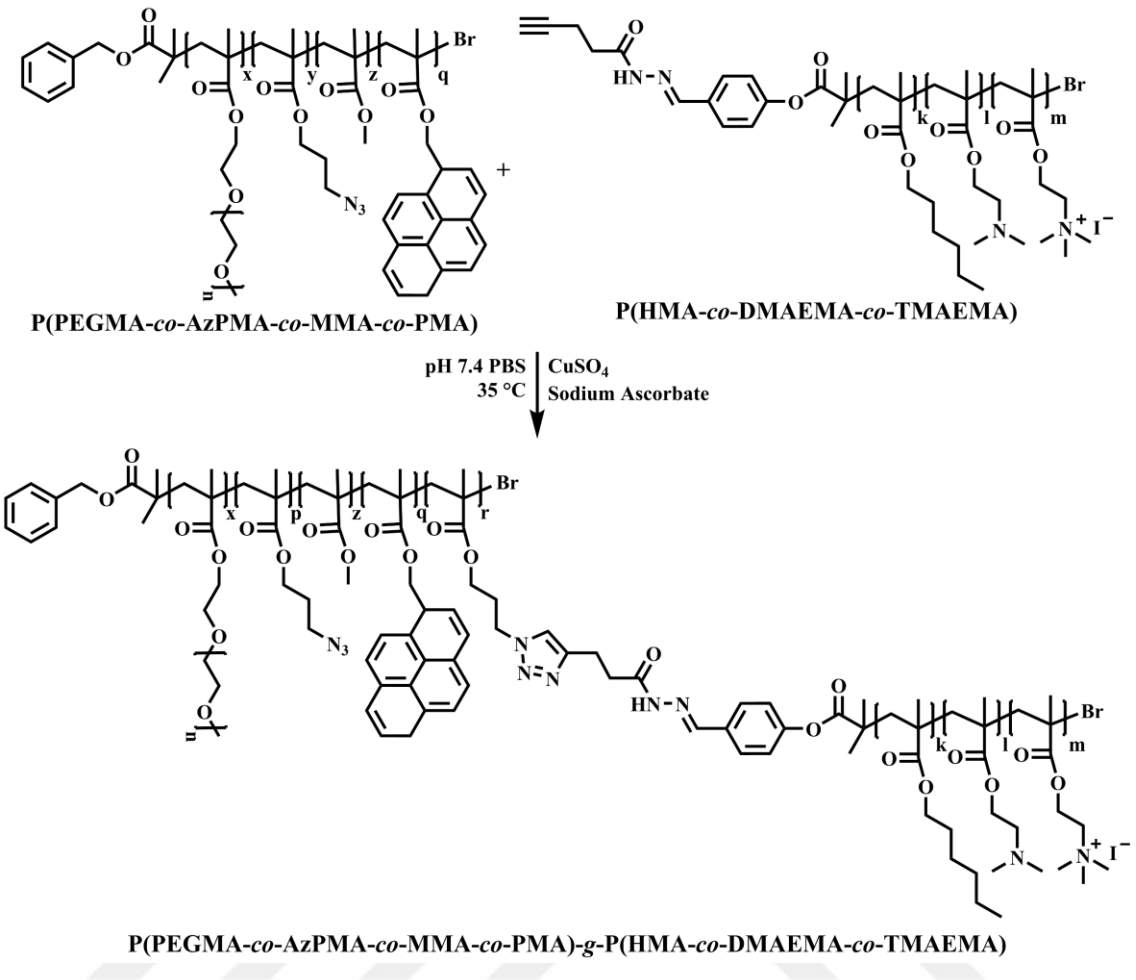


Figure 3.11: Synthesis of PAMP-*g*-CP.

3.4. Preparation of PEGylated rGO Derivatives

3.4.1. PEGylation of GO and simultaneous reduction

P(PEGMA-*co*-MMA-*co*-PMA) (**Figure 3.12a**) or P(PEGMA-*co*-AzPMA-*co*-MMA-*co*-PMA)-*g*-P(HMA-*co*-DMAEMA-*co*-TMAEMA) (**Figure 3.12b**) (15 eq by weight) was dissolved in DMF and added dropwise on GO solution (1 eq w/w, pH set to 8) in water (DMF: Water=1:2 by volume), stirred for 2 hours at room temperature. Afterward, hydrazine hydrate (1µL per 1 mg GO) was added, and the reaction mixture was placed in a pre-heated oil bath at 80 °C for 24 hours. The dark brown color of the reaction mixture was turned into black over time, the mixture was centrifuged, discarding supernatant was followed by 3 wash steps by dispersing precipitate in water and acetone. Obtained solid P(PEGMA-*co*-MMA-*co*-PMA) (PMP) coated rGO (PMP-rGO) or P(PEGMA-*co*-AzPMA-*co*-MMA-*co*-PMA)-*g*-P(HMA-*co*-DMAEMA-*co*-TMAEMA) (PAMP-*g*-CO) coated rGO (PAMP-CP-rGO) was dispersed in distilled water and lyophilized till dryness

[210]. The resulting black products were characterized by TGA, SEM, TEM, FTIR, XPS, Raman, and AFM.

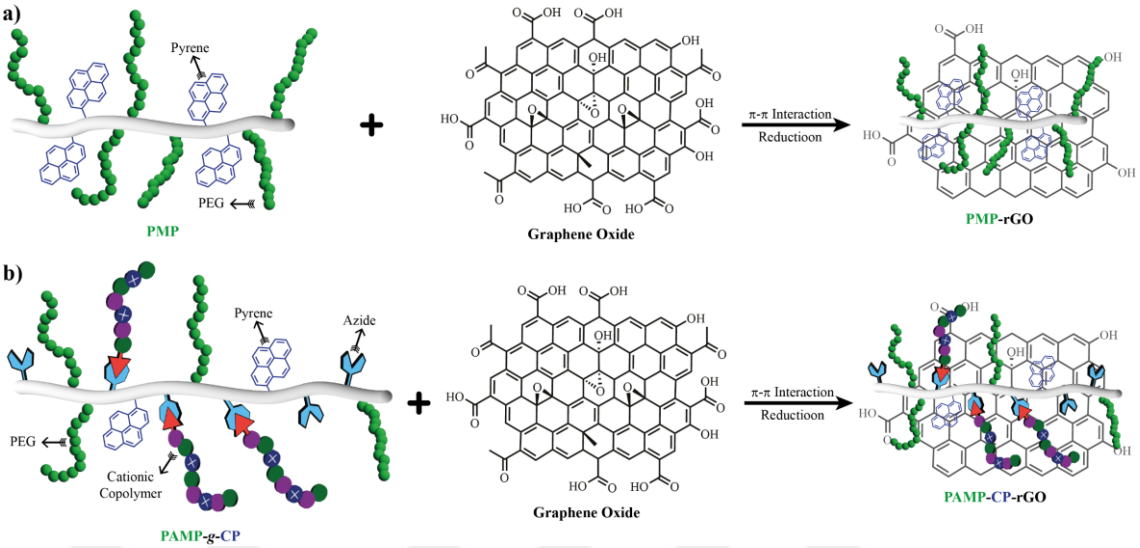


Figure 3.12: Coating of **a)** PMP and **b)** PAMP-*g*-CP on GO and simultaneous reduction to obtain PMP-rGO and PAMP-CP-rGO respectively.

3.4.2. Synthesis of alkyne-PEG-EPPT1

Alkyne-PEG-NHS (1.1 eq, 3000 g/mol), EPPT1-NH_2 (1 eq, 1817.06 g/mol, Sequence: YCAREPPTRTFAYWG, C terminus capped, N terminus free), EDC (1 eq), and NHS (0.5 eq) were dissolved in pH 8.2 PBS and stirred at 37 °C for 24 hours (**Figure 3.13**). The reaction mixture was transferred into a 1 kDa MWCO dialysis bag and dialyzed against pH 8.2 PBS to remove excess EDC and NHS, consecutively dialyzed against slightly alkaline water to remove buffer components [211]. Following the dialysis process solution was lyophilized and characterized by ^{1}H NMR and GPC (Yield: 92.4%). ^{1}H NMR (500 MHz, D_2O) δ (ppm) = 7.62-6.68 (m, 18H, Ar*H*), 3.98-3.46 (br, αH, -C*H*$_2$-C*H*$_2$-O- repeating unit), 3.43 (t, 2H, -O-C*H*$_2$-CH$_2$-CH$_2$-), 2.41 (s, 2H, -COO-C*H*$_2$-), 2.11-1.98 (br, 3H, -COO-CH$_2$-C*H*$_2$- & -C≡C*H*).

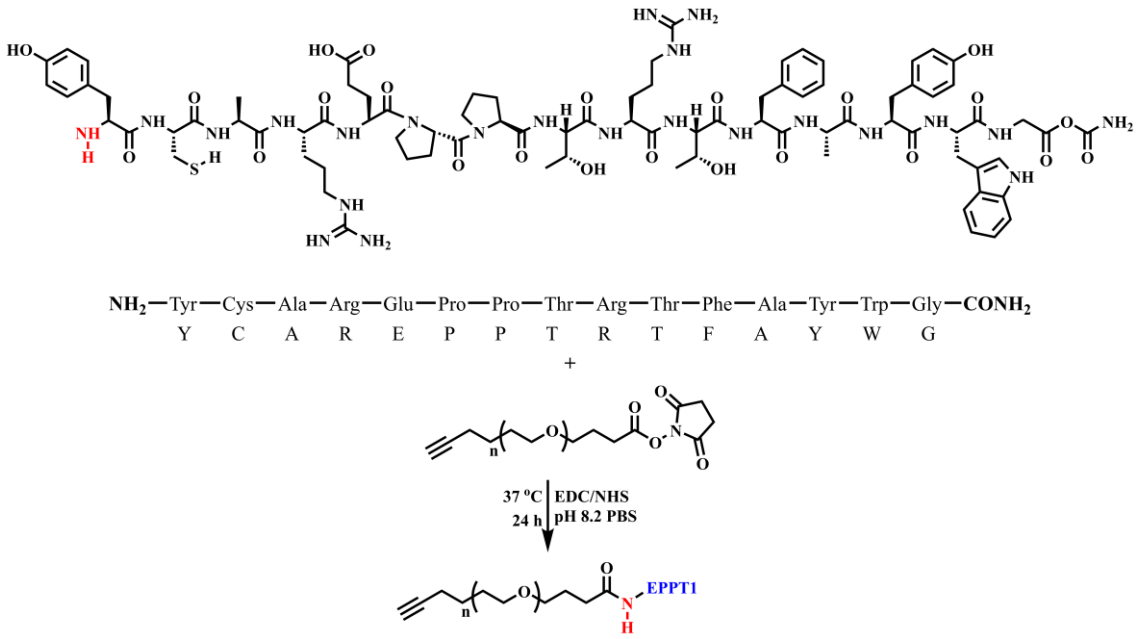


Figure 3.13: Synthesis of alkyne-PEG-EPPT1.

3.4.3. Conjugation of EPPT1 on PAMP-CP-rGO

PAMP-CP-rGO (1 eq of PAMP-*g*-CP), alkyne-PEG-EPPT1 (3 eq), copper sulfate (3 eq), and sodium ascorbate (6 eq) were dissolved in pH 8 PBS respectively. The reaction mixture was degassed by 3 FPT cycles, placed in a preheated oil bath at 35 °C, and stirred overnight (**Figure 3.14**). The following day reaction mixture was divided into microtubes, centrifuged, and washed first with pH 8 PBS and later with distilled water. The supernatant was saved for determination of remaining alkyne-PEG-EPPT1 by Bradford assay where the pellet was dispersed in distilled water and lyophilized.

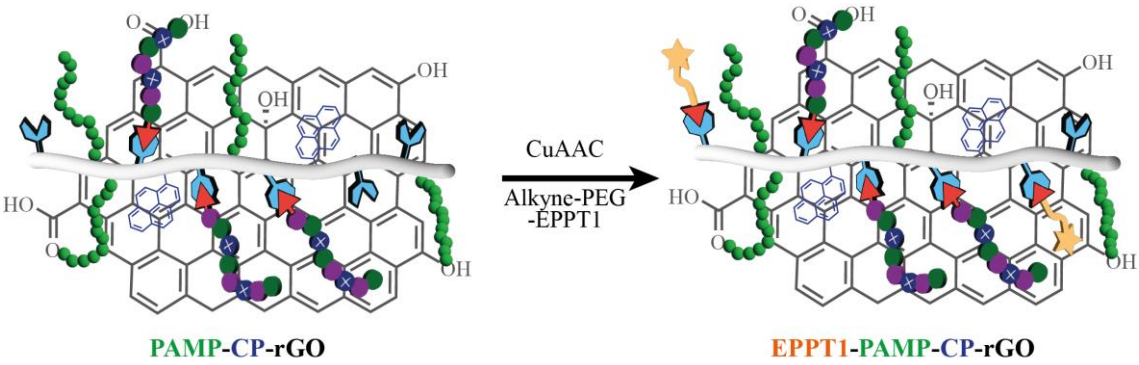


Figure 3.14: Synthesis of targeted EPPT1-PAMP-CP-rGO.

3.4.4. Doxorubicin loading on PEGylated rGO and determination of drug release profile and release kinetics

Targeted or non-targeted PAMP-CP-rGO (1 eq by mass) was dispersed with probe sonication in pH 8 PBS and transferred into a round bottom flask. While stirring, doxorubicin (1 eq by mass) which is dissolved in DMSO (10% of the final volume) was added dropwise onto the rGO dispersant (**Figure 3.15**). The mixture was stirred at 35 °C degrees overnight at dark, following day purification was performed by multiple centrifugations and washing steps with pH 8 PBS and distilled water. The first supernatant was saved for free Dox determination to relate loaded Dox amount on the graphene surface, UV absorbance of three 200 µL samples of the supernatant was detected at 483 nm and by comparing drug feed and free drug amounts percentage of drug loading was calculated (**3.1**). Pellet was lyophilized after dispersing in distilled water and the solid product was stored at +4 °C.

$$Loaded\ Dox\ \% = 100 - \frac{Free\ Dox\ (mg)}{Dox\ Feed\ (mg)} x100 \qquad \textbf{(3.1)}$$

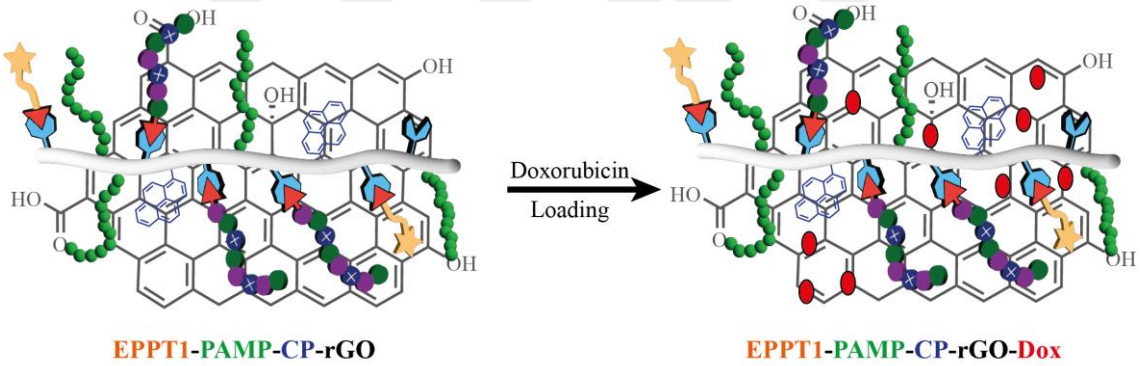


Figure 3.15: Doxorubicin loading on EPPT1-PAMP-CP-rGO.

Dox-loaded samples were dispersed in pH 7.4 and pH 5.5 PBS solutions in triplicate, placed in 3.5 kDa dialysis bags, and transferred into flasks containing relevant PBS solutions at 37 °C, and stirred at a low rpm. At predetermined time points, 200 µL samples were taken from the flasks in triplicates, UV absorptions were recorded at 483 nm and samples were returned to the flask. The released Dox percentage was calculated by comparing the initial Dox amount placed in the dialysis bag and determined Dox in the outer PBS.

It is possible to analyze the drug release rate using a variety of kinetic models defined by the mathematical functions, various models have been applied for profiling drug releases.

In parallel to the literature, the release kinetics of dox-loaded nanocarriers were studied using the data obtained during 108 h release study by zero-order (**3.2**), first order (**3.3**), Higuchi (**3.4**), Korsmeyer-Peppas (**3.5**) and Weibull (**3.6**) models [212]. The data was interfered with by using Microsoft Excel software and curve fitting was performed using GraphPad Prism 9 software. In the listed functions below F denotes the fraction of Dox released at time t, where k_0, k_f, k_H, k_{KP} α, and β are the constants of the kinetic models.

$$F = k_0 t \quad \textbf{(3.2)}$$

$$Ln\ (1 - F) = -k_f \cdot t \quad \textbf{(3.3)}$$

$$F = k_H \cdot t^{1/2} \quad \textbf{(3.4)}$$

$$Ln(F) = Ln(k_{KP}) + n \cdot Ln(t) \quad \textbf{(3.5)}$$

$$Ln[-Ln(1-F)] = -Ln\ \alpha + \beta \cdot Ln\ t \quad \textbf{(3.6)}$$

3.5. Agarose Gel Retardation Assay

To observe the siRNA loading capacity of PAMP-CP-rGO derivatives, a gel electrophoresis assay was performed. GAPDH or Bcl-2 siRNA was mixed with PAMP-CP-rGO at different weight ratios (1:25, 1:30, 1:35, 1:40), and incubated at room temperature for 20 minutes to allow the complexation to complete (**Figure 3.16**). After incubation, the DNA ladder, free siRNA, and siRNA complexes were transferred into 1% agarose gel wells that are prepared in Tris-acetate-EDTA buffer containing 1x RedSafe™ after the addition of loading dye and electrophoresed at 60 V for 60 minutes. The gel image was captured by the Bio-Rad ChemiDoc XRS+ system and processed with BD ImageLab software.

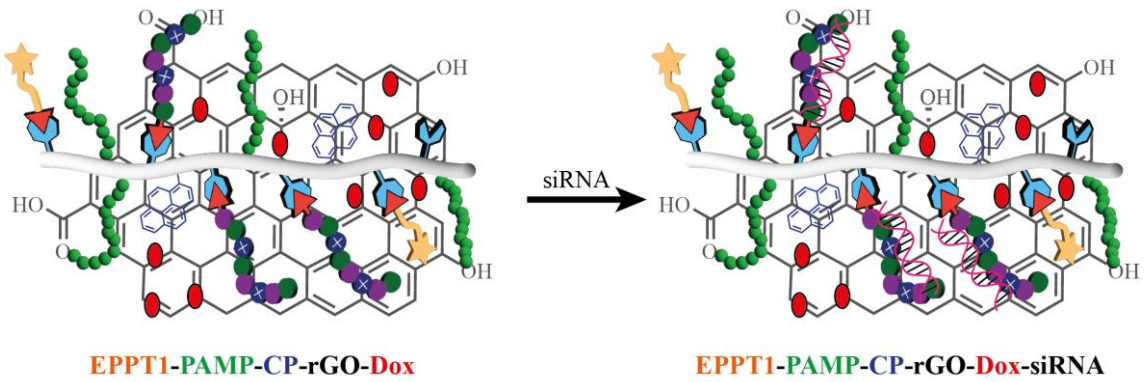


Figure 3.16: Complexation of EPPT1-PAMP-CP-rGO-Dox and siRNA (anti-GAPDH or anti-Bcl-2).

3.6. Zeta Potential and Size Measurements

Size and zeta potential measurements were performed by using a Malvern Zetasizer Ultra device in water environment. Size measurements were conducted in a transparent PS cuvette with a detector angle of 12.78° (forward scattering), where zeta potential measurements were performed by using the DTS1070 capillary cuvette in automatic settings. The concentration of PMP-rGO and PAMP-CP-rGO derivatives in water was tuned to prevent multiple scattering, flare, or fluorescence originating from the samples. For the siRNA complexes, cationic carriers were dispersed in water and freshly complexed at room temperature before each measurement with the siRNAs at 25/1, 30/1, 35/1, 40/1, and 45/1 mass ratios by increasing the PAMP-CP-rGO rate against siRNA in triplicate.

3.7. Coomassie (Bradford) Protein Assay Protocol

The total protein concentration of any given sample was determined by using Pierce™ Coomassie (Bradford) Protein Assay Kit. Protocol shared by the manufacturer was revised according to needs, as a general procedure, a 13.2 µL sample from cell lysate or any protein-containing solution was transferred into a 1.5 mL microtube in triplicates, 660 µL of Bradford reagent was transferred into each tube and mixed gently by pipetting up and down and incubated at room temperature for 10 minutes. After the incubation time, three aliquots of 200 µL from each sample or blank solution were transferred into a 96-well plate and their absorbance was recorded at 595 nm by a plate reader. Depending on the solution containing proteins that are tested lysis buffer, PBS or water was used as negative control and their absorption was recorded along with the samples. The absorption average of the blank solutions was subtracted from the sample's absorption values and total protein concentrations were calculated by using a calibration curve that was prepared by using a standard BSA solution (2 µg/mL) that was supplied with the kit. A serial dilution of BSA solution was prepared to cover a concentration range of 50 to 2,000 µg/mL, tested with the same method, and the results were plotted absorbance values against BSA concentration to fit a four-parameter (quadratic) curve.

3.8. Protein Adsorption Profiles of GO, rGO, and PAMP-CP-rGO

In order to show the blood-protein interaction, GO, rGO, and PAMP-CP-rGO were dispersed in 10% FBS containing PBS solution at pH 7.4 at a concentration of 0.5 mg/mL

and placed in a shaker at 37 °C [213], [214]. At predetermined time points, 50 µL samples were taken and centrifuged, and precipitate and supernatant were separated and stored at -20 ºC. Protein concentrations in collected supernatants were determined by using the Bradford assay and protein adsorption percentages were calculated by comparing free protein amount to the feed.

3.9. *In Vitro* Studies

3.9.1. Cell culture procedure

Human epithelial embryonic kidney cells (HEK-293T), human fibroblast lung cells (MRC-5), and epithelial human breast adenocarcinoma cells (ER+ MCF-7 and triple-negative MDA-MB-231) were maintained in DMEM supplemented with 10% fetal bovine serum (FBS), 1% L-glutamine, 1% MEM non-essential amino acids and 1% Penicillin/Streptomycin and epithelial human breast non-tumorigenic cells (MCF-10A) were cultured in MEBM™ Mammary Epithelial Cell Growth Basal Medium that is supplemented with 5% FBS and MEGM™ Mammary Epithelial Cell Growth Medium Single Quots™ kit containing supplements and growth factors and incubated at 37 °C with 5% CO_2 in a humidified environment.

3.9.2. Hemocompatibility of PMP-rGO derivatives

Hemolytic activity of GO, PMP2, PMP_{500}-rGO1, PMP_{500}-rGO2, PMP_{500}-rGO3, PMP5, PMP_{2000}-rGO4, PMP_{2000}-rGO5, and PMP_{2000}-rGO6 on red blood cells (RBCs) was tested to see the interaction between RBCs and rGO coated with a copolymer having different numbers and lengths of PEG brushes by using a common method with slight modifications [215]–[217]. A 5 mL sample of full blood donated by a volunteer was centrifuged at 3,500 rpm for 5 minutes. Serum was replaced with isotonic 0.15 M saline solution and the cell suspension was centrifuged again for 5 minutes. This process was repeated three times to wash the RBCs and after the last centrifuge, saline solution was replaced with PBS (pH 7.4) solution. Obtained RBCs were diluted by 1:10 with PBS to obtain 10^8 cells in 200 µL of solution. PMP-rGO derivatives were dispersed in PBS by probe-sonication at a final concentration of 2 mg/mL and tested for different concentrations, namely 5, 50, 100, 150, 200, and 300 µg/mL. PMP-rGO derivatives were first transferred into 1.5 mL microtubes, PBS solution was added to each sample to make the final volume 1 mL in total and lastly, 200 µL of RBC dilute was gently added to the

tube and mixed a few times by inversion. Tubes were incubated for an hour in a water bath at 37 °C and centrifuged at 13,000 rpm to remove all material and RBCs from the solution and absorption of 200 µL supernatant was recorded at 541 nm in a 96-well plate in triplicates. 1% Triton X-100 was used as positive control where non-treated RBCs were used as negative control and hemolysis of the materials was calculated using equation (**3.7**).

$$Hemolysis\% = \frac{Test\ well - Negative\ Control}{Positive\ Control - Negative\ Control} x100 \qquad \textbf{(3.7)}$$

3.9.3. MTS assay

The effect of the PMP-rGO derivatives on the viability of healthy and cancer cells was evaluated by using MTS ([3-(4,5-dimethylthiazol-2-yl)-5-(3-carboxymethoxyphenyl)-2-(4-sulfophenyl)-2H-tetrazolium]) (CellTiter 96® AQ_{ueous} One Solution Cell Proliferation Assay (MTS), Promega Corporation) reduction by following the protocol that was supplied by the manufacture. Briefly, 10.000 cells per well were seeded in 96-well plates incubated overnight for adherence, the medium was replaced with GO, PMP2, PMP_{500}-rGO1, PMP_{500}-rGO2, PMP_{500}-rGO3, PMP5, PMP_{2000}-rGO4, PMP_{2000}-rGO5 and PMP_{2000}-rGO6 solutions at 50, 100, 150, 200 and 300 µg/mL PMP-rGO concentrations in growth medium and incubated for 24 or 48 hours with the materials. After the washing steps, cells were incubated with an MTS reagent mixture for 2 hours, and from the UV absorption data recorded at 490 nm cell viability was calculated with respect to untreated controls by following equation (**3.8**).

$$Cell\ Viability\ \% = \frac{Test\ well - Negative\ Control}{Positive\ Control - Negative\ Control} \times 100 \qquad \textbf{(3.8)}$$

3.9.4. Resazurin assay

Determination of cell viability of Dox carrying nanoplatforms was carried out by resazurin assay (7-hydroxy-3H-phenoxazin-3-one-10-oxide sodium salt) in tissue-culture treated black-walled, clear bottom 96 well-plates. 10,000 cells were plated in each well overnight at 37 °C with 5% CO_2, then the medium in the wells was replaced with growth medium containing Dox, PAMP-CP-rGO-siRNA, EPPT1-PAMP-CP-rGO-siRNA, PAMP-CP-rGO-Dox-siRNA and EPPT1-PAMP-CP-rGO-Dox-siRNA at 1, 2.5, 5, 7.5, 10, 15 and 20 µg/mL Dox or equivalent PAMP-CP-rGO doses and incubated for 24 or 48

hours. The following day cells were washed with PBS to remove the remaining vectors, 5% resazurin solution was applied in the culture medium and incubated for 2 hours. Cell viability was determined by recording the fluorescence of metabolized resorufin at 590 nm by excitation at 550 nm with a microplate reader. Percent cell viability was calculated against untreated positive control wells after subtracting background fluorescence as seen in equation (**3.8**).

3.9.5. Clonogenic assay

To start from singlet cells, 500 MCF-7 cells were seeded into a 24-well plate in 0.5 mL full growth medium, incubated overnight for attachment, and Dox, PAMP-CP-rGO-siRNA, EPPT1-PAMP-CP-rGO-siRNA, PAMP-CP-rGO-Dox-siRNA and EPPT1-PAMP-CP-rGO-Dox-siRNA at 1, 2.5, 5 and 10 µg/mL Dox or equivalent PAMP-CP-rGO concentrations were applied in triplicates. After 24 hours of incubation with nanoplatforms, wells were washed twice with PBS and 0.5 mL of fresh full growth medium was added. After 10 days of incubation with regular medium change, colonies were formed consisting of 20 to 100 cells. Plates were removed from the incubator, the medium was removed and washed with PBS. Cells were fixed with ice-cold methanol at +4 °C, MeOH was removed from the wells and the cell surface was covered with 0.5% Crystal Violet Solution (Formulation: 0.5 g Crystal Violet, 250 mL methanol, 750 mL PBS), incubated with the dye at room temperature for 10 minutes. Dye was removed and wells were washed with PBS two times and pictures of wells were recorded for analysis by using a smartphone macro-1.9x lens with auto settings at equal illumination and colonies were counted by Fiji (V:2.5.0) software [218]–[221].

3.9.6. LDH release assay

For LDH (lactate dehydrogenase) assay (Thermo Scientific, Pierce LDH Cytotoxicity Assay Kit) 96-well plate seeded cells were incubated with GO, PMP2, PMP_{500}-rGO1, PMP_{500}-rGO2, PMP_{500}-rGO3, PMP5, PMP_{2000}-rGO4, PMP_{2000}-rGO5 and PMP_{2000}-rGO6 for 24 hours at concentrations of 50, 100, 150, 200, and 300 µg/mL in a total volume of 110 µL serum-free medium. After incubation with samples, 50 µL of medium from each well was transferred to another plate and incubated for 30 minutes in dark after the addition of 50 µL LDH reaction mixture which was prepared by mixing Substrate Mix solution and Assay Buffer that are supplied by the assay kit. Reactions were stopped by the addition of 50 µL Stop Solution and the absorbance of each well was examined at 490

nm and 680 nm. LDH activity was determined by subtracting 680 nm absorbance from 490 nm absorbance and the cytotoxicity rate was calculated by following equation (**3.9**). Untreated cells were used for spontaneous LDH activity control, while lysed cells were used for maximum LDH activity control.

$$\%\ Cytotoxicity = \frac{Test\ well\ LDH\ activity - Spont.LDH\ activity}{Max.LDH\ activity - Spont.LDH\ activity} \times 100 \quad \textbf{(3.9)}$$

3.9.7. Detection of induced reactive oxygen species (ROS)

ROS generation has been determined by employing Cellular Reactive Oxygen Species Detection Assay Kit (Deep Red Fluorescence) from ABCAM. The instruction obtained from the manufacturer was followed, briefly, cells were plated in a 96-well plated and treated with PMP2, PMP_{500}-rGO2, PMP_{500}-rGO3, PMP5, PMP_{2000}-rGO4, PMP_{2000}-rGO5 and PMP_{2000}-rGO6 for 24 hours at 100, 150, 200 and 300 µg/mL PMP-rGO concentrations. Following incubation time, cells were washed with PBS twice and treated with ROS Deep Red working solution, incubated for 45 minutes, and the increase in fluorescence was determined by excitation at 650 nm and emission at 675 nm. Induced ROS was determined according to equation (**3.10**) with respect to the untreated cells as negative control and hydrogen peroxide treated cells used as the positive control.

$$\%\ ROS\ Level = \frac{Compound\ treated\ Cells - Negative\ Control}{Positive\ Control - Negative\ Control} \times 100 \quad \textbf{(3.10)}$$

3.9.8. Determination of cellular uptake of rGO derivatives by confocal fluorescence microscopy

200,000 healthy or cancerous cells were seeded in 35 mm glass-bottomed culture dishes in a 1.5 mL full growth medium and incubated overnight at physiological conditions for adherence, following day medium was removed from the dishes, cells were washed with PBS, and treated with PMP-rGO or PAMP-CP-rGO derivatives. Meantime PMP-rGO derivatives were stained in PBS for 90 minutes with Alexa Fluor™ 488 (Thermo Scientific) and triple-washed with PBS to remove unbound dye. PAMP-CP-rGO derivatives were complexed with 25 nM anti-Bcl-2-siRNA or FAM labeled siRNA and consecutively were applied onto cells along with free Dox, and free siRNA in 1 mL of FBS-free medium for 2, 4, 6 or 24 hours at different trials. After completion of incubation time, cells were washed with PBS for three times to remove any free material and

incubated with 1 µL Hoechst dye-containing 1 mL fresh medium for 10 minutes, followed by sealing with parafilm to keep the atmosphere unchanged and images were captured by Zeiss LSM780 or LSM800 confocal microscope with Plan-Apochromat 20x/0.8 M27 objective or Plan-Apochromat 40x/1.3 Oil DIC M27, by using equal settings for all samples. Captured images were processed and analyzed by Zeiss Zen 3.3 blue edition software.

3.9.9. Determination of cellular uptake of Dox carrying PAMP-rGO and PAMP-CP-rGO derivatives by fluorescence-activated cell sorting technique

300,000 MCF-7 or MDA-MB-231 cells were plated in 6-well plates in 2.5 mL of culture medium and allowed to adhere to the well surfaces overnight. The next day, Dox, PAMP-rGO-Dox, EPPT1-PAMP-rGO-Dox, PAMP-CP-rGO-Dox-siRNA, and EPPT1-PAMP-CP-rGO-Dox-siRNA were applied at 50 nM anti-Bcl-2 siRNA or 2.5 µg/mL Dox concentration to the wells in 1 mL fresh medium and incubated with the cells under physiological conditions for 2 hours. After this period, nanoplatform containing solutions were removed from the wells, wells were washed with PBS twice to remove free nanoplatforms, then cells were detached from the well surface with 200 µL of Trypsin/EDTA solution, transferred to separate 15 mL centrifuge tubes, and centrifuged at 200 g for 5 minutes. The supernatants were discarded, and the cell pellet was dispersed in 500 µL PBS containing 2% FBS by volume and transferred to FACS tubes by passing through a nylon cell strainer. Tubes were kept on ice and analyzed in a flow cytometry device, for 10,000 events fluorescence intensity of Dox was recorded and processed by FlowJo™ software (V:10.6.2, Becton, Dickinson and Company, USA).

3.9.10. Determination of cell apoptosis levels induced by the combination of Dox and siRNA through APC-Annexin-V/Helix NP Blue double staining

Determination of the apoptotic effect of nanoplatforms was conducted with a similar approach, following cell seeding and 4-hour treatment with free siRNA, Dox, PAMP-CP-rGO-siRNA, EPPT1-PAMP-CP-rGO-siRNA, EPPT1-PAMP-CP-rGO-SCR/siRNA, PAMP-CP-rGO-Dox-siRNA, EPPT1-PAMP-CP-rGO-Dox-siRNA and EPPT1-PAMP-CP-rGO-Dox-CR/siRNA at 50 nM anti-Bcl-2 siRNA or scrambled siRNA or 2.5 µg/mL Dox concentration, cells were washed and incubated for 48 hours in fresh medium, harvested by Trypsin/EDTA solution, washed with 1x binding buffer (0.01 M HEPES, 0.14 M NaCl, 0.0025 M $CaCl_2$ at pH7.4), centrifuged and the supernatant was discarded.

A fresh staining solution was prepared by mixing 5 µL APC-Annexin-V (4 µg/mL), 0.5 µL Helix NP Blue (5 mM) and completed to 100 µL with 1x binding buffer per sample. Cell pellets were dispersed in 100 µL staining solution, incubated for 15 minutes in the dark at room temperature, diluted with 400 µL 1x binding solution, and centrifuged. The supernatant was removed completely from each tube, and cell pellets were redispersed in 2% FBS and 2.5 mM $CaCl_2$ containing PBS solution, then passed through a nylon cell strainer into FACS tubes and placed on ice. Cells were stored on ice and fluorescence intensities of APC-Annexin-V and Helix NP Blue were recorded for 10,000 events. Recorded data were processed by FlowJo™ software.

3.9.11. Determination of change in GAPDH levels by KDalert™ assay kit

40,000 MCF-7 cells were plated in 24-well plates in a 500 µL full growth medium and incubated overnight. 50 nM anti-GAPDH siRNA or scrambled siRNA complexes were prepared including Lipofectamine-siRNA, PAMP-CP-rGO-siRNA, EPPT1-PAMP-CP-rGO-siRNA, EPPT1-PAMP-CP-rGO-SCR/siRNA, PAMP-CP-rGO-Dox-siRNA, EPPT1-PAMP-CP-rGO-Dox-siRNA and EPPT1-PAMP-CP-rGO-Dox-CR/siRNA in triplicate and transferred onto cells. After 4 hours of incubation and cells were washed 2 times with PBS and post-incubated for 48 hours with a fresh medium. Medium on the cells was removed, cells were washed with PBS, 0.3 mL KDalert Lysis Buffer was added to each well and the plate was incubated at 4 °C for 30 min to lyse the cells completely. The cell lysates were pipetted up and down 4-5 times to homogenize the lysate and protein concentration was determined with the Bradford assay. An equal amount of protein from each well was transferred to a black 96-well plate, with 90 µL of KDalert Master Mix to each well. The plate was immediately placed in an Elisa reader and the fluorescence of the samples was recorded at room temperature using the kinetic mode to take a reading every 1 min for 10 min (λex = 560 nm, λem = 590 nm). Changes in protein levels were calculated according to the manufacturer's method.

3.9.12. Determination of change in gene expression levels by real-time polymerase chain reaction

500,000 MDA-MB-231 or MCF-7 cells were seeded in 6 well plates, after adherence to the well bottom cells were treated with free siRNA, PAMP-CP-rGO-siRNA, EPPT1-PAMP-CP-rGO-siRNA, EPPT1-PAMP-CP-rGO-SCR/siRNA, PAMP-CP-rGO-Dox-siRNA, EPPT1-PAMP-CP-rGO-Dox-siRNA, and EPPT1-PAMP-CP-rGO-Dox-

SCR/siRNA at 50 nM anti-Bcl-2-siRNA or scrambled siRNA concentration for 4 hours and washed twice with PBS. Cells were incubated in a fresh medium at physiological conditions for 48 or 72 hours to achieve gene knockdown.

3.9.12.1. RNA isolation

After incubation time cells were lysed according to the manufacturer's protocol, briefly old medium was removed, cells were washed and RNA lysis solution containing β-mercaptoethanol at room temperature was added to each well. After incubation at room temperature with a slow rocking, lysates were transferred into QIAshredders and centrifuged into clean 2 mL microtubes. Homogenized lysates were transferred to RNA spin columns and inserted into a 2 mL collection tube that binds all RNA and DNA from the solution. Isolated DNA was cleaned by DNase treatment and following wash steps total RNA was collected into RNase-free tubes with nuclease-free water. Obtained RNA concentrates were characterized by NanoDrop™ and stored at -80 °C.

3.9.12.2. Reverse transcription

Obtained total RNA was converted to cDNA by using the Omniscript Reverse Transcriptase Kit (QIAGEN) according to manufacturer protocol. 500 ng of total RNA from each sample was transferred to 0.2 mL microtubes, dNTP, random hexamers, and RNase inhibitor was mixed in a total volume of 20 µL, briefly vortexed, spined down, and incubated at 37 °C for one-hour to produce cDNA copies of the RNA, synthesized cDNAs were stored in -20 °C.

3.9.12.3. Determination of quantitative gene expression

cDNA samples were transferred to 8-strip 0.2 mL microtubes as triplicates, TaqMan Universal PCR Master Mix and FAM/MGB gene expression assay probes either human Bcl-2 or eukaryotic 18S rRNA endogenous control were added to the tubes to a final volume of 20 µL, 8 strips were sealed and placed in Bio-Rad CFX Connect Real-Time PCR Detection System which set to run 40 thermal cycles (2 minutes at 50 °C (one time), 10 minutes at 95 °C (one time), 40 cycles of the following two steps:15 seconds at 95 °C, 1 minute at 60 °C and fluorescence measurements at this step) to monitor qPCR reactions. From obtained data Ct values were used to determine mean fold change in gene expression levels by the $2^{-\Delta\Delta Ct}$ method [222].

3.9.13. SDS-Page and Western-Blot analysis for determination of Bcl-2 protein expression

MDA-MB-231 or MCF-7 cells were seeded at a density of 400,000 cells per well in duplicates in 6-well plates and incubated overnight for attachment. Once cells were attached to the well surfaces they were treated with free siRNA, Dox, PAMP-CP-rGO-siRNA, EPPT1-PAMP-CP-rGO-siRNA, EPPT1-PAMP-CP-rGO-SCR/siRNA, PAMP-CP-rGO-Dox-siRNA, EPPT1-PAMP-CP-rGO-Dox-siRNA and EPPT1-PAMP-CP-rGO-Dox-SCR/siRNA at 50 nM anti-Bcl-2-siRNA or scrambled siRNA concentration for 4 hours and incubated for 48 hours in the fresh medium after removal of material dispersant and wash with PBS. Once incubation time was completed cells were washed with PBS and trypsinized, duplicate wells were combined into 1.5 mL microtubes, centrifuged and cell pellets were lysed with 60 µL of RIPA lysis buffer containing PMSF solution, sodium orthovanadate solution, and protease inhibitor cocktail for an hour on ice. Cell lysates were centrifuged, the supernatant containing proteins transferred into clean microtubules, stored at -80 °C, and quantified with Coomassie (Bradford) protein assay.

An equal amount of total protein from each sample was transferred into clean microtubes topped with water and β-mercaptoethanol containing 4x Laemmli buffer. Each tube was incubated at 95 °C for 5 minutes to cleave intermolecular disulfide bonds and denature proteins, quickly transferred onto the ice. TGX Stain-Free™ FastCast™ Acrylamide Kit was used to cast 10% acrylamide gels between glass plates with a 1.0 mm spacer, ammonium persulfate (APS) was used as a free radical source, and tetramethyl ethylenediamine (TEMED) as a free radical stabilizer. After polymerizing stacker and resolver gel for 30 minutes at room temperature, the gel was placed into a vertical electrophoresis cell containing 1x tris-glycine-sodium dodecyl sulfate (TGS) solution, 20 µL from each sample, and pre-stained protein ladder was placed in gel wells and electrophoresed by applying 60-80 V of potential difference.

Separated protein bands were transferred to a 0.2 µm PVDF membrane by a semi-dry BioRad Trans-Blot Turbo Transfer System followed by blocking in 5% non-fat milk in tris-buffered saline solution with Tween® 20 detergent (TBST) for 1 hour at room temperature. The membrane was sliced into two pieces concerning protein marker to separate the protein of interest Bcl-2 and highly expressed housekeeping protein β-Actin. Blocking was followed by overnight incubation at 4 °C with the 1° β-actin and Bcl-2 mouse monoclonal IgG1κ antibodies, with mild racking in separate containers. The

following day membranes were washed several times in TBST buffer and incubated with 2° mouse IgG kappa binding protein (m-IgGκ BP) conjugated Horseradish Peroxidase (HRP) antibody for 1 hour at room temperature. Following this step, the membranes were washed with TBST to remove any remaining antibodies and the blots were exposed to Clarity™ Western ECL Substrate then images were taken with ChemiDoc XRS+ system, and images were analyzed by Bio-Rad Image Lab software.

To quantify inhibition in Bcl-2 expression band intensities were calculated by Image J software and protein expression levels were calculated by equation (**3.11**) against the control group and housekeeping gene.

$$\%Bcl\text{-}2\ Exp. = \frac{Bcl\text{-}2\ Band\ Int.\ /\ \beta\text{-}Actin\ Band\ Int.}{Cont.\ Bcl\text{-}2\ Band\ Int.\ /\ Cont.\ \beta\text{-}Actin\ Band\ Int.} * 100 \qquad \textbf{(3.11)}$$

3.10. *In vivo* Therapeutic Effect of Nanoplatforms

3.10.1. Animal care

All animal procedures were approved (Date:21.08.2015, Approval Number: 60, Document Number: 38828770-604.01.01-E.1814) by Istanbul Medipol University Animal Experiments Ethics Local Committee (İMÜ-HADYEK). All mice were purchased from the Center for Medical Research (MEDITAM) at the Research Institute of Health Science and Technologies (SABITA). They were housed under environmentally controlled standard conditions at 25 °C and 30-70% humidity. The day/night cycle is adjusted to be 12 hours with light and 12 hours in the dark and they were given free access to food and water. All studies were conducted in accordance with the local regulations and appropriate methods were selected during procedures to ensure that pain, suffering, and distress are kept to a minimum. Three endpoint criteria were set, and when any of the criteria were met the experiment was terminated: i) tumor size exceeding 800 mm^3, ii) body weight loss ≥15% or iii) any sign of discomfort and/or immobility.

3.10.2. Murine breast cancer model

6-8 weeks old (20-25 g) female outbred athymic nude mice (RRID:IMSR_JAX:007850, The Jackson Laboratory) were used as the animal model. MDA-MB-231 cells were passaged, counted, and dispersed in DMEM at a rate of 50,000 cells/µL and kept on ice

before the injection. 50 µL cell suspension containing 2.5 million cells was mixed with 50 µL Matrigel, drawn into a sterile 0.45x13 mm (26Gx1/2''), 1 mL injector, and kept on ice. In a container that was placed in a well-ventilated hood, mice were anesthetized with isoflurane, once they stopped moving, they were removed from the box and tagged on the ear with stamped metal ear tags for easy identification. Immediately injection area was wiped with alcohol solution and cells were injected subcutaneously into the right flank [223]–[225]. Mice were examined for xenograft size every third day, two perpendicular diameters were measured with a caliper and recorded with mouse weight, and the volume of the growing tumor was calculated by using equation (**3.12**) [226], [227].

$$Tumor\ Volume = \frac{(Short\ Axis)^2 * Long\ Axis}{2} \quad \textbf{(3.12)}$$

3.10.3. *In vivo* examination of anticancer effect

When the tumor volume reached 50-100 mm^3 MDA-MB-231 tumor-bearing mice were divided randomly into 6 groups (n=4 per group) and PBS, Dox, EPPT1-PAMP-rGO-Dox, EPPT1-PAMP-CP-rGO-siRNA, PAMP-CP-rGO-Dox-siRNA and EPPT1-PAMP-CP-rGO-Dox-siRNA (dispersed in PBS) were injected through the tail vein for 3 times at 3-day intervals using 0.5 mL, 0.30x8 mm (30G) injectors at a dose of 5 mg Dox per kg of body weight [10], [228]–[230]. The tumor volume and body weight of each mouse were recorded for 21 days and sacrificed at the end of the experiment duration or when any endpoint criteria were met. The relative tumor volumes were reported as the ratio of tumor volume at any point post injection (V_x) and tumor volume on the day of the first injection (V_0) (**3.13**) [231]–[235].

$$Relative\ Tumor\ Volume = \frac{V_x}{V_0} \quad \textbf{(3.13)}$$

3.11. Statistical Analysis

All experiments were conducted independently at least 3 times and results were reported as the arithmetic means with standard error of the mean. IC_{50} values were calculated by the nonlinear regression method and the statistical difference was evaluated with the two-way Anova analysis followed by the Tukey multiple comparison test using GraphPad Prism (V:9.4.0, USA). Colony, TEM, and confocal microscopy images were processed by Fiji (ImageJ, V:2.5.0) [236] or Zen Blue (Carl Zeiss GmbH, V:3.6.095) software.

CHAPTER 4

4. RESULTS AND DISCUSSION

4.1. Development of an Effective PEGylation Method to Improve Biocompatibility of Graphene Derivatives

4.1.1. Synthesis and characterization of P(PEGMA-*co*-MMA-*co*-PMA) coated rGO derivatives

Multiple pyrene units containing P(PEGMA-*co*-MMA-*co*-PMA) (PMP) copolymers with different PEG (500 and 2000 g/mol) brush numbers were prepared with the intention of determining the most efficient monomer ratio for high rates of rGO PEGylation and well biocompatibility.

Well-defined copolymers for PEGylation were synthesized with different compositions via atom transfer radical polymerization (ATRP) (**Figure 4.1**). Since the effect of the number of pyrene groups on coating and the effect of the number of PEGMA brushes on biocompatibility were mainly investigated in this study, a controlled polymerization technique was chosen however, synthesis of the copolymer using commercially available monomers via free radical polymerization could have been a practical way for straightforward applications.

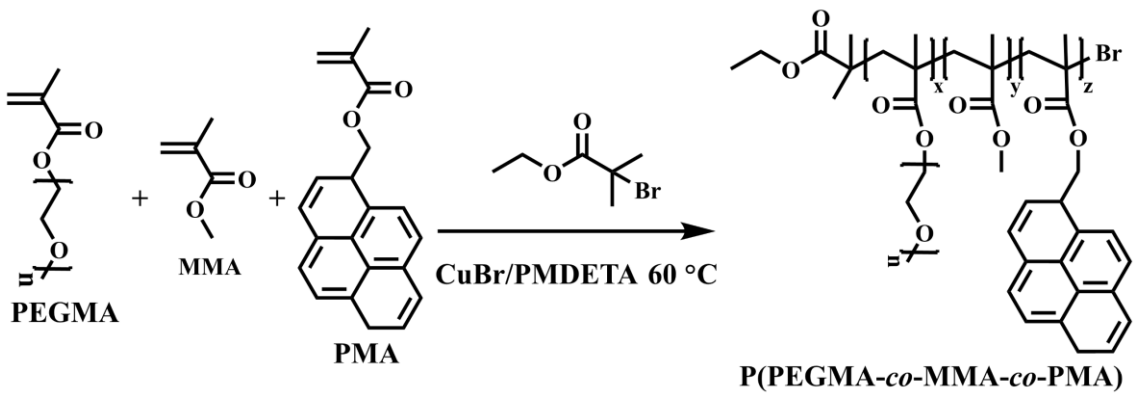


Figure 4.1: Reaction scheme of P(PEGMA-*co*-MMA-*co*-PMA) synthesis.

As can be seen in **Table 4.1**, monomers were copolymerized with different feeding ratios to tune copolymer compositions such as the number of pyrenes, number of PEGMA brushes, and density of PEG. 500 g/mol PEGMA macromonomer was used for PMP1, PMP2, and PMP3, and 2000 g/mol PEGMA macromonomer was used for PMP4, PMP5, and PMP6 compositions to tune the PEG content in the copolymer structure. Molecular weights and composition of the copolymers were determined via ^{1}H NMR (**Figure 4.2**) by determining the number of monomers in the copolymer using the ratio between pyrene, PEG, and MMA hydrogen atom signals. The obtained library of P(PEGMA-*co*-MMA-*co*-PMA) consists of copolymers that have 3-7 pyrene units, 7-18 PEG brushes, 40%-86% PEG contents, and molecular weights ranging from 8,700 to 39,000 g/mol (**Table 4.1**).

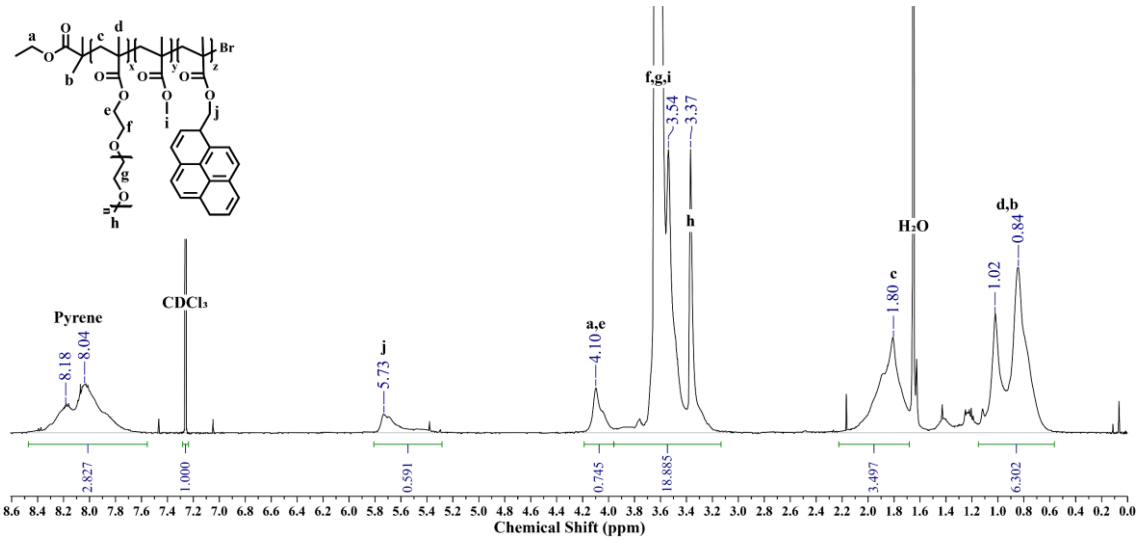


Figure 4.2: ^{1}H NMR spectra of P(PEGMA-*co*-MMA-*co*-PMA) (PMP1).

The number of the pyrene units in the copolymers was also calculated via UV-Vis spectroscopy through a calibration curve (**Figure 4.3**) using maximum absorption at

344.5 nm in dichloromethane and the molar absorption coefficient of pyrene was calculated as 52,746.39 L/mol.cm in accordance with the literature [237].

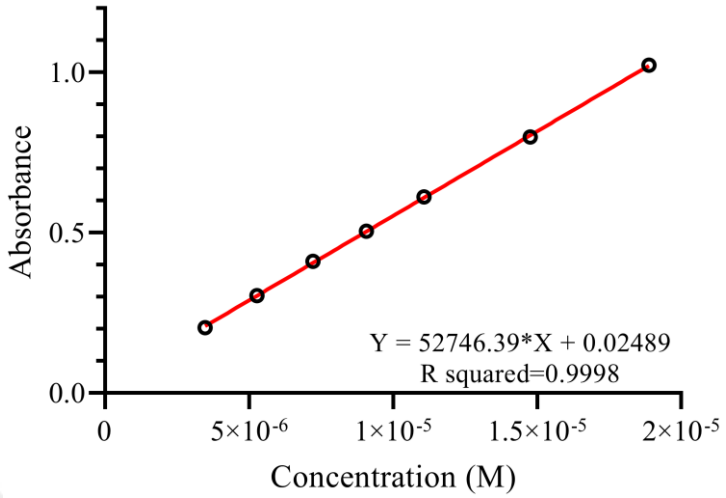


Figure 4.3: Calibration curve of pyrene at 344.5 nm in DCM.

Table 4.1: Features of chosen copolymers for PEGylation.

	Feed Ratio	$M_{n\text{NMR}}$[a]	DP_n[a]	**# of PEGMA**[a]	**# of MMA**[a]	**# of PMA**[a]	**# of PMA**[b]	**%PEG (w/w)**[c]
PMP1	20/65/15	8764	44.0	7.2	30.4	6.5	7.8	40.9%
PMP2	35/50/15	9719	39.4	11.4	22.9	5.1	3.2	58.7%
PMP3	70/15/15	11574	32.4	18.7	10.3	3.4	3.5	80.6%
PMP4	15/70/15	18481	45.9	7.0	33.4	5.9	4.7	75.2%
PMP5	35/50/15	21323	30.1	9.2	17.9	3.0	3.2	86.4%
PMP6	35/50/15	39246	58.4	16.7	34.3	7.4	7.1	85.1%

[a] Calculated from ^{1}H NMR by using signal ratios.
[b] Calculated by using UV-Vis spectroscopy.
[c] Mass fraction of PEG in the copolymer.

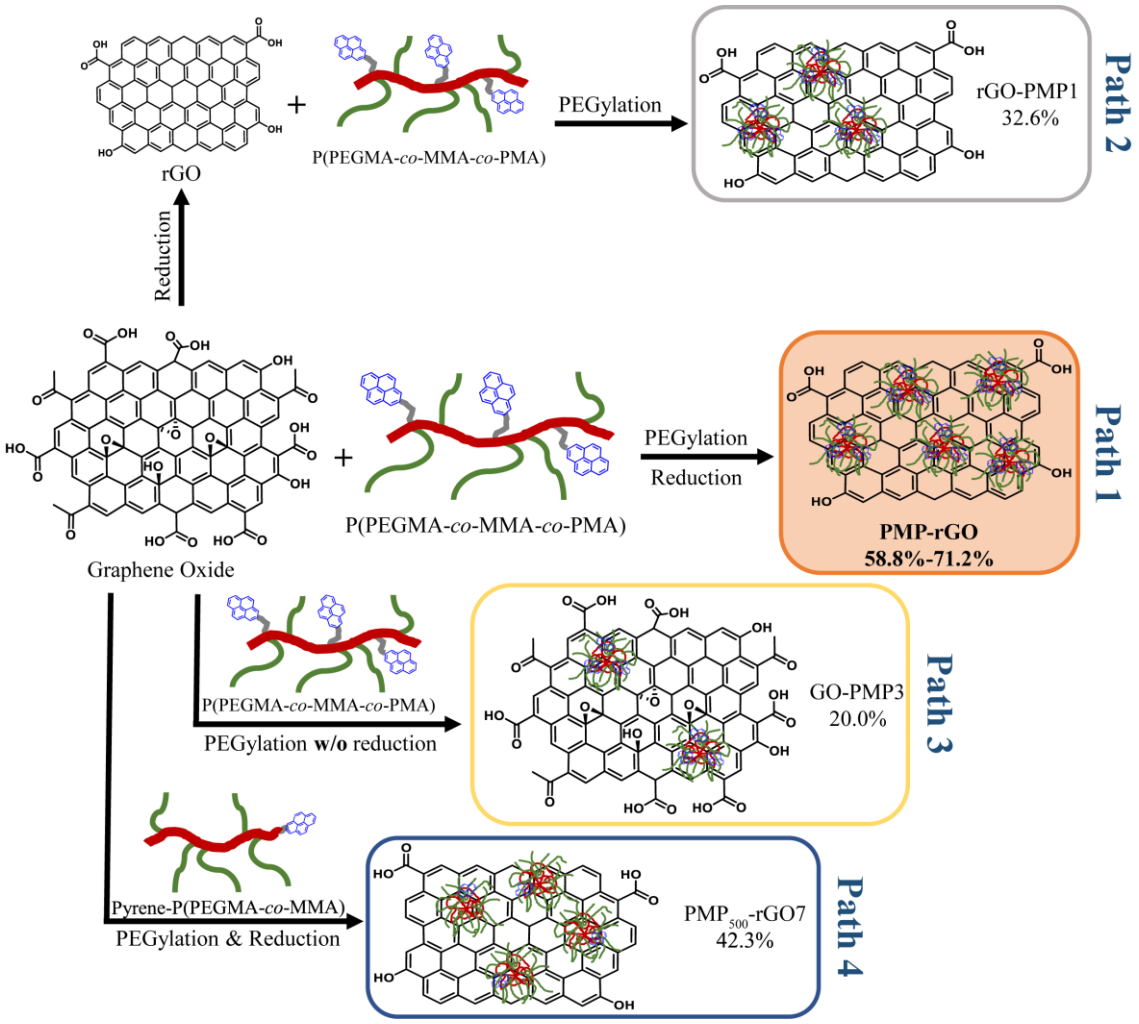


Figure 4.4: Schematic representation of possible paths for PEGylation of graphene derivatives.

For the proposed effective PEGylation method, P(PEGMA-*co*-MMA-*co*-PMA) copolymers were coated on the GO surface through π-π interaction of pyrene groups, and meanwhile, GO was reduced to rGO using hydrazine as a reducing agent to obtain PEGylated reduced graphene oxide (PMP-rGO) (**Figure 4.4, Path 2**). Used hydrazine concentration for the reduction was low (0.94 mg/mL, 29.3 mM) and did not cause any damage or side reaction on coated copolymer based on before and after coating data comparison (**Figure 4.2** and **Figure 4.5**). The PMP-rGO derivatives were collected via centrifugation and washed multiple times with water and acetone to remove any unbounded copolymer from the system. ^{1}H NMR analysis of dispersed PMP_{500}-rGO1 solution showed signals that originate from methylene groups of PEG and methyl protons of MMA from 3.0 ppm to 4.35 ppm. Pyrene signals along with rGO signals and backbone protons of the copolymer can be clearly seen at aromatic and aliphatic regions, respectively in **Figure 4.5**.

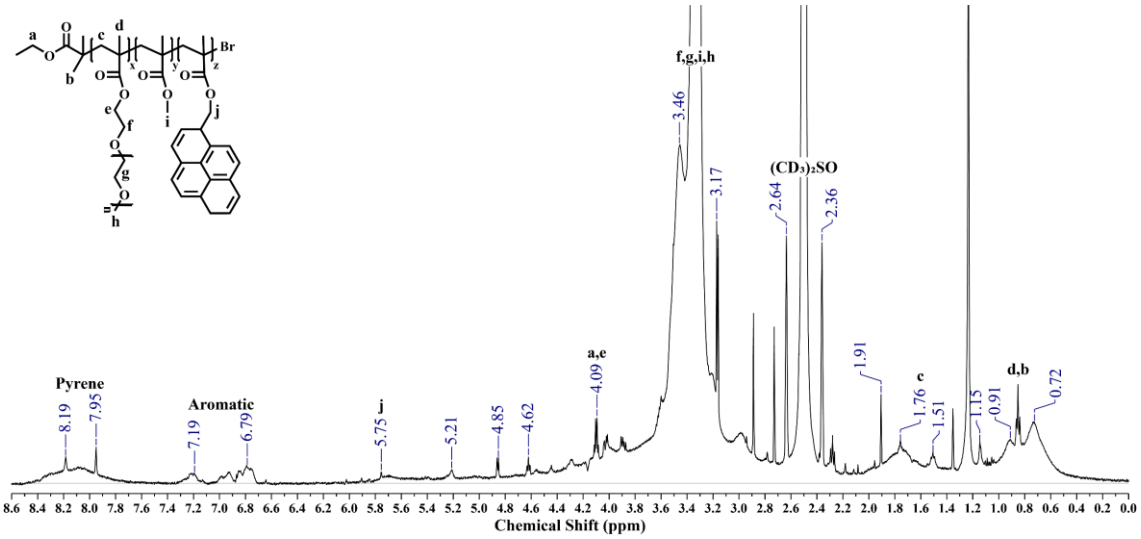


Figure 4.5: ^{1}H NMR spectrum of PMP1 coated rGO (PMP_{500}-rGO1).

Pyrene groups in the copolymer structure showed characteristic optical absorbance between 300-350 nm, which was similarly observed for PMP-rGO derivatives indicating the presence of the copolymer on the surface (**Figure 4.6a**). An equal amount of pyrene containing free copolymer and the coated copolymer on the rGO surface was excited at 345 nm, and PMP3 showed a characteristic emission spectrum of pyrene while PMP_{500}-rGO1 exhibited the same emission with a decreased intensity because of the quenching of pyrene units on the graphene surface (**Figure 4.6b**).

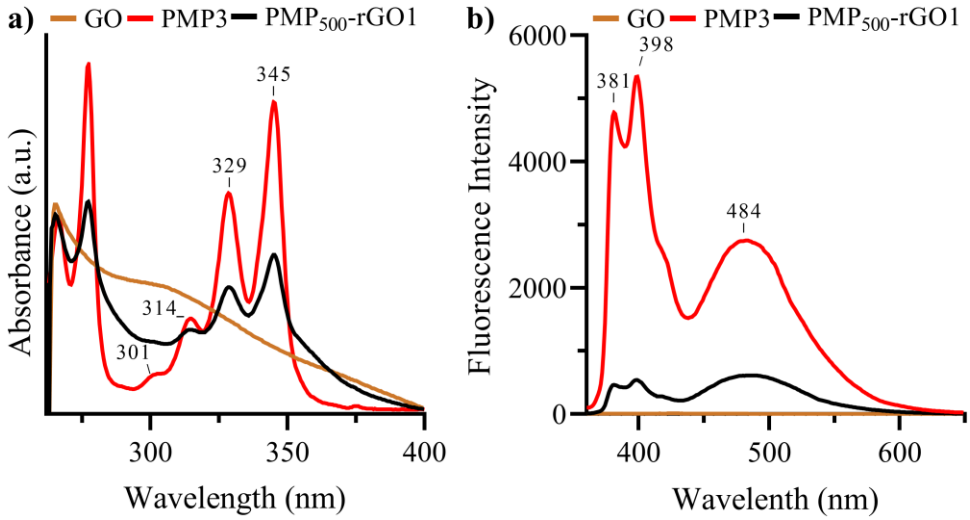


Figure 4.6: a) UV-Vis and **b)** Fluorescence spectrum of GO, PMP3, and related PMP_{500}-rGO1.

From the FTIR spectra of GO characteristic broad -O-H stretching band at 3200 cm^{-1}, the carbonyl group of carboxyl at around 1730 cm^{-1}, -C=C- signals at 1623 cm^{-1} and -C-O-C- stretching signal at 1044 cm^{-1} can be clearly seen, whereas at PMP-rGO spectrum no

-O-H stretching band was observed, indicating successful reduction. Besides, aliphatic -C-H peaks in the range of 3000-2800 cm^{-1} and -C=O groups at 1727 cm^{-1} from the copolymer spectrum can also be seen on the PMP-rGO spectrum, indicating the presence of copolymer on the rGO (**Figure 4.7**).

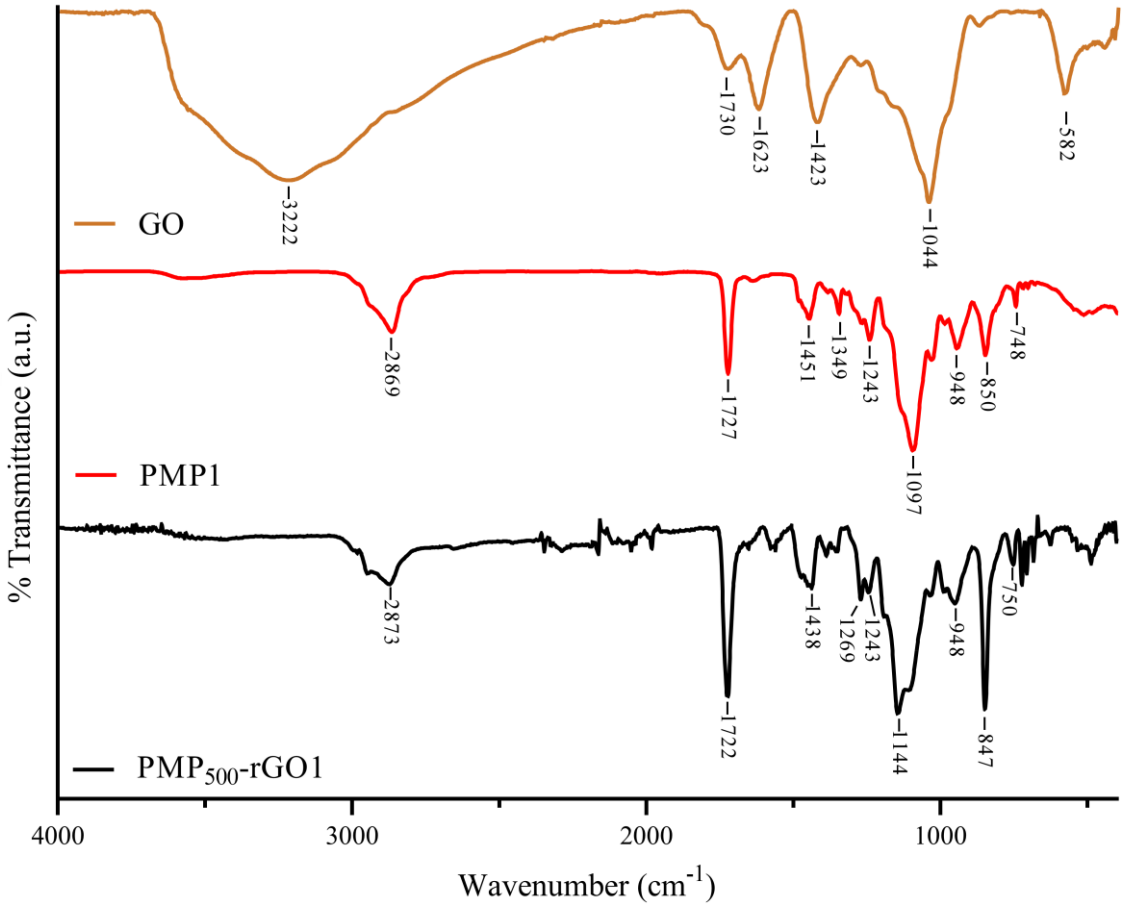


Figure 4.7: FTIR spectra of GO, PMP1, and PMP_{500}-rGO1.

PEGylation and simultaneous reduction of GO to rGO were further confirmed by Raman spectroscopy (**Figure 4.8**). GO commonly displays characteristic D and G bands, which indicates the change of electronic configuration on the carbon lattice. D band is associated with sp^3 hybridization of carbon atoms, and the G band originates from sp^2 carbon atoms vibrations on the plane. The reduction of GO to rGO changes the degree of in-plane defects and functionalities on the surface resulting change in the ratio of D and G band intensity [238]. GO showed D and G bands at 1319 cm^{-1} and 1586 cm^{-1}, respectively and the G band shifted to 1588 cm^{-1} once GO was reduced to rGO causing a slight decrease in I_D/I_G ratio from 1.31 to 1.29. After PEGylation and simultaneous reduction D band shifted downward to 1306 cm^{-1} and 1308 cm^{-1} and the G band shifted upward to 1595 cm^{-1} and 1591 cm^{-1} for PMP_{500}-rGO3 and PMP_{2000}-rGO5, respectively, and resulted in a

narrower G band. The decreased I_D/I_G ratio increased once GO was PEGylated and reduced, which indicates the interaction between P(PEGMA-*co*-MMA-*co*-PMA) copolymer and graphene surface [239]. The 2D band that reflects the stacking of rGO plates has not been observed at a high intensity (data not shown).

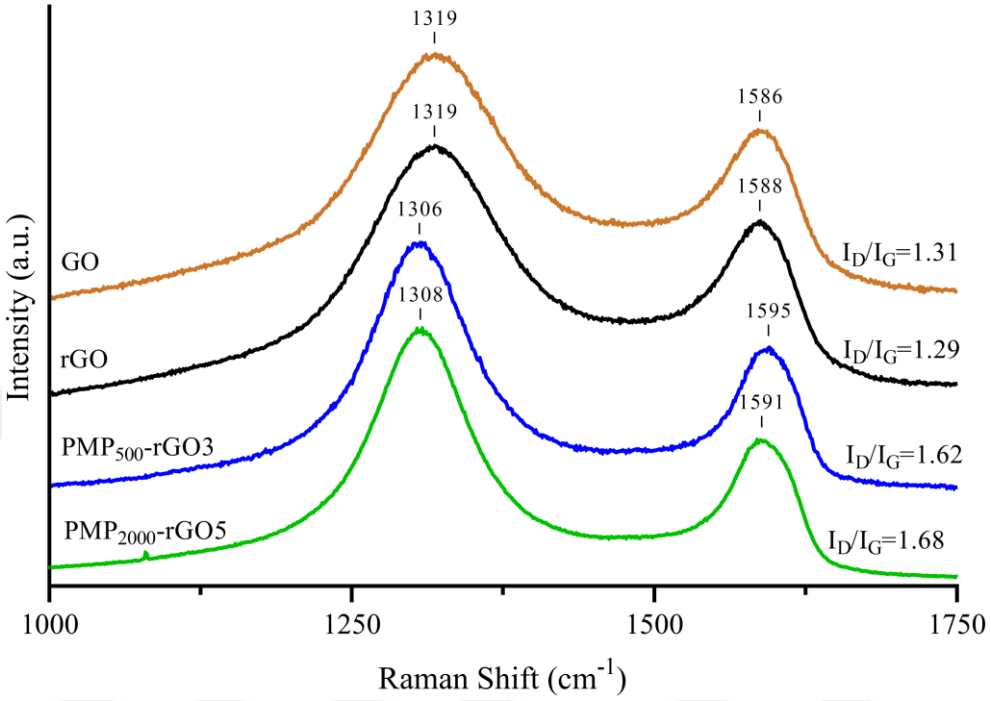


Figure 4.8: Raman spectra of GO, rGO, PMP_{500}-rGO3, and PMP_{2000}-rGO5.

The weight percentage of the copolymer conjugated onto the rGO was calculated through TGA measurement. **Figure 4.9** shows the typical TGA curves of rGO, GO, PMP1, PMP5, and PMP_{500}-rGO3 and PMP_{2000}-rGO5 between 30 to 800 °C heated at the rate of 10 °C/min under a nitrogen atmosphere. The TGA curve of rGO showed only 28% gradual weight loss until 800 °C as expected, whereas GO has a rapid mass loss above 180 °C due to the decomposition of oxygen-containing groups [240]. PMP1 and PMP5 as selected P(PEGMA-*co*-MMA-*co*-PMA) copolymers with different PEG brush lengths showed multistep degradation profiles including main weight lost at 360 °C onset temperature. PMP-rGO derivatives obtained using PMP1 and PMP5 exhibited a similar degradation profile with their copolymer however, their thermal stability has been improved due to the elimination of oxygen-containing functionalities from the GO surface through reduction. Weight loss associated with copolymer degradation was used to calculate the weight percentage of coated copolymer on the graphene surface since it is the main degradation between the range of 200 and 55 °C. The weight loss of rGO at this temperature range was subtracted to have only copolymer contribution to the weight

loss. The calculated values in the range of 58.8% to 71.2% were also called coating efficiency or degree of PEGylation of PMP-rGO derivatives (**Table 4.2**).

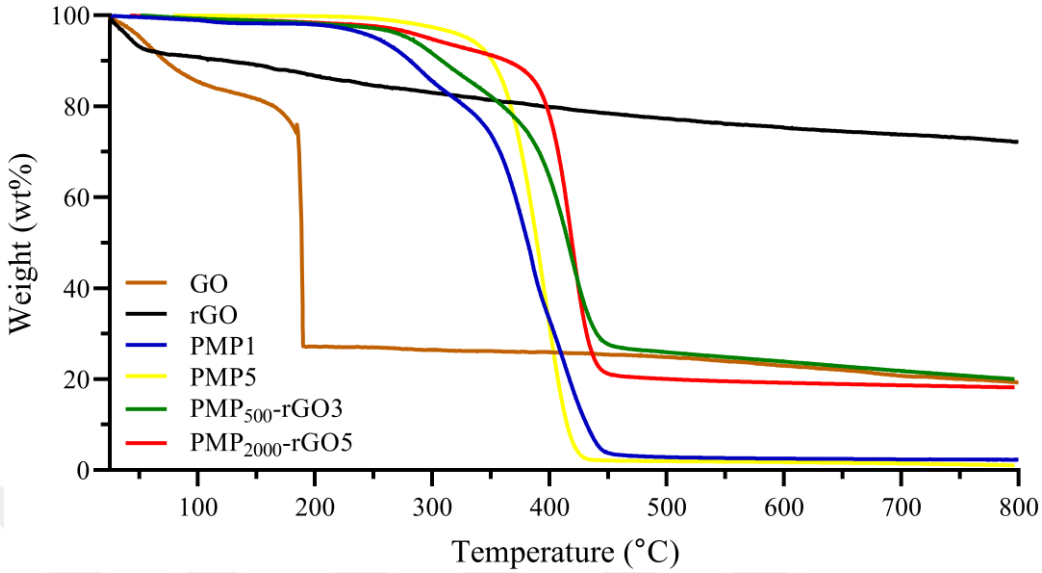


Figure 4.9: Thermogravimetric analysis of GO, rGO, PMP1, PMP5, PMP_{500}-rGO3, and PMP_{2000}-rGO5.

Table 4.2: Features of copolymers used for PEGylation, %PEG content, and coating efficiency of PMP-rGO derivatives.

Code	PMP/GO (w/w)	# of PEGMA	# of MMA	# of PMA	M_n (g/mol)	%PEG (w/w)	Coating Efficiency[a]
PMP_{500}-rGO1	10	7.2	30.4	6.5	8764	40.9%	58.8%
PMP_{500}-rGO2	10	11.4	22.9	5.1	9719	58.7%	64.5%
PMP_{500}-rGO3	15	18.7	10.3	3.4	11574	80.6%	64.5%
PMP_{2000}-rGO4	10	7.0	33.4	5.9	18481	75.2%	67.2%
PMP_{2000}-rGO5[b]	28	9.2	17.9	3.0	21323	86.4%	71.2%
PMP_{2000}-rGO6	20	16.7	34.3	7.4	39246	85.1%	66.4%

[a] Weight loss of rGO between 200-550 °C is 10.6%. Coating efficiencies were calculated by using the weight loss difference.
[b] Number of pyrene units per GO set equal to PMP_{500}-rGO1 reaction conditions.

The possible paths for PEGylation were investigated to show superiority the path takes place via multiple pyrenes containing PEGylation and simultaneous reduction of GO (**Figure 4.4** and **Figure 4.10**). For instance, when GO was coated with P(PEGMA-*co*-MMA-*co*-PMA) copolymer without reducing it to rGO (**Figure 4.4, Path 3**), coating efficiency was only obtained as 20.0% (TGA result can be seen in **Figure 4.11**) indicating the contribution of enhanced, the defect-free surface of rGO to coating efficiency which increases the chance of π-π interaction. This may raise the question of whether rGO can

be used as a starting material. To address this question, rGO was used as starting material instead of GO for PEGylation (**Figure 4.4, Path 2**). GO was reduced to rGO with hydrazine hydrate prior to the PEGylation and solid product rGO was re-dispersed in water and interacted with P(PEGMA-*co*-MMA-*co*-PMA) with standard protocol without hydrazine addition for the reduction. The results showed the importance of beginning with water-dispersible derivatives of GO as starting material. Coating efficiency was obtained as 32.6% (TGA result can be seen in **Figure 4.11**) because of the difficulty of obtaining a well-dispersed solution of rGO. Summarized results in **Table 4.3** collectively show that starting with the most soluble and well dispersible derivatives of graphene allows initial interaction with copolymer and meanwhile reduction further increases the interaction with pyrene groups. Initial PEGylation of GO before its reduction maintains the solubility of PEGylated layers and it yields highly coated and still dispersible layers when they were reduced to rGO efficiency (**Table 4.2**).

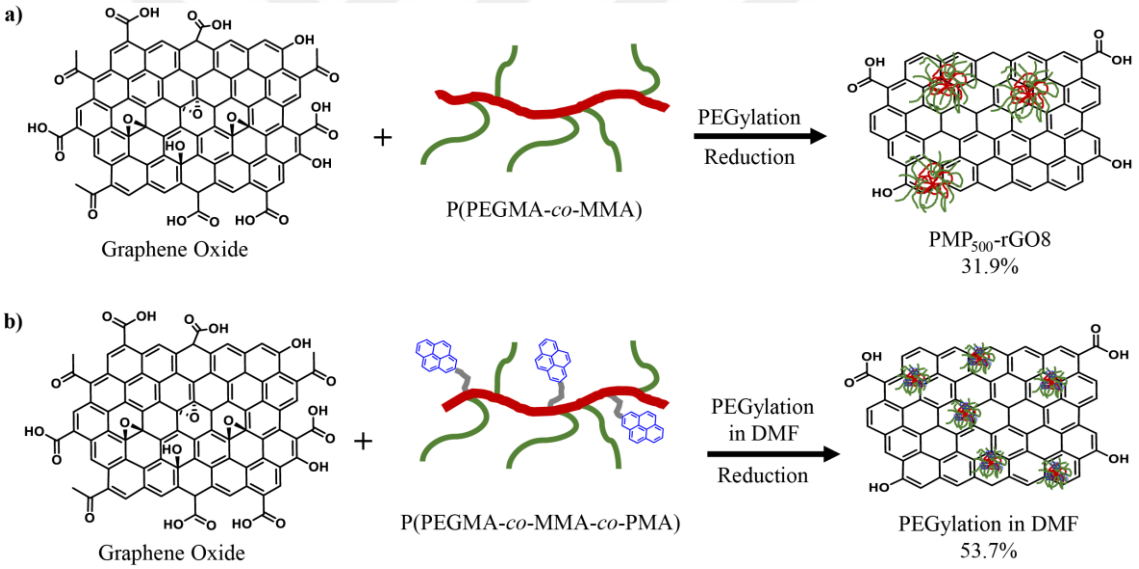


Figure 4.10: a) PEGylation and reduction of GO by using P(PEGMA-*co*-MMA) (no pyrene) and **b)** simultaneous PEGylation and reduction of GO in DMF.

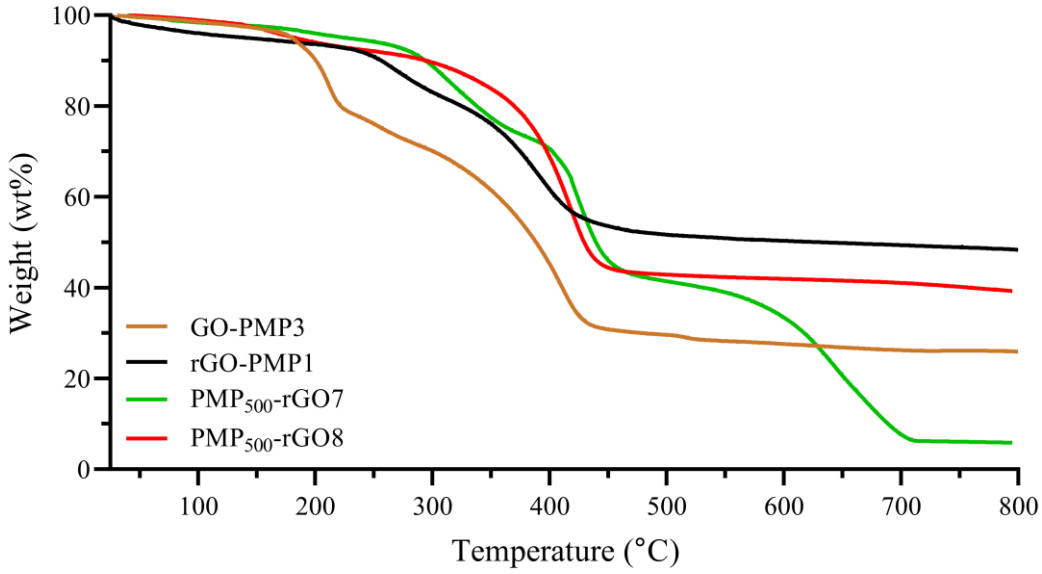


Figure 4.11: Thermogravimetric analysis of GO-PMP3, rGO-PMP1, PMP_{500}-rGO7, and PMP_{500}-rGO8.

Furthermore, the effects of the PMP/GO ratio and the number of the pyrene units on the side chain of the copolymers on coating efficiency were investigated. **Table 4.2** showed that increasing the PMP/GO (w/w) ratio increased the coating efficiency from 58.8% to 71.2% as expected. Coating efficiency was also enhanced by increasing the percentage of PEG content in the copolymer which contributes to the solubility of coated graphene that enhances the further interaction between copolymers and already coated GO. Here, the number of pyrene units in the copolymer is a parameter that needs to be addressed whether it contributes to the coating efficiency. The data represented in **Table 4.2** showed that the number of pyrene on copolymer did not significantly affect coating efficiency as it is comparable with the contribution of increasing PMP/GO ratio and PEG content. However, the necessity of the multiple pyrene groups for effective coating was investigated with a model reaction including a single pyrene functional Pyrene-P(PEGMA-*co*-MMA) copolymer under the same coating conditions (**Figure 4.4, Path 4**). For this purpose, a pyrene functional ATRP initiator was synthesized (**Figure 3.2**) and PEGMA (500 g/mol) and MMA were copolymerized to obtain a single pyrene functional PEG brush containing copolymers. The coating condition was applied by including the same number of pyrenes with PMP_{500}-rGO3 by arranging the amount of polymer (PMP/GO:65) and the results showed 42.3 % coating efficiency (**Table 4.3,** PMP_{500}-rGO7). Although increasing PMP/GO ratio increases the coating efficiency, it did not work in the same way when the copolymer includes a single pyrene group suggesting the importance of multiple pyrene groups on coating efficiency. Moreover, the coating

efficiency of non-pyrene-containing copolymer on the graphene surface indicated the contribution of the multiple pyrenes. So, P(PEGMA-*co*-MMA) copolymer without a pyrene group was synthesized to see whether it contributes to coating efficiency by itself even if it does not contain any pyrene groups. Molecular weight and the repeating units of P(PEGMA-*co*-MMA) copolymer were arranged in the range of multiple pyrenes containing copolymers, and the same coating conditions were applied to have a better comparison (**Figure 4.10a**). The results showed that the copolymer itself also interacts with the graphene surface and gets coated on the rGO surface with an efficiency of 31.9% (**Table 4.3,** PMP_{500}-rGO8). The results collectively supported that along with the multiple pyrene groups as the main contributor, copolymer itself has a contribution to coating efficiency as well.

Table 4.3: Features of copolymers used for control of PEGylation, coating efficiency, and %PEG content of PMP-rGO derivatives.

Code	PMP/GO (w/w)	# of PEGMA	# of MMA	# of PMA	M_n (g/mol)	%PEG (w/w)	Coating Efficiency[a]
GO-PMP3	10	18.7	10.3	3.4	11574	80.6%	20.0% [b]
rGO-PMP1	10	7.2	30.4	6.5	8764	40.9%	32.6%
PMP_{500}-rGO7[c]	65	34.2	48.2	1	22319	76.6%	42.3%
PMP_{500}-rGO8[d]	10	20.6	37.9	-	14094	73.1%	31.9%
PEGylation in DMF	28	9.2	17.9	3.0	21323	86.4%	53.7%

[a] Weight loss of rGO between 200-550 °C is 10.6%. Coating efficiency was calculated by using the weight loss difference.
[b] Weight loss of GO between 100-550 °C is 50.4%. Coating efficiency was calculated by using the weight loss difference.
[c] Reaction was set to match the pyrene concentration of PMP_{500}-rGO3.
[d] Copolymer was synthesized with EiBr with no pyrene unit.

X-ray photoelectron spectroscopy (XPS) was performed on GO, rGO, PMP_{500}-rGO3, and PMP_{2000}-rGO5 to evaluate change in the graphene surface properties related with reduction and PEGylation (**Figure 4.12**). Deconvolution of the C1s XPS spectrum of GO showed 3 peaks with binding energies of 283.6, 285.6, and 287.4 eV credited to -C-H (C-C/C=C), -C-O-C- (ether, epoxy) and -C=O species respectively [241], [242]. After the reduction of GO, the intensity of the -C-O-C- bond reduced significantly due to the reduced number of epoxy functionalities, and a 290.3 eV new signal emerged representing π-π* shake-up satellite (**Figure 4.12b**) which indicates increased conjugated structure [243], [244]. Survey scans of GO and rGO exhibited 67.3% and 88.2% C1s and 30.4% and 9.3% O1s, respectively, showing successful reduction (**Table 4.4**). Introducing the high ethylene oxide and acrylate-containing copolymer via π-π stacking

onto the graphene surface increased the intensity of ether signal at 285.7 eV and carbonyl signal at 288.0 eV while resulting in similar signals with rGO. PMP_{500}-rGO3 showed 70.3% C1s and 25.4% O1s whereas longer brushes containing PMP_{2000}-rGO5 had 78.3% C1s and 19.4% O1s. Once more, it was concluded that PEGylation and reduction took place successfully and copolymer was grafted on the surface of the rGO [245], [246].

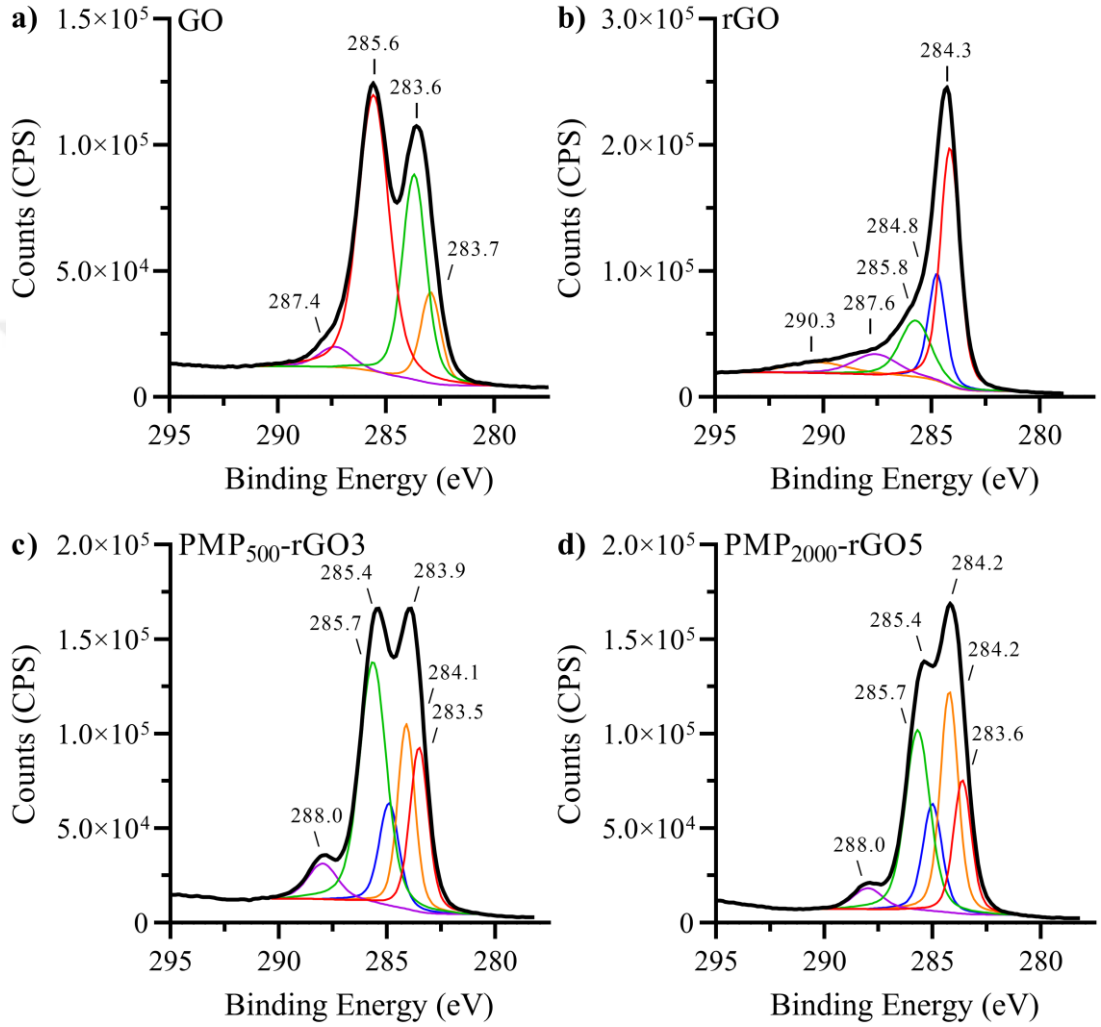


Figure 4.12: XPS spectra of **a)** GO, **b)** rGO, **c)** PMP_{500}-rGO3 and **d)** PMP_{2000}-rGO5.

Table 4.4: Atomic percentage, which is determined by XPS survey scan of GO, rGO, PMP_{500}-rGO3, and PMP_{2000}-rGO5.

Code	% C1s	% O1s	% N1s	% S2p	% Si2p
GO	67.29	30.41	0.68	1.62	
rGO	88.15	9.33	2.52		
PMP_{500}-rGO3	70.33	25.41			4.26
PMP_{2000}-rGO5	78.27	19.38			2.35

Morphological changes of GO and PMP-rGO derivatives were further investigated using atomic force microscopy (AFM). Samples were prepared by deposition of 0.05 mg/mL

dispersant on the mica substrate by drop casting. Single graphene oxide sheets can be seen in **Figure 4.13a** with a layer thickness of around 1 nm similar to the literature [247], [248]. When GO was reduced to rGO without PEGylation as a control sample, the thickness of the rGO sample reached 40 nm because of the stacking of rGO layers (**Figure 4.13b**). AFM images of PMP-rGO derivatives showed obvious morphological changes when compared to both GO and rGO, although reduction of GO simultaneously takes place during PEGylation, it did not significantly cause layer stacking supporting the advantage of the PEGylation method. However, shorter PEG brushes may not be as effective as longer brushes to prevent layer stacking. The average thickness for PMP_{500}-rGO3 was found to be around 5 nm to 8 nm showing the contribution of polymer coating on the reduced graphene oxide surface and few layers stacking (**Figure 4.13c**), while the average thickness for PMP_{2000}-rGO5 was found to be around 3 nm (**Figure 4.13d**). This result was supported by the water dispersibility and stability properties of PMP_{2000}-rGO5, which showed a better profile compared to PMP_{500}-rGO3 (**Figure 4.17a**) To better understand copolymer-GO interactions a physical mixture of PMP5 and GO as control was applied on a mica substrate, as can be seen in **Figure 4.13e** no visible copolymer localization has been found on GO plates, indicating the importance of reduction for π-π interaction between copolymer and GO.

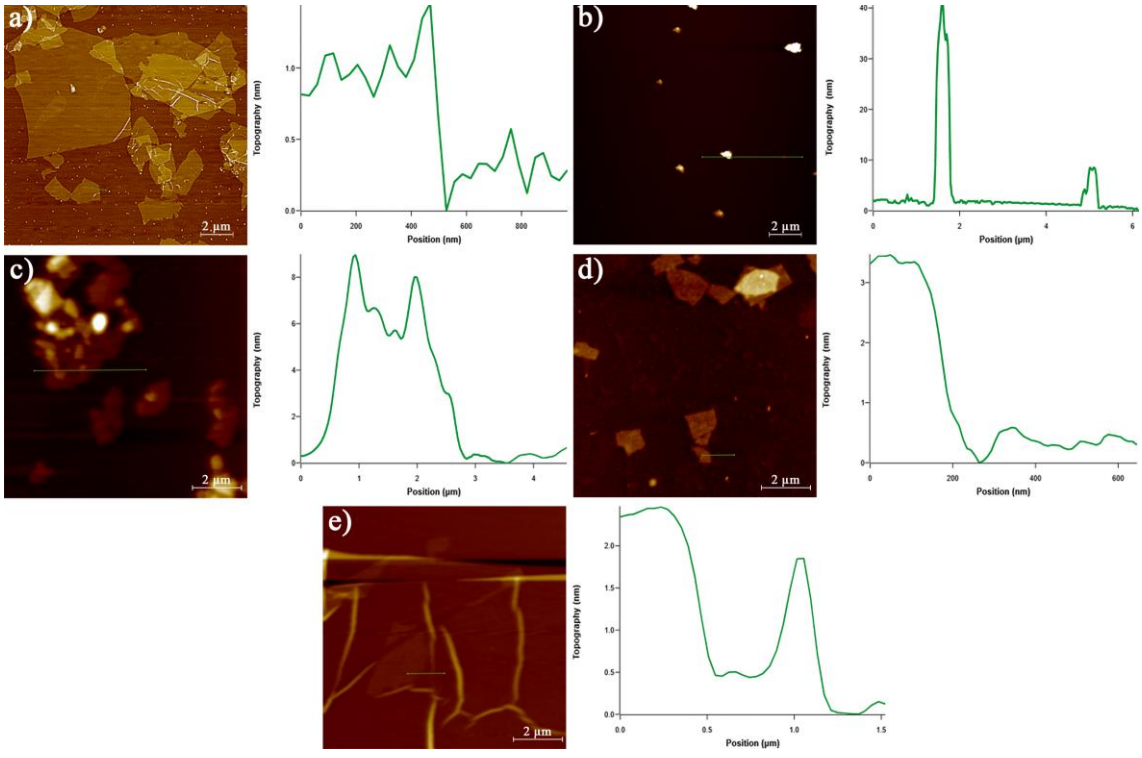


Figure 4.13: AFM images of **a)** GO, **b)** rGO, **c)** PMP_{500}-rGO3, **d)** PMP_{2000}-rGO5, and **e)** GO and PMP5 physical mixture.

The dynamic light scattering (DLS) method was employed to determine the size of PMP-rGO derivatives, results can be seen in **Figure 4.14**. The size of GO is found to be 410 nm where PMP-rGO derivatives range between 250 nm and 340 nm with a negative surface charge as expected. Due to the sonication during the redispersion of PMP-rGO derivatives for sample preparation, the size of the PMP-rGO becomes lower than GO which can be considered a tool to lower the size of PMP-rGO derivatives when it is needed [249].

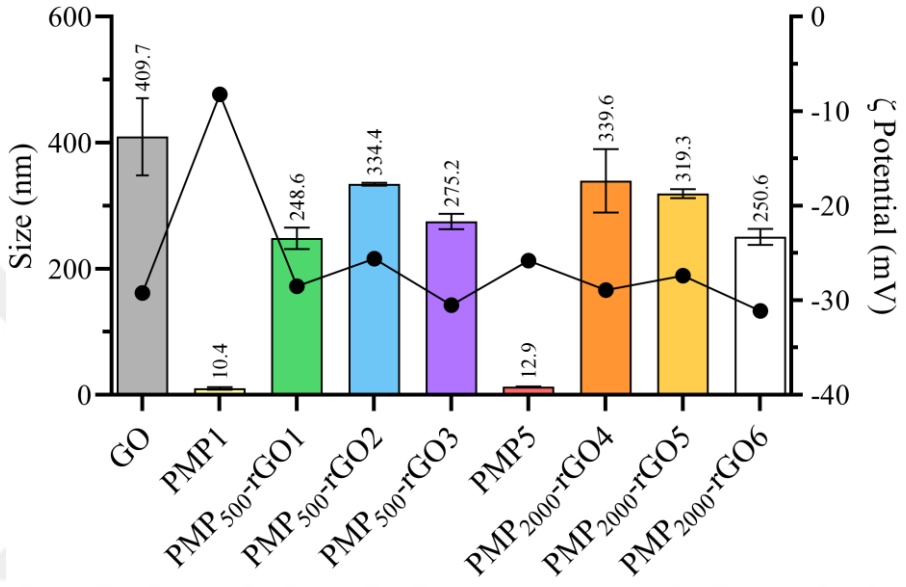


Figure 4.14: Size and Zeta Potential of copolymers and rGO conjugates, where rGO has a size of 27878 ±528.2 nm and ζ Potential -27.6 mV.

On the other hand, since DLS is more suitable for the size determination of spherical particles, transmission electron microscopy (TEM) was applied as a second method to determine the size and visualize the PMP-rGO derivatives. The size of the PMP-rGO derivatives was calculated by Fiji software using related TEM images using an average of 15-17 graphene sheets for GO and 40-45 sheets for each PMP-rGO derivative as 2167 ±364 nm, 736 ±79 nm, and 639 ±56 nm for GO, PMP_{2000}-rGO5 and PMP_{500}-rGO3 respectively due to the asymmetrical geometry. **Figure 4.15** shows the pristine graphene sheet (**Figure 4.15a**) and copolymers on the sheet after PEGylation (**Figure 4.15b-c**) at 100,000 magnification. The images showed that easily water-dispersed PMP-rGO derivatives displayed single or few-layer sheets without any sign of agglomeration. When PMP_{500}-rGO3 and PMP_{2000}-rGO5 derivatives were compared, it supports the idea that increasing PEG% on the surface decreases the chance of stacking graphene sheets (**Figure 4.15b** vs **Figure 4.15c**). The role of the solvent system on coating was also

investigated and tried to visualize via TEM imaging. Because copolymer has a hydrophobic backbone and pyrene groups with hydrophilic PEG brushes, it may have good and bad solvents together in DMF/water mixture environment that might result in an organization or increased hydrophobic interaction between copolymer and rGO. This prediction was tested using only DMF as a good solvent for PEGylation of GO with PMP5 by regular coating procedure to see whether it cause any difference in coating efficiency (**Figure 4.10b**). The obtained PMP_{2000}-rGO5 was analyzed by TGA and 53.7% coating efficiency was determined which is around 10% lower than other coatings in H_2O:DMF (2:1) solution (**Table 4.3**). TEM image of the PMP_{2000}-rGO5 derivative obtained in DMF showed smaller polymer aggregates (**Figure 4.15d**) on the graphene surface that is different from the one obtained in DMF/water environment (**Figure 4.15b** and **c**).

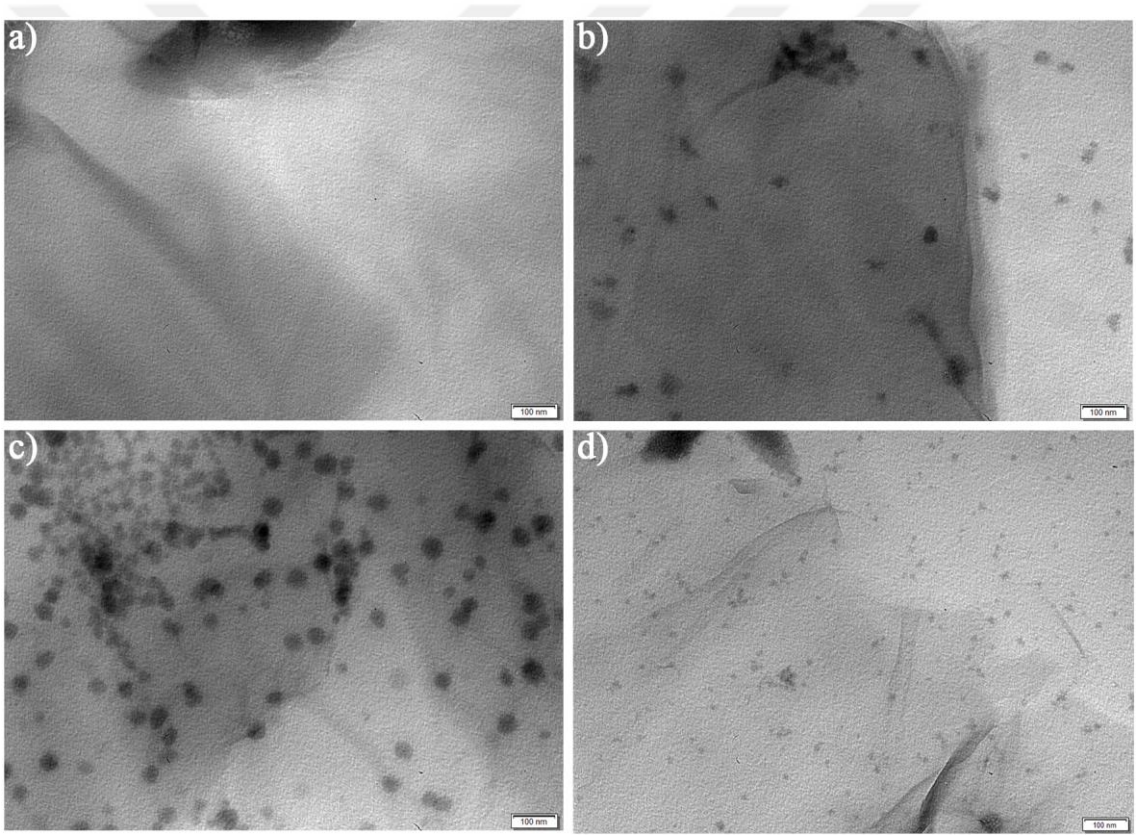


Figure 4.15: TEM images of **a)** GO, **b)** PMP_{500}-rGO3, **c)** PMP_{2000}-rGO5, and **d)** GO coating product of PMP5 in DMF at 100,000 magnification (Scale bar: 100 nm).

4.1.2. Biocompatibility and cytotoxicity evaluation of P(PEGMA-*co*-MMA-*co*-PMA) coated rGO derivatives (PMP-rGO)

Hemocompatibility of developed PMP-rGO derivatives is an important parameter for biological applications that involve intravenous injections [250]. Evaluation of blood compatibility of PMP-rGO derivatives was tested on fresh human erythrocytes against

Triton X-100 as a positive control with different concentrations for 1 hour of incubation. Since the preparation of a well-dispersed solution of rGO in a buffer is not possible and using aggregated solutions will cause misinterpretation, rGO was not tested for any biocompatibility assays. As can be seen in **Figure 4.16**, GO showed its dose-dependent toxicity profile by not causing red blood cell hemolysis at low concentrations like 5 and 50 µg/mL but showed hemolytic activity starting at 100 µg/mL concentration. Hemolytic activity of GO was observed as high as 77.4% for the highest concentration (300 µg/mL). On the other hand, copolymers and PMP-rGO derivatives were found to be more blood compatible compared to GO. Both copolymers, PMP2 and PMP5, did not show significant hemolytic activity (<10%) for all concentrations. Among PMP-rGO derivatives with the shorter PEG brushes, PMP_{500}-rGO1 looks like it shows the best profile with a hemolytic activity smaller than 10% even at 200 µg/mL concentration. However, this composition has 7 PEG brushes per copolymer on the rGO surface, which is not enough to ensure complete dispersion in an aqueous environment (**Figure 4.17a**). Since this derivative precipitate over time in the aqueous medium, it does not interact with red blood cells and as a result, it reflects the hemolytic activity inaccurately. PMP_{500}-rGO2 and PMP_{500}-rGO3 with the number of brushes of 11 and 19, respectively, have better dispersibility in water as proportional to % PEG content on the graphene surface. The results indicated that PMP_{500}-rGO3 is the best composition for shorter brush-containing derivatives with 80.6% PEG content disrupting just 7.6% of RBC at a concentration as high as 150 µg/mL due to the better water dispersibility and its hemolytic activity at higher concentration is better than 58.7% PEG containing PMP_{500}-rGO2. As can be seen in **Figure 4.17a**, longer brushes containing PMP_{2000}-rGO derivatives have better stability in the aqueous environment due to their high PEG content ranging between 75.2-86.4%. The Same stability study showed that even GO as a water-soluble derivative of graphene gets precipitated in the medium over time, while the PEGylated version provides more stable dispersion, even if they were reduced to rGO. PMP_{2000}-rGO5 showed better hemocompatibility at all concentrations when it is compared to other analogous as 18.1% hemolysis of RBC at 300 µg/mL. Interestingly, even though PMP_{2000}-rGO6 has 16-brushes with 85% PEG content, it disrupted more RBCs as compared to PMP_{2000}-rGO4 and PMP_{2000}-rGO5, especially at higher concentrations. This might be associated with the high molecular weight (longer hydrophobic backbone) of the coated copolymer (**Table 4.2**).

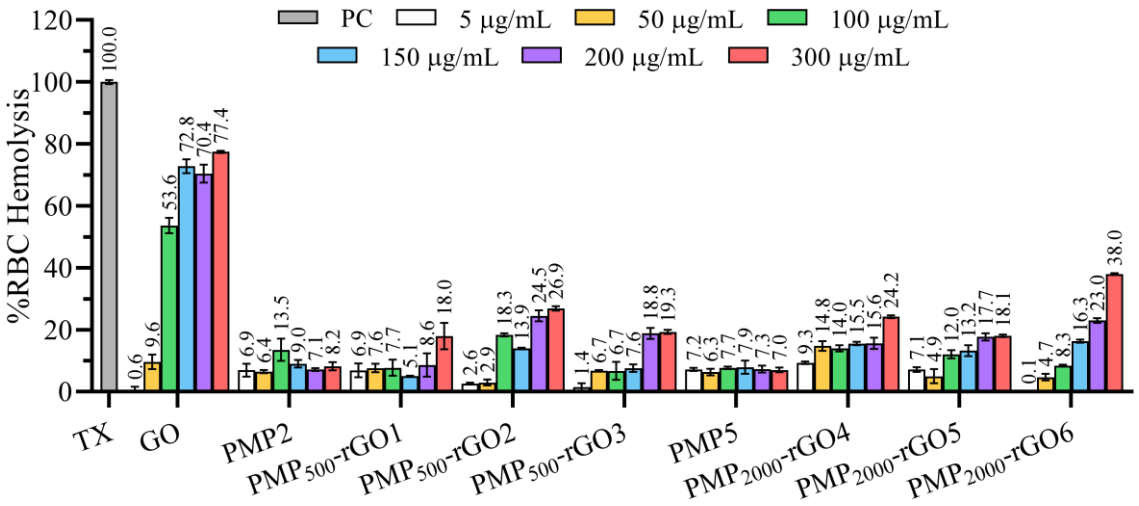


Figure 4.16: Hemolytic activity of GO, PMP2, PMP5, and PMP-rGO derivatives.

In addition to the stability study in the water environment, the stability and dispersibility of selected PMP_{2000}-rGO5 were also studied (**Figure 4.17b**). Equal amounts of material were prob-sonicated for one minute in a certain volume of commonly known organic solvents and observed for 24 hours at room temperature. Homogenous dispersants in most of the solvents were achieved such as in acetone, acetonitrile, ethyl acetate, methanol, tetrahydrofuran, and toluene but after 12 and/or 24 hours partial precipitation was observed. It was not possible to disperse PMP_{2000}-rGO5 in non-polar, aprotic n-hexane. Conversely, polar, aprotic solvents N,N'-dimethyl formamide, and dimethyl sulfoxide dispersed PMP_{2000}-rGO5 homogenously with ease, and even after 24 hours, no-precipitation was observed making DMF and DMSO ideal solvents for non-aquatic procedures.

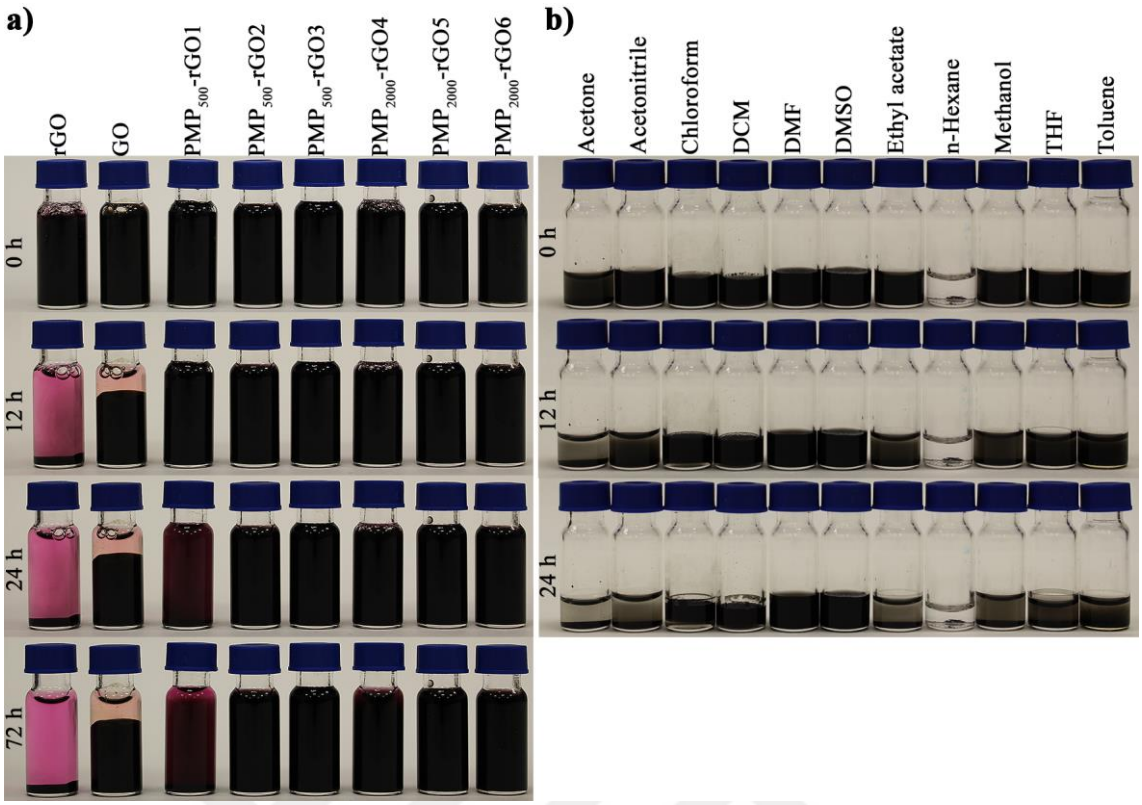


Figure 4.17: a) Stability of GO, PMP_{500}-rGO, and PMP_{2000}-rGO derivatives in 10% FBS containing DMEM and **b)** stability and dispersibility of PMP_{2000}-rGO5 in common organic solvents.

In vitro cytotoxicity of PMP-rGO derivatives was determined by MTS, LDH, and ROS assays, to investigate the different cytotoxicity mechanisms using healthy human embryonic kidney cells (HEK-293T) and human fibroblast lung cells (MRC-5) since intravenous administration of graphene derivatives result in higher accumulation in lungs and kidney [86], [99], [186], [251]–[253]. First, cytotoxicity of PMP-rGO derivatives was investigated with MTS assay at increasing concentration of the material to detect the effect on cell viability. **Figure 4.18** shows the quantitative comparison of cell viability of GO, copolymers, and PMP-rGO derivatives for MRC-5 (**Figure 4.18a**) and HEK-293T (**Figure 4.18b**) cell lines. The results clearly showed that pristine GO caused a reduction in cell viability and it showed higher toxicity for lung cells than kidney cells which is consistent with the previously reported findings in the literature that showed long-term accumulation potential of GO inducing different diseases such as dose-dependent lung inflammatory response [254], lung granuloma [255] and pulmonary thromboembolism [256] in lungs. Copolymer itself with hydrophobic backbone and pyrene units affects the cell viability of both cell lines, especially at the highest concentration (300 µg/mL) after 24 h of exposure. Even though PMP_{500}-rGO derivatives caused concentration-dependent

cytotoxicity, overall PMP-rGO derivatives showed better cell viability compared to pristine GO. Furthermore, the increase in PEG chain length from 500 Da to 2000 Da resulted in an improvement in biocompatibility. Among all short PEG brushes containing derivatives, only PMP_{500}-rGO3 with 19 PEGMA brushes were able to keep the viability above 85% at all concentrations (**Figure 4.18b**) for HEK-293T cells. However, all longer PEG brush-containing derivatives resulted in cell viability higher than 90% for concentrations up to 200 µg/mL and higher than 85% for the highest concentration (**Figure 4.18b**). PEG_{2000} derivatives also showed a better profile for the MRC-5 cell line, which is more sensitive against graphene derivatives. Especially, PMP_{2000}-rGO5 showed 81.4% cell viability even at the highest concentration indicating the significance of longer PEG chain contribution on the biocompatibility of rGO derivatives (**Figure 4.18a**). It should be noted that the maximum exposure concentration of our study (300 µg/mL) is higher than most of the reported PEGylated rGO derivatives [91], [257].

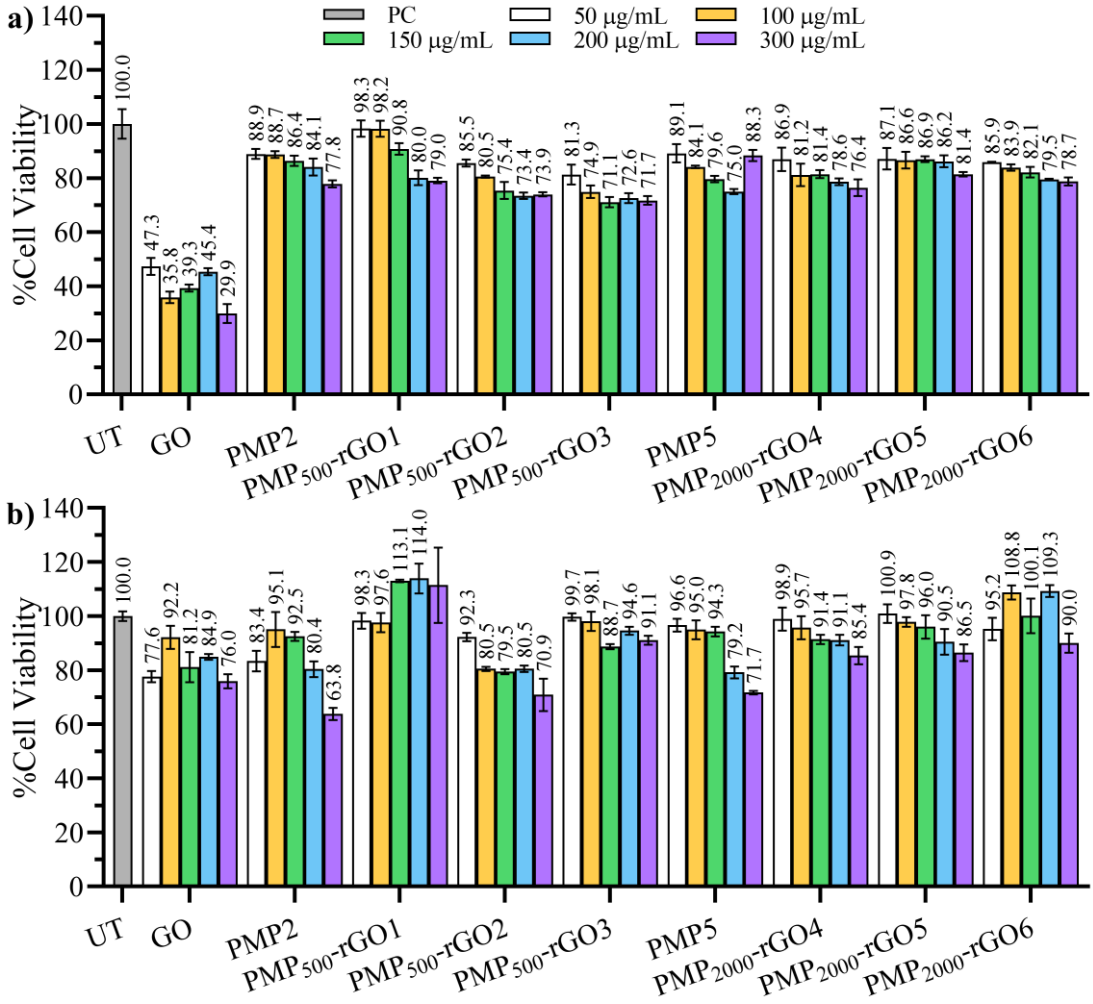


Figure 4.18: a) MRC-5 and **b)** HEK-293T cell viability results detected by MTS assay after PMP-rGO treatment for 24 hours.

The effect of PMP-rGO derivatives on cell membrane integrity was determined by the level of lactate dehydrogenase (LDH) enzyme leaked into the incubation medium that can only be released to the extracellular environment in case of membrane damage. LDH assay was performed for GO, copolymers, and PMP-rGO derivatives on plated HEK-293T and MRC-5 cells for 24 hours at various concentrations by following the manufacturer's protocol, and the results were normalized against the released LDH level of lysed cells. For all PMP-rGO derivatives regardless of their brush length and PEG content, LDH release was observed lower than 15.2 % even at 300 µg/mL concentration for HEK-293T cell lines (**Figure 4.19b**). It should be noted here that the superior profile of PMP_{500}-rGO1 (**Figure 4.19b**) similar to GO is not because they are non-toxic, it is because they precipitate in the cell culture medium during incubation time (**Figure 4.17a**) and do not interact with the cells resulting lower membrane damage and lower LDH release to the incubation medium. Similar to the MTS assay results, PMP-rGO derivatives showed more cytotoxicity against the MRC-5 cell line indicating that these cells are more vulnerable to graphene derivatives (**Figure 4.19a**). Dose-dependent cytotoxicity can be significantly seen at high concentration values which almost reach as twice as high LDH level for PMP_{500}-rGO derivatives when it is increased from 200 to 300 µg/mL (**Figure 4.19a**). As a more promising candidate for MRC-5 cells, PMP_{2000}-rGO derivatives showed lower LDH release than free copolymers and PMP_{500}-rGO derivatives (**Figure 4.19a**), however, this was insufficient to guarantee adequate biocompatibility for this cell line at high concentration values. It can be concluded that 150 µg/mL is a safe concentration limit for the MRC-5 cell line based on LDH assay results, regardless of coated copolymer compositions and overall PEG content while even at the highest concentration of PMP_{2000}-rGO can be considered a safe concentration for HEK-293T cells.

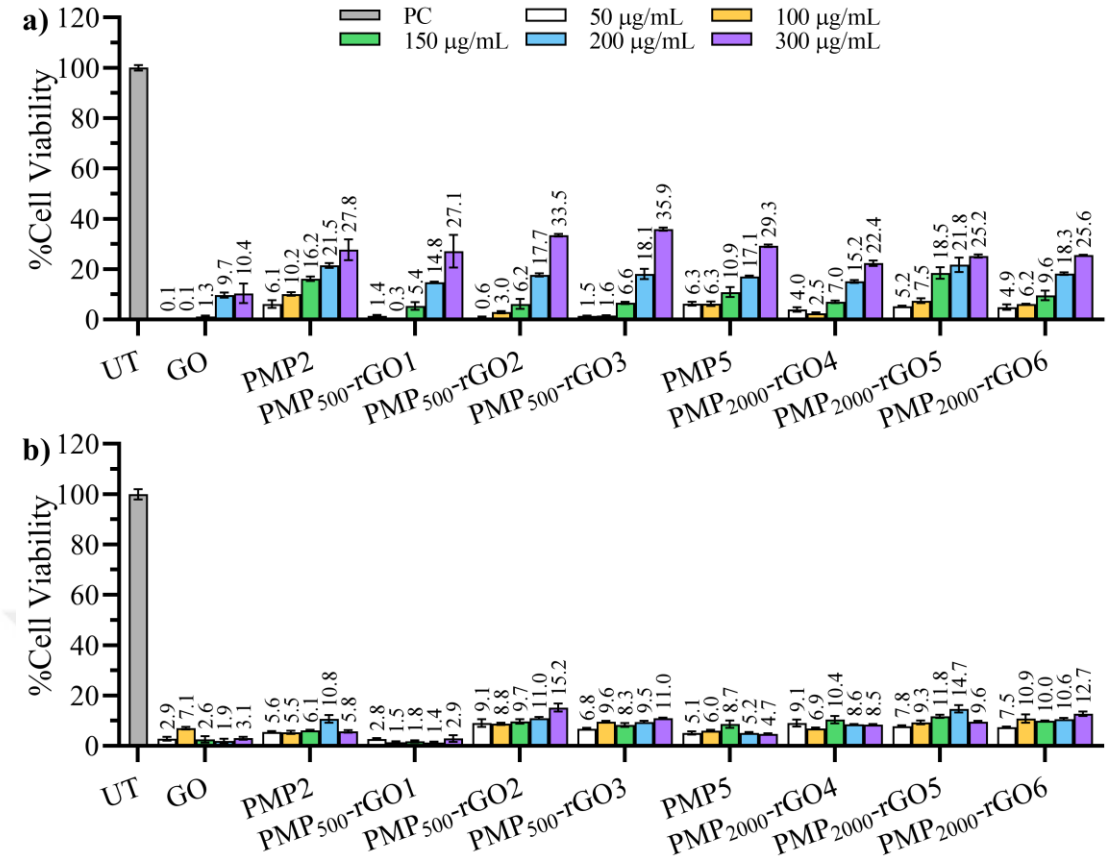


Figure 4.19: LDH release rate of PMP-rGO compositions on **a)** MRC-5 and **b)** HEK-293T cells.

As mentioned before, some of the PMP-rGO derivatives have the stability issue resulting in precipitation in cell mediums like rGO and GO that can also be visually observed during *in vitro* experiments (**Figure 4.17**). This behavior is critical for the reliability of the *in vitro* results obtained. To justify the cell interaction behavior of PMP-rGO derivatives the intracellular localization was investigated using confocal fluorescence microscopy on MRC-5 cells (**Figure 4.20**). PMP-rGO derivatives were fluorescently tagged with Alexa Fluor™ 488 (green fluorescent) by simply mixing with a free dye that was adsorbed on the graphene surface by intermolecular forces such as hydrophobic interactions and π-π bonds. Cells were treated with labeled PMP-rGO derivatives at 100 µg/mL concentration for 2, 6, and 24 hours, washed to remove free PMP-rGOs and the nucleus of the cells was stained with Hoechst dye (blue fluorescent) in fresh medium. The images were taken by the multiphoton confocal microscope Zeiss LSM780 with equal settings for each image. Captured images showed that the green fluorescence of Alexa Fluor™ 488 got stronger over the time of 24 h for both PMP_{500}-rGO3 and PMP_{2000}-rGO5 compositions showing an increase in cellular internalization. Fluorescence intensity differences between PMP_{500}-rGO3 and PMP_{2000}-rGO5 became visible starting from 6

hours and it gets significant after 24 h where PMP_{2000}-rGO5 showed much stronger fluorescence intensity after 24 hours showing superior cellular uptake than PMP_{500}-rGO3.

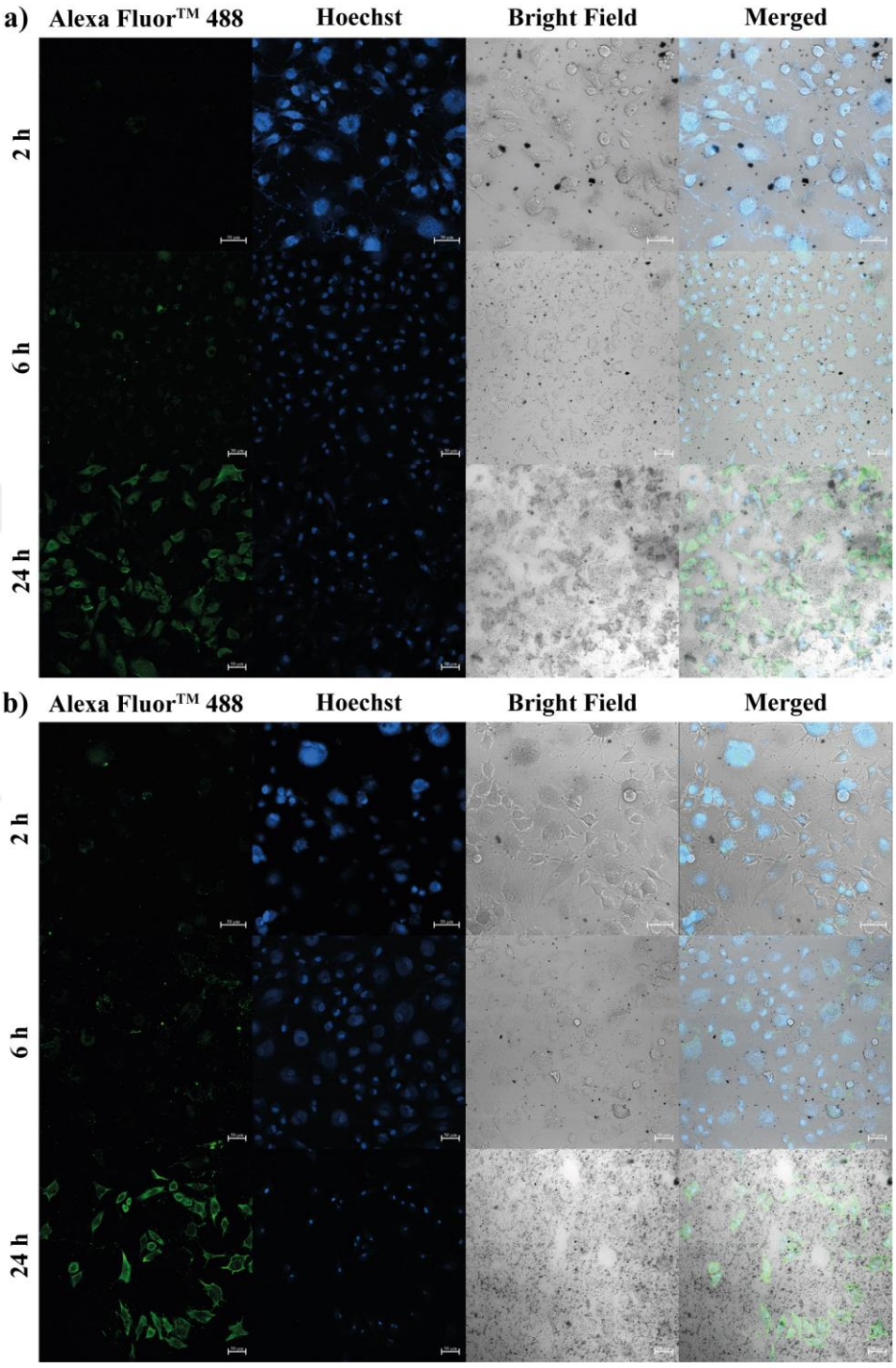


Figure 4.20: Confocal fluorescent images showing the internalization of **a)** PMP_{500}-rGO3 and **b)** PMP_{2000}-rGO5 into MRC-5 cells after 2, 6, and 24 hours of incubation. The green fluorescent originates from Alexa Fluor™ 488 stained PMP-rGO derivatives where Hoechst dyed nucleus shows blue fluorescence. (Scale bar: 50 μm)

Finally, reactive oxygen species (ROS) generation due to the presence of copolymers and PMP-rGO derivatives was tested on HEK-293T, since the generation of ROS is a well-known oxidative stress mechanism of GO. Due to the instability of GO and PMP_{500}-rGO1 in the cell culture medium, they were excluded from the assay (**Figure 4.21**). PMP2 and PMP5 have a significant contribution to the ROS generation at 42% and 45% at 300 µg/mL, respectively, calculated by comparing to ROS generation of H_2O_2 as a positive control. PMP_{500}-rGO2 reduced the ROS generation by half compared to PMP2 while PMP_{2000}-rGO5 was reduced by 1/3 of its copolymer showing that PEGylation and simultaneous reduction significantly reduce the ROS generation.

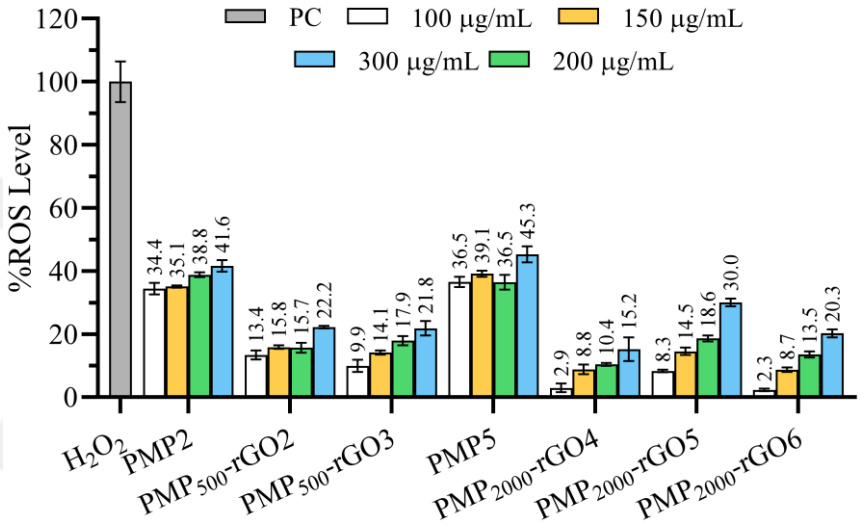


Figure 4.21: Effect of PMP-rGO derivatives on ROS generation rate on HEK-293T cells.

An efficient PEGylation method to improve biocompatibility and stability of graphene derivatives has been studied in detail, the method uses water dispersed GO as starting graphene derivative and simultaneously reduces it to a less defected rGO form while PEGylates the platform by using π-π interaction with well-defined P(PEGMA-*co*-MMA-*co*-PMA) copolymers. It was found that PMP-rGOs that have a PEG content lower than 60% have a tendency to agglomerate in the aqueous environments, while platforms with a PEG content of 80% were found to be the most stable in water environment and showed the highest biocompatibility regardless of PEG brush length. From this point on, this method was employed to prepare a targeted dual delivery platform that can be tuned with easy by simple reaction steps according to needs and which has the potential to be used against several cancer types.

4.2. Preparation of PEGylated Reduced Graphene Oxide as Nanoplatform for Targeted Gene and Drug Delivery

The goal of this research is to develop reduced graphene oxide-based water dispersible, pH-sensitive nanoplatforms that can successfully pack a large dose of nucleic acids and hydrophobic chemotherapeutic agents onto nanocarrier which can then be internalized by targeted cancer cells. rGO is decorated with a multifunctional copolymer containing PEG for enhanced solubility, pyrene for π-π interaction, cationic copolymer that has an ability to synergistically escape from endosome through proton sponge effect and hydrophobic disruption, and finally EPPT1 peptide for cell-specific internalization. Once its chemotherapeutic and nucleic acid cargo was loaded on the nanoplatform, it was hypothesized all components work effectively to improve the desired treatment effect.

Preparation of PEGylated reduced graphene oxide nanoplatforms was initiated by preparation of P(PEGMA-*co*-AzPMA-*co*-MMA-*co*-PMA) (**Figure 4.22a**). As it was previously mentioned PEGMA macromonomer was responsible for water dispersibility and increasing biocompatibility, while PMA makes π-π interactions with the rGO surface, AzPMA was employed for further modification by CuAAC. Subsequently, by the combination of 3 common reactions a multi-functional, stimuli-responsive ATRP initiator was synthesized (**Figure 4.22c**), and cationic copolymers (**Figure 4.22d**) were synthesized by using this initiator which is targeted to have alkyne end functionality and pH-sensitive hydrazone bridge. Cationic copolymers (CPs) were built by using HMA and DMAEMA monomers followed by quaternization of DMAEMA into TMAEMA, HMA and DMAEMA were tasked for endosomal escape by membrane disruption and proton sponge effect, respectively, where TMAEMA was responsible for nucleic acid complexation. With the purpose of producing a well-characterized polymer structure prior to rGO coating CP was grafted onto PAMP copolymer (**Figure 4.22b**), by this approach ratio between PAMP and CP could be controlled and could be altered if needed.

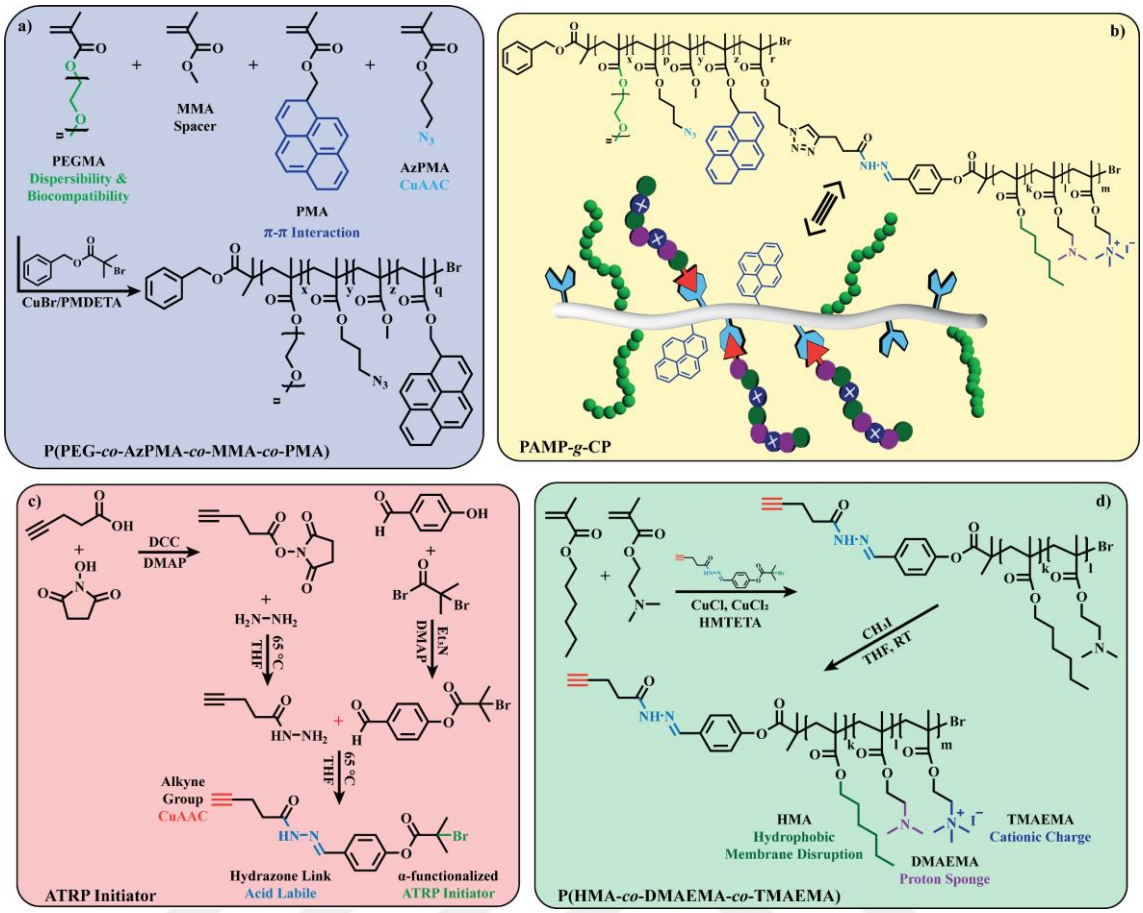


Figure 4.22: a) Synthesis of P(PEGMA-*co*-AzPMA-*co*-MMA-*co*-PMA), **b)** Schematic representation of P(PEGMA-*co*-AzPMA-*co*-MMA-*co*-PMA)-*g*-P(HMA-*co*-DMAEMA-*co*-TMAEMA), synthesis of **c)** functional ATRP initiator, **d)** P(HMA-*co*-DMAEMA) and P(HMA-*co*-DMAEMA-*co*-TMAEMA).

4.2.1. Synthesis of 3-azidopropyl methacrylate

Synthetic procedures were initiated by the synthesis of 3-azido-1-propanol (**Figure 3.7**) using sodium azide and 3-chloro-1-propanol. The crude product was purified by vacuum distillation and characterized by ^{1}H NMR spectroscopy, as seen in **Figure 4.23a** methylene protons neighboring the hydroxyl group were detected at 3.72 ppm where azide neighboring methylene protons were recorded at 3.42 ppm and at 1.81 ppm central methylene protons were observed. The hydroxyl groups on the 3-azido-1-propanol were used to react with methacryloyl chloride to obtain 3-azidopropyl methacrylate overnight and the product was purified by extraction and vacuum distillation. **Figure 4.23b** shows the ^{1}H NMR spectrum of the pure product, while retaining methylene protons originating from 3-azido-1-propanol two alkenyl protons were recorded at 6.10 and 5.57 ppm with additional methyl signal at 1.94 ppm.

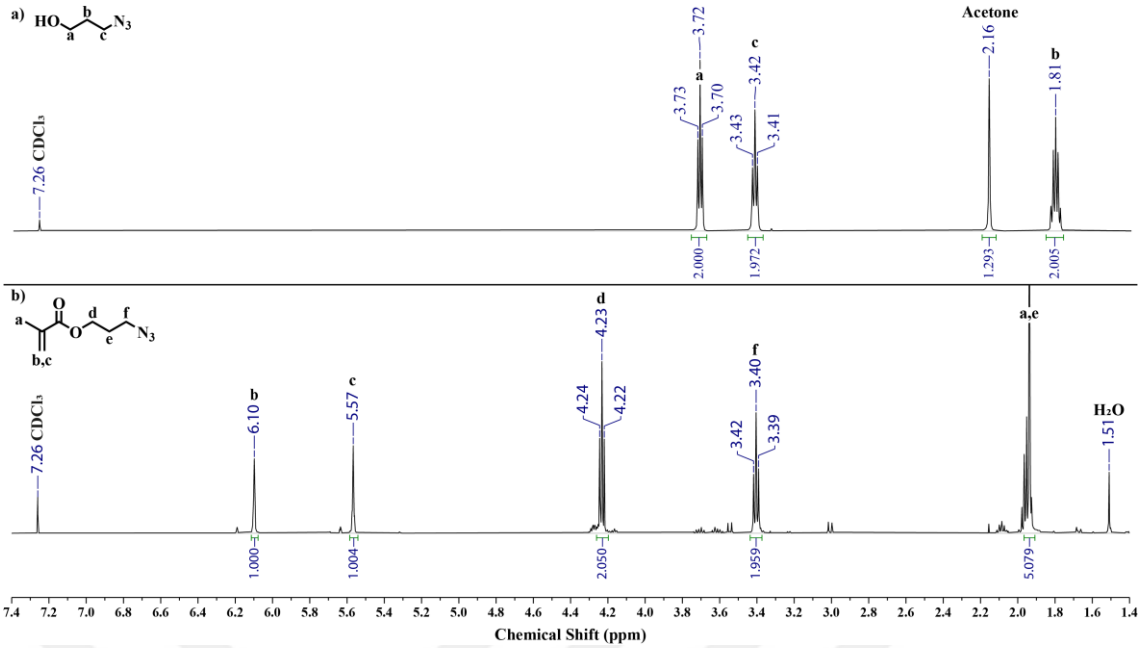


Figure 4.23: ^{1}H NMR spectrum of **a)** 3-azido-1-propanol and **b)** 3-azidopropyl methacrylate.

4.2.2. Synthesis of 2-bromo-2-methyl propanoate (benzyl initiator)

For the convenience of the calculations of polymer repeating units from ^{1}H NMR spectrums a benzyl group carrying an ATRP initiator was synthesized. In this respect, 2-bromo-2-methyl propanoate was prepared by starting from benzyl alcohol and purified by column chromatography. ^{1}H NMR spectrum of benzyl initiator can be seen in **Figure 4.24**, while 5 aromatic protons found in the benzyl group detected between 7.40-7.31 ppm, 2 methylene hydrogens attached to the benzyl group and methyl group originating protons were clearly seen at 5.21 ppm and 1.96 ppm respectively.

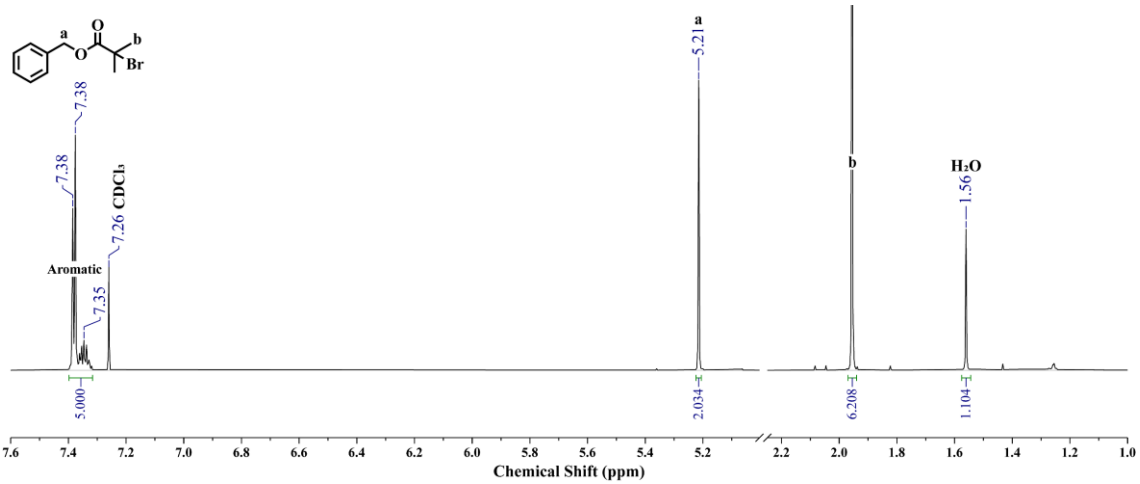


Figure 4.24: ^{1}H NMR spectrum of 2-bromo-2-methyl propanoate.

4.2.3. Synthesis, and characterization of PAMP-*g*-CP

Preparation of the smart nanoparticles was initiated with the synthesis of P(PEGMA-*co*-AzPMA-*co*-MMA-*co*-PMA) (PAMP), by using benzyl 2-bromo-2-methylpropanoate (**Figure 3.1**) as ATRP initiator, PEGMA, AzPMA (**Figure 3.8**), MMA, and PMA as monomers. Polymer synthesis was carried out by using ATRP (**Figure 4.22a**), which has been proved to result in well-defined copolymers, at different monomer feed ratios copolymers have been synthesized (**Table 4.5**).

Table 4.5: Mol percent distribution of monomers during copolymer synthesis.

Type	%$PEGMA_{2000}$	%AzPMA	%MMA	%PMA
C1	20	20	45	15
C2	40	20	25	15
C3	40	15	25	20

Obtained copolymers were primarily characterized by using ^{1}H NMR spectroscopy, by taking methylene signal as a reference at 5.05 ppm originating from the initiator copolymer composition was determined (**Figure 4.25, Table 4.6**). Characteristic absorbance of the pyrene groups has been determined between 300 and 375 nm, where N=N=N stretching of azide groups was observed at 2099 cm^{-1} on the FTIR spectrum (**Figure 4.26**) with slightly decreased intensity when compared to AzPMA monomer signal as expected. Even though multiple copolymers were synthesized the copolymer that meets the requirements for producing stable rGO composites as stated in our previous study [210] PAMP4 was selected, the molecular weight of the copolymer calculated from the ^{1}H NMR spectrum is 35,517 g/mol with 81.7% PEG content by mass, it carries 9.5 azide and 12.0 pyrene units on the chain and used for the rest of the study.

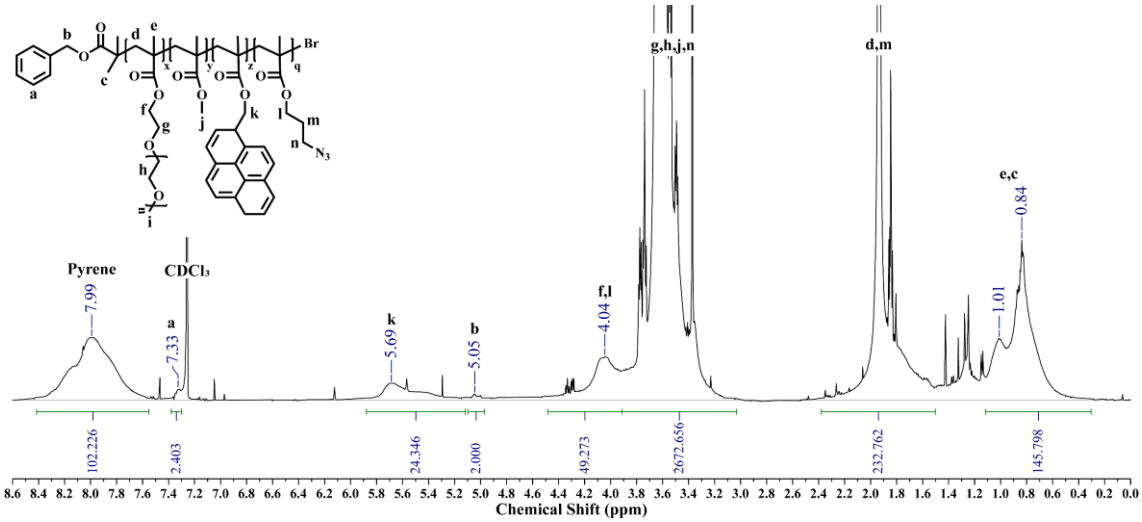


Figure 4.25: ^{1}H NMR spectrum of P(PEGMA-*co*-AzPMA-*co*-MMA-*co*-PMA).

Table 4.6: Characteristics of synthesized PAMP copolymers.

Copolymer	Type	Time (h)	M_{nNMR} (g/mol)	DPn	# of PEGMA	# of MMA	# of PMA	# of AzPMA
PAMP1[a]	C1	3	37,473	83.1	13.6	13.4	45.6	10.5
PAMP2[a]	C2	3	21,256	34.5	8.7	5.6	16.9	3.3
PAMP3[b]	C2	3	22,854	32.1	9.6	7.6	11.5	3.4
PAMP4[b]	C3	5	35,517	46.6	14.5	9.5	10.6	12.0

Monomers/PMDETA/CuBr/Initiator:100/1/1/1
Mn_{NMR} and monomer ratios were calculated from ^{1}H NMR.
The reaction volume was set to [a]10 mL or [b]15 mL by toluene addition.

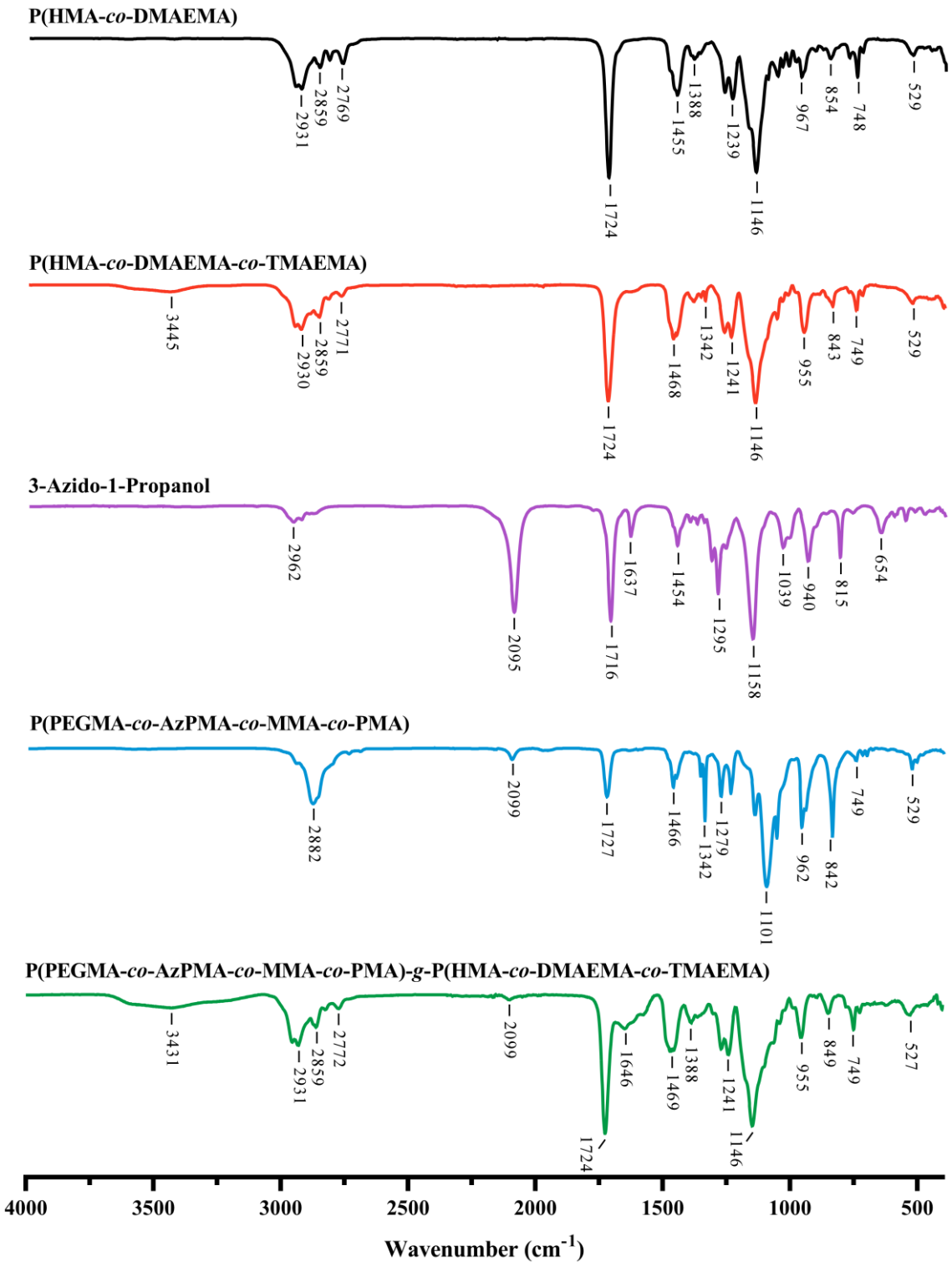


Figure 4.26: FTIR spectrum of P(HMA-*co*-DMAEMA), P(HMA-*co*-DMAEMA-*co*-TMAEMA), 3-azido-1-propanol, P(PEGMA-*co*-AzPMA-*co*-MMA-*co*-PMA) and P(PEGMA-*co*-AzPMA-*co*-MMA-*co*-PMA)-*g*-P(HMA-*co*-DMAEMA-*co*-TMAEMA).

Cationic charge on the nanoplatforms for siRNA complexation was introduced to the system by P(HMA-*co*-DMAEMA-*co*-TMAEMA), and cationic copolymers (CP) were synthesized with a stimulus-responsive multi-functional ATRP initiator that is being

reported for the first time (**Figure 4.22c**) in the literature. Synthesis of 4-((2-(pent-4-ynoyl) hydrazineylidene) methyl) phenyl 2-bromo-2-methylpropanoate was carried out in 4 steps starting from esterification reaction between 4-pentynoic acid and N-hydroxysuccinimide to introduce an easily leaving group. ^{1}H NMR spectrum of 2,5-dioxopyrrolidin-1-yl pent-4-ynoate shows alkyne proton at 2.05 ppm, where ethylene protons originating from NHS group and methylene protons neighboring carbonyl group can be seen between 2.91-2.79 ppm (**Figure 4.27a**). 2,5-dioxopyrrolidin-1-yl pent-4-ynoate was reacted with hydrazine hydrate and pure pent-4-ynehydrazide was obtained with ease, the disappearance of NHS's ethylene signal and appearance of two new peaks at 6.96 ppm for N*H* and 3.93 ppm for NH_2 protons show the structure clearly where coupling constants (J) for neighboring alkyne and methylene protons were calculated to be 7.2 and 2.6 Hz respectively (**Figure 4.27b**). In parallel 4-formylphenyl 2-bromo-2-methylpropanoate was prepared by the reaction between 4-hydroxybenzaldehyde and 2-bromo-2-methylpropanoyl bromide, by silica gel column chromatography the product was purified, and characterized by ^{1}H NMR spectroscopy as seen in **Figure 4.27c**, aldehyde, aromatic and methylene protons were determined at 10.01, 7.96, 7.33 and 2.08 ppm respectively with matching integrated ratios with hydrogen numbers.

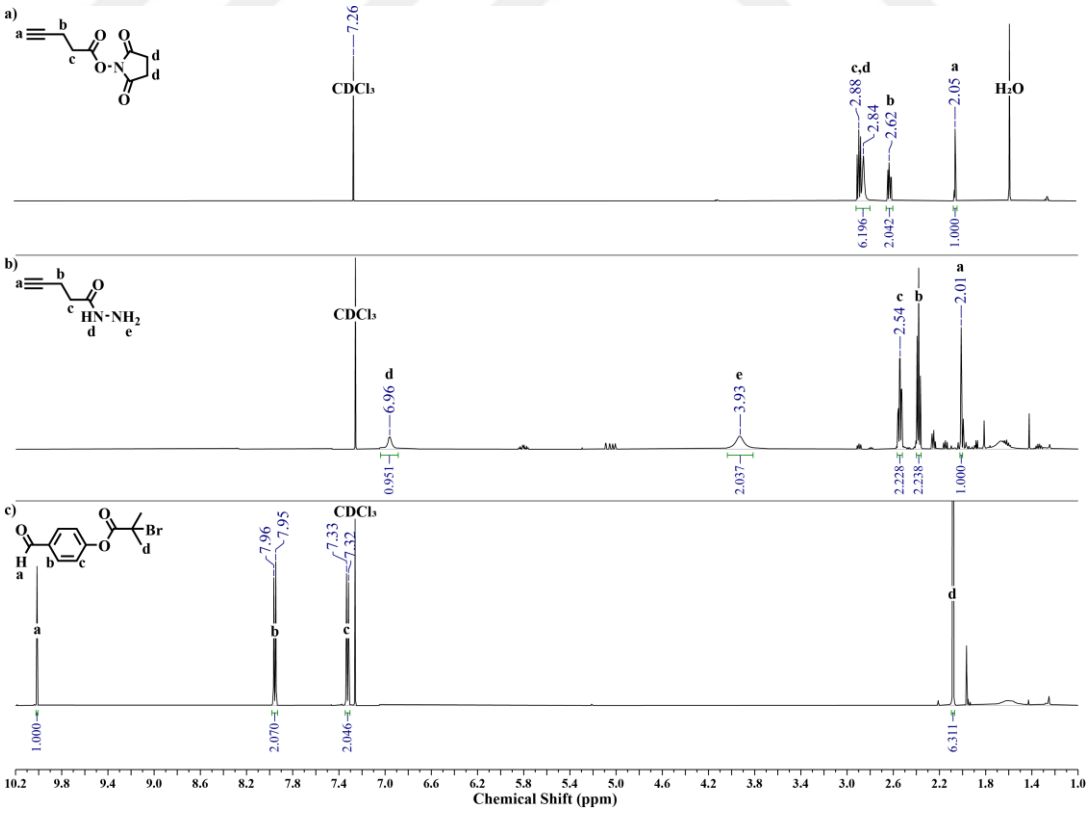


Figure 4.27: ^{1}H NMR spectrum of **a)** 2,5-dioxopyrrolidin-1-yl pent-4-ynoate, **b)** pent-4-ynehydrazide and **c)** 4-formylphenyl 2-bromo-2-methylpropanoate.

The formation of the acid labile hydrazone bond between pent-4-ynehydrazide and 4-formylphenyl 2-bromo-2-methylpropanoate was achieved by refluxing these two components in THF under a nitrogen atmosphere, the crude product was purified by a series of silica gel column chromatography and crystallization. When the ^{1}H NMR spectrum (**Figure 4.28**) was examined alkyne and methyl protons were detected at 2.00 and 2.08 ppm, whereas phenylic protons were found to be at 7.77 and 7.71 next to -N*H* proton at 9.33 ppm. The structure was also confirmed by mass spectrometry as calculated exact mass of 364.04 (**Figure 4.29**) by showing the base peak at 363 m/z ratio and the molecular peak at 365 m/z ratio indication successful synthesis of stimulus-responsive multi-functional ATRP initiator.

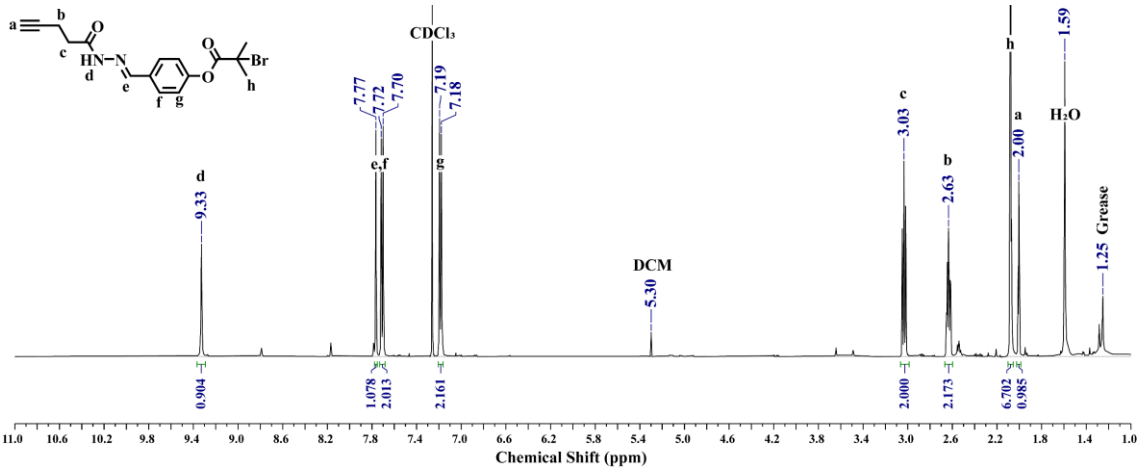


Figure 4.28: ^{1}H NMR spectrum of 4-((2-(pent-4-ynoyl) hydrazineylidene) methyl) phenyl 2-bromo-2-methylpropanoate.

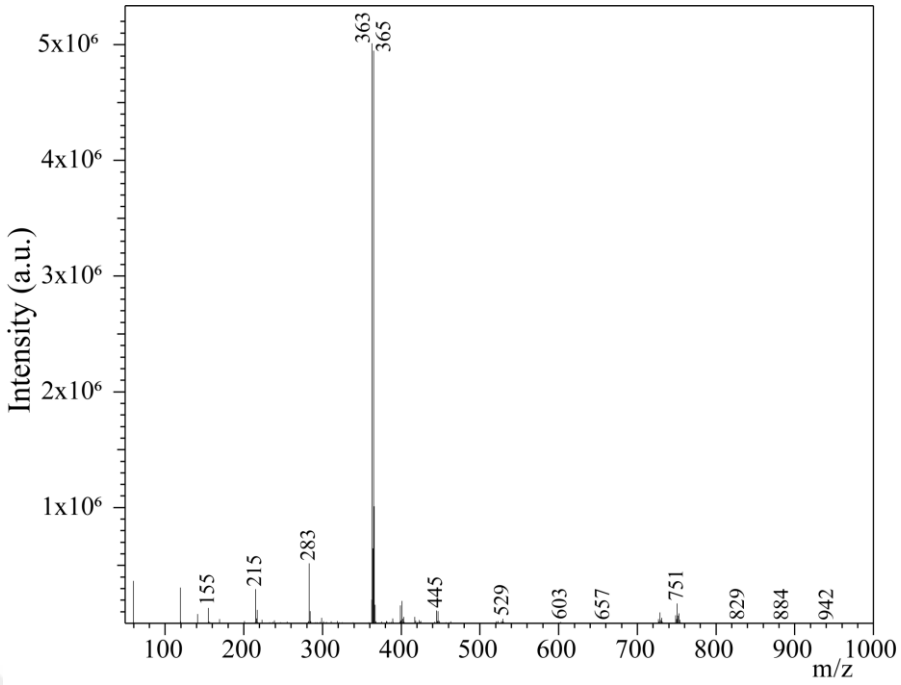


Figure 4.29: Ion mass spectra of 4-((2-(pent-4-ynoyl) hydrazineylidene) methyl) phenyl 2-bromo-2-methyl propanoate.

P(HMA-*co*-DMAEMA) was synthesized by ATRP yielding copolymers with α-alkyne and hydrazone functionalities with consistent monomer ratios on the structure as supplied during the reaction (HMA:DMAEMA=1:1), and followed by the quaternization of half of the DMAEMA units with methyl iodide. Following the literature molecular weight of the P(HMA-*co*-DMAEMA-*co*-TMAEMA) was intentionally kept below 25 kDa to prevent toxicity caused by cationic charge [171]. Precursor and quaternized products were characterized by ^{1}H NMR spectroscopy (**Figure 4.30**), their compositions were determined by taking alkyne and phenyl protons as a reference where methylene signals from HMA (-O-CH_2-CH_2-) at 1.62 ppm, 6 methyl protons on tertiary amine at 2.27 ppm, ester bond neighboring methyl groups of DMAEMA and HMA at 4.05 and 3.92 ppm respectively and quaternary amine methyl groups at 3.62 ppm were employed for quantitative analysis of copolymers, deconvolution of NMR spectrum used to determine the number of repeating units and consecutively molecular weights, results were listed in **Table 4.7**. Synthesized copolymers were analyzed with gel permeation chromatography (GPC) by using different buffers and eluents to determine the molecular weight and polydispersity, but the number average molecular weight from the ^{1}H NMR spectra was used in this research in all subsequent calculations, due to the interaction between DMAEMA and TMAEMA monomers and the packing material of GPC columns, leading to incomplete results [171], [258].

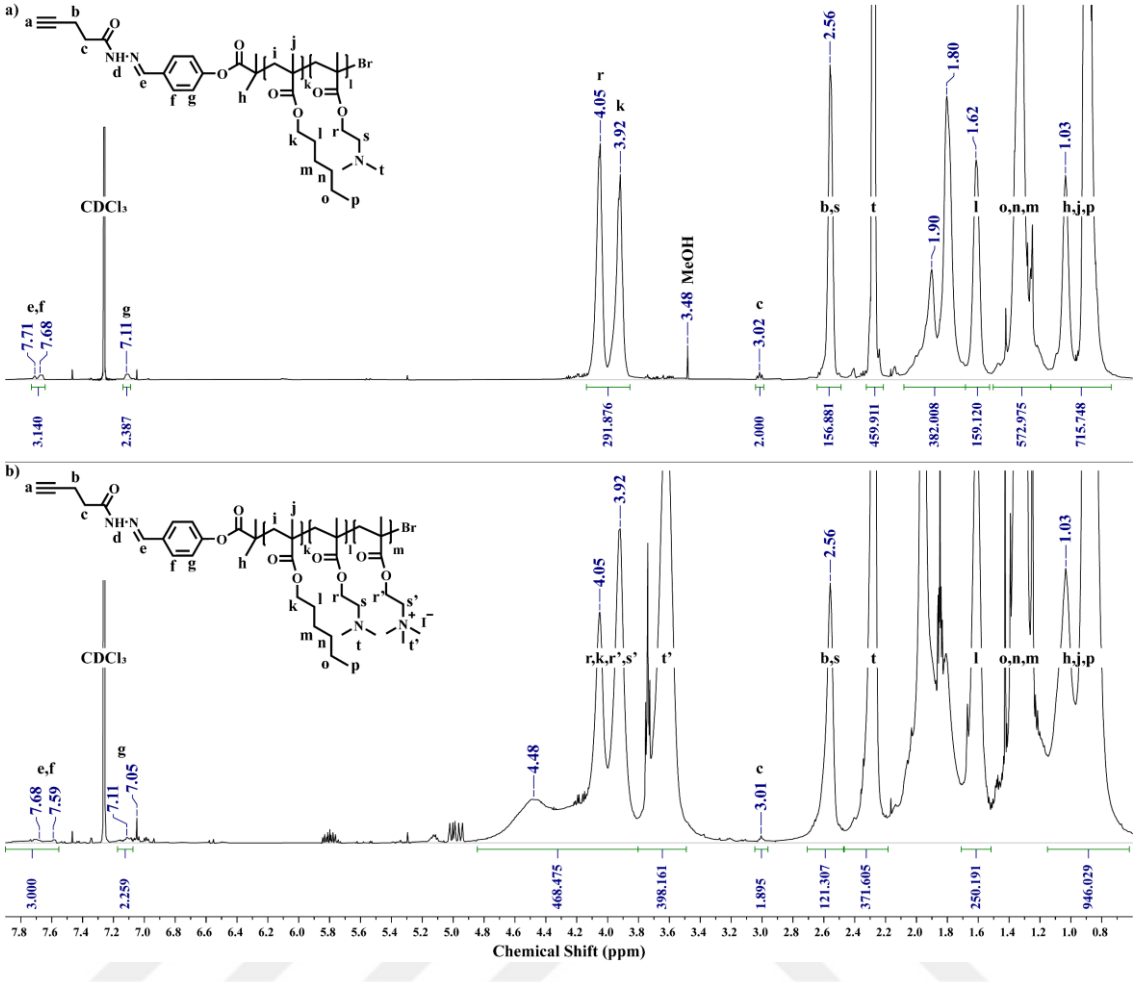


Figure 4.30: ^{1}H NMR spectrum of **a)** P(HMA-*co*-DMAEMA) and **b)** P(HMA-*co*-DMAEMA-*co*-TMAEMA).

Table 4.7: Characteristics of synthesized copolymers.

	M_{nNMR} (g/mol)	DPn	# of HMA	# of DMAEMA	# of TMAEMA
P(HMA-*co*-DMAEMA)	17486.6	105.2	45.18	60.05	
P(HMA-*co*-DMAEMA-*co*-TMAEMA)	22269.2	109.7	47.75	33.40	28.53

Copper catalyzed azide-alkyne cycloaddition (CuAAC) reaction between P(HMA-*co*-DMAEMA-*co*-TMAEMA) and P(PEGMA-*co*-AzPMA-*co*-MMA-*co*-PMA) was conducted in PBS by taking advantage of their solubility in water. In a Schlenk tube, copolymers were dissolved in PBS, $CuSO_4$ and sodium ascorbate were added sequentially, and the reaction was degassed by 3 FPT cycles. Completion of reaction time followed by dialysis against PBS and then water to remove unreacted copolymers, catalyst couple, and buffer salts, and after lyophilization graft copolymer (PAMP-*g*-CP) was precipitated in cold hexane. ^{1}H NMR spectrum of graft copolymer exhibit the characteristic signals from both copolymers (**Figure 4.31**), pyrene and phenylic protons

detected between 8.4 and 7.5 ppm, where methylene protons linked to the pyrene group found at 5.69 ppm neighboring benzyl methylene protons at 5.00 ppm. While the methylene protons adjacent to the ester bonds were detected between 4.79 and 3.79 ppm, the ethylene signals that form the PEG main chain and the methyl signals of the quaternary amine were detected between 3.79 ppm and 3.22 ppm, similarly, the 6 protons on the tertiary amines were observed at 2.27 ppm. The methylene signal of the pyrene group which is located at 5.69 ppm used as a reference and 7.51 CP grafts onto PAMP main chain was calculated as intended. After CuAAC reaction sharp azide stretching signal at 2099 cm^{-1} decreased significantly but kept its presence as expected (**Figure 4.26**) since 2-3 azide groups were reserved for alkyne-PEG-EPPT1 conjugation.

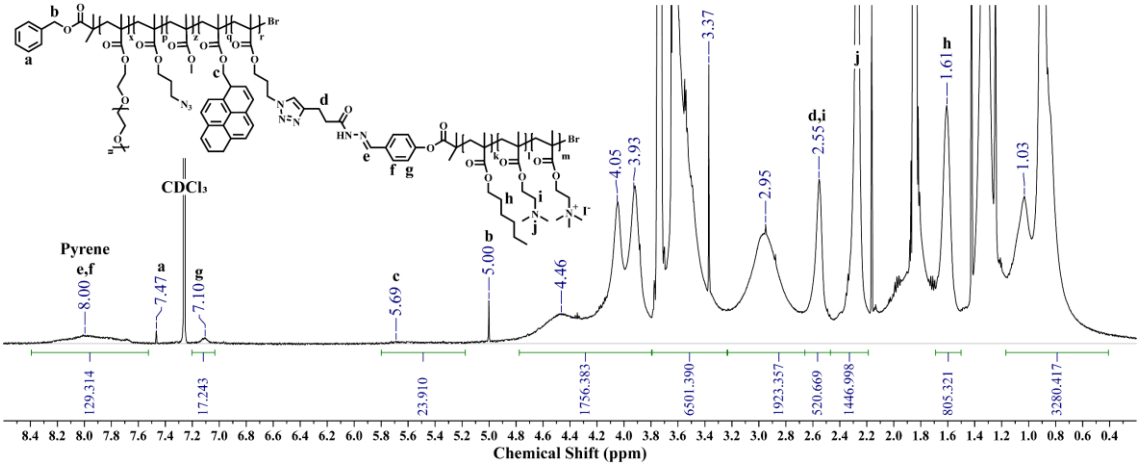


Figure 4.31: ^{1}H NMR spectrum of PAMP-*g*-CP.

4.2.4. Synthesis of alkyne-PEG-EPPT1

A transmembrane glycoprotein expressed by the MUC1 gene has been discovered to be one of the early hallmarks of tumorigenesis, expressed in a variety of human epithelial cell adenocarcinomas, including 90% of breast cancer [190], [191]. Considering the MUC1 receptor is highly expressed in human tumors, causing alterations in distribution and glycosylation of the protein, a synthetic nonimmunogenic tumor-selective peptide EPPT1 (YCAREPPTRTFAYWG) was created to successfully target the MUC1 tumor antigen [160], [192]–[194]. EPPT1 peptide was synthesized by Metabion International AG with NH_2-YCAREPPTRTFAYWG-$CONH_2$ sequence allowing amidation from free primary amine of the peptide and NHS ester of alkyne-PEG-NHS (**Figure 3.13**). Lyophilized product was characterized by ^{1}H NMR spectroscopy, along with alkyne-PEG-NHS and free peptide for ease of comparison. From the examination of ^{1}H NMR spectra (**Figure 4.32**) of three mentioned compounds, the final product alkyne-PEG-

EPPT1 depicts specific signals from building blocks, namely, PEG main chain signals are simply detected from 3.25 to 4.00 ppm, aromatic protons from amino acid groups within a range of 7.60 to 6.60 ppm, while NHS ethylene signals seen at 2.96 ppm were found to have almost vanished. Additionally, it was observed that there was the free alkyne-PEG-NHS presence, which remains unreacted and cannot be removed at this stage since it has similar molecular properties to the product, was detected to be 16.16% by mol, while the alkyne-PEG-EPPT1 compound was 83.84% by mol in the product. Conjugation of alkyne-PEG-EPPT1 onto PAMP-CP-rGO was accomplished by CuAAC reaction without further purification of the product since it can contribute to PEGylation if it is reacted with the targeted azide group or it can be washed away during purification if it is unreacted.

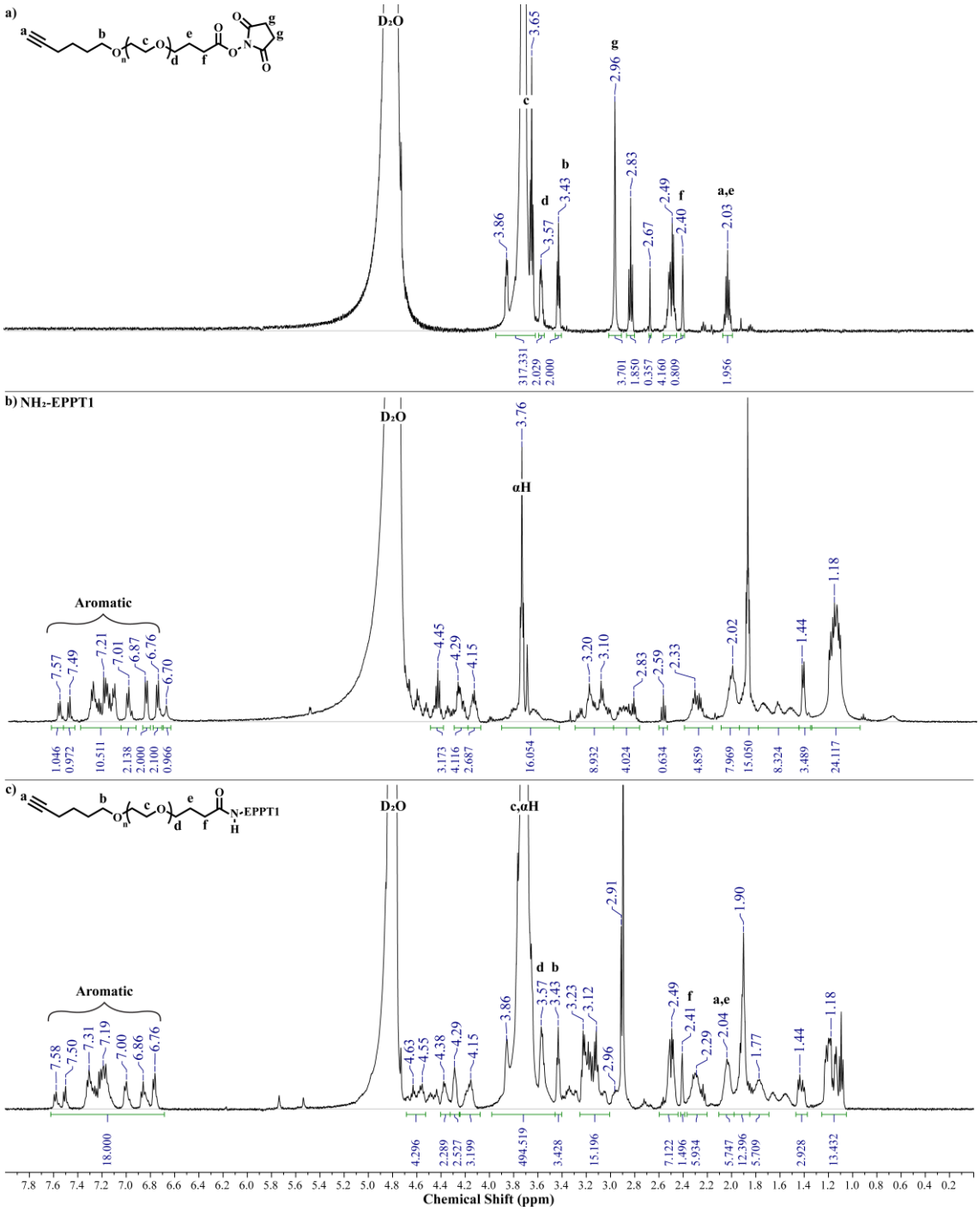


Figure 4.32: ^{1}H NMR spectrum of **a)** alkyne-PEG-NHS, **b)** EPPT1, and **c)** alkyne-PEG-EPPT1.

4.2.5. Preparation of EPPT1-PAMP-CP-rGO-Dox-siRNA and derivatives

Synthetic processes were finalized by adding up all small parts to fabricate the final nanoplatform, for the purpose of controlled experiments non-targeted and Dox-free derivatives along with scramble siRNA complexes were prepared. The first step of the fabrication was one pot coating GO with PAMP-*g*-CP and reduction by hydrazine

hydrate, which was followed by alkyne-PEG-EPPT1 conjugation, Dox loading and siRNA complexation (**Figure 4.33**).

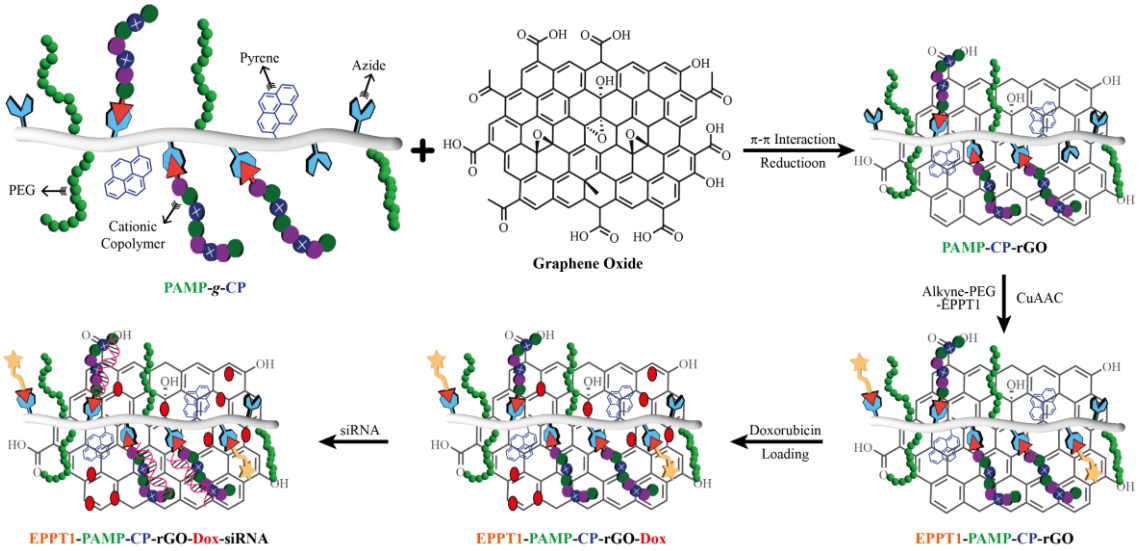


Figure 4.33: Preparation steps of pH sensitive, targeted, siRNA and chemotherapeutic agent carrying drug delivery agent.

One-pot PAMP-*g*-CP coating and reduction of GO was carried out in water DMF mixture at first room temperature then 80 °C, the color of the solution was turned from dark brown to black due to the reduction since no precipitate was formed in the flask PAMP-CP-rGO was forcibly gathered by high-speed centrifugation. Collected solids were redispersed and centrifuged multiple times to remove any unbound graft copolymer from the product. After the last centrifugation particles were dispersed in distilled water, immediately froze with liquid nitrogen, and lyophilized till dryness. Nanoplatforms were mainly characterized by TGA analysis conducted under a nitrogen atmosphere between 25-800 °C with a 10 °C/min heating rate (**Figure 4.34**). As a result of thermal degradation between 100 °C and 500 °C (onset temperature: 171.77 °C) GO loses 49.5% of its weight and it showed 57.6% total mass loss at the end of the analysis. On the other hand, the rGO profile showed improved thermal stability, when reaching 500 °C only 10.5% and when reaching 800 °C 26.0% weight has been lost. As expected from methacrylate derivative copolymer PAMP-*g*-CP shows its main degradation between 200-500 °C (onset temperature: 231.79 °C and 384.33 °C) with 88.3% weight loss, by taking advantage of this characteristic degradation the mass ratio of PAMP-*g*-CP on the rGO surface was assessed. Examination of PAMP-CP-rGO displays identical degradation of the graft copolymer and 59.9% of the total mass was decomposed at the same region (onset temperature: 266.64 °C and 345.75 °C), considering 6.6% rGO thermal degradation in

the same region 53.3% PAMP-*g*-CP by weight on rGO surface was detected. Since the contribution of EPPT1 conjugation to total mass is insignificant, no change was recorded during the TGA analysis of EPPT1-PAMP-CP-rGO and due to the vaporization of Dox during the analysis, an accurate TGA profile could not be recorded for Dox loaded particles, nevertheless change in thermal degradation behavior under inert atmosphere between ensuing materials proves efficient reduction and coating.

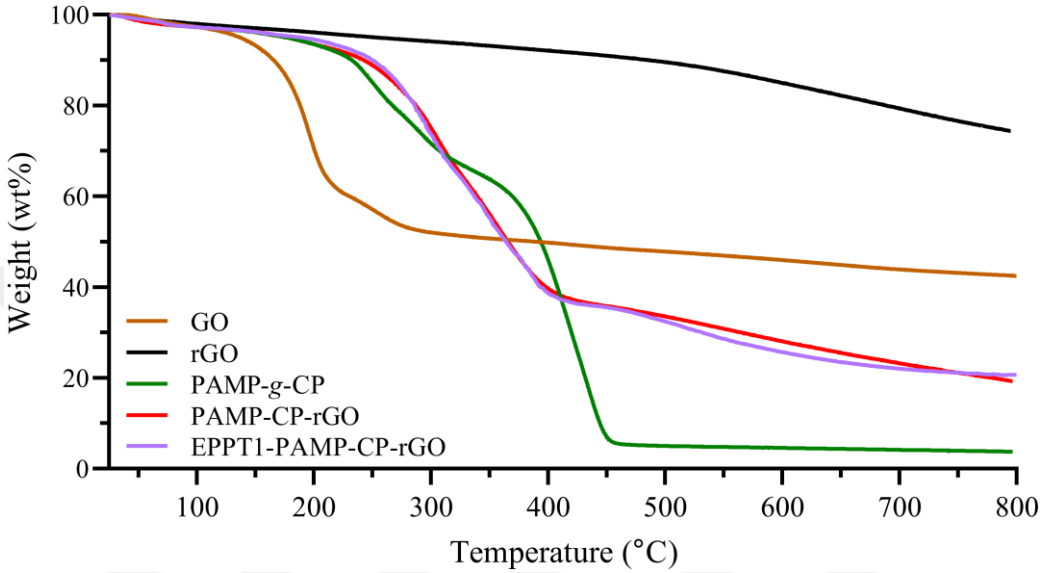


Figure 4.34: TGA thermogram of GO, rGO, PAMP-*g*-CP and PAMP-CP-rGO.

Taking advantage of the remaining azide side groups on PAMP-CP-rGO, alkyne-PEG-EPPT1 was incorporated into the rGO surface using a CuAAC in pH 8 PBS. The Bradford assay (**Figure 4.35**) revealed traces of protein in the reaction mixture's supernatant, and when compared to the initial concentration, it was discovered that 98.2% of the protein had been attached to the PAMP-CP-rGO surface producing EPPT1-PAMP-CP-rGO.

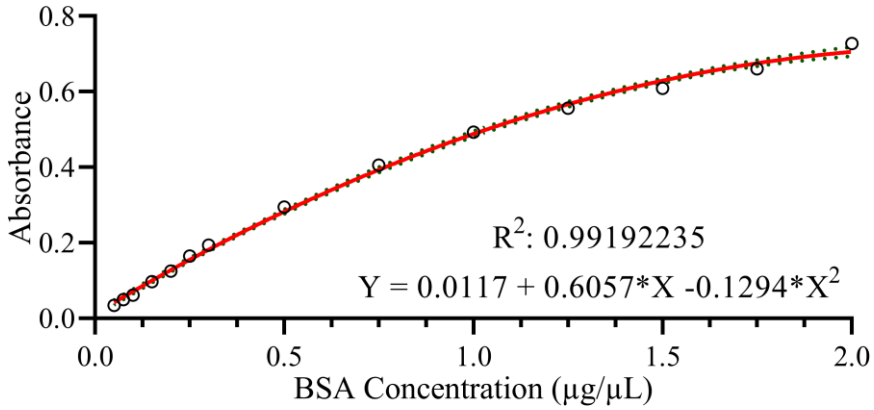


Figure 4.35: Bradford calibration curve prepared at various bovine serum albumin (BSA) concentrations.

As a final step for multifunctional drug carrier preparation, doxorubicin was loaded onto the rGO surface, by leaving this process to the end, it was desired to prevent Dox release from the surface during the intermediate steps. Drug loading conditions were optimized by following literature which is affected by temperature and pH [259]. rGO derivatives and Dox were mixed overnight in pH 8 PBS at 35 °C and purified by centrifugation and washing steps, solid Dox loaded carriers were obtained after lyophilizing products that are dispersed in water. The amount of Dox loaded on the rGO surface was calculated by determining the amount of residual Dox that remained in the solution, which was collected from the first centrifuge. Calibration curves at different pH levels in PBS were prepared (**Figure 4.37**) and employed for the calculations. Almost complete internalization of Dox on the carrier surface has been achieved, 96.3% of the Dox was loaded on PAMP-CP-rGO where 97.0% was captured by EPPT1-PAMP-CP-rGO, and resulting drug-loaded carriers have 49.1% and 49.3% Dox by mass on their surfaces revealing high loading capacity regarding the hydrophobic drug.

Scanning electron microscopy (SEM) images of GO, rGO, PAMP-CP-rGO, EPPT1-PAMP-CP-rGO, PAMP-CP-rGO-Dox, and EPPT1-PAMP-CP-rGO-Dox reveals morphological differences caused by surface modification of GO and rGO can be seen in **Figure 4.36**. GO could be seen as thin single plates, wrinkled and randomly aggregated, but after reduction, rGO piles up on top of each other, forming a more densely packed, over-diametered, flatter structure as anticipated [260], [261]. When GO plates were PEGylated by PAMP-CP and reduced resulting composite resembled rGO but they exhibit a looser packing than rGO. Significant morphological changes were not observed when Dox and EPPT1 peptide were included in the structure, but when the structures were elementally analyzed with an EDAX sensor, it was observed that the distribution percentages between atoms changed with the addition of functional groups. As seen in **Table 4.8** reduction of GO results in an increase in C and N percentages and a decrease in O percentages. While PAMP-rGO obtained as a result of PEGylation of rGO showed increased O ratio and the azide groups in its structure were determined as 1.37% nitrogen from the nanoplatform. As a result of Dox loading on this structure, the percentage of nitrogen increased to 2.06%, and again with the contribution of EPPT1 peptide to this structure, the nitrogen ratio increased to 2,49% with the contribution of amide groups originating from peptide backbone. Although these modifications resulted in small variations in the percent distribution among scanned atoms, the most significant change

was observed with the inclusion of the cationic copolymer in the structure, where the nitrogen percentage increased to 4.38% thanks to the secondary and tertiary amine groups on the DMAEMA and TMAEMA monomers.

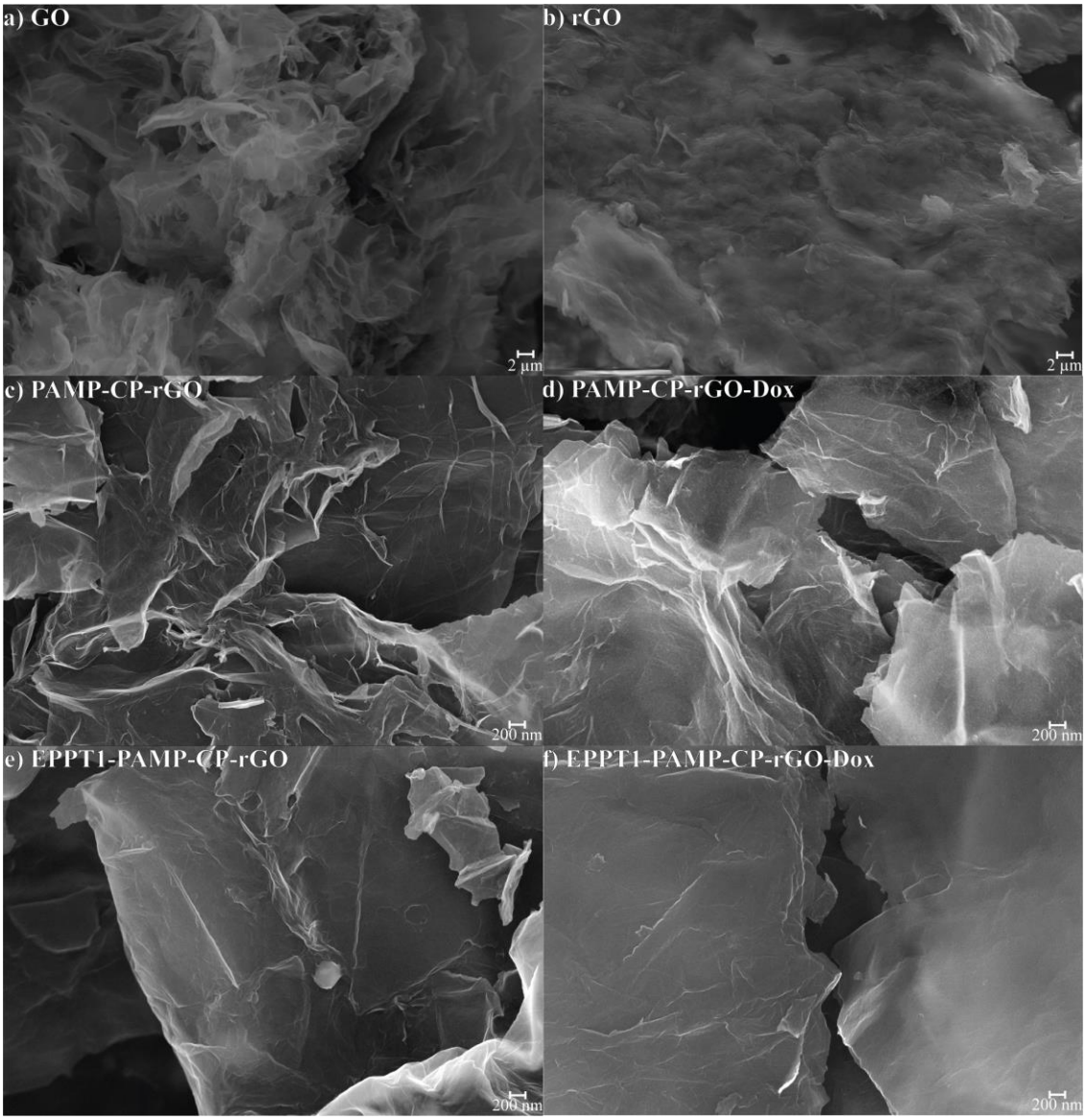


Figure 4.36: Scanning electron microscopy images of GO, rGO, PAMP-CP-rGO, EPPT1-PAMP-CP-rGO, PAMP-CP-rGO-Dox, and EPPT1-PAMP-CP-rGO-Dox

Table 4.8: Elemental composition of rGO derivatives determined by SEM-EDAX scan.

	% C	**% O**	**% H**	**% N**
GO	56.51	37.97	4.93	0.59
rGO	83.43	13.49	0.01	3.08
Dox	57.35	33.25	0	5.06
PAMP-rGO	68.88	29.72	0.02	1.37
PAMP-rGO-Dox	66.36	31.46	0.01	2.09
EPPT1-PAMP-rGO-Dox	63.80	33.70	0.01	2.49
PAMP-CP-rGO-Dox	44.28	51.18	0.17	4.38

Dox release profiles of the carriers were assessed by placing material dispersant into 3.5 kDa dialysis bags that are submerged in PBS solutions at pH 7.4 and 5.5, and results were calculated by using a calibration curve prepared at relevant pH levels (**Figure 4.37**). The only difference between the two carriers is EPPT1 conjugation as the targeting agent, since physicochemical changes that are induced by PEG-EPPT1 addition to the system are negligible, this difference did not result in a significant change in the drug release profiles (**Figure 4.38a**). The carriers are expected to behave pH-dependent for their release profiles, at pH 7.4, around 10% of the drug was released after 48 hours from both targeted and non-targeted carriers but at pH 5.5 this release reaches 45.3% for PAMP-CP-rGO-Dox and 43.5% for EPPT1-PAMP-CP-rGO-Dox showing an accelerated profile by following the decrease in the pH. After passing early stages, observation was continued till 108 h, the pH 7.4 test revealed to release of only 25.95% on average of the drug, whereas at pH 5.5 cumulative release reached a maximum rate of 52.9% for EPPT1-PAMP-CP-rGO-Dox.

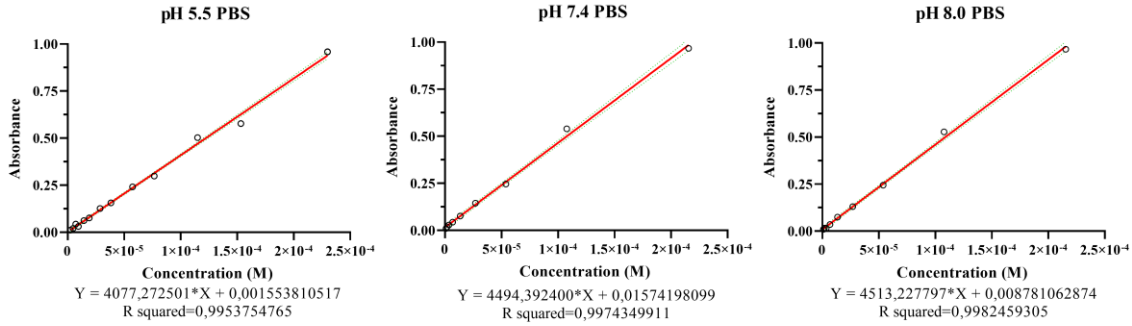


Figure 4.37: Change in absorption based on Dox concentration at different pH levels in PBS.

The primary defining significant characteristic of a smart drug delivery system is the drug release mechanism which can be defined by modeling release kinetics. For this purpose 5 well-known mathematical models were selected focusing on the graphene and Dox-containing systems [262] and after processing the data according to the model function in Microsoft Excel, obtained data was analyzed by linear regression curve fitting to determine the most suitable model. The regression modules of each model were compared and summarized in **Table 4.9** to assist in selecting the optimal drug release kinetic model and in **Figure 4.38b** and **c** plots show the best fitting models. The results showed that the Weibull model was better fitted for the experimental data obtained at pH 5.5 for both PAMP-CP-rGO-Dox (R^2=0.9395) and EPPT1-PAMP-CP-rGO-Dox (R^2=0.9601). The shape parameter β is related to the shape of the release curve against time, for β values

smaller than 1 demonstrate a parabolic graph as obtained from the pH 5.5 release curve and indicate a release profile showing a biphasic drug release with a short burst release phase at the early stages and followed by a steady, much slower release [263], [264]. The Weibull model is commonly used for comparison of drug release of heterogenous matrices, having a network of grafted polymers on graphene surface might be acting as a matrix and after the first release stage retarding Dox from rapidly leaving the rGO surface and releasing the drug at a constant rate for the rest of the release [265]. On the other hand, once the pH was switched from the acidic region to the neutral region Dox becomes de-protonated, changing amine functionality from $-NH_3^+$ to $-NH_2$ which decreases the hydrophilicity and solubility of Dox in the water environment, as result release profile at neutral pH levels changes from Weibull model to zero-order model for both PAMP-CP-rGO-Dox (R^2=0.9828) and EPPT1-PAMP-CP-rGO-Dox (R^2=0.9821) suggesting a linear release rate by time independent of the concentration. The rate of the release is defined by k_0, the release constant, and calculated to be 0.2321 and 0.2374 for non-targeted and targeted formulation respectively, that is indicating a slow release rate by the time [266]. It is infallible to point out the stability of the drug-loaded particles at neutral pH levels and accelerated release at acidic pH levels indicating protection of the cargo during blood circulation and quick release in the cancer cell.

Table 4.9: Regression modules (R^2) of tested mathematical models.

	Zero Order	**First Order**	**Higuchi**	**Korsmeyer-Peppas**	**Weibull**
PAMP-CP-rGO-Dox, pH 5.5	0.8540	0.5861	0.1293	0.9173	**0.9395**
EPPT1-PAMP-CP-rGO-Dox, pH 5.5	0.8753	0.6781	0.3574	0.9527	**0.9601**
PAMP-CP-rGO-Dox, pH 7.4	**0.9828**	0.9264	0.9192	0.8942	0.8857
EPPT1-PAMP-CP-rGO-Dox, pH 7.4	**0.9821**	0.8840	0.9469	0.9415	0.9350

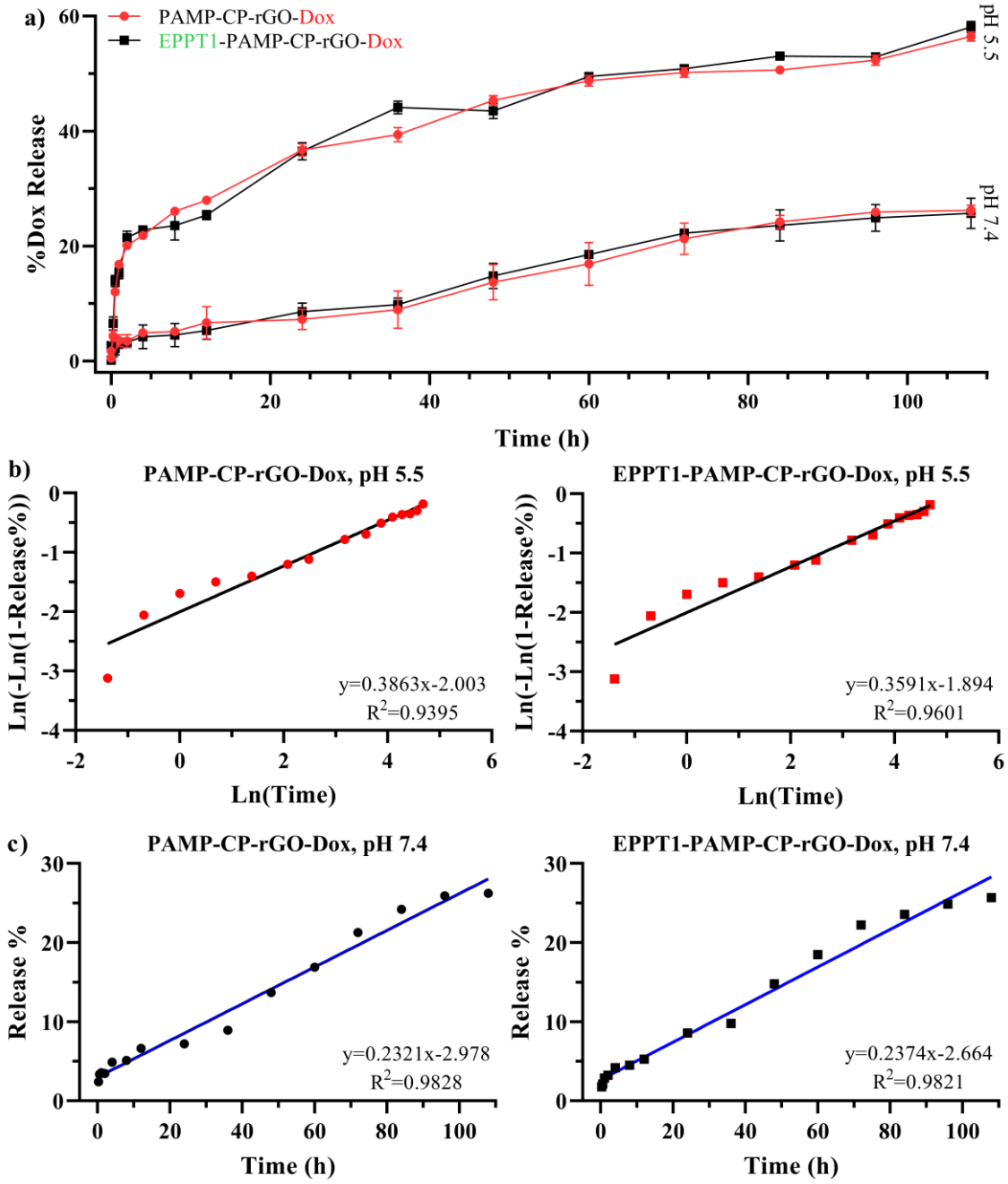


Figure 4.38: a) Dox release profile by time, **b)** Weibull Model and **c)** zero-order linear regression graphs of EPPT1-PAMP-CP-rGO-Dox and PAMP-CP-rGO-Dox at pH 7.4 and pH 5.5.

During blood circulation, plasma proteins pose a risk of adsorption onto the wide rGO surface forming a protein corona which creates the risk of change in carrier characteristics. Evaluation of this possibility was tested by mixing PAMP-CP-rGO dispersant with 10% FBS in PBS at 37 °C, where GO and rGO were used as controls, at predetermined time points samples of the mixtures were drawn and residual FBS concentrations were determined by Bradford assay (**Figure 4.35**).

When these three graphene derivatives were compared with each other, the highest FBS adsorbing material was found to be GO, while rGO and PAMP-CP-rGO exhibited similar profiles (**Figure 4.39**) in parallel to the literature [214]. Although PAMP-CP-rGO overcomes the water dispersion problems unlike rGO, it followed a parallel profile to rGO in interaction with protein adsorption. After 72 hours of mixing, PAMP-CP-rGO has only adsorbed 13.3% of the total FBS, while GO adsorbed 26.5%. From this point of view, it is possible to say that the copolymer coating on the rGO surface can lower the opsonization of carriers by shielding the carriers against proteins during blood circulation which provides a safer vehicle for cargo.

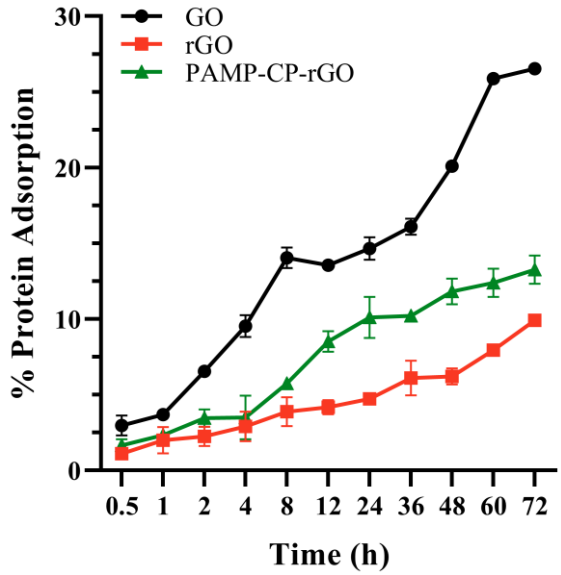


Figure 4.39: Protein adsorption by GO, rGO, and PAMP-CP-rGO at physiological conditions.

As the next step, a second cargo was introduced into the system as either anti-GAPDH-siRNA as the model gene or anti-Bcl-2-siRNA as the target gene. Using gel electrophoresis, the siRNA-complexation properties of rGO derivatives carrying cationic charges were investigated. Since the number of the vector charged nitrogen atoms are not realistic to determine the molar ratio was replaced with the mass ratio of rGO derivatives to siRNA (anti-GAPDH and anti-Bcl-2) and complexes at various mass ratios were prepared (nanoplatform:siRNA(w/w)=25/1, 30/1, 35/1, 40/1, 45/1, 50/1) and tested by agarose gel electrophoresis [267], [268]. The siRNA molecules that were attached to the PAMP-CP-rGO and derivatives were unable to migrate, but the free siRNA molecules can move through the gel, as seen from the gel image (**Figure 4.40a** and **b**) at the mass ratio of 25/1 anti-GAPDH and at 40/1 anti-Bcl-2 migratory siRNAs were observed and

fully complexed at the ratio of 30/1 and 45/1 for each composition respectively, showing PAMP-CP-rGO derivatives could form stable complexes with anti-GAPDH-siRNA at 30/1 and with anti-Bcl-2-siRNA at 45/1 or higher mass ratios and throughout the study, 30/1 and 45/1 mass ratios have been used.

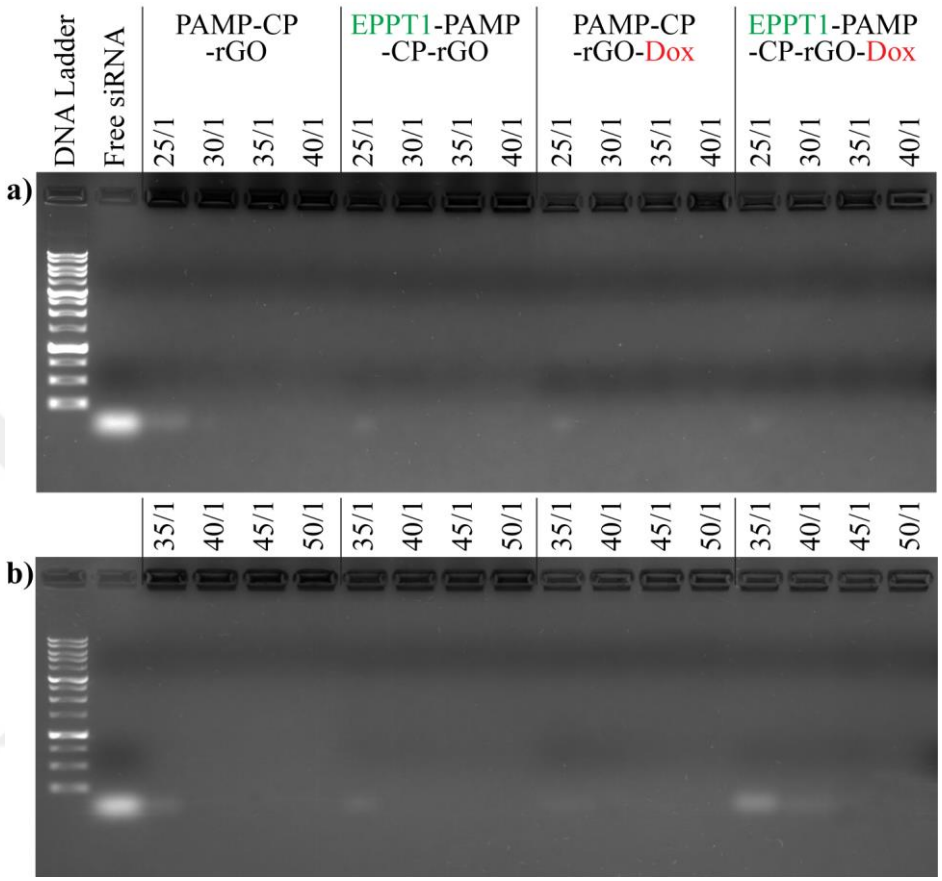


Figure 4.40: Agarose gel electrophoresis assays performed by using **a)** anti-GAPDH-siRNA and **b)** anti-Bcl-2-siRNA (DNA ladder and free siRNA were used as the control for gel retardation).

The size and surface charge of the complexes were determined by DLS analysis at multiple N/P mass ratios in water, namely at 25/1, 30/1, 35/1, 40/1, and 45/1 in compliance with gel retardation assay results and non-complexed carriers (1/0). Complexes were prepared with anti-GAPDH-siRNA and size and zeta potentials were recorded in triplicates. As can be seen in **Figure 4.41** modifications to the GO reduced the particle size from 646.1 nm to around 550 nm despite the chemical reduction to water-insoluble reduced graphene oxide. The introduction of siRNA to the system increases the size of the carriers in parallel to increased rGO derivatives ratio, since DLS mostly focuses on spherical particles, it does not provide highly accurate data for 2D particles, nevertheless obtained size distributions were found to be consistent with each other and

the polydispersity index (PDI) ranging between 0.2 to 0.8 indicating carriers to have a wide particle size distribution [269]–[271]. The effective electric charge on the starting material GO was -42.5 mV, subsequently, the cationic charge carrying PEG-*g*-CP graft copolymer increased the charge to the positive region. EPPT1 conjugation to the non-targeted PAMP-CP-rGO-siRNA carrier surface decreases the charge by 12 mV whereas Dox loading on the targeted carrier increases the charge from 25.4 mV to 41.6 mV. The Zeta potential of the nanocarriers had a negative or neutral value at the 25/1 ratio due to free siRNA, and in parallel, to the increase in carrier/siRNA mass ratio, the surface charge increases in the positive range ensuring complete and stable complexation.

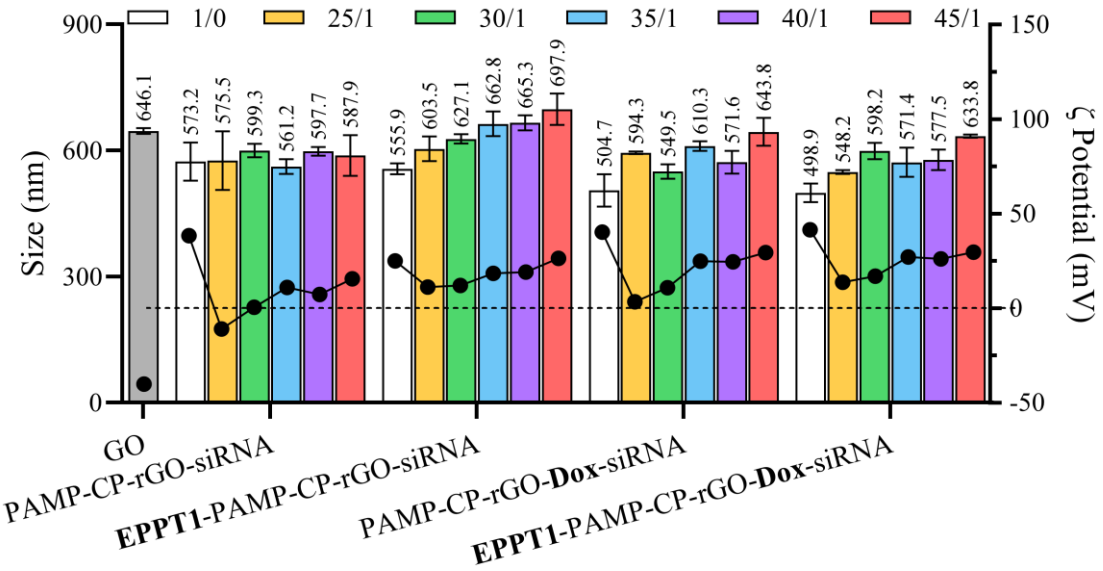


Figure 4.41: Size and zeta potential results of GO, PAMP-CP-rGO, PAMP-CP-rGO-Dox, EPPT1-PAMP-CP-rGO, and EPPT1-PAMP-CP-rGO-Dox at various mass ratios.

4.3. *In Vitro* Evaluation of PAMP-CP-rGO Nanoplatforms

4.3.1. Determination of induced cytotoxicity by PAMP-CP-rGO nanoplatforms using resazurin assay

Introduction of Dox onto nanoplatforms surfaced the risk of false positive results during the determination of cell viability due to its wide absorbance range and autofluorescence, to prevent any interaction during measurements assay that was used during the cell viability study of PMP-rGO derivatives was changed from MTS assay to resazurin assay for the assessment of cellular cytotoxicity of Dox and/or siRNA-loaded nanoplatforms, which is converted to fluorescently active resorufin by cellular activity allowing detection by excitation at 550 nm and reading emission at 590 nm (**Figure 4.42**).

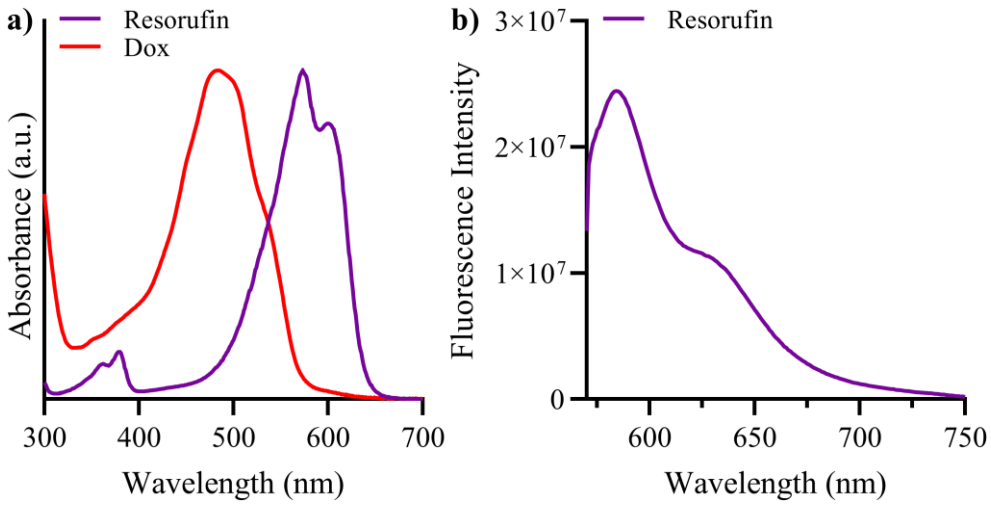


Figure 4.42: a) UV absorbance of Dox and resorufin, **b)** fluorescence spectrum of resorufin.

To measure the cell viability of ER+ MCF-7 or triple-negative MDA-MB-231 breast cancer cells were plated in black-walled 96 well plates and were incubated separately with nanocarriers at various Dox concentrations (Dox free carriers were applied to corresponding PAMP-CP-rGO concentrations) in triplicate for 24 or 48 hours along with control wells, after incubation time wells were washed with PBS and resazurin solution was applied in fresh medium, followed by incubation at physiological conditions for 2 hours. From the comparison of test and control well's fluorescence intensity cell viability percentage was calculated and cell viability percentages were plotted against material concentration.

The first trial was conducted by the complexes of anti-GAPDH-siRNA with an incubation time of 24 hours, as seen in **Figure 4.43**. PAMP-CP-rGO-siRNA and EPPT1-PAMP-CP-rGO-siRNA did not show significant cytotoxicity at lower concentrations, meanwhile, the introduction of Dox to the carriers increased cell death as participated. In parallel to the dose-dependent cellular toxicity of all rGO derivatives, EPPT1-PAMP-CP-rGO-Dox-siRNA's cell viability seems to be improved slightly when compared to the non-targeted version at lower concentrations by the introduction of the EPPT1 to the carrier but showed the highest toxicity at 20 µg/mL by leaving 37.1% viable cells. In contrast to Dox-loaded rGO derivatives, free Dox leaves 38.1% of cells viable even at the lowest concentration and shows slight differences between concentrations, and could not be controlled effectively without a carrier. From the plotted data IC_{50} values were calculated by nonlinear fit and found to be 1.87 µg/mL for free Dox while PAMP-CP-rGO-siRNA and EPPT1-PAMP-CP-rGO-siRNA were found to have IC_{50} values of 25.86 µg/mL and 29.17

µg/mL respectively. When Dox was introduced to the carrier system IC_{50} values were decreased to 10.17 µg/mL and 13.42 µg/mL for PAMP-CP-rGO-Dox-siRNA and EPPT1-PAMP-CP-rGO-Dox-siRNA respectively showing substantial improvement on cellular toxicity.

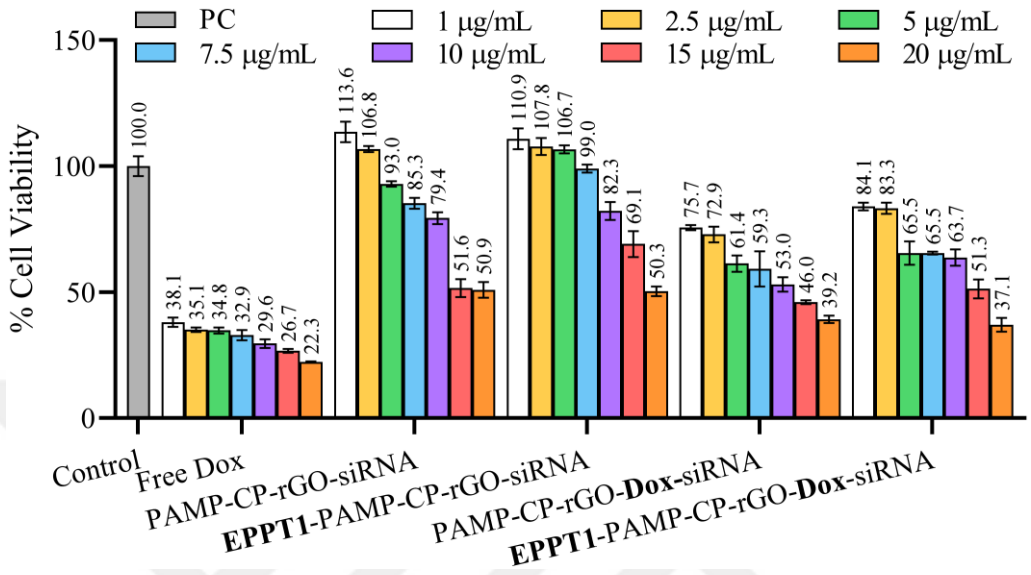


Figure 4.43: Cell viability results of anti-GAPDH-siRNA complexed nanoplatform derivatives with MCF-7 after 24 hours of incubation.

After studying anti-GAPDH-siRNA as a model for optimization of the test conditions anti-Bcl-2-siRNA was complexed with nanoplatforms and subjected to resazurin assay for the detection of their effect on the cell viability. When compared to the results obtained by using anti-GAPDH-siRNA a similar Dox profile was obtained while improved cytotoxicity was achieved especially at high concentrations for nanoplatforms without Dox after 24 hours of incubation (**Figure 4.44a**), cell viability rate decreased from around 50% to 30% rates for both PAMP-CP-rGO-siRNA and EPPT1-PAMP-CP-rGO-siRNA. Overall cell viability of Dox carrying compounds was decreased after switching to anti-Bcl-2-siRNA, for instance at 5 µg/mL concentration viability of MCF-7 cells was decreased by around 10% for PAMP-CP-rGO-Dox-siRNA and EPPT1-PAMP-CP-rGO-Dox-siRNA. Calculated IC_{50} values for PAMP-CP-rGO-siRNA and EPPT1-PAMP-CP-rGO-siRNA were found to be 13.28 µg/mL and 11.64 µg/mL revealing improved efficacy against MCF-7 cells. While it was decreased almost by half, for PAMP-CP-rGO-Dox-siRNA it was found to be 7.33 µg/mL and 6.45 µg/mL EPPT1-PAMP-CP-rGO-Dox-siRNA. Unlike the anti-GAPDH-siRNA results, IC_{50} values were decreased further by 1-1.5% after the addition of the EPPT1 peptide. Increasing

incubation time from 24 hours to 48 hours (**Figure 4.44b**) decreased the efficacy of targeted selectivity and dose-dependent response.

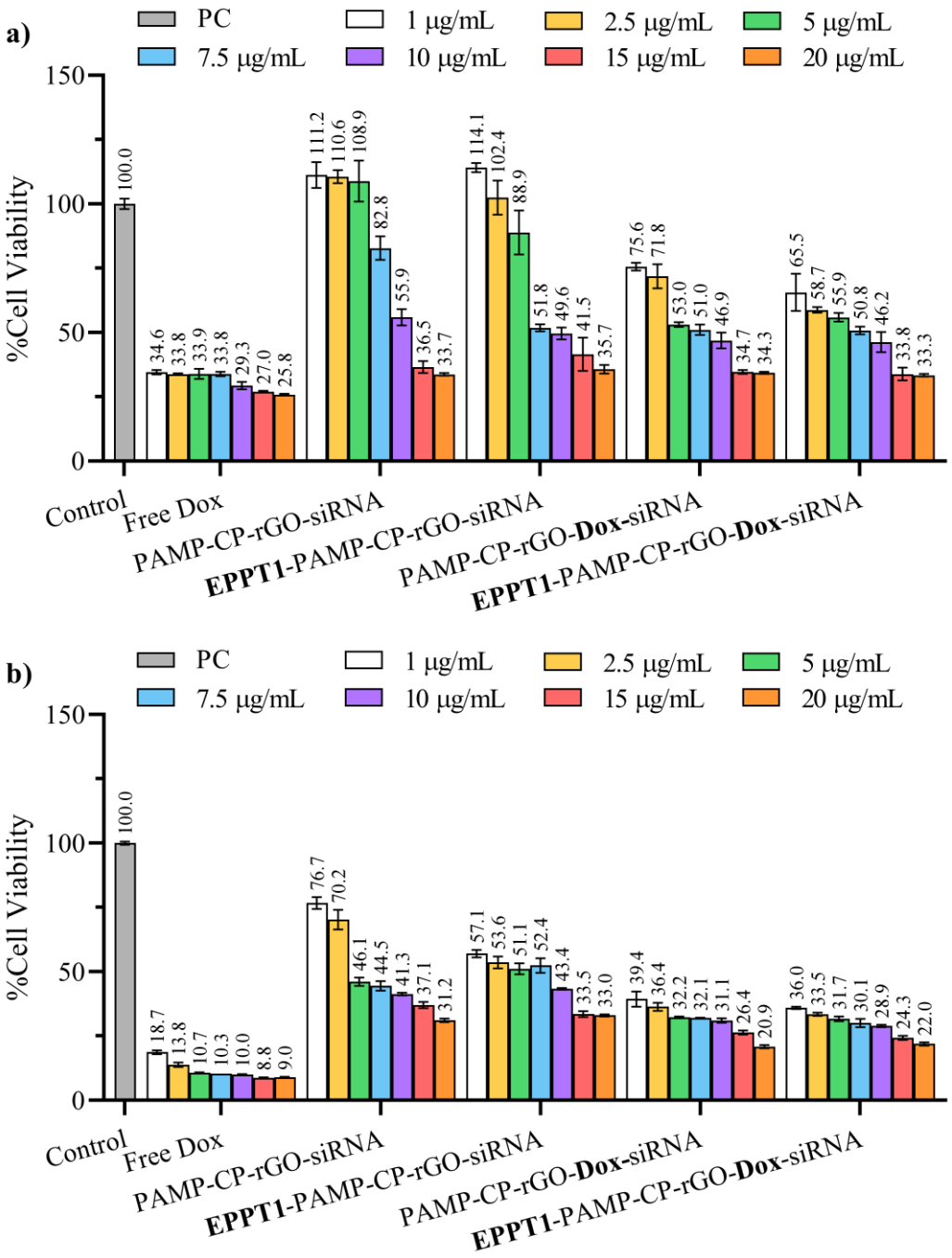


Figure 4.44: Cell viability results of anti-Bcl-2-siRNA complexed nanoplatform derivatives with MCF-7 after **a)** 24 and **b)** 48 hours of incubation.

Figure 4.45 shows the cell viability results after 24 and 48 hours of incubation obtained by employing MDA-MB-231 cells, when examined, it was observed that cell death occurred in parallel at 24 hours but was found to be at lower rates compared to MCF-7 cells at 48 hours of incubation. While a decrease in cell viability was detected in parallel

with the increasing concentration, treatment with nanocarriers for 24 hours caused the highest cell death by targeted, anti-cancer drug and siRNA-loaded EPPT1-PAMP-CP-rGO-Dox-siRNA, while PAMP-CP-rGO-siRNA did not cause significant toxicity. On the other hand, after expanding the nanocarrier incubation time to 48 hours, EPPT1-PAMP-CP-rGO-siRNA composition was found to be more biocompatible than its non-targeted counterpart, this effect can be related to the positive contribution of PEG-EPPT1 in biocompatibility by increasing PEG content (**Figure 4.45b**). This effect should be taken into account when comparing untargeted PAMP-CP-rGO-Dox-siRNA, which carries both anti-cancer drug and siRNA, and untargeted EPPT1-PAMP-CP-rGO-Dox-siRNA. Although EPPT1-PAMP-CP-rGO-Dox-siRNA showed a higher cell viability rate than PAMP-CP-rGO-Dox-siRNA at certain concentrations, it could be used more effectively as the targeted carrier activity increases linearly depending on the concentration. In addition, the decrease in cell viability of around 50% at low concentrations provides the opportunity to work at low concentrations where possible toxicity from the carrier platform could be neglected. Examination of IC_{50} values of PAMP-CP-rGO-Dox-siRNA and EPPT1-PAMP-CP-rGO-Dox-siRNA resulted in a low regression coefficient since the obtained viability rates were close to the 50% range. Consequently, the ER+, non-invasive, and poorly aggressive MCF-7 cell line [272] was found to be more susceptible to Dox and anti-Bcl-2-siRNA carrying nanoplatforms than triple-negative, highly aggressive, and invasive MDA-MB-231 cells [273], a dose-dependent response was detected for all particles while final composition EPPT1-PAMP-CP-rGO-Dox-siRNA demonstrated the best performance against both of the cell lines.

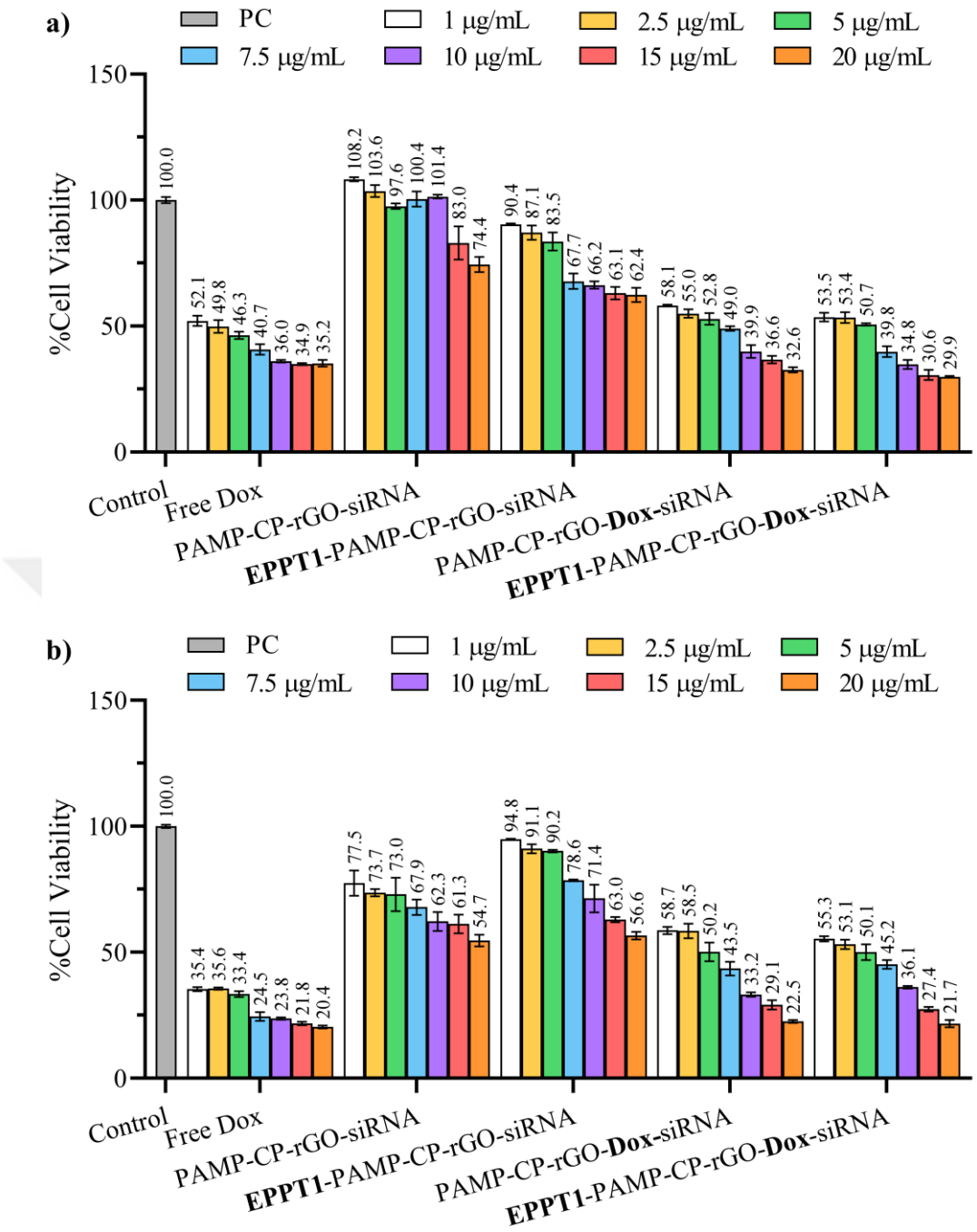


Figure 4.45: Cell viability results of anti-Bcl-2-siRNA complexed targeted carrier and derivatives with MDA-MB-231 after **a)** 24 and **b)** 48 hours of incubation.

4.3.2. Determination of induced cytotoxicity by PAMP-CP-rGO nanoplatforms using the clonogenic assay

In addition to the previously performed biocompatibility tests, the clonogenic assay was studied, and the results were compared with the previous resazurin assay results for confirmation. 500 MCF-7 cells were seeded into 24 well-plate in 0.5 mL full growth medium to have a single cell distribution on the well bottom. The following day cells

were treated with anti-Bcl-2-siRNA complexed nanocarriers for 24 hours, washed, and incubated in a fresh medium for 7 days to grow colonies to be counted with regular medium change. Cell colonies were fixed with methanol and stained with 0.5% crystal violet solution, after wash steps images of the wells were recorded with a smartphone macro 1.9x lens with equal illumination. Each well was individually examined with Fiji software, wells were isolated from walls, converted to 16-bit grayscale, applied watershed filter to divide merged colonies, and counted with the Cell Counter plugin of Fiji (**Figure 4.46**) [218]–[221].

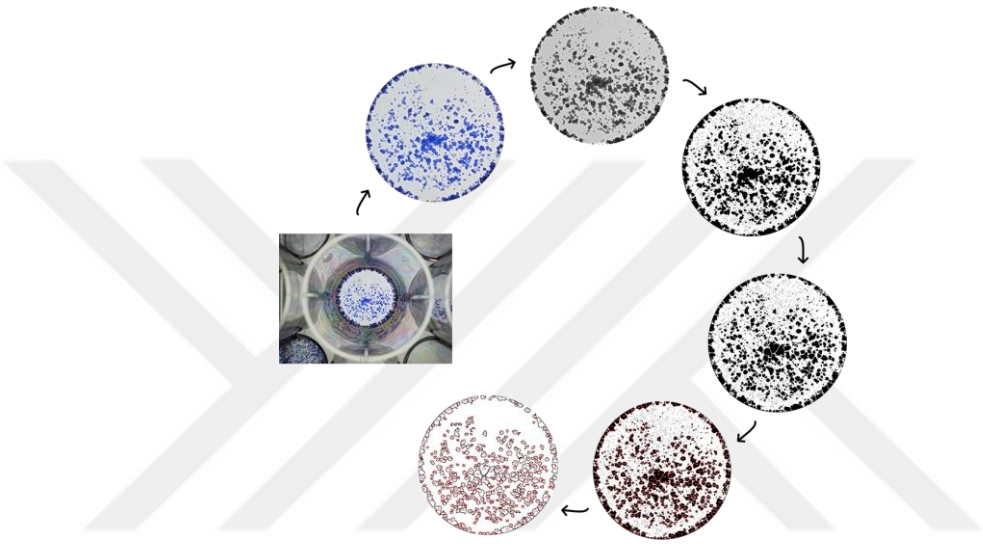


Figure 4.46: Step-by-step colony counting process.

Counted colonies were transferred to a spreadsheet, and results were calculated against control wells, as seen in **Figure 4.47**. Dose-responsive curves were observed through nanocarriers, PAMP-CP-rGO-siRNA treated cells show an 86.1% colony formation rate at the smallest dose where targeted EPPT1-PAMP-CP-rGO-siRNA increases this rate to 92.4% at this concentration and improves colony formation rate, on the other hand even at very low concentrations free Dox kills all viable cells and prevents any colony formation. A similar increase in viability with the addition of EPPT1 can be seen in Dox-loaded carriers and this can be attributed to the additional PEG content results from EPPT1 functionalization. The addition of Dox onto the structure (PAMP-CP-rGO-Dox-siRNA) instantly reduces colony formation rate when compared to nanoplatform without Dox. Even though EPPT1 addition to the structure improves the colony formation rate of MCF-7 cells a clear dose-dependent profile has been observed from EPPT1-PAMP-CP-rGO-Dox-siRNA, conversely the number of the formed colonies was found to be high in number, but their population was lower than nanoplatforms without Dox. From the

examination of plotted data IC_{50} value for EPPT1-PAMP-CP-rGO-Dox-siRNA was found to be 5.63 µg/mL to be very close to the value of 6.45 µg/mL which was determined by resazurin assay. By employing clonogenic assay possible difficulties that could have been faced with spectrometric assays were overcome and the direct result has been achieved.

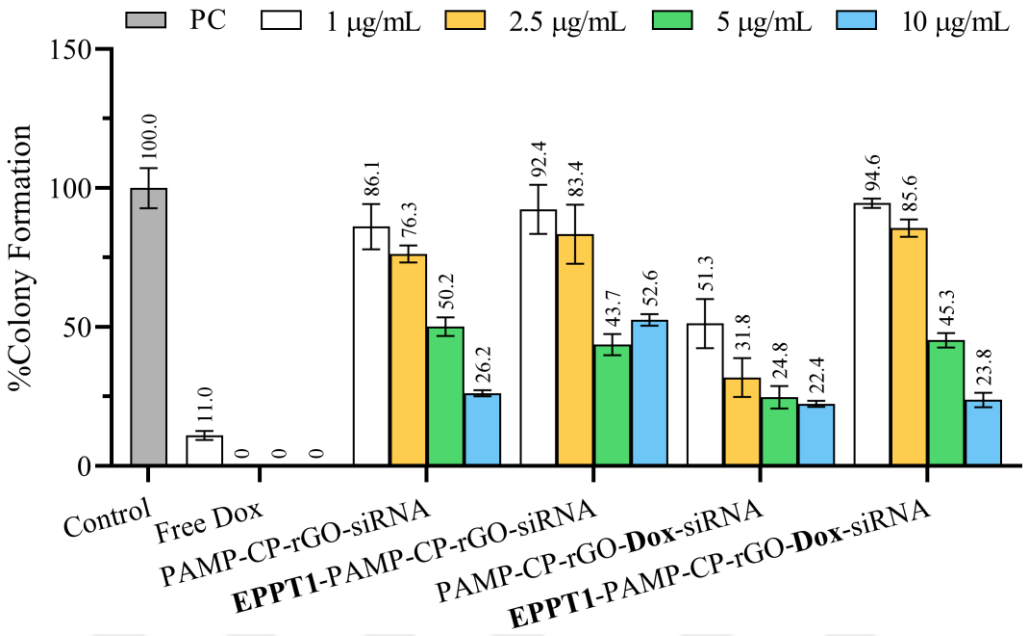


Figure 4.47: Colony formation rates of MCF-7 cells after incubation with nanocarriers.

4.3.3. Determination of cellular uptake of nanoplatforms by confocal fluorescence microscopy

Precursors of the smart nanoplatform were tested for their cellular uptake on healthy MRC-5 cell line to prove that PMP-rGO derivatives could enter the cells (**Figure 4.20**), to further study the effectiveness of the cellular uptake, and compare their targeting ability nanoplatforms were tested with MCF-7 cancer cell line and MCF-10A healthy cell line. Briefly, 200,000 cells were seeded on a glass-bottom 35 mm cell culture dish in 1.5 mL of growth medium and incubated overnight. The following day cells were treated with 25 nM siRNA complexed PAMP-CP-rGO derivatives for 4 hours. Dox carrying versions were tested based on the autofluorescence of Dox while nanoplatforms without Dox were complexed with FAM labeled siRNA. To stop cell-material interaction Petri dishes were washed 3 times with 1 mL PBS and supplied with a fresh medium. The nuclei of the cells were stained with 1 µL Hoechst dye and images were recorded by Zeiss LSM800 confocal microscope by using a Plan-Apochromat 40x/1.3 Oil DIC M27 objective, wavelength settings can be seen in **Table 4.10**. All images were captured with the same parameter

settings such as gain, offset, and pinhole settings and analyzed by Zeiss Zen 3.3 blue edition software by following the same procedure.

Table 4.10: Wavelength settings for confocal microscopy studies.

nm\Dye	Alexa Fluor™ 488	Hoechst	Dox	Hoechst	FAM	Hoechst
Excitation	488	348	501	348	492	348
Emission	563	455	552	455	518	455
Detection	495-630	400-495	535-700	400-530	510-700	400-510

In the first study, interactions of MCF-7 cells and free Dox, PAMP-CP-rGO-Dox-siRNA, and EPPT1-PAMP-CP-rGO-Dox-siRNA were scanned, multiple images were captured, and the images obtained from 3 channels selected for comparison among the recorded images were listed in **Figure 4.48**. Selection of MCF-7 cell line over MDA-MB-231 cell line was to observe selective uptake depending on targeting in short incubation instances since MUC1 expression on MCF-7 cell surface was found to be higher than MDA-MB-231 cells that were targeted by EPPT1 peptide [274]. When the fluorescence signal recorded in the Dox channel was examined, it is observed that free Dox penetrates the cell rapidly due to its small structure mainly by passive diffusion [275], while like other nano-sized materials PAMP-CP-rGO-Dox-siRNA and EPPT1-PAMP-CP-rGO-Dox-siRNA were primarily internalize by the cells via slower path endocytosis [95] and they when were compared, the targeted carrier shows brighter fluorescence on the Dox channel, therefore, it was determined that the targeted version entered the cell at a higher rate than nontargeted version.

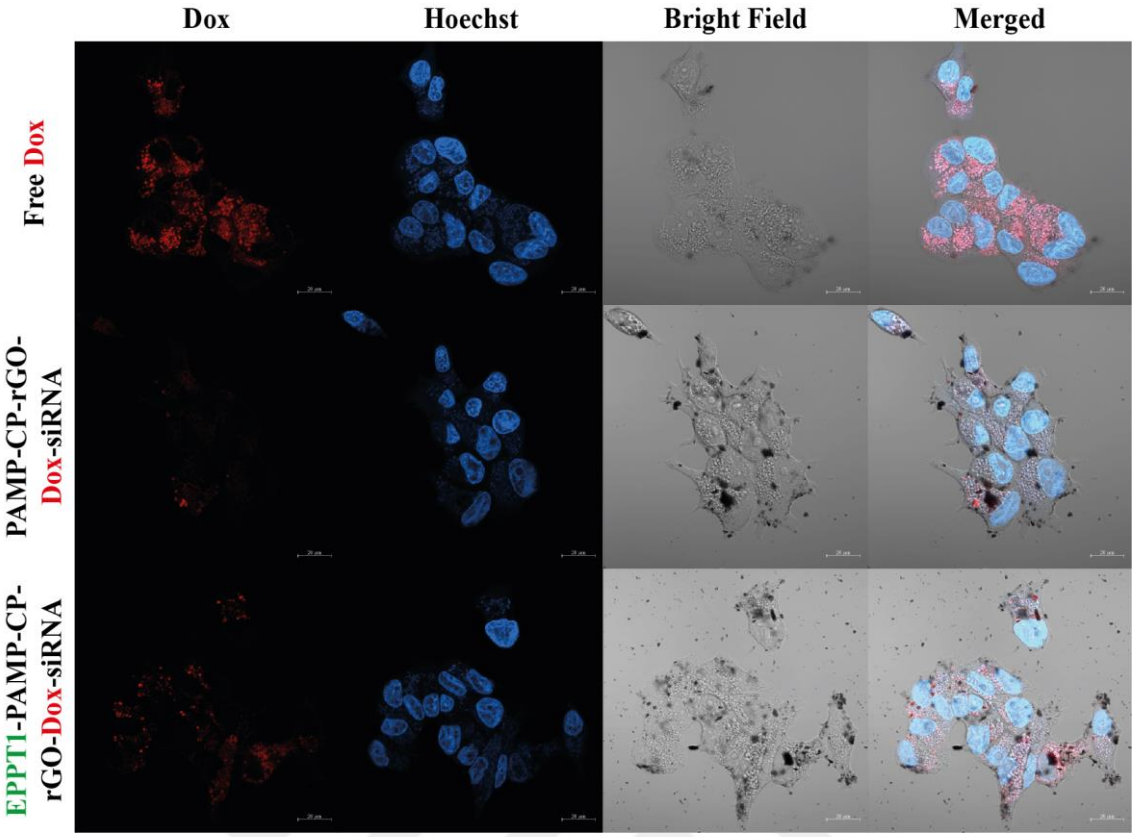


Figure 4.48: Confocal microscope images of Dox-loaded nanoplatforms with MCF-7 cancer cells after 4 hours of incubation. (Scale bar: 20 µm)

While it is possible to capture images with Dox-loaded nanoplatforms by tracking the autofluorescence of Dox, an additional dye was needed for nanoplatforms without Dox, for this purpose, a certain concentration of FAM-labeled siRNA was complexed on nanocarriers, and images were recorded with the same protocol. When green FAM fluorescence intensity was compared between the test groups, as seen in **Figure 4.49**, negatively charged free FAM-siRNA failed to show an effect on cell entry, while targeted EPPT1-PAMP-CP-rGO-FAM-siRNA showed the brightest FAM fluorescence when compared to PAMP-CP-rGO-FAM-siRNA and free FAM-siRNA, as a result, it achieved the highest cell penetration thanks to the contribution of the targeting agent.

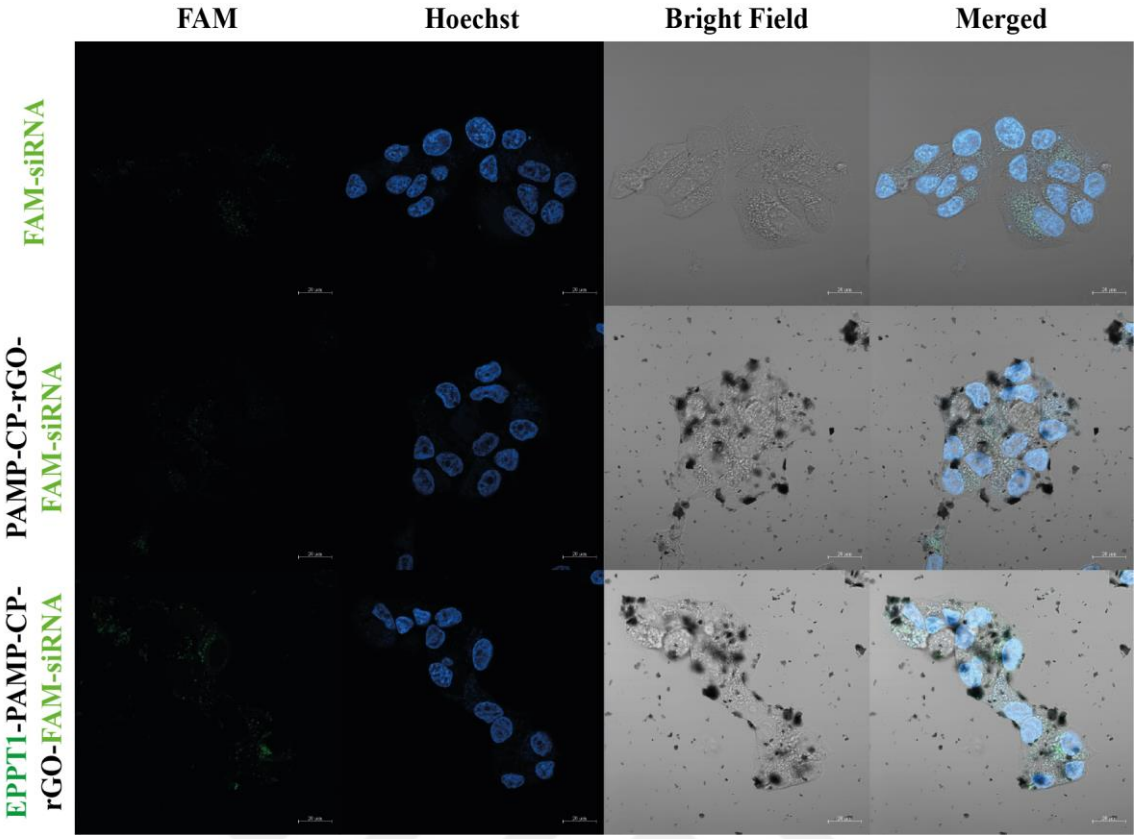


Figure 4.49: Confocal microscope images of FAM-labeled siRNA-loaded nanoplatforms with MCF-7 cancer cells after 4 hours of incubation. (Scale bar: 20 µm)

Although the fluorescence intensity differences could be compared visually in order to make comparisons a more subjective method was applied by converting the microscope images to numerical values. The recorded intensities of Hoechst, Dox, and FAM channels were measured by selecting areas around 7 cells on at least 3 different microscope images in the Zen Blue Edition software, the Dox and FAM radiations were normalized against the Hoechst fluorescence intensity, and the results were given graphically in **Figure 4.50**. This approach clearly identified the differences between the fluorescence intensities in **Figure 4.48** and **Figure 4.49** were determined. As seen in **Figure 4.50a**, free DOX is statistically shown to enter the cells with the highest proportion compared to the targeted EPPT1-PAMP-CP-rGO-DOX-siRNA and non-targeted PAMP-CP-rGO-DOX-siRNA while positive effect from the introduction of EPPT1 targeting on cellular uptake was proven statistically as well. In parallel with microscope images shown in **Figure 4.49**, the uptake of free FAM-siRNA was negligible when compared to the targeted nanoplatform (**Figure 4.50b**). Although the statistical analysis was done for this graph, a statistically significant difference was not detected.

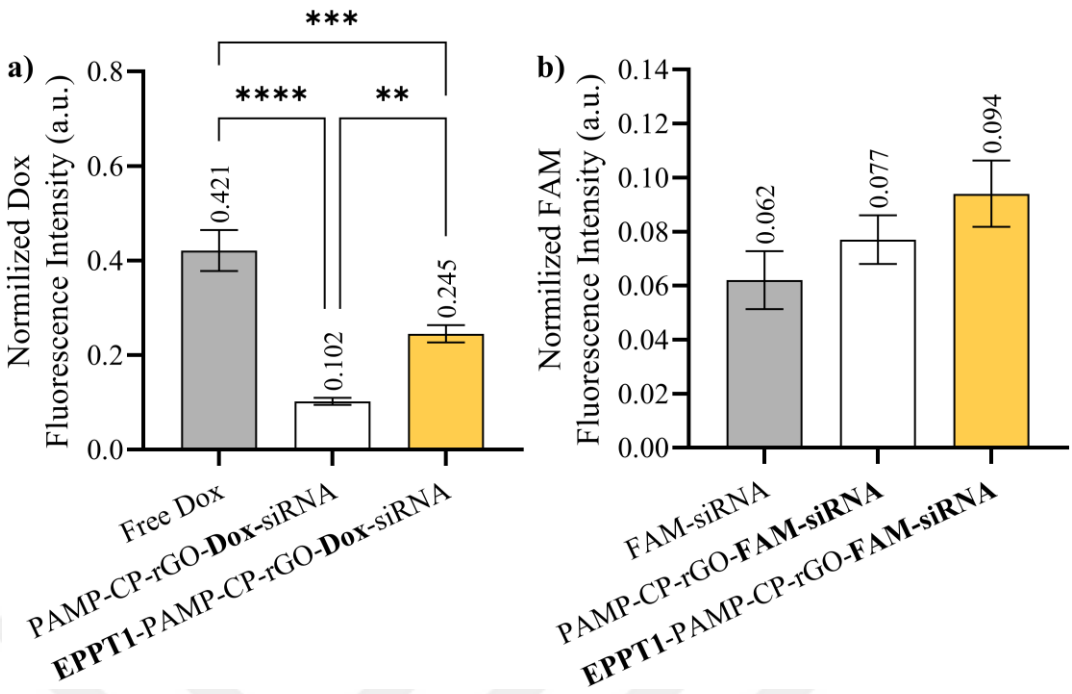


Figure 4.50: Comparison of **a)** Dox and **b)** FAM fluorescent intensities normalized against Hoechst intensity. (n=7, ****p<0.0001, ***p<0.001, **p<0.01)

In addition to examining the cellular uptake of targeted and non-targeted nanoparticles into the cancer cells, their interactions with healthy cells were also examined. In the non-circulated petri dish environment, particles that are present in the culture medium are naturally expected to enter the cells at a certain ratio, but this value is expected to be lower than the MUC1 receptor-rich cancer cells. For this purpose, the MCF-10A cells were planted in Petri dishes and the cellular uptake of nanoplatforms was determined.

Following 4 hours-long incubation with selected materials cells were washed with PBS and cell nuclei were dyed with Hoechst and images were recorded with the same protocol. Free Dox and Dox-loaded nanoparticle images can be seen in **Figure 4.51**, unsurprisingly free Dox entering cells with simple diffusion was found to show the highest intracellular radiation while no significant difference was observed between the targeted and non-targeted nanoplatforms other than showing faint fluorescence irradiation.

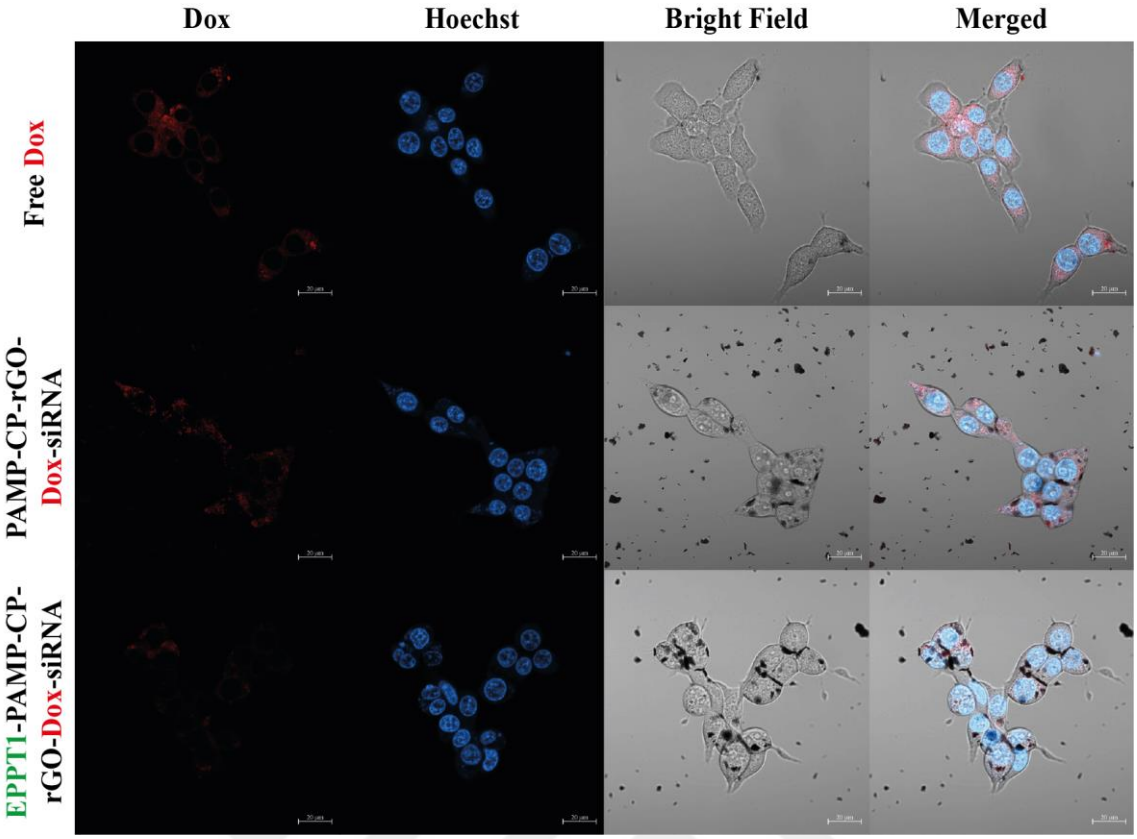


Figure 4.51: Confocal microscope images of Dox-loaded nanoplatforms with MCF-10A cancer cells after 4 hours of incubation. (Scale bar: 20 µm)

As seen in **Figure 4.52** very faint FAM signal could be detected by visual examination of free FAM-siRNA and FAM-siRNA complexed nanoplatform images. Captured images were examined for their fluorescent intensities as mentioned earlier (**Figure 4.53**), comparison between targeted and non-targeted carriers shows no significant difference according to the statistical analysis but as seen in **Figure 4.53a** and **Figure 4.53b** targeted particles have slightly higher fluorescence intensity than non-targeted particles. In light of the results of this study, it was determined that nanoplatforms were internalized by healthy cells at lower rates compared to MCF-7 cancer cells, and it was shown that the targeting agent EPPT1 peptide was more selective for the cancer cells.

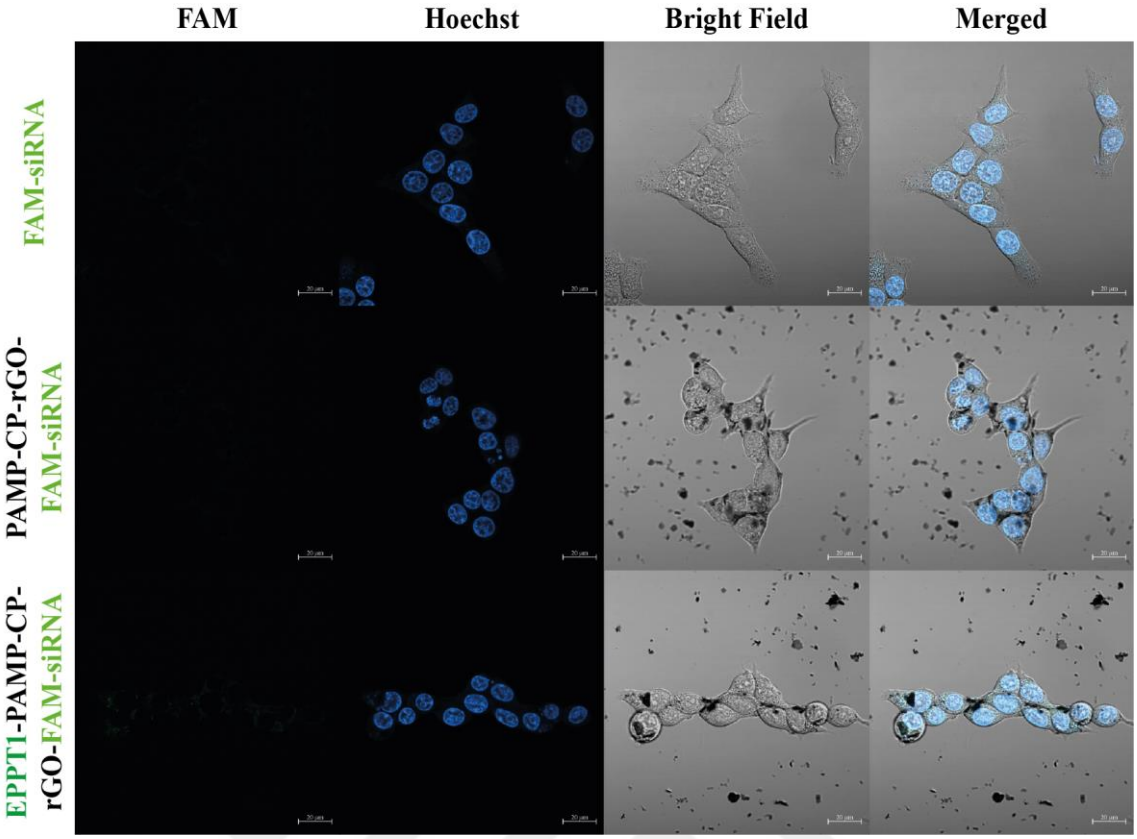


Figure 4.52: Confocal microscope images of FAM-siRNA-loaded nanoplatforms with MCF-10A cancer cells after 4 hours of incubation. (Scale bar: 20 µm)

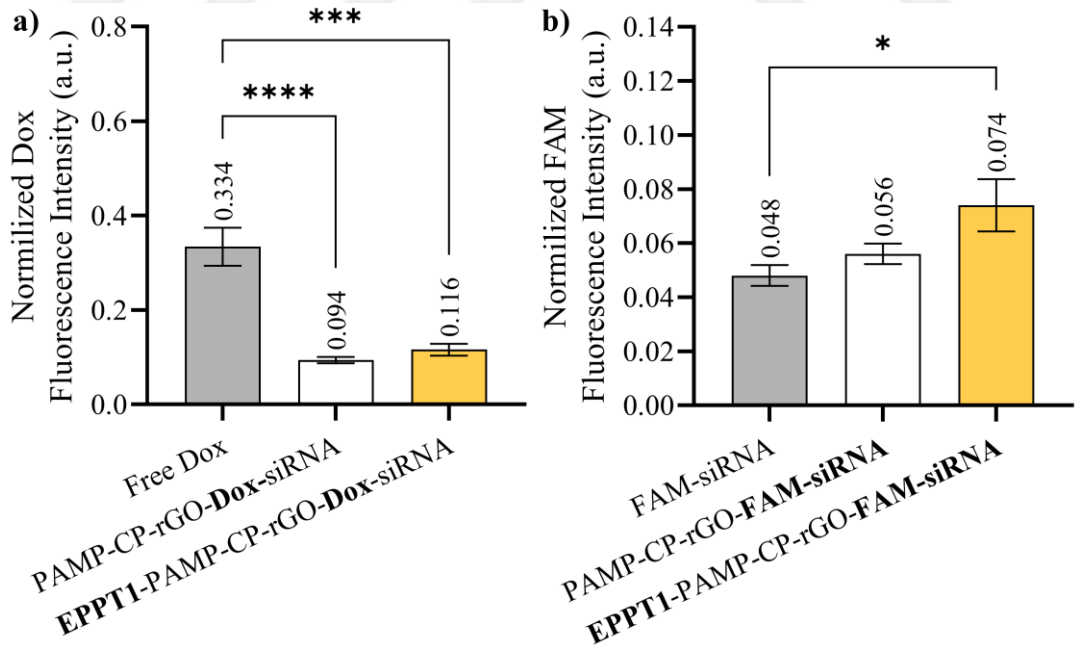


Figure 4.53: Comparison of **a)** Dox and **b)** FAM fluorescent intensities normalized against Hoechst intensity. (n=7, ****p<0.0001, ***p<0.001, **p<0.01)

4.3.4. Localization of EPPT1-PAMP-CP-rGO-Dox-siRNA in MCF-7 cells

LysoTracker® Green DND-26 is a green fluorescent probe that selectively stains acidic compartments in the live cells [276], [277]. From the examination of excitation and emission wavelength of DND-26, it was found more suitable to be used with Dox-loaded nanoplatforms since the overlap between detection ranges is negligible. EPPT1-PAMP-CP-rGO-Dox-siRNA was incubated for 4 hours with MCF-7 cells in a glass-bottomed 35-mm petri dish, washed 2 times with PBS, and incubated with LysoTracker® Green DND-26 in fresh medium at 50 nM concentration for 30 minutes and at the last 10 minutes of the incubation time, Hoechst was added onto the cells. Images were captured by following standard protocol and experiment conditions including excitation laser and detection wavelength range can be seen in **Table 4.11**.

Table 4.11: Wavelength settings for LysoTracker Green DND-26 and Dox loaded nanoplatform detection.

	Hoechst	**LysoTracker**	**Dox**
Excitation Wavelength (nm)	348	503	501
Emission Wavelength (nm)	455	509	552
Detection Wavelength (nm)	400-500	450-535	555-700

In the confocal microscope images shown in **Figure 4.54**, the red channel was assigned to Dox fluorescence while the green channel was set for LysoTracker Green DND-26 fluorescence. From the examination of the images that were recorded over 3 channels, Dox and DND-26 signals can be seen at the same locations, and it was possible to visualize from the merged image that the yellow-orange glow originating from overlapping red and green signals, as well as the red and green radiation coming from separate locations. From this point of view, the presence of targeted, Dox-loaded EPPT1-PAMP-CP-rGO-Dox-siRNA in the cell components with acidic pH (such as endosome, and lysosome) could be clearly detected. In addition, the Dox radiations, which do not coincide with the green radiation, show the presence of nanoplatforms in the non-acidic compartments of the cell.

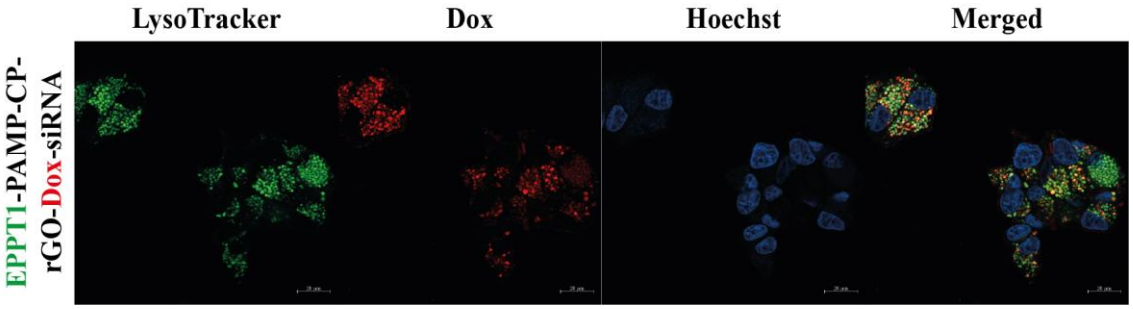


Figure 4.54: Colocalization of EPPT1-PAMP-CP-rGO-Dox-siRNA with LysoTracker Green DND-26 in MCF-7 cells. (Scale bar: 20 µm)

4.3.5. Determination of cellular uptake of nanoplatforms by fluorescence-activated cell sorting (FACS)

As another approach to inspecting differences between targeted and nontargeted vectors by the means of cellular uptake FACS analysis was employed. Dox-loaded particles have the advantage of autofluorescence of Dox to be tracked by fluorescent imaging. 300.000 MDA-MB-231 cells were seeded in 2 mL growth medium into wells of 6 well plates after adherence cells were treated with Dox-loaded targeted and nontargeted nanoplatforms for 2 hours and washed with PBS twice, cells were removed from wells by Trypsin/EDTA solution, collected in 15 mL centrifuge tubes, washed two times with PBS and placed on ice after passing through nylon cell strainers into FACS tubes. Cells were analyzed within the hour, 10.000 events were recorded, and counted cells were plotted against Dox fluorescence intensity.

As seen in **Figure 4.55**, the untreated control MDA-MB-231 cells did not show any significant fluorescence rather than scattering, while the highest fluorescence intensity was detected on cells treated with free Dox. From the fluorescence intensities of PAMP-rGO-Dox and EPPT1-PAMP-rGO-Dox, which do not carry cationic copolymer, the targeted composition showed higher fluorescence intensity than the non-targeted version. Similarly, between PAMP-CP-rGO-Dox-siRNA and EPPT1-PAMP-CP-rGO-Dox-siRNA, the latter targeted platform showed higher fluorescence signal rate after free Dox implying the effectiveness of EPPT1 targeting together with CP-containing platforms.

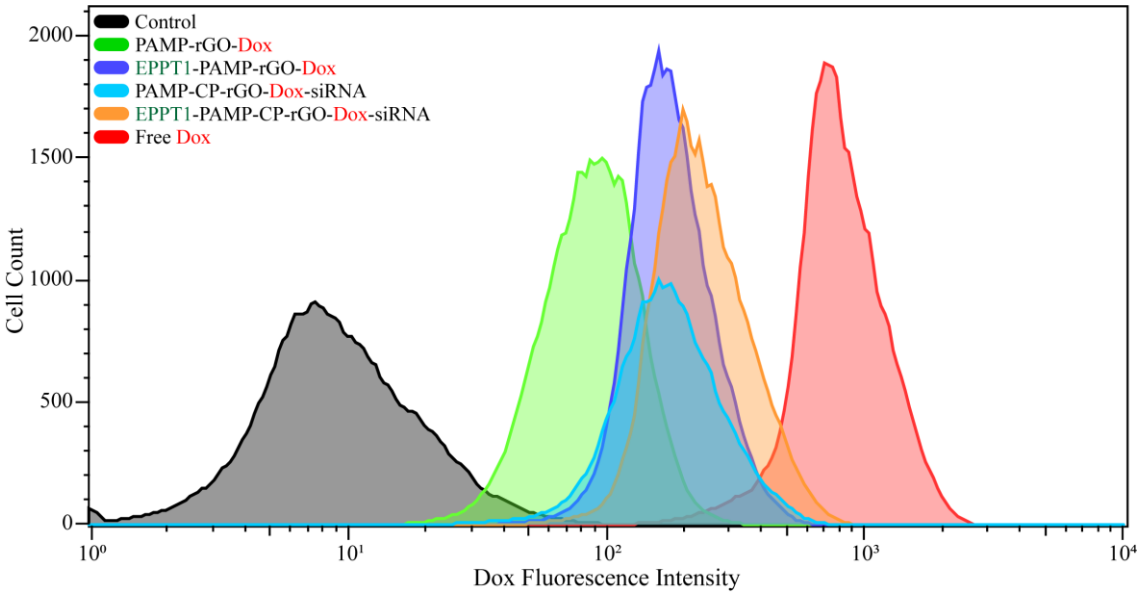


Figure 4.55: Flow cytometric Dox fluorescence measurements of MDA-MB-231 cells after treatment of 2 hours with free Dox and anti-Bcl-2-siRNA complexed nanoplatforms against non-treated cells.

Parallel results with the MDA-MB-231 cell line were observed when this method was applied by using the MCF-7 cell line. Plotted Dox fluorescence intensity against cell count as seen in **Figure 4.56**, similarly, untreated cells were used as the control, free Dox, PAMP-CP-rGO-Dox-siRNA, and EPPT1-PAMP-CP-rGO-Dox-siRNA were compared. Even though similar results with the MDA-MB-231 cells have been obtained where the highest cellular intake was achieved by free Dox and targeted nanoplatform, the gap between non-treated and targeted platforms was increased showing closer fluorescence intensity to free Dox treated cells. Change in intensity can refer to higher cellular internalization by MCF-7 cells as expected since MUC1 receptor expression was found to be higher than MDA-MB-231 cells [274].

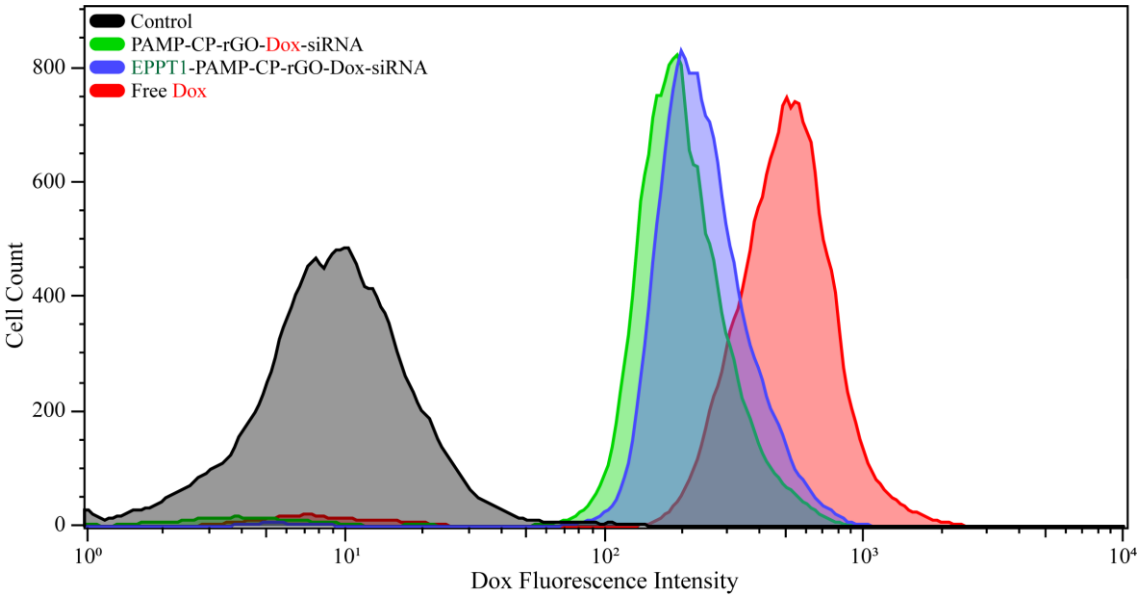


Figure 4.56: Flow cytometric Dox fluorescence measurements of MCF-7 cells after treatment of 2 hours with free Dox and anti-Bcl-2-siRNA complexed nanoplatforms against non-treated cells.

4.3.6. Detection of cell apoptosis induced by the combination of Dox and siRNA through APC-Annexin-V/Helix NP Blue double staining

As a common apoptosis detection method combination of Annexin-V and propidium iodide (PI) staining is a well-established method, early apoptotic cells can be detected by the presence of phosphatidylserine an anionic phospholipid on the surface which selectively binds Annexin-V in the presence of calcium cations [278], [279]. PI on the other hand has no permeation to healthy or early apoptotic cells and cannot stain the nucleus unless the cell undergoes late apoptosis or necrosis [280]. A series of flow cytometry experiments were conducted to investigate anti-Bcl-2-siRNA and Dox-loaded nanoplatforms' impact on the induction of cell apoptosis, during experiment design, excitation and emission wavelengths of the fluorophores should be selected correctly to prevent auto-fluorescence, falls positive or negative results. Due to the presence of chemotherapy agent Dox, APC conjugated Annexin-V (Biolegend, 640941) and PI alternative Helix NP Blue (Biolegend, 425305) were selected for these experiments [281]. Excitation and emission wavelengths that are adjusted to the lasers equipped on the FACS device can be seen in **Table 4.12**.

Table 4.12: List of excitation and emission wavelengths of the designed experiment.

	Excitation (nm)	Emission (nm)
Helix NP Blue	405	460
Doxorubicin	488	580
APC-Annexin-V	640	670

In general, 300,000 cells were seeded in 6 well plates, incubated overnight for attachment, and treated with chosen materials. PAMP-CP-rGO derivatives were chosen to be able to compare different properties, their complexes were prepared with anti-Bcl-2-siRNA and scrambled siRNA at 50 nM siRNA concentration by 1/45 complexation ratio and the equal amount of Dox was treated to one well as control (14.1 µg/mL, 24.2 µM) to determine the effect of free Dox. After 4 hours of incubation with materials, cells were washed with PBS twice and cultured for 48 hours in physiological conditions. Completion of incubation time was followed by removal of medium, wash with PBS, and cell harvest by Trypsin/EDTA solution. Trypsinized cells, medium, and wash PBS were collected into 15 mL falcon tubes with the intention to collect detached cells, centrifuged and washed with 1x binding buffer, and dispersed in the staining mixture. The staining mixture was prepared by the addition of 5 µL/test APC-Annexin-V and 0.5 µL/test Helix NP Blue into the 1x staining buffer. Cells were incubated for 15 minutes at room temperature in dark, centrifuged to remove the unbound dye, and dispersed in $CaCl_2$ and 2% FBS containing PBS. Cell dispersants were passed through cells strained into FACS tubes and placed on ice until analysis. Collected data were plotted by the fluorescence intensities of Helix NP Blue vs. APC-Annexin-V, obtained graphs were divided into 4 rectangular gates according to the untreated control group, the upper-left (Q1, APC-Annexin-V -, Helix NP Blue +) and lower-left (Q4, APC-Annexin-V -, Helix NP Blue -) quadrants in each panel indicate the populations of necrotic cells and normal cells, while the upper-right (Q2, APC-Annexin-V +, Helix NP Blue +) and lower-right (Q3, APC-Annexin-V +, Helix NP Blue -) quadrants in each panel indicate the populations of late and early apoptotic cells, respectively.

Free-siRNA, free-Dox, PAMP-CP-rGO-siRNA, EPPT1-PAMP-CP-rGO-siRNA, EPPT1-PAMP-CP-rGO-SCR/siRNA, PAMP-CP-rGO-Dox-siRNA, EPPT1-PAMP-CP-rGO-Dox-siRNA and EPPT1-PAMP-CP-rGO-Dox-SCR/siRNA were tested on MCF-7 (**Figure 4.57**) and MDA-MB-231 (**Figure 4.58**) cell lines. When comparing MCF-7 and MDA-MB-231 results, there was no noticeable difference between the control group and free siRNA-treated cells. Following the cell viability results, Dox-treated MCF-7 cells

were more sensitive to the drug and detected necrosis, and apoptosis levels were much higher. Although the cationic surface charge on the nanocarriers was balanced with the negative charge carrying nucleic acids, carrier-induced toxicity was observed at a low rate. PAMP-CP-rGO-siRNA, EPPT1-PAMP-CP-rGO-siRNA, and EPPT1-PAMP-CP-rGO-SCR/siRNA were the nanoplatforms that do not contain Dox on the structure, yet they have affected more than 10% of the MDA-MB-231 cell population to shift early apoptosis state (**Figure 4.58**) where the presence of EPPT1 on the platforms this shift decreased by 1%-2% overall. The introduction of Dox onto these compositions triples the early apoptosis population and reaches 35.1% on the same cell line, the necrotic cell population decreases slightly and a similar reduction was observed with EPPT1 present platforms (33.6%).

When compared with MCF-7 cells a similar trend can be seen, Dox loaded platforms increase the rate of early apoptotic cells by 7%-8% while the necrotic cell population decreases slightly. The distinct difference between anti-Bcl-2-siRNA and scrambled-siRNA loaded particles can be easily detected by comparison of Dox loaded or Dox-free platforms, while keeping the early apoptotic cell population almost at the same rate as normal cells increase in population by 7% to 10%. By the comparison of the final composition EPPT1-PAMP-CP-rGO-Dox-siRNA and scrambled siRNA version on MCF-7 data early apoptotic cell rates were very close to each other, 12.9% and 12.4% respectively, necrotic cell population decreased from 4.85% to 0.71% when scrambled siRNA platform was used. Even though this change was not detected on MDA-MB-231 cells these findings overlap with the cell viability results proving MCF-7 cells to be affected at a higher rate by nanoplatforms than triple-negative MDA-MB-231 cells.

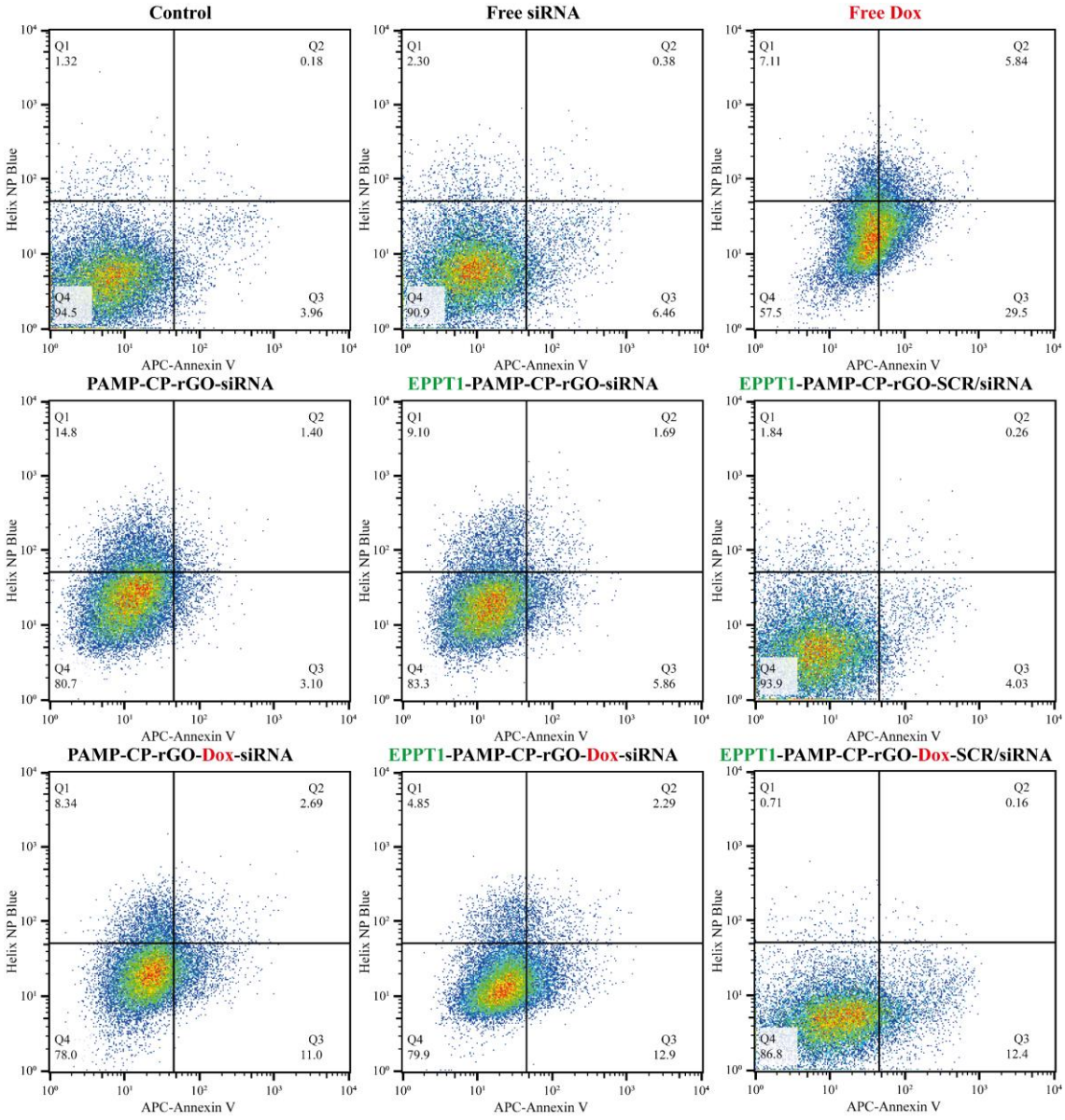


Figure 4.57: Normal, early apoptotic, late apoptotic, and necrotic cell populations of MCF-7 determined by flow cytometry analysis after incubating 4 hours with nanoplatforms and 48 hours with fresh medium.

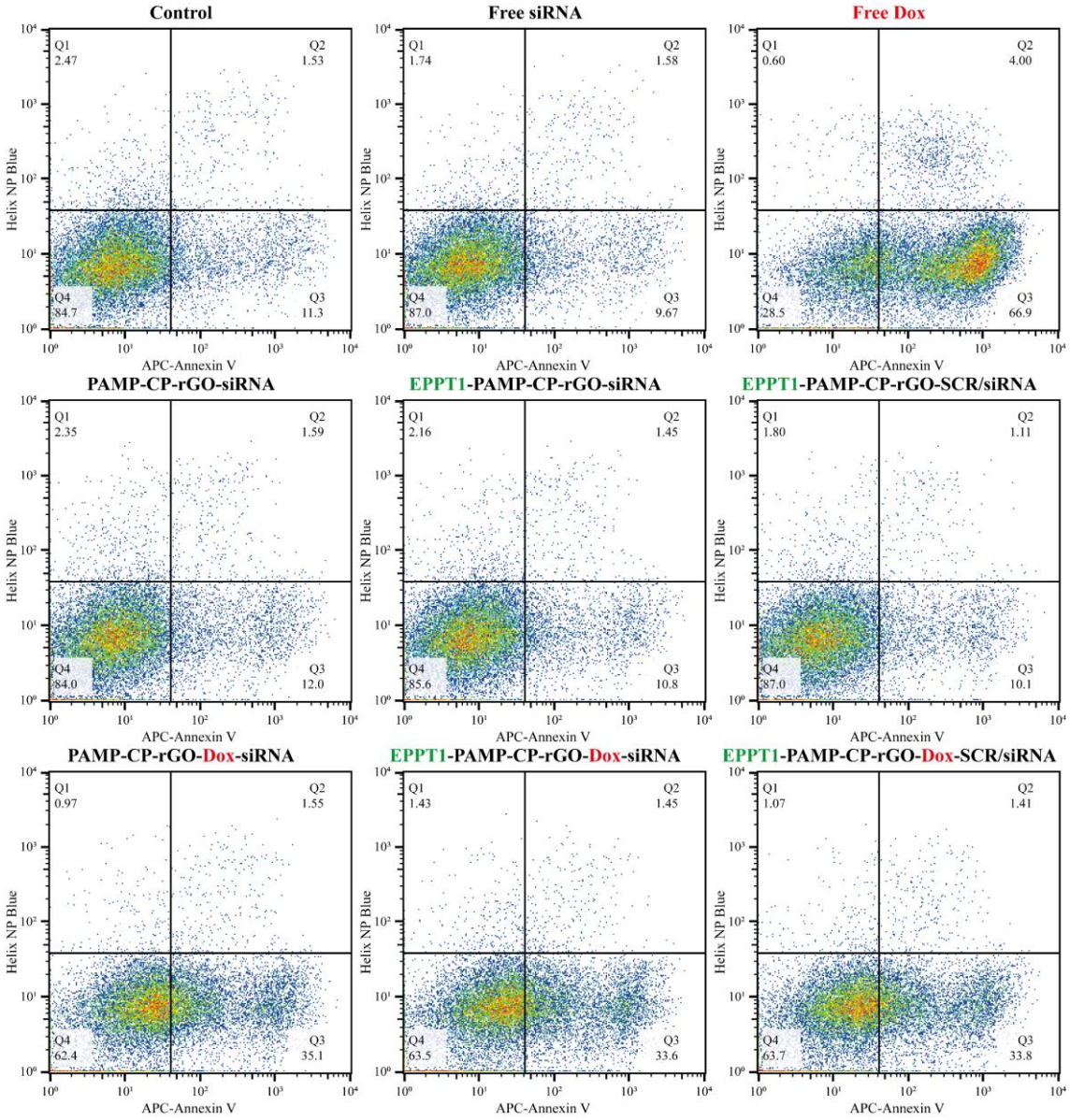


Figure 4.58: Normal, early apoptotic, late apoptotic, and necrotic cell populations of MDA-MB-231 determined by flow cytometry analysis after incubating 4 hours with nanoplatforms and 48 hours with fresh medium.

The short incubation time with nanoplatforms was increased from 4 hours to 24 hours to determine the change in apoptotic cell populations. After 24 hours, a medium containing nanoplatforms was removed from the wells and MDA-MB-231 cells were prepared for the analysis as discussed before. In this trial, two different concentrations of selected materials were applied to the cells and the results were compared. 2.5 µg/mL (corresponding siRNA concentration at 1/45 w/w: 8.9 nM) and 14.1 µg/mL (corresponding siRNA concentration at 1/45 w/w: 50 nM) Dox concentrations were studied. Results can be seen in **Figure 4.59**, on the middle queue 50 nM siRNA and 14.1 µg/mL Dox treated cells, on the bottom queue 8.9 nM and 2.5 µg/mL Dox treated cells

can be seen against the untreated control on the top. Extension of incubation time results in a higher number of early apoptotic cells which were treated with free Dox. Concentration-dependent behavior of Dox can be seen between two free Dox dosages, decrease from 14.1 µg/mL to 2.5 µg/mL reduces early apoptotic cells from 43.3% to 6.84%. Even though this reduction in cell population was distinctly observed for free Dox-treated cells, changes in nanoplatform derivatives treated cells have been found to be at similar levels. Scrambled siRNA complexed EPPT1-PAMP-CP-rGO-Dox was found to induce 6.90% early apoptosis and when switched to anti-Bcl-2-siRNA early apoptotic cell population was found to increase by 8.46% at 50 nM siRNA concentration, a similar change has been observed for lower concentration to be increasing from 6.93% to 8.57% since the only difference between these two platforms was loaded siRNA, this decrease was related with the absence of anti-Bcl-2-siRNA. While necrosis rates were observed at low levels for the anti-Bcl-2-siRNA conjugated nanoplatforms at 50 nM siRNA concentration, these levels were found to be slightly increased for EPPT1-PAMP-CP-rGO-Dox at a lower concentration.

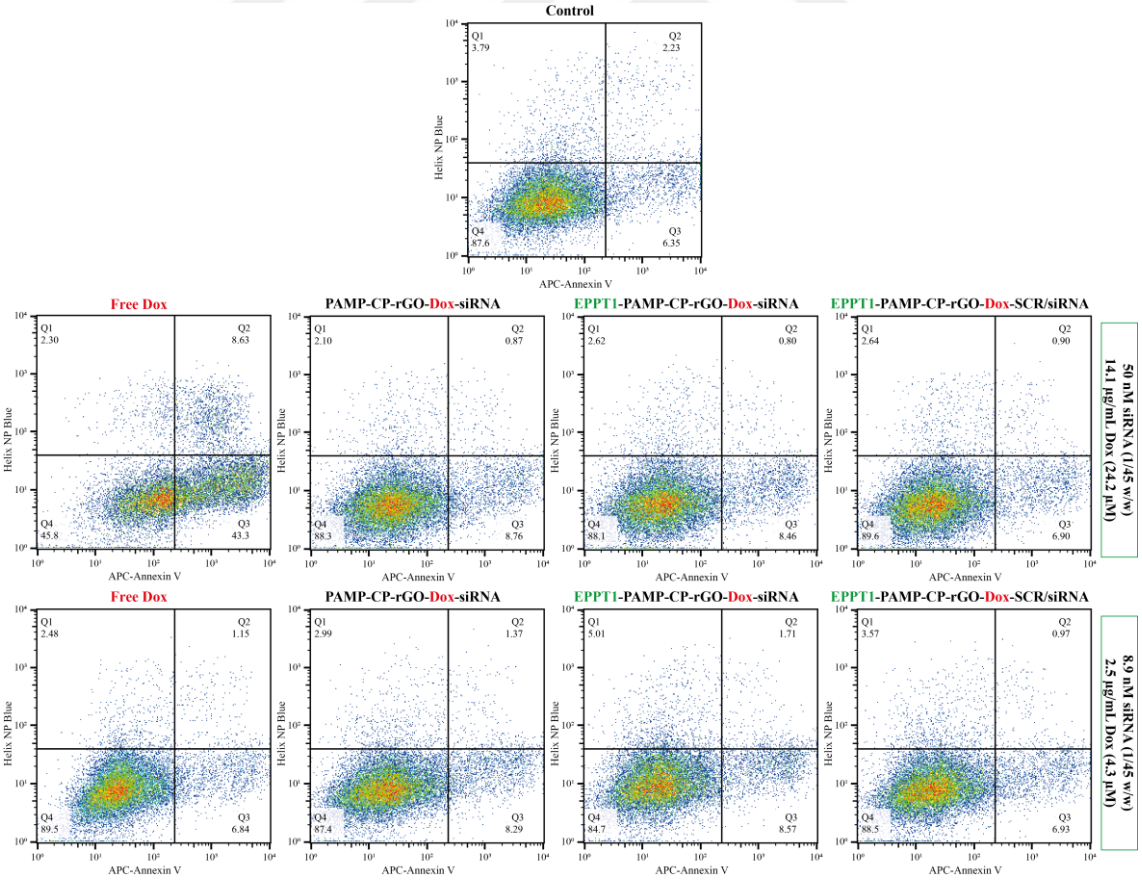


Figure 4.59: Normal, early apoptotic, late apoptotic, and necrotic cell populations of MDA-MB-231 determined by flow cytometry analysis after 24 hours of incubation with nanoplatforms.

4.3.7. Comparative transfection efficiency of anti-GAPDH and anti-Bcl-2 siRNA carrying nanoplatforms

4.3.7.1. Effect of anti-GAPDH-siRNA carrying nanoplatforms on GPADH protein expression levels

GAPDH is recognized as a glycolytic enzyme in the cytoplasm and was recently found to be involved in several subcellular functions [282], due to its high expression in different cells and tissues GAPDH protein is routinely employed as the housekeeping protein [283]. In parallel to this approach transfection efficiency of nanocarriers was tested against the GAPDH protein by using KDalert™ assay kit following 48 hours of incubation with anti-GAPDH siRNA loaded particles, compared to commercially available Lipofectamine and scrambled siRNA loaded particles (**Figure 4.60**). Cells treated with EPPT1-PAMP-CP-rGO-Dox-siRNA complexes showed the highest reduction in protein expression by 43.49% whereas non-targeted PAMP-CP-rGO-Dox-siRNA only reduces the expression to 76.82%. In comparison to commercially available gene delivery agent Lipofectamine, targeted EPPT1-PAMP-CP-rGO and EPPT1-PAMP-CP-rGO-Dox shows comparable knockdown efficiencies. In spite of equal protein content used for the assay to eliminate the toxic effect of Dox carrying positively charged nanoplatforms that were prepared by scrambled siRNA loading decreased the GAPDH protein expression by ~20% and ~30%, this decrease in protein levels was observed upon treatment is indicative of their effects on cell viability [284]–[286]. The efficacy of the particles formed by combining therapeutic nucleic acids with PAMP-CP-rGO derivatives as gene and drug carriers was further supported by these results.

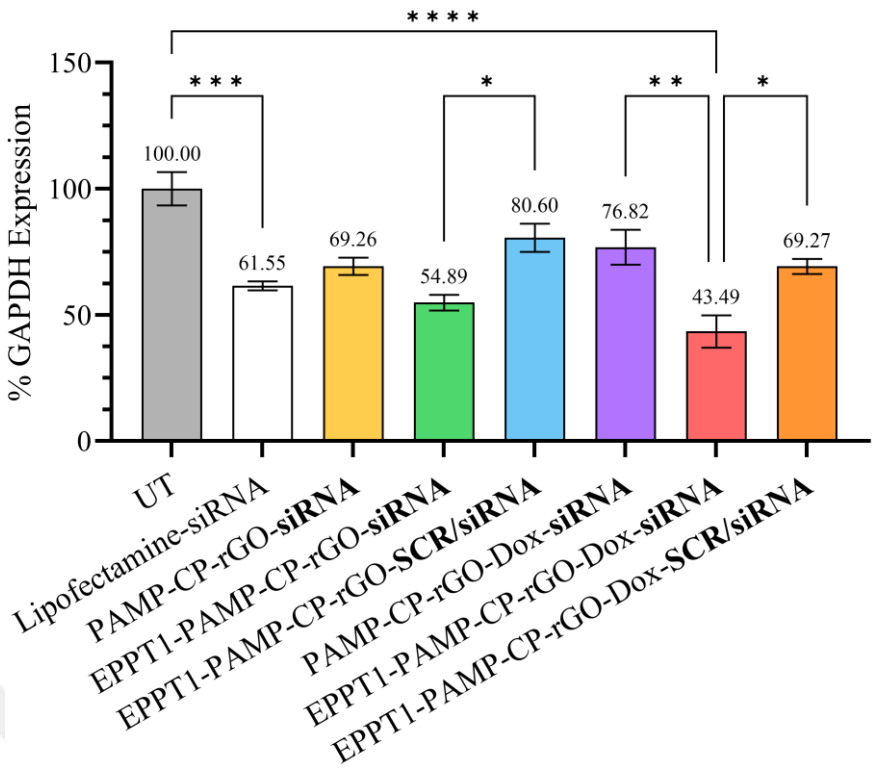


Figure 4.60: The effect of anti-GAPDH siRNA and scrambled siRNA loaded nanoplatforms on GAPDH protein expression levels, after 2 hours of incubation with nanoplatforms and 48 hours in fresh medium relative to the untreated cells. (*p≤0.05, **p≤0.01, ***p≤0.001 and ****p≤0.0001)

4.3.7.2. Determination of change in Bcl-2 gene expression levels by the real-time polymerase chain reaction

The downregulation of the Bcl-2 gene on MDA-MB-231 and MCF-7 cells were determined by utilizing real-time quantitative polymerase chain reaction (qPCR) after treating cells with 50 nM anti-Bcl-2-siRNA complexed nanoplatforms. A general study was started by plating 500,000 MDA-MB-231 or MCF-7 cells into 6 well plates, and treatment for 4 hours with anti-Bcl-2-siRNA or scrambled siRNA carrying. Then cells were washed twice with PBS to remove free nanocarriers and incubated under physiological conditions for 48 or 72 hours to achieve effective and detectable transfection rates. Following post-incubation cells were lysed, homogenized by QIAshredders, and total RNA was isolated from cell lysates by using an RNA purification kit, concentrates were characterized by NanoDrop™ and stored at -80 °C.

Obtained total RNA was converted to cDNA by using the Omniscript Reverse Transcriptase Kit (QIAGEN) according to manufacturer protocol. Briefly, a 500 ng RNA sample was transferred to 0.2 mL microtubes, dNTP, random hexamers, and RNase inhibitor was mixed in a total volume of 20 µL and incubated at 37 °C for one-hour and

synthesized cDNAs were stored in -20 °C until further use. cDNAs that were prepared from total RNA concentrates were subjected to qPCR analysis to determine to mean fold change in Bcl-2 gene expression levels by using human Bcl-2 FAM labeled MGB gene expression assay probe relative to endogenous control human eukaryotic 18S rRNA probe. Equal amounts of cDNA samples were transferred to 0.2 mL microtubes in triplicates, TaqMan Universal PCR Master Mix and relevant probe added to the tube to a final volume of 20 µL, qPCR reactions were monitored by Bio-Rad CFX Connect Real-Time PCR Detection System. The device was set to run for 40 thermal cycles as specified in the procedure part, Ct data were collected and used to determine the mean fold change in gene expression levels by the $2^{-\Delta\Delta Ct}$ method by normalizing against untreated cells.

Average Bcl-2 mRNA gene expression results obtained from the MDA-MB-231 cell line can be seen in **Figure 4.61** and **Figure 4.62**, at two-time points of 48 and 72 hours. As expected, the targeted siRNA carrying nanoplatform EPPT1-PAMP-CP-rGO-siRNA showed much higher efficacy in reducing gene expression at both incubation times than the non-targeted version PAMP-CP-rGO-siRNA. The addition of Doxorubicin to the platform yielded similar results, after 48 hours of incubation final version of the nanoplatform that is targeted, Dox and siRNA loaded EPPT1-PAMP-CP-rGO-Dox-siRNA yielded similar results with non-targeted version but at 72-hour time point the lowest gene expression was achieved by the targeted final version among derivatives. The therapeutic effect resulting from EPPT1 peptide selectivity was clearly seen in gene-only systems that do not contain Dox. While EPPT1-PAMP-CP-rGO-siRNA decreased the mRNA expression level by 69% in 48 hours, this value increased to 83% in 72 hours. When the scrambled siRNA complexes of Dox-free nanocarriers were examined, no significant reduction was observed (up to 9%) as expected. The effect of EPPT1-PAMP-CP-rGO-Dox-SCR/siRNA on gene expression was seen in the 72-hour graph given in **Figure 4.61b**, it can be explained by the negative effect of Dox in this structure on the collected RNA samples lowering viability and consecutively lowering quality and concentration of collected total RNA extract from lysed cells.

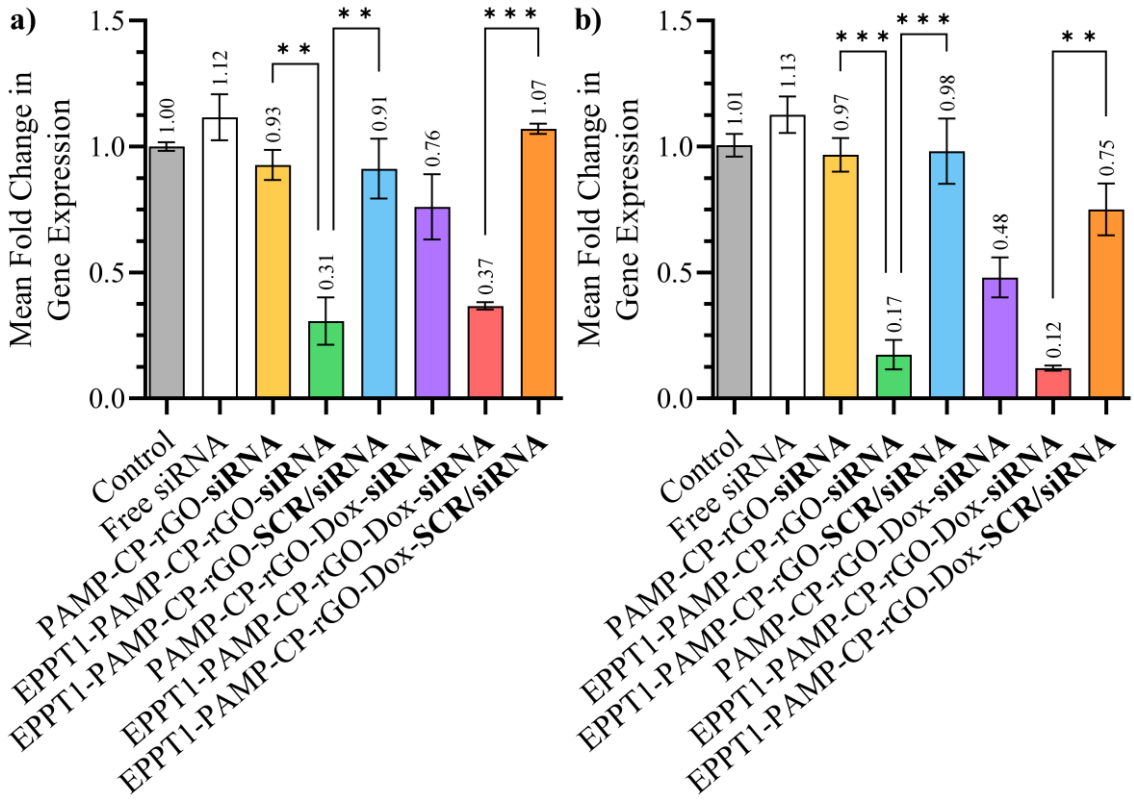


Figure 4.61: Detected mean fold change in Bcl-2 mRNA expression levels of MDA-MB-231 cells after incubating 4 hours with nanoplatforms and **a)** 48 and **b)** 72 hours post-incubation in fresh medium. (*p≤0.05, **p≤0.01 and ***p≤0.001)

The same approach was followed for the MCF-7 cell line to obtain different responses by different cancer cell types, a similar activity that was obtained for MBD-MB-231 cells was observed at a slightly lower level of decrease as seen in **Figure 4.62**. Changing from anti-Bcl-2-siRNA to scrambled siRNA acted similarly but the overall decrease was found to be at a lower level which can be reasoned by the structural differences between the two cancer cell lines. While the MCF-7 cell line does not follow an invasive profile and needs estrogen and EGF, the triple negative, non-hormone dependent MDA-MB-231 cell line is more aggressive and invasive [287]. Therefore, the responses they give to the applied nanoplatforms may reveal different results from each other. When the graphs are examined, increasing the incubation time in the study with MCF-7 cell line, did not have a great effect on the decrease of Bcl-2 mRNA expression as in the study with MDA-MB-231.

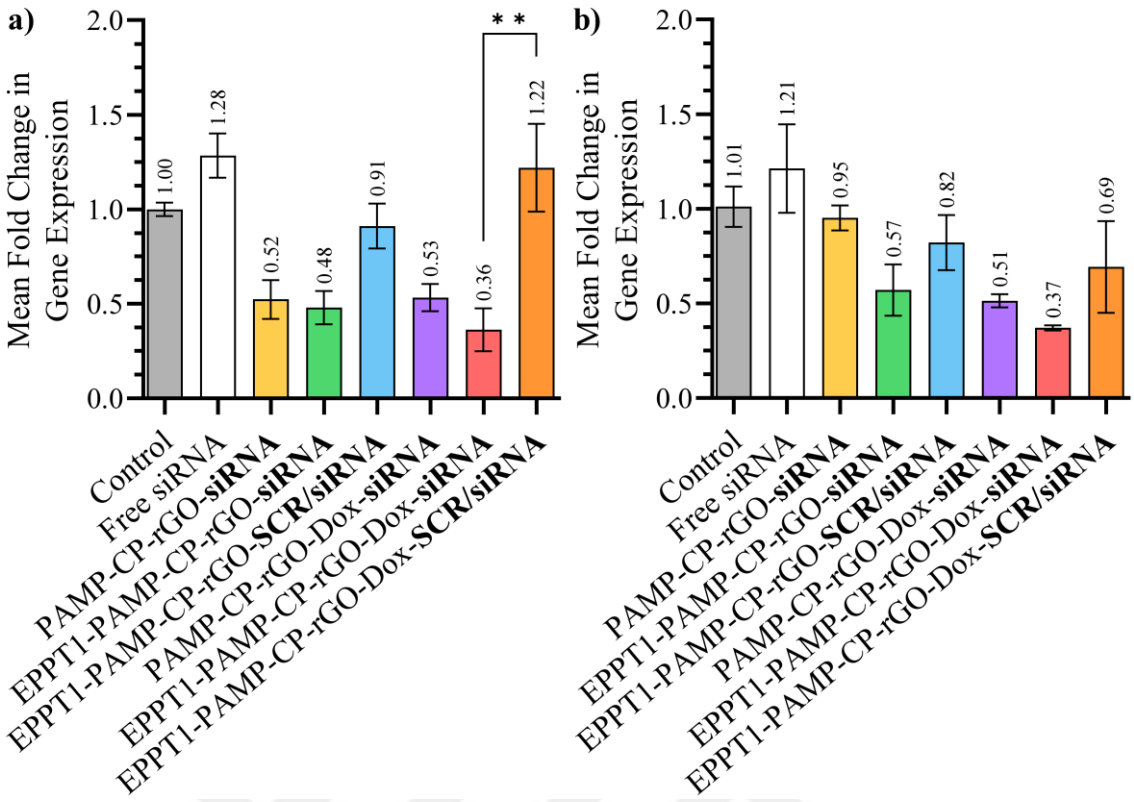


Figure 4.62: Detected mean fold change in Bcl-2 mRNA expression levels of MCF-7 cells after incubating 4 hours with nanoplatforms and **a)** 48 and **b)** 72 hours post-incubation in fresh medium. (**p≤0.01)

4.3.7.3. SDS-Page and Western-Blot Analysis for determination of Bcl-2 protein expression

The reason anti-GAPDH-siRNA was selected as the model gene, GAPDH protein levels can be practically analyzed by using a commercially available KDalert™ assay kit, however, the determination of the change in the Bcl-2 protein levels caused by anti-Bcl-2-siRNA needed Western Blot analysis. 400,000 MDA-MB-231 and MCF-7 cells were plated in duplicates in 6-well plates for each nanoplatform composition and incubated overnight for attachment and they were treated with chosen materials that complexed with either anti-Bcl-2-siRNA or scrambled siRNA at a concentration of 50 nM for 4 hours and incubated for 48 hours in the fresh medium after removal of material dispersant and wash with PBS. Once incubation time was completed cells were washed PBS and trypsinized, and duplicate wells were combined and lysed with 60 µL of RIPA buffer containing PMSF solution, sodium orthovanadate solution, and protease inhibitor cocktail. Cell lysates were quantified with a Bradford protein assay for calculating total protein concentration.

An equal amount of total protein-containing samples were topped with water and β-mercaptoethanol containing 4x Laemmli buffer. Each tube was heated to 95 °C for 5 minutes, cooled to room temperature, and loaded to 10% acrylamide gel, by applying 60 V of potential difference electrophoresed in 1x TGS buffer. Separated proteins were transferred to a 0.2 µm PVDF membrane by a semi-dry BioRad Trans-Blot Turbo Transfer System followed by blocking in 5% non-fat milk in TBST buffer for 1 hour at room temperature. Blocking was followed by overnight incubation at 4 °C with 1° antibody (β-actin: SANTA CRUZ sc-47778, Bcl-2: SANTA CRUZ sc-7382) with mild racking in separate containers. The following day membranes were washed several times in TBST buffer and incubated with 2° antibody (β-actin and Bcl-2: SANTA CRUZ sc-516102). The blots were exposed by Clarity™ Western ECL Substrate and images were taken with the ChemiDoc XRS+ system.

It was previously reported that Bcl-2 protein expression decreases after Dox treatment [288]–[290], free-Dox was included in test samples to assess its effect on Bcl-2 protein expression. Results from 2 cell lines were overlayed in **Figure 4.63**, where top bands belong to MCF-7 and bottom bands to the MDA-MB-231 cell line. By using a pre-stained protein ladder molecular weight of β-actin and Bcl-2 bands were calculated and listed in **Table 4.13**, molecular weights for both of the bands were calculated very close to the values reported in the literature showing proper separation of the bands [291], [292]. The overall profile shows that the MDA-MB-231 cell line was more susceptible to anti-Bcl-2-siRNA, and the effect of free Dox on Bcl-2 protein levels has been more evident in this cell line in parallel to the results obtained from the qPCR studies. The effectiveness of the targeting agent EPPT1 can be observed with the reduction of Bcl-2 bands in comparison to PAMP-CP-rGO-siRNA and EPPT1-PAMP-CP-rGO-siRNA. When looking at the effect of Dox-loaded targeted composition on MDA-MB-231 cell line protein levels, the targeted composition almost completely erased the Bcl-2 band, while the significant volume of the non-targeted composition's band was evidently visible. Anti-Bcl-2-siRNA loaded particles caused the reduction as expected in the Bcl-2 protein bands, while scrambled siRNA (SCR/siRNA) loaded compositions did not have this effect. The decrease in the Bcl-2 band intensity in the free Dox applied cells can be associated with the Dox presence as shown in the literature [275], [289], [293], where a decrease in the Bcl-2 band caused by EPPT1-PAMP-CP-rGO-Dox-SCR/siRNA can be associated with the presence of Dox on the structure.

Table 4.13: Calculated and standard molecular weight of β-actin and Bcl-2 proteins.

	Calculated Mw, kDa	Standard Mw, kDa
β-Actin	39.51	42
Bcl-2	26.02	26

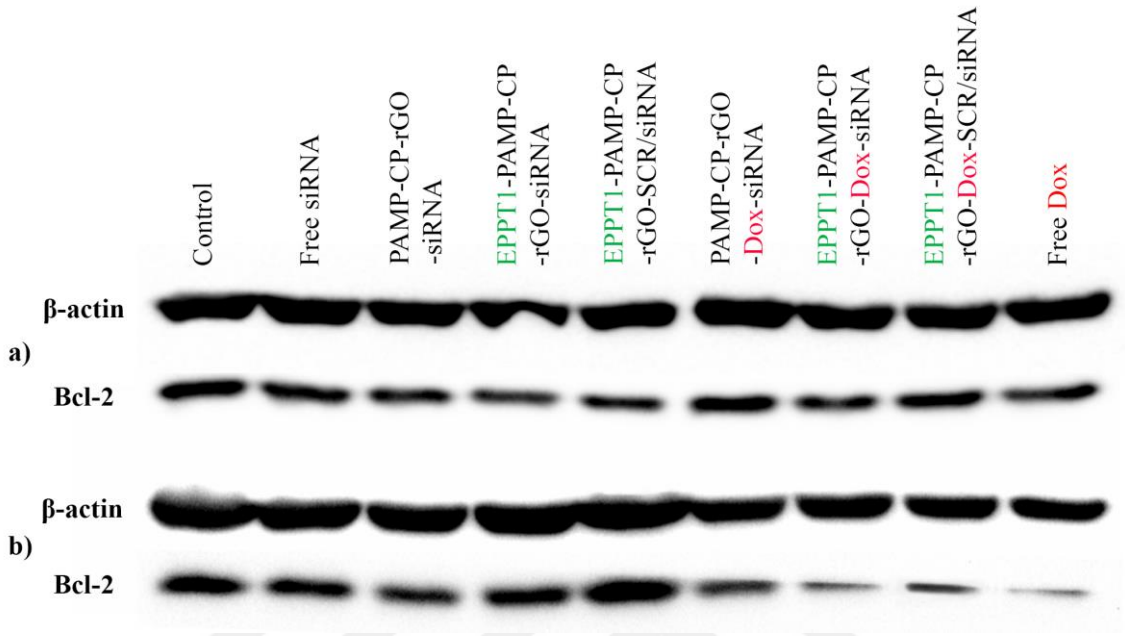


Figure 4.63: Western blot analysis of β-Actin and Bcl-2 expressions detected from **a)** MCF-7 and **b)** MDA-MB-231 cell lysates after treatment with free siRNA, free Dox, and nanoplatforms, following 4 hours with materials and 48 hours of incubation in fresh medium against untreated control cells.

When the graphs generated as a result of this approach (**Figure 4.64**) are examined, the points identified by visually compared bands are more noticeable. The decrease caused by free Dox in Bcl-2 protein band intensity, the difference between anti-Bcl-2-siRNA and SCR-siRNA, and the effectiveness of the targeting agent were observed in the MCF-7 graph (**Figure 4.64a**), but more noticeable in the MDA-MB-231 graph (**Figure 4.64b**). In **Figure 4.64b** PAMP-CP-rGO-DOX-siRNA, which does not carry a targeting agent, has been able to decrease the Bcl-2 expression to only 87.3%, this value has dropped sharply to 36.9% with the addition of EPPT1 to the system. From the comparison of EPPT1-PAMP-CP-rGO-DOX-siRNA and SCR/siRNA complexed versions, it is possible to see the effect of siRNA with an almost 10% difference in Bcl-2 expression. Collective results from both of the cell lines show clear evidence of the effectiveness of the nanocarriers against Bcl-2 protein expression.

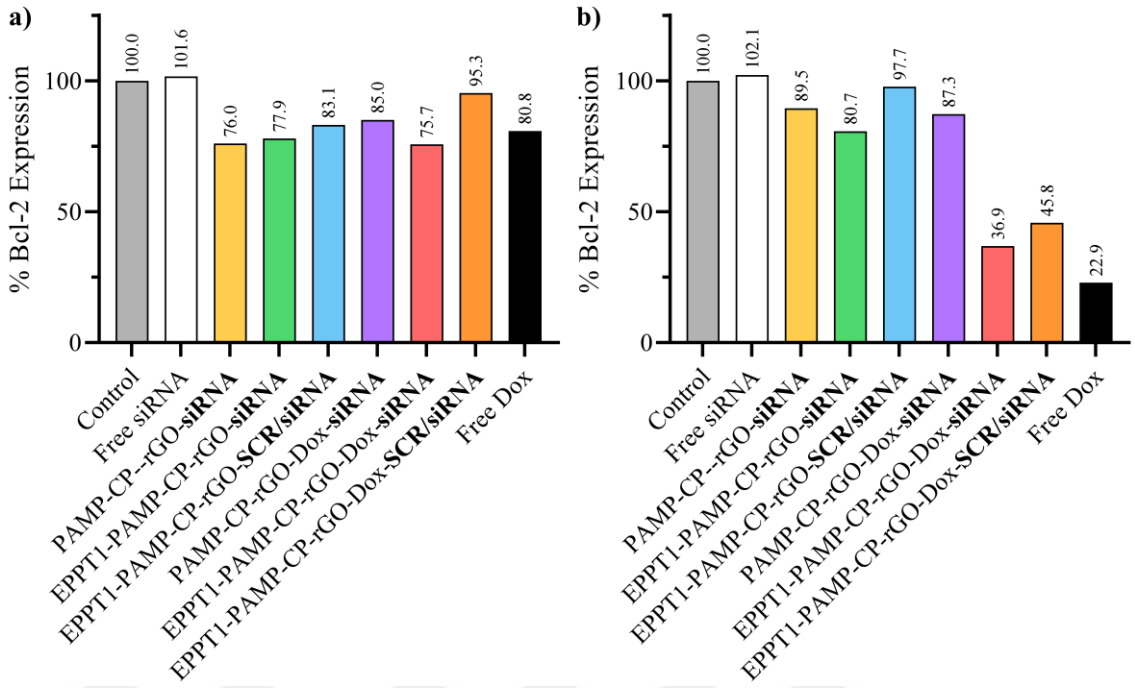


Figure 4.64: Percent Bcl-2 expression normalized against the housekeeping protein and untreated control **a)** MCF-7 and **b)** MDA-MB-23 cell lines.

4.4. *In vivo* Studies

6-8 weeks old athymic nude mice weighing around 20-25 grams were obtained from MEDITAM and 2.5 million triple negative MDA-MB-231 cancer cells in 100 µL DMEM and Matrigel mixture (1:1 by volume) were injected subcutaneously into the right flank of isoflurane-anesthetized mice. Ensuring animal welfare, mice were ear tagged for easy identification and monitored every three days following the aseptic technique. Once a palpable tumor was identified, tumor size was measured by using a caliper, and tumor size was calculated by equation **3.12** using two perpendicular diameters and recorded with body weight. Tumor sizes reached 50-100 mm^3 in 3-5 weeks post-inoculum and mice were divided into 6 (n=4) groups for examination of antitumor effect of nanoplatforms respectively.

4.4.1. Anticancer activity of nanoplatforms

The therapeutic efficacy of Dox-loaded nanoplatforms was validated using triple negative MDA-MB-231 tumor-bearing athymic nude mice. PBS, Dox, EPPT1-PAMP-rGO-DOX, EPPT1-PAMP-CP-rGO-siRNA, PAMP-CP-rGO-DOX-siRNA, and EPPT1-PAMP-CP-rGO-DOX-siRNA were injected through the tail vein on day 0, 3 and 6 at 5 mg/kg Dox concentration and tumor size and body weight were measured every 3 days for 21 days

(**Figure 4.66**). Since the initial tumor volume had small variations between mice in each group, instead of reporting tumor volume in mm^3, as a common approach tumor volume was normalized using equation **3.13** (**Figure 4.65**). The tumor volume of PBS-treated mice grows around 10.5-fold of its initial size while Dox treatment decelerates tumor growth and in the end, the tumor grows 2.4 times in volume. EPPT1-PAMP-CP-rGO-siRNA and non-siRNA carrying EPPT1-PAMP-rGO-Dox were found to show an inconspicuous effect on tumor growth by growing rates of 6.4- and 5.4-fold respectively. On the other hand, PAMP-CP-rGO-DOX-siRNA and EPPT1-PAMP-CP-rGO-DOX-siRNA showed parallel suppressions on tumor progress with Dox and at the end of 21 days, 4.6- and 3.6-fold increase in tumor volume was detected respectively, while the difference in the final volume for targeted and non-targeted nanoplatforms can be credited to the presence of targeting agent EPPT1 on the structure. In comparison to control group Dox, PAMP-CP-rGO-DOX-siRNA and EPPT1-PAMP-CP-rGO-DOX-siRNA were found to decelerate tumor progress significantly ($p<0.05$) with no substantial loss in body weight (>15%) was not detected.

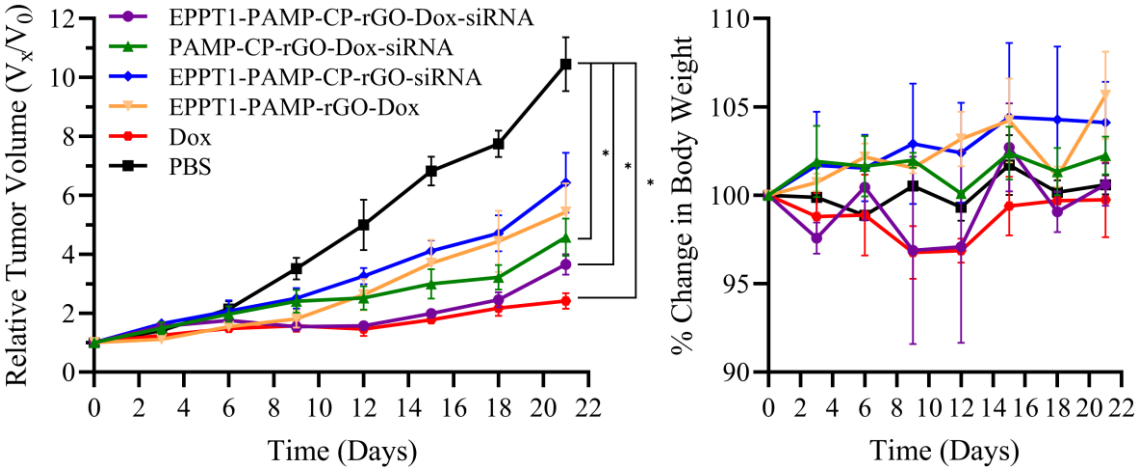


Figure 4.65: a) Relative tumor volume **b)** body weight changes in the subcutaneous MDA-MB-231 tumor-bearing mice over 21 days after 3 drug injections on days 0, 3, and 6 (n=4, *$p<0.05$).

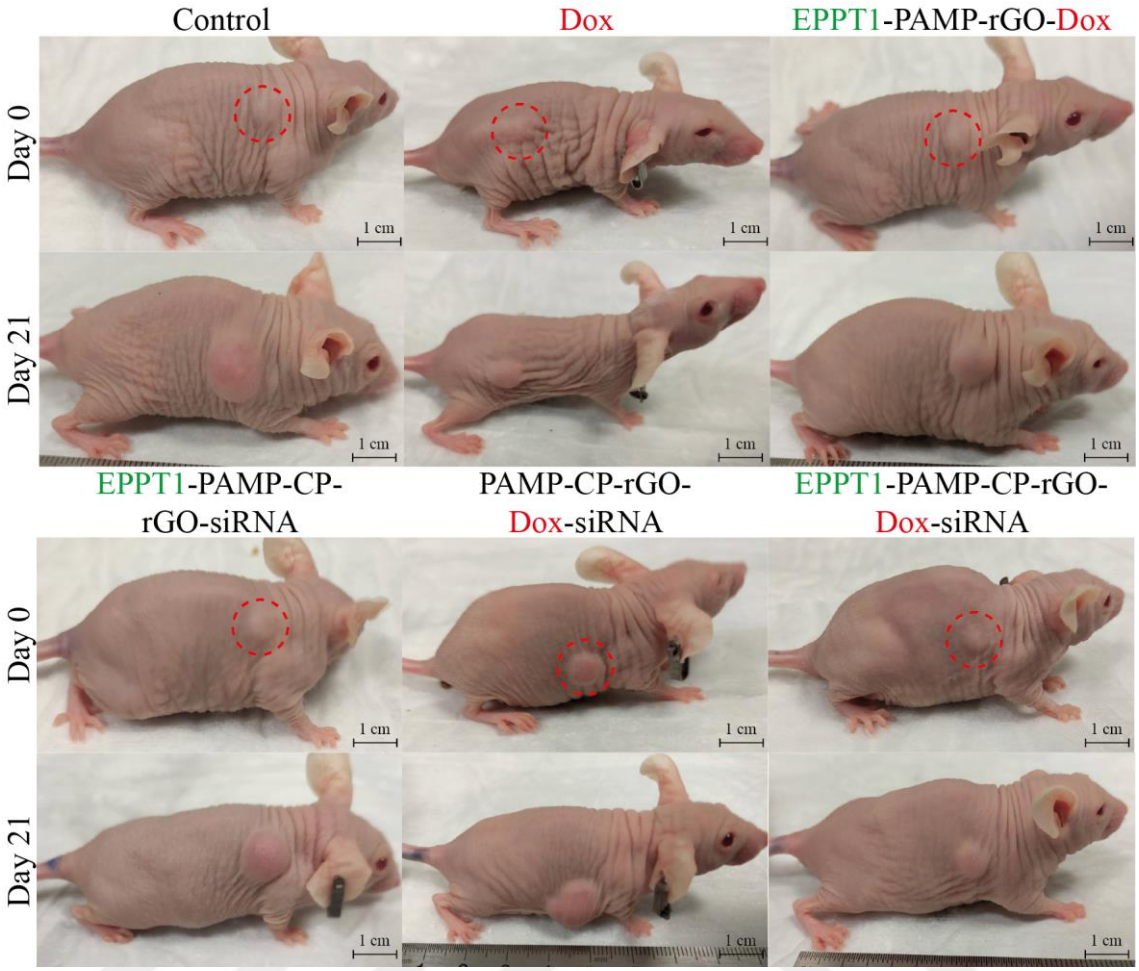


Figure 4.66: Images of tumor-bearing mice before and after treatment.

4.5. Final Evaluation of Nanoplatforms, Promise, and Achievements

Conventional medicine utilizes several chemotherapeutics as a tool in the treatment of cancer, but their use results in many side effects, damage to different parts of the body, and causes the treatment process to become inefficient. The idea of delivering not only anti-cancer drugs but also complementary therapeutic agents like gene therapy agents to the targeted tissue or tumor more efficiently has been studied for a long time, and nanocarriers are prominent in this field [35]. Various nanocarrier systems in the literature have low stability and low drug loading capacity, while there are very few successful nanocarriers that combine features such as the controlled release of the loaded drug, the delivery of the transported genetic material to the cytoplasm or nucleus, and the selective targeting of cancer cells along this pathway [32], [33]. In order to overcome these problems listed here, the nanoplatform developed within the scope of this doctoral study was built on reduced graphene oxide. For this purpose, the study was divided into two

stages, in the first stage an ideal PEGylation method was developed to increase the biocompatibility of graphene derivatives and improve their stability in the water environment, and then in the second stage, using this approach a targeted drug delivery platform carrying chemotherapy agent and oligonucleotide has been developed and its biological applications have been tested *in vitro* and *in vivo*.

Despite the superior properties of GO and rGO, their use in biological applications is limited mainly because of induced cytotoxicity and instability in the water environment. This is commonly prevented by coating the surface with natural or synthetic biocompatible polymers, and a similar but innovative approach has followed in this study, copolymers that were made of a different number of pyrene and PEG units were prepared and the GO surface was coated with these copolymers with simultaneous reduction. Easily synthesized P(PEGMA-*co*-MMA-*co*-PMA) copolymers that were made of PEGMA (500 or 2000 Da), PMA, and MMA, mainly characterized by ^{1}H NMR spectroscopy (**Figure 4.2** and **Table 4.2**), were used multiple pyrene units as anchors to bind rGO surface via π-π stacking (**Figure 4.4**) with the highest coating efficiency was reached to 71.2%. Although the resultant product was based on highly hydrophobic rGO, copolymer presence yielded stable dispersants in aqueous solutions and many organic solvents (**Figure 4.17**). Physicochemical properties of PMP-rGO were examined by multiple methods to better understand the structure, from the FTIR spectrum of PMP_{500}-rGO1 broad -OH stretching around 3200 cm^{-1} disappears indicating reduction from GO to rGO while -C=O stretching appears on the same wavenumber units as the copolymer showing copolymer presence on the surface (**Figure 4.7**). One of the important tests run to understand chemical bonding and intramolecular bonds in Raman spectroscopy analysis, from the ratio of D and G band intensities it is possible to compare the change of electronic configuration of carbon lattice (**Figure 4.8**). While reduction reduced the I_D/I_G ratio compared to GO, PMP coating resulted in an increase that can be attributed to new functional groups carried on copolymer [238], [239]. TGA analysis revealed characteristic thermal degradation profiles for GO, rGO, PMP, and PMP-rGO derivatives, reducing the well-improved thermal stability of rGO while PMP quickly degraded at 360 °C onset temperature (**Figure 4.9**). By taking advantage of these distinctive degradation profiles copolymers' weight percentage on rGO was calculated and accepted as coating efficiency. The importance of the pyrene presence on copolymer for PEGylation was tested by using the absence of pyrene and a single pyrene unit bearing copolymers and

their coating efficiencies were found to be 31.9% and 42.3% showing the importance of multiple pyrene units. On the other hand, this surfaced starting material for PEGylation, in one trial GO was not reduced during PEGylation, the rate reached 20.0% and in another rGO used as starting material coating efficiency only reached 32.6% indicating the importance of well dispersed starting material that followed by reduction (**Figure 4.11** and **Table 4.3**). In parallel to these findings XPS spectroscopy results further supported efficient reduction and PEGylation, aside from the comparison of carbon and oxygen bonding examination, survey scans revealed a decrease in oxygen content of rGO and an increase following PEGylation (**Figure 4.12** and **Table 4.4**) [245], [246]. Examination of AFM images obtained by drop casting well-dispersed samples showed an increase in layer thickness after reduction of GO to rGO from 1 nm to 40 nm respectively, unlike plain rGO, PEGylated rGO samples had a layer thickness between 5 to 8 nm as seen in **Figure 4.13**. The size of PMP-rGO derivatives was studied by DLS (**Figure 4.14**) and TEM (**Figure 4.15**) scans, even though smaller size values were measured for PMP-rGO derivatives in the range of 250-340 nm, TEM images revealed lateral size to be 736 ±79 nm, and 639 ±56 nm for PMP_{2000}-rGO5 and PMP_{500}-rGO3. In addition, single or few-layered sheets were observed for PMP-rGO derivatives where PMP_{2000}-rGO5 having a higher PEGylation rate than PMP_{500}-rGO3 revealed less stacking supporting the positive effect of higher PEG content on stability.

Copolymer synthesis and optimization of PEGylation were followed by *in vitro* testing of PMP-rGO, from examination of their hemolytic activity (**Figure 4.16**) tested copolymers did not cause any notable activity while GO disrupted around 70% of the RBCs at 200 µg/mL, PEGylation and reduction highly improved this behavior and hemolysis rate stayed below 25% for all compositions. This can be noted as an important achievement if it is considered that the cell membrane and graphene interaction cause disruption and is accepted as one of the main cytotoxicity mechanisms of graphene-based material. The obtained improved hemolytic activity indirectly supported the improvement of elimination of the side effect of membrane interaction. The cellular uptake rate of PMP-rGO3 and PMP-rGO5 was examined on MRC-5 cells by confocal microscopy images that were recorded after 2, 6, and 24 hours of incubation with nanomaterials, and it was found that the PEG_{2000} version significantly internalized higher than PEG_{500} version by time (**Figure 4.20**) indicating the contribution of improving solubility and aqueous dispersibility of the system. Cytotoxicity of PMP-rGO derivatives was tested by using

healthy kidney (HEK-293T) and lung (MRC-5) cell lines with MTS (**Figure 4.18**), LDH (**Figure 4.19**), and ROS (**Figure 4.21**) assays basically their high uptake of graphene derivatives [99], [186]. From the cumulative results of these 3 assays, the effect of plain GO on cytotoxicity has been significantly improved by PMP conjugation and reduction. PMP-rGO derivatives demonstrated high cell viability rates even at the highest concentrations and induce negligible LDH release and ROS generation. Taking into account the copolymer composition for comparison of PMP-rGO derivatives, the presence of multiple pyrene units increased coating efficiency, and a PEG content of 80% was found to be the most stable in the water environment and showed the highest biocompatibility regardless of PEG brush length rivaling many studies in the literature [294], these findings were published in the European Polymer Journal [210].

Continuum of the project followed by the inspiration from the first stage generating highly biocompatible PMP-rGO derivatives, a targeted nanoplatform that can carry genetic material and hydrophobic drugs construction started with the synthesis of the building blocks needed for the synthesis of the PAMP copolymers. 3-azidopropyl methacrylate was synthesized in two steps starting from 3-chloro-1-propanol (**Figure 3.7** and **Figure 3.8**), the product in liquid form was purified by vacuum distillation and stored under a nitrogen atmosphere at -20 °C, 3-azidopropyl methacrylate showed characteristic signals in ^{1}H NMR spectrum (**Figure 4.23**) and strong azide stretching was spotted on FTIR spectrum at 2095 cm^{-1} (**Figure 4.26**), while benzyl functional ATRP initiator that was employed to simplify ^{1}H NMR analysis of the PAMP copolymers synthesized with a one-step reaction and characterized by ^{1}H NMR (**Figure 4.24**) after purification steps. PAMP copolymers were synthesized by using 2-bromo-2-methyl propanoate as initiator, PEGMA, 3-azidopropyl methacrylate (AzPMA), MMA, and PMA as monomers via ATRP. As a controlled polymerization method ATRP yielded copolymers complying with the feed ratios while the molecular weight of the copolymer tuned accordingly, while characterization was mainly conducted by ^{1}H NMR spectroscopy (**Figure 4.25**) by using aromatic protons of the benzyl group and neighboring methylene signals as reference (**Table 4.6**). In compliance with the first stage of the study PAMP4 with a molecular weight of 35,517 g/mol, 81.7% PEG content by mass, and 9.5 azide and 12.0 pyrene units on the chain were selected and used for the rest of the study.

To introduce the CP on the graphene surface a new ATRP initiator was synthesized (**Figure 4.22c**) as a functional bridge between CP and the rGO surface. This initiator that

was used directly in CP synthesis, contains the alkyne end group for CuAAC reactions and pH-sensitive hydrazone linkage for the degradation in acidic pH. To the best of our knowledge, this initiator was the first time reported and used for the control polymerization.

It is important for effective transfection activity to have cationic copolymers with the ability to combine different properties apart from condensing negatively charged nucleic acid. For instance, the cationic copolymer that combines the endosomal buffering capacity of DMAEMA and membrane destabilization properties of hydrophobic HMA monomers was used as an arm of a cyclodextrin cored star polymer as an ideal gene delivery system [171]. It was shown that copolymer uses a dual mechanism to effectively escape from endosome and delivers its cargo to the cytoplasm. This well-defined copolymer was synthesized with a controlled polymerization technique and a certain portion of the DMAEMA monomer was converted to the cationic TMAEMA monomer to initially complex with the siRNA. Further, DMAEMA sense the pH drop and gets protonated, and contributes to the endosomal swelling mechanism while the hydrophobic alkyl chain of HMA causes membrane disruption on the endosome. Moreover, it was shown that molecular weight lower than 25 kDa, equal molar of HMA and DMAEMA, and %50 of quaternization of DMAEMA to obtain TMAEMA were ideal to have enhanced transfection efficiency. In the light of all these findings, the cationic copolymer that will use in this study was synthesized by a special design multifunctional initiator initiated ATRP using equal mol ratio of HMA and DMAEMA monomers followed by 50 % quaternization of DMAEMA into TMAEMA (**Figure 4.22d**). As mentioned, HMA and DMAEMA were tasked for endosomal escape by membrane disruption and proton sponge effect whereas TMAEMA was responsible for nucleic acid complexation. The overall molecular weight of P(HMA-*co*-DMAEMA-*co*-TMAEMA) was intentionally kept below 25 kDa to prevent toxicity of cationic charge. This synthesized copolymer was primarily characterized by ^{1}H NMR before and after quaternization, and their copolymer compositions regarding monomer numbers and molecular weight were determined (**Figure 4.30** and **Table 4.7**). Unfortunately, it was not possible to use GPC for characterization due to the interactions between DMAEMA and TMAEMA monomers and the packing material of GPC columns [171], [258]. In order for the targeting agent EPPT1 to be added to the nanoplatform structure by CuAAC click reaction, EPPT1 peptide was reacted with alkyne-PEG-NHS from the free amine end and

alkyne-PEG-EPPT1 was obtained (**Figure 3.13**). The chain length (3000 Da) of the used PEG was intentionally selected longer than coated PEG chains to allow flexibility and easy access to the targeting agent to the targeted receptor on the cell surface without getting effected by the stearic hindrance. The resulting alkyne-PEG-EPPT1 was characterized by ^{1}H NMR (**Figure 4.32**), PEG backbone protons, and aromatic protons originating from building blocks of EPPT1 were clearly detected while NHS group protons disappeared after conjugation.

After all the components required for the construction of the nanoplatform have been prepared, the order in which these parts should be put together has been examined in a separate study. The different routes tried were evaluated in terms of ease of characterization, dispersibility in water systems, drug loading and release profiles of the loaded drug, and of course biocompatibility and targeting efficiency. Ideally, after the preparation of PAMP-*g*-CP copolymer, it was coated on the GO surface and the reduction of GO with hydrazine to rGO was followed by EPPT1, Dox, and siRNA conjugation onto the system, respectively (**Figure 4.33**).

Once the synthesis order was determined, the nanoplatform production was started with the synthesis of PAMP-g-CP (**Figure 4.22b**) and coated on the GO surface after characterization by ^{1}H NMR spectroscopy, while GO was reduced in-situ. By examining the TGA thermograms, it was determined that the PAMP-*g*-CP copolymer degraded in two stages with onset temperatures of 231.79 °C and 384.33 °C in the 200-500 °C range, parallelly PAMP-CP-rGO showed a similar degradation profile with onset temperatures of 266.64 °C and 345.75 °C and using this PAMP-*g*-CP degradation at this region it was determined that PAMP-*g*-CP coated on the rGO surface constituted 53.3% by mass of the final product (**Figure 4.34**). The attachment of EPPT1 to PAMP-CP-rGO surface by CuAAC with a 98.2% efficiency was followed by Dox loading on the nanoplatform surface, following wash steps by using UV absorbance calibration curve (**Figure 4.37**) it was determined that an average of 96.7% of Dox used during the reaction was loaded onto nanoplatform surface revealing high loading capacity regarding the hydrophobic drug. Furthermore, examination of nanoplatforms and precursors by SEM (**Figure 4.36**) revealed morphological changes by modifications, GO could be seen as thin single plates, wrinkled and randomly aggregated, but after reduction, rGO piled up on top of each other, forming a more densely packed, flatter structure. On the other hand, PEGylation by PAMP-CP and reduction produces composite resembling rGO but due to surface coating,

they exhibit a looser packing than rGO as anticipated [260], [261]. In parallel to SEM imaging, EDAX sensor scans shed a light on the atomic composition of nanoplatforms, in addition to other physicochemical characterizations this test confirmed the addition of functionalities on each step (**Table 4.8**).

Dox release of PAMP-CP-rGO-Dox and EPPT1-PAMP-CP-rGO-Dox was examined at pH 7.4 and 5.5 (**Figure 4.38a**), at the early stages around 10% of the drug was found to be released while at pH 5.5 a burst release of 45.3% was observed. At the end of the test, a maximum release of 25.95% was detected at pH 7.4 while 52.9% of the Dox was found to be released at pH 5.5. Between PAMP-CP-rGO-Dox and EPPT1-PAMP-CP-rGO-Dox, no significant difference was detected for both pH levels, and from examination of the release profiles regarding the drug release kinetics at pH 5.5 nanoplatforms correlate with Weibull model and at pH 7.4 this changed to zero order parallel with the reported models in the literature [263]–[266]. These results indicate a pH-dependent release profile while traveling through the bloodstream majority of the hydrophobic drug would be conserved but after cellular uptake on the tumor site parallel to pH decrease in the cell compartments anticancer drug would be released into the cell as intended. Nanoplatforms were efficiently loaded with hydrophobic drugs simply due to their wide surface area, although they protect the loaded drug during blood circulation, it is important that its surface properties should not change to preserve their effectiveness, after making contact with blood proteins. Since, during blood circulation, plasma proteins pose a risk of adsorption onto the wide rGO surface forming a protein corona which creates the risk of opsonization and change in characteristics of the carriers. General practice to overcome this risk is to coat the rGO surface with PEG or hydrophilic other polymers [295]. PEGylation technic that is suggested and the coating that has been made in this study naturally might provide more protein resistance surface. The potential improvement in the interaction of protein was evaluated by mixing the dispersant of PAMP-CP-rGO with 10% FBS in PBS at 37 °C, where GO and rGO were used as controls. The samples were drawn at predetermined time points and were analyzed to quantify the residual FBS concentrations using Bradford assay. As can be seen in given comparison in **Figure 4.39**. the highest protein adsorbing material was found to be GO, while rGO observed the lowest percent of protein in parallel to the literature [214]. PAMP-CP-rGO exhibited a similar profile at an early time point and slightly differentiated from rGO showing a slight increase in protein absorption. Although PAMP-CP-rGO exhibited a similar profile to rGO in terms of protein

adsorption, it overcame the water dispersion problem, which needs to be overcome in biological environments, unlike rGO. After 72 hours of mixing, PAMP-CP-rGO has only adsorbed 13.3% of the total FBS, while GO adsorbed two times more (26.5%). From this point of view, it is possible to say that the copolymer coating on the rGO surface can lower the opsonization of carriers by shielding the carriers against proteins during blood circulation which provides a safer vehicle for cargo. This result is very valuable considering that one of the toxicity mechanisms of graphene is to absorb the nutrients and proteins of the cell and drive it to starvation.

Although the number of N on the rGO surface can be determined using the data gathered from ^{1}H NMR and TGA, the mass ratio was used since it is mostly preferred for graphene-based systems in the literature. The N/P value by mass was determined by preparing nanoplatform complexes with anti-GAPH and anti-Bcl-2 siRNA at varying rates, and free siRNA was visualized by gel electrophoresis (**Figure 4.40**). PAMP-CP-rGO derivatives were found to form stable complexes with anti-GAPDH-siRNA at 30/1 and with anti-Bcl-2-siRNA at 45/1 or higher mass ratios, these values show similar or lower complexing rates compared to most of the other examples given in the literature and prove the high oligonucleotide loading capacity [296]–[298].

Comparable to size measured from TEM images of PMP-rGO derivatives, PAMP-CP-rGO derivative's size measurements by DLS were found to be in the range of 500-600 nm, modification of PAMP copolymer to include cationic copolymer and followed by siRNA complexation might have caused the increase in size. On the contrary, the DLS method does not provide highly accurate data for two-dimensional particles, nevertheless obtained size distributions were found to be consistent with each other, and the PDI ranged between 0.2 to 0.8 indicating nanocarriers to have a wide particle size distribution [269]–[271]. As seen in **Figure 4.41** increasing the nanoplatform to siRNA ratio yields higher particle size might be observed due to intermolecular entanglement. Zeta potential measurements showed a positive charge for plain nanoplatforms which decreases significantly by siRNA addition and increases slightly by reduced siRNA ratio.

Once the carrier components were combined and the final product EPPT1-PAMP-CP-rGO-Dox-siRNA was obtained, the biological activities of the nanoplatform and its derivatives were tested. In order to observe the effects of nanoplatforms on cell viability, unlike PMP-rGO derivatives, the resazurin assay was used instead of the MTS assay. This change was simply made to eliminate the false absorbance readings that might occur due

to Dox presence on the structure, even though MTS and MTT assays are highly used with Dox carrying nanoparticles [184], [299]–[301] studying resazurin assay by its fluorescence was found to be more suitable for cell viability analysis with Dox carrying nanoplatforms (**Figure 4.42**). Two cancer cell line has been employed for viability tests, ER+, non-invasive and poorly-aggressive MCF-7 cell line [272], and triple-negative, highly aggressive, and invasive MDA-MB-231 cell line [273]. The first cell viability assay with anti-GAPH-siRNA complexed PAMP-CP-rGO nanoplatforms were conducted with the MCF-7 cell line following 24 hours of incubation with nanoplatforms. As seen in **Figure 4.43** every Dox concentration viability was found to be below 40% while nanoplatforms without Dox show significantly lower cytotoxicity, especially at low concentrations that decreased immensely by Dox introduction on nanoplatform. IC_{50} values were calculated to be 25.86 µg/mL and 29.17 µg/mL for PAMP-CP-rGO-siRNA and EPPT1-PAMP-CP-rGO-siRNA where these values were decreased to 10.17 µg/mL and 13.42 µg/mL for PAMP-CP-rGO-Dox-siRNA and EPPT1-PAMP-CP-rGO-Dox-siRNA respectively showing substantial improvement on cellular toxicity. The test was repeated with the same cell line but instead of anti-GAPDH-siRNA this time anti-Bcl-2-siRNA was loaded on nanoplatforms and incubated for 24 and 48 hours (**Figure 4.44**). In parallel to the results obtained from the anti-GAPDH-siRNA test, a dose-dependent profile was observed where induced cytotoxicity was improved especially at higher concentrations. For instance, after 24 hours of incubation (**Figure 4.44a**) cell viability rate decreased from around 50% to 30% rates for both PAMP-CP-rGO-siRNA and EPPT1-PAMP-CP-rGO-siRNA. The same effect was experienced for Dox-loaded nanoplatforms, use of anti-Bcl-2-siRNA decreased cell viability from around 60% to 50% at 5 µg/mL for both Dox-loaded nanoplatform and at 15 µg/mL concentration targeted version was at 51.3% when anti-GAPDH-siRNA was used and after the change of siRNA to anti-Bcl-2 this value decreased to 33.8%. This effect could also be detected by calculated IC_{50} values, nanoplatforms without loaded Dox resulted in almost half of the anti-GAPDH-siRNA results, namely, to be 13.28 µg/mL and 11.64 µg/mL for non-targeted and targeted versions respectively, similarly, for PAMP-CP-rGO-Dox-siRNA it was found to be 7.33 µg/mL and 6.45 µg/mL EPPT1-PAMP-CP-rGO-Dox-siRNA with substantial improvement. Since anti-GAPH-siRNA would have only affected the GAPDH mRNA and protein levels, there would be no contribution to induced cell death, on the other hand by using anti-Bcl-2-siRNA a direct impact was implied to one of the well-known anti-apoptotic mechanisms and decrease in cell viability and IC_{50} values

would be caused by the contribution of anti-Bcl-2-siRNA. After increasing the incubation period to 48 hours, nanoplatforms carrying Dox generally showed higher mortality rates than 24 hours of incubation results, but no difference could be detected between the targeted and untargeted systems. This could be explained by the fact that for nanoplatforms incubated with cells for 48 hours, rather than a selective cell entry due to the targeting agent presence, the prolonged incubation time caused an obligatory interaction between cells and nanoplatforms, consecutively selectivity for cellular uptake has been tested in detail in subsequent *in vitro* and *in vivo* studies.

In the trial with the MDA-MB-231 cell line, it was observed that cell death occurred in a parallel profile at 24 hours of incubation, but cell mortality was found to be decreased at lower doses compared to MCF-7 cells after 48 hours of incubation and increased at higher doses catching up with MCF-7 profile. A dose-dependent profile was obtained especially for 24 hours results (**Figure 4.45a**) and the highest mortality was obtained with the final composition EPPT1-PAMP-CP-rGO-Dox-siRNA after 24 hours of incubation, while when the incubation time was increased to 48 hours (**Figure 4.45b**), no significant difference was observed between targeted and untargeted variant. In addition, the decrease in cell viability of around 50% at low concentrations provides the opportunity to work at a lower concentration range where possible toxicity from the carrier platform could be neglected. IC_{50} values could not be calculated due to calculated low regression coefficients. When the results were examined in detail for both of the cell lines, by addition of PEG-EPPT1 to the nanoplatforms, minor positive improvements in cell viability rates were observed, which attributed to the positive contribution of EPPT1 and PEG to biocompatibility. On the other hand, the milder MCF-7 cancer cell line was found to be affected more than the aggressive MDA-MB-231 cell line by Dox and anti-Bcl-2-siRNA carrying nanoplatforms after 48 hours of incubation. This might be related with the level of Bcl-2 expression in the cells which is more expressed in MCF-7 [302]. From the comparison of 24 hours data at lower doses, MDA-MB-231 cells were more sensitive to the nanoplatforms complying with previously reported results in the literature [289], [303], [304] while at higher doses response from both of the cell lines caught up. In addition to their biomolecular differences, elevated MCF-7 sensitivity could be connected to the higher expression of the MUC1 receptor on the surface of MCF-7 cells compared to MDA-MB-231 cells, making it more prone to the targeted nanoplatforms [274]. Where a dose-dependent response was detected for all particles for the final composition EPPT1-

PAMP-CP-rGO-Dox-siRNA demonstrating the best performance against both of the cell lines.

By utilizing the third method, the effect of nanoplatforms on cell viability was observed to improve the reliability of the previously obtained results. For this purpose, singlet MCF-7 cells were seeded, incubated with nanoplatforms, and allowed to form colonies which were then individually counted after crystal violet staining, by comparing the colony numbers to the positive control cell viability was calculated without using spectroscopic data. As seen in **Figure 4.47**, it was observed that viability decreased with increasing nanoplatform dosage, and the positive contribution of EPPT1 to the biocompatibility was observed again not only for the gene carrying system but also for the dual drug carrying nanoplatform pairs. Although colony formation is observed to be higher in the targeted system, it was still superior to its non-targeted analog in allowing a concentration-dependent selective treatment. The plotted data showed that the IC_{50} value for EPPT1-PAMP-CP-rGO-Dox-siRNA was found to be 5.63 µg/mL to be very close to the value resazurin assay determined value of 6.45 µg/mL, viability results parallel to the resazurin trial proved the reputability and suitability of selected cell viability detection methods and also showed to be overcoming difficulties encountered in systems containing Dox.

The EPPT1 selective cellular internalization of nanoplatforms was investigated in detail using confocal microscopy and FACS analysis. In confocal microscopy studies, while Dox-loaded nanoplatforms were detected using Dox autofluorescence, nanoplatforms without Dox were complexed with FAM-labeled siRNA and their images were recorded with the excitation, emission, and detection wavelengths specified in **Table 4.10** so that all synthesized vectors were localized in cells. MCF-7 cell line was selected for confocal microscopy studies over the MDA-MB-231 cells line to observe selective uptake depending on targeting in short incubation instances since MUC1 expression on the MCF-7 cell surface was found to be higher than MDA-MB-231 cells that were targeted by EPPT1 peptide [274]. The microscope images obtained from the experiments based on the selectivity of nanoplatforms without saturation of the cells with elongated cell-material interactions and short-term incubations were examined. All images were captured with the same acquisition parameters, from the examination of the images seen in **Figure 4.48** the incorporation of EPPT1 onto the nanoplatform structure was found to be increasing the cellular uptake of the EPPT1-PAMP-CP-rGO-Dox-siRNA when

compared to non-targeted PAMP-CP-rGO-Dox-siRNA. The positive effect of the presence of the targeting agent EPPT1 on the cellular uptake of EPPT1-bearing nanoplatforms by the cancer cells was also observed in the study performed with FAM-siRNA complexed PAMP-CP-rGO-siRNA and EPPT1-PAMP-CP-rGO-Dox-siRNA (**Figure 4.49**). Relative fluorescence intensities were obtained by measuring the FAM, Dox, and Hoechst radiation intensities with the help of Zen Blue Edition software and normalizing them with the nucleus dye Hoechst (**Figure 4.50**). When the cellular uptake of targeted and untargeted variants was compared, parallel with the results obtained by examining the visual microscope images were obtained, it was determined that a higher rate of the targeted carriers was taken up into the cell for both FAM and Dox loaded nanoplatforms. The cellular uptake efficacy of the MCF-7 cell line was compared with that of the healthy MCF-10A cell line. In the experiment with MCF-10A, it was observed that the cellular uptake decreased and the Dox (**Figure 4.51**) and FAM (**Figure 4.52**) fluorescence intensities fade out in the images recorded by keeping all the settings equal. While calculated relative fluorescence intensities of FAM and Dox against Hoechst did not reveal significant differences between targeted and untargeted systems for healthy cells, it was shown once again that the values obtained from MCF-10A cells were lower than those obtained from cancer cells **Figure 4.53**. With the straightforward comparison of healthy and cancerous cells at this level, it was concluded that nanoplatforms actively prefer cells that show high MUC1 expression. Although it has been determined that the smart drug delivery system prefers cancer cells selectively, their location in the cell is important for the activity of the carrier in the treatment of the cell. Confocal images of the MCF-7 cells were recorded after 4 hours of incubation with targeted, Dox-loaded EPPT1-PAMP-CP-rGO-Dox-siRNA, and cells were simultaneously stained with LysoTracker, which has a high affinity for acidic organelles [276], [277] and Hoechst. When the images were examined in **Figure 4.54**, Dox fluorescence was observed in the same regions with LysoTracker stained organelles that have acidic pH levels, which could be endosomes and/or lysosomes, in addition, Dox signals that do not overlap with LysoTracker stained regions were recorded, indicating the presence of nanoplatforms that have passed into the cytoplasm. In parallel with the confocal microscope study, the fluorescence intensity of Dox-bearing nanoplatforms was measured by using the single cell fluorescence reading feature of flow cytometry. The first measurements were conducted with MDA-MB-231 cells as seen in **Figure 4.55**, the highest cellular uptake was achieved by free Dox which can passively diffuse into cells as expected, while

variants with and without cationic copolymer were compared regarding targeting, and higher fluorescence values were seen in EPPT1 conjugated nanoplatforms while the highest uptake rate was found to be achieved by final version of nanoplatforms, EPPT1-PAMP-CP-rGO-Dox-siRNA. In the second study supporting these results, a clearer differentiation was observed with the MCF-7 cell line (**Figure 4.56**), results were equivalent to the results of confocal microscopy, depicting higher uptake with targeted nanoplatforms and finally the selectivity of EPPT1 targeting agent was confirmed by two different methods.

The apoptosis and necrosis caused by the nanoplatforms in the cells via anti-Bcl-2-siRNA and Dox they carry, the synergistic efficiency of the load, and change in response to the use of scrambled siRNA were determined by flow cytometry analysis using APC conjugated Annexin-V and Helix NP Blue co-staining (**Figure 4.57** and **Figure 4.58**). While anti-Bcl-2-siRNA loaded nanoplatforms caused early and late apoptosis with the contribution of EPPT1, this was observed more as necrosis in untargeted nanoplatforms. The MDA-MB-231cell line was found to be more responsive to Dox-bearing nanoplatforms, and higher apoptosis and necrosis levels were observed than MCF-7 cells. While an overall decrease in necrosis and apoptosis levels was observed after replacing anti-Bcl-2-siRNA with SCR/siRNA as witnessed in cell viability studies of anti-GAPDH-siRNA bearing nanoplatforms case, targeting efficiency and synergistic effect were confirmed considering these two parallel results, in compliance with the expected effect of the decrease in Bcl-2 protein levels induced by anti-Bcl-2-siRNA, resulting a decrease in apoptosis resistance would be observed and cells should be more sensitive to the chemotherapy drug as obtained [200], [228]. Design of the first two trials mentioned above was conducted with a short 4-hour incubation with nanocarriers to seek the effect of selectivity by limited exposure, while this approach does not give the cells to uptake high doses of nanoplatforms a third trial was conducted to observe the change in an apoptotic cell population with 24 hours of exposure at two concentrations, 50 nM siRNA (14.1 µg/mL Dox) and 8.9 nM siRNA (2.5 µg/mL Dox) (**Figure 4.59**). Decreasing Dox concentration highly impacted the early apoptotic cell population for the free Dox treated group and the rate decreased from 43.3% to 6.84%, while the early apoptotic cell population has stayed almost at the same level for nanoplatforms. Scrambled siRNA complexed EPPT1-PAMP-CP-rGO-Dox generates a 6.90% and 6.93% early apoptotic cell population, when switched to anti-Bcl-2 siRNA this rate increased to 8.46% and

8.57%. Since the only difference between these groups was the complexed siRNA, anti-Bcl-2-siRNA induced apoptosis can be confirmed. Although the aim of this study was to observe increased apoptosis levels for better comparison of the nanoplatforms, as a result of decreased Bcl-2 expression, in some cases cell death may have resulted from different mechanisms other than through apoptosis mechanism.

The anticancer effect induced by nanoplatforms on cell viability, the selectivity of the targeting agent EPPT1, and the synergistic effect of siRNA and Dox were examined. Following these steps, the therapeutic effect of siRNA, one of the fundamental components of the dual drug system, has been tested in three common methods, namely detecting GAPDH protein levels by KDalert™ assay, change in Bcl-2 mRNA expression by qPCR, and Bcl-2 protein levels by Western-Blotting. In theory, nanoplatforms should release the siRNA into the cytoplasm and once siRNA is released it is supposed to selectively decrease the expression of the targeted gene [155], to test the efficiency of transfection first nanoplatforms were tested against the housekeeping protein GAPDH as a model [283]. Anti-GAPDH-siRNA complexed nanoplatforms and Lipofectamine were incubated with MCF-7 cells for 4 hours and post-incubated for 48 hours. By following the KDalert™ assay kit protocol change in GAPDH protein expression was detected. Even though an equal protein content was used for each sample to eliminate a decrease in the number of viable cells, it was not possible to compensate for decreased protein extract quality fully for Dox loaded and cationic charge carrying nanoplatforms and even with the use of scrambled siRNA, a decrease in the GAPDH protein expression was observed as predicted by the literature [284]–[286]. As seen in **Figure 4.60** non-targeted PAMP-CP-rGO-Dox-siRNA treated cells showed 76.82% GAPDH protein expression, targeted EPPT1-PAMP-CP-rGO-Dox-siRNA treated cells this rate fell to 43.49%. By comparison of scrambled siRNA and anti-GAPDH-siRNA complexed nanoplatforms, it was possible to detect a significant difference between protein expression levels as expected Lipofectamine, a well-known commercially available gene delivery agent could not reach the knockdown levels of targeted nanoplatform. When the combined results were examined, there is no doubt that anti-GAPDH-siRNA was delivered to cancer cells and effectively knocked down GAPDH protein levels.

As model GAPDH experiment, it is aimed to inhibit the mRNA responsible for anti-apoptotic Bcl-2 protein synthesis in the cell with the delivery of anti-Bcl-2-siRNA as targeted, and in this case, while the mRNA levels decrease by anti-Bcl-2-siRNA

inactivation, the protein level is expected to decrease accordingly. For this purpose, techniques in which both Bcl-2 encoding mRNA and Bcl-2 protein levels could be observed were employed. Firstly, as can be seen in **Figure 4.61**, MDA-MB-231 cells were incubated with nanoplatforms and the total RNA from the cells was isolated and examined by qPCR. Due to the negative charge and instability of the free siRNA, it would not enter the cell and did not cause a change in gene expression for both time points. On the other hand, when targeted and untargeted nanoplatforms carrying only siRNA were compared, Bcl-2 mRNA was still 93% expressed at the end of 48 hours of post-incubation (**Figure 4.61a**), while this value was reduced to 31% with a targeted carrier containing EPPT1, and after 72 hours the targeted carrier system was suppressed mRNA levels by 83% (**Figure 4.61b**). When nanoplatforms carrying Dox and siRNA were examined, nontargeted nanoplatform mRNA expression by 24%, the targeted system managed to reduce it by 63% (**Figure 4.61a**), and at the end of 72 hours these values were determined as 52% and 87%, respectively (**Figure 4.61b**) while in parallel with previous studies use of scrambled siRNA did not yield meaningful decrease in gene expression after 48 hours but caused a suppression around 31% when used with the final composition of nanoplatform. This effect was connected with the presence of Dox in the system, and it is discussed in detail in the following part. When this experiment was performed using the MCF-7 cell line (**Figure 4.62**), although a difference was observed between the targeted and non-targeted nanoplatforms, it was not observed with such high differences in this cell line as was observed in the MD-MBA-231 which appears to be more sensitive to anti-Bcl-2-siRNA.

It is expected that the decrease in Bcl-2 coding mRNA expression will also be reflected in the related protein synthesis and the level of Bcl-2 protein expressed in the cells will decrease after transfection. The change in protein levels was detected by Western blot analysis, the transfection efficiency was compared by detecting Bcl-2 protein expression against the endogenous β-actin protein. Anti-Bcl-2-siRNA complexed, Dox loaded and targeted nanoplatform EPPT1-PAMP-CP-rGO-Dox almost deleted Bcl-2 band for MDA-MB-231 cell line while reducing the band significantly for MCF-7 cells (**Figure 4.63**). Other than targeting, anti-Bcl-2-siRNA loaded particles were observed to induce a reduction in Bcl-2 protein levels, while scrambled siRNA loaded nanoplatforms did not have this effect. [275], [289], [293]. The values obtained by proportioning the volumes of the Bcl-2 bands to the β-actin bands were plotted and as seen in **Figure 4.64**, the lowest

protein level observed for MCF-7 cells was determined as 75.7% in the cells to which the final nanoplatform composition was applied group (**Figure 4.64a**). These values revealed a higher decrease in Bcl-2 protein expression more clearly for the MD-MBA-231 cell line in proportion to the mRNA expression obtained in the qPCR results (**Figure 4.64b**), although the Dox carrying, scrambled siRNA complexed nanoplatform did not decrease band intensity as much as the anti-Bcl-2 complexed EPPT1-PAMP-CP-rGO-Dox, it resulted in a significant reduction in protein levels as well. Similarly, a decrease in Bcl-2 protein band intensities was observed after treatment of the free Dox or Dox loaded and/or scrambled siRNA complexed nanoplatforms applied cells, this decrease in the absence of anti-Bcl-2-siRNA was associated with the Dox presence which found to be downregulating Bcl-2 protein expression by itself along with different proteins [275], [289], [293]. Taking account of band images and calculated change in expression of Bcl-2 protein levels after the treatment, it is clear that the rGO nanoplatforms deliver the oligonucleotide and Dox cargo into the cell safely to take effect as designed. When cell lines were compared the MDA-MB-231 cell line was found to be highly affected by anti-Bcl-2-siRNA and Dox combination than the MCF-7 cell line, proving the MDA-MB-231 cell line to be more susceptible to anti-Bcl-2-siRNA in parallel to the results obtained from the qPCR studies. While MCF-7 is a better target for EPPT1 and milder profile it was expected to be affected higher than the aggressive, triple negative MDA-MB-231 cell line. This phenomenon could be explained by the Bcl-2 protein expression in these two cell lines where MCF-7 cells express Bcl-2 at higher levels when compared to MDA-MB-231 which has been shown by multiple studies in the literature[302], [305]–[307].

Completion of *in vitro* studies was followed by *in vivo* studies to test the anticancer activity of nanoplatforms. A xenograft model that uses MDA-MB-231 cells in athymic nude mice was studied, during early injections, cells were injected in PBS subcutaneously and no significant tumor growth was observed. To improve the efficiency of the cell delivery PBS was changed to an equal part mixture of DMEM and Matrigel and in 3 to 5 weeks tumors at desired size range were obtained. Anticancer activity of nanoplatforms was tested by injecting PBS, free Dox, and nanoplatforms through the tail vein on days 0, 3, and 6 at 5 mg/kg Dox concentration, and growth in tumor size was recorded for 21 days. **Figure 4.66** shows a mouse from each group at the beginning of the study and at the end after 21 days, from visual inspection of the images difference in the tumor size can be specified. The enormous growth of the tumor of the PBS injected control group

was suppressed with Dox and Dox-carrying nanoplatforms. From the measured tumor volumes in **Figure 4.66** change in volume size was clearly detected, the control group had a growth of 10.5-fold while Dox treated tumor was grown only 2.4 times in volume. PAMP-CP-rGO-DOX-siRNA and the final version of the nanoplatforms EPPT1-PAMP-CP-rGO-DOX-siRNA showed a parallel suppression with Dox by 4.6 and 3.6-fold increase in tumor volume respectively, the difference between growth suppression levels is attributed to the presence of EPPT1 targeting. EPPT1-PAMP-CP-rGO-DOX-siRNA showed a very close profile to free Dox for the first 18 days of treatment. It should be noted that compared to Dox, EPPT1-PAMP-CP-rGO-DOX-siRNA as a targeted carrier possesses more advantages such as long circulation time, selective accumulation, and effective internalization into target cells. Once Dox was removed from the system change was found to be 6.4-fold for EPPT1-PAMP-CP-rGO-siRNA and by removal of siRNA and cationic copolymer yielded a tumor growth by 5.4-fold for EPPT1-PAMP-rGO-Dox at the end of the study proving the importance of combination therapy. In comparison to control group Dox, PAMP-CP-rGO-DOX-siRNA and EPPT1-PAMP-CP-rGO-DOX-siRNA were found to decelerate tumor progress significantly ($p<0.05$) while no test group showed the loss in body weight higher than 15%.

CHAPTER 5

5. CONCLUSIONS AND FUTURE WORK

To summarize, this study was designed and studied in two stages to determine the most efficient and effective approach to using graphene and its derivatives as an advanced drug delivery system. In this regard, an efficient PEGylation method to improve the biocompatibility and stability of graphene derivatives was first studied synthetically and biologically in detail. Well-defined, pyrene and different lengths of PEGMA (500 Da and 2000 Da) containing unique P(PEGMA-*co*-MMA-*co*-PMA) copolymers were prepared and coated on rGO surface via π-π stacking with coating efficiencies ranging between 58.8% and 71.2%. The method uses water-dispersed GO as starting graphene derivative and simultaneously reduces it to less defected rGO during PEGylation. Multiple pyrene groups in the copolymer significantly contribute to the coating efficiency along with simultaneous reduction that even further increases the interaction between pyrene and the conjugated surface of rGO. Thoroughly characterized water-dispersible PMP-rGO derivatives showed high hemocompatibility and low cytotoxicity comparing the starting GO and copolymer itself. The results of *in vitro* studies collectively showed that PMP_{2000}-rGO derivatives with longer PEG brushes were more biocompatible than PMP_{500}-rGO derivatives since dispersibility and stability in aqueous systems have been maintained better with higher PEG content. PEG content lower than 60% has a tendency to agglomerate in aqueous environments, while PEG content of 80% was found to be the most stable in cell medium and biocompatible among PMP-rGO derivatives regardless of PEG brush length. The dose-dependent cytotoxicity profile of PMP-rGO was varied based on the tested cell line, however, it could be used up to 150 μg/mL safely for both HEK-293T and MRC-5 cells based on the results of MTS, LDH, and ROS assays.

Determination of the ground rules to be followed while preparing drug delivery systems with P(PEGMA-*co*-MMA-*co*-PMA) copolymer coated rGO on the second stage a

targeted dual delivery agent was prepared by modification onto the copolymer to enable further improvement of the nanoplatform. By adding azide functional monomer to the copolymer structure consisting of methyl methacrylate, PEG, and pyrene repeating units, different modifications could be made by using CuAAC. In parallel with the preparation of P(PEGMA-*co*-AzPMA-*co*-MMA-*co*-PMA), a new multifunctional ATRP initiator was synthesized and using this initiator, a copolymer was prepared that was responsible for endosomal escape and cationic charge. Alkyne end functional P(HMA-*co*-DMAEMA-*co*-TMAEMA) copolymer was grafted onto P(PEGMA-*co*-AzPMA-*co*-MMA-*co*-PMA) and obtained graft copolymer (PAMP-*g*-CP) was used for the PEGylation of GO in reductive conditions to obtain PAMP-CP-rGO. The remaining azide groups on the graft copolymer were employed for the conjugation of the alkyne-PEG-EPPT1 targeting agent, this step was followed by Dox and siRNA loading to result in the final composition of nanoplatform as EPPT1-PAMP-CP-rGO-Dox-siRNA. The final dual drug delivery system exhibits a pH-sensitive drug release profile ensuring minimal drug loss during travel to the tumor site and controlled release once internalized by the cell. By studying the effect of nanoplatform on cell viability a dose-dependent cytotoxic response was recorded. Targeting ability of EPPT1 conjugation was tested by examination of cellular uptake after a short duration of incubation with rGO derivatives by confocal microscopy and FACS showed that nanoplatforms' selectively uptake by MUC1-rich cancer cells rather than healthy cells, in addition, by staining acidic compartments in the cell nanoplatform presence in cell compartments was approved. Apoptotic effects of nanoplatforms were examined by staining with APC-Annexin-V/Helix NP Blue, it was observed that anti-Bcl-2-siRNA loaded nanoplatforms caused early and late apoptosis with the contribution of EPPT1 on the structure while a general decrease on apoptotic and necrotic cell population was observed after switching siRNA to scrambled version, in the light of these two results, the targeting efficiency and the synergistic effect were confirmed. A qPCR study was conducted to assess the Bcl-2 gene knockdown capacity of the nanoparticles resulting in adequate knockdown on mRNA levels, especially on triple-negative MDA-MB-231 cells and these findings were supported by testing changes in protein expressions. GAPDH and Bcl-2 protein expressions were tested by KDalert assay and Western-Blot assay respectively showing successful delivery of the loaded siRNA inducing a decrease in targeted protein levels, Western-Blot results showed that MDA-MB-231 cell to be more prone to the siRNA-Dox combination. MDA-MB-231 tumor-bearing mice were treated with nanoplatforms and

Dox to determine the anti-cancer effect of the nanocarriers. It was found that a parallel profile with the therapeutic drug Dox was exhibited by EPPT1-PAMP-CP-rGO-Dox-siRNA and a positive contribution to tumor suppression by the addition of targeting agent EPPT1 was observed.

The biological functions of the basic components of the system, which require intensive chemical optimization, have been tested using different methods and the synergy therapy effect has been demonstrated. In addition, the selectivity of the targeting agent against the cancer cells and the effect of this selectivity on the treatment was also shown. The targeting agent EPPT1 was tested only against breast cancer cells, but MUC1 is known to be highly expressed by lung, liver, colon and pancreatic cancers as well, allowing this carrier system to be easily adapted to different cancer types and used for different treatments. By employing the developed advantageous PEGylation method nanoplatforms can be easily altered to be used against listed cancer types to determine their effectiveness as a therapeutic agent. In addition, it is possible to modify graphene not only for use as a therapeutic agent but also as a theranostic agent by introducing bioimaging agents. Although this modular system is open to improvement and the addition of new components, the binding dynamics between the GO surface and copolymers, hydrophobic drug, and siRNA contain many different possibilities, and chemical testing of all of them requires significant time and resources. At this point, different synthetic routes can be determined as “in-silico”, which can be examined with the help of molecular dynamics simulations using computer models.

BIBLIOGRAPHY

[1] K. Riehemann, S. W. Schneider, T. A. Luger, B. Godin, M. Ferrari, and H. Fuchs, "Nanomedicine-Challenge and Perspectives," *Angew. Chem. Int. Ed.*, vol. 48, no. 5, pp. 872–897, Jan. 2009, doi: 10.1002/anie.200802585.

[2] J. Damodharan, "Nanomaterials in medicine – An overview," *Mater. Today Proc.*, vol. 37, pp. 383–385, 2021, doi: 10.1016/j.matpr.2020.05.380.

[3] V. Thakur and R. V. Kutty, "Recent advances in nanotheranostics for triple negative breast cancer treatment," *J. Exp. Clin. Cancer Res.*, vol. 38, no. 1, p. 430, Dec. 2019, doi: 10.1186/s13046-019-1443-1.

[4] Y.-E. Choi, J.-W. Kwak, and J. W. Park, "Nanotechnology for Early Cancer Detection," *Sensors*, vol. 10, no. 1, pp. 428–455, Jan. 2010, doi: 10.3390/s100100428.

[5] Y. Zhang, M. Li, X. Gao, Y. Chen, and T. Liu, "Nanotechnology in cancer diagnosis: progress, challenges and opportunities," *J. Hematol. Oncol.J Hematol Oncol*, vol. 12, no. 1, p. 137, Dec. 2019, doi: 10.1186/s13045-019-0833-3.

[6] V. Gubala *et al.*, "Engineered nanomaterials and human health: Part 1. Preparation, functionalization and characterization (IUPAC Technical Report)," *Pure Appl. Chem.*, vol. 90, no. 8, pp. 1283–1324, Aug. 2018, doi: 10.1515/pac-2017-0101.

[7] S. Augustine, J. Singh, M. Srivastava, M. Sharma, A. Das, and B. D. Malhotra, "Recent advances in carbon based nanosystems for cancer theranostics," *Biomater. Sci.*, vol. 5, no. 5, pp. 901–952, 2017, doi: 10.1039/C7BM00008A.

[8] G. Hong, S. Diao, A. L. Antaris, and H. Dai, "Carbon Nanomaterials for Biological Imaging and Nanomedicinal Therapy," *Chem. Rev.*, vol. 115, no. 19, pp. 10816–10906, Oct. 2015, doi: 10.1021/acs.chemrev.5b00008.

[9] J. Safari and Z. Zarnegar, "Advanced drug delivery systems: Nanotechnology of health design A review," *J. Saudi Chem. Soc.*, vol. 18, no. 2, pp. 85–99, 2014, doi: 10.1016/j.jscs.2012.12.009.

[10] T. Yin *et al.*, "Redox Sensitive Hyaluronic Acid-Decorated Graphene Oxide for Photothermally Controlled Tumor-Cytoplasm-Selective Rapid Drug Delivery," *Adv. Funct. Mater.*, vol. 27, no. 14, p. 1604620, Apr. 2017, doi: 10.1002/adfm.201604620.

[11] M. Dolatkhah *et al.*, "Stimuli-responsive graphene oxide and methotrexate-loaded magnetic nanoparticles for breast cancer-targeted therapy," *Nanomed.*, vol. 16, no. 24, pp. 2155–2174, Oct. 2021, doi: 10.2217/nnm-2021-0094.

[12] S. Gooneh-Farahani, M. R. Naimi-Jamal, and S. M. Naghib, "Stimuli-responsive graphene-incorporated multifunctional chitosan for drug delivery applications: a review," *Expert Opin. Drug Deliv.*, vol. 16, no. 1, pp. 79–99, Jan. 2019, doi: 10.1080/17425247.2019.1556257.

[13] F. Bray, M. Laversanne, E. Weiderpass, and I. Soerjomataram, "The ever-increasing importance of cancer as a leading cause of premature death worldwide," *Cancer*, vol. 127, no. 16, pp. 3029–3030, Aug. 2021, doi: 10.1002/cncr.33587.

[14] H. Sung *et al.*, “Global Cancer Statistics 2020: GLOBOCAN Estimates of Incidence and Mortality Worldwide for 36 Cancers in 185 Countries,” *CA. Cancer J. Clin.*, vol. 71, no. 3, pp. 209–249, May 2021, doi: 10.3322/caac.21660.

[15] World Health Organization (WHO), “Global health estimates 2020: Deaths by Cause, Age, Sex, by Country and by Region.” https://www.who.int/data/gho/data/themes/mortality-and-global-health-estimates/ghe-leading-causes-of-death (accessed Jul. 21, 2022).

[16] V. Çetinkaya and P. V. Marquez, “Tobacco Taxation in Turkey: An Overview of Policy Measures and Results,” 2017, doi: 10.13140/RG.2.2.36300.21128.

[17] M. Roser and H. Ritchie, “Cancer,” *First published in July 2015*, 2019. https://ourworldindata.org/cancer (accessed Jul. 21, 2022).

[18] R. Hesketh, “‘Cancer genes’: mutations and cancer development,” in *Introduction to Cancer Biology*, 1st ed., Cambridge University Press, 2012. doi: 10.1017/CBO9781139012904.

[19] M. Abotaleb *et al.*, “Chemotherapeutic agents for the treatment of metastatic breast cancer: An update,” *Biomed. Pharmacother.*, vol. 101, pp. 458–477, May 2018, doi: 10.1016/j.biopha.2018.02.108.

[20] C. M. Perou *et al.*, “Molecular portraits of human breast tumours,” *Nature*, vol. 406, no. 6797, pp. 747–752, Aug. 2000, doi: 10.1038/35021093.

[21] R. Haque *et al.*, “Impact of Breast Cancer Subtypes and Treatment on Survival: An Analysis Spanning Two Decades,” *Cancer Epidemiol. Biomarkers Prev.*, vol. 21, no. 10, pp. 1848–1855, Oct. 2012, doi: 10.1158/1055-9965.EPI-12-0474.

[22] X. Dai *et al.*, “Breast cancer intrinsic subtype classification, clinical use and future trends,” *Am. J. Cancer Res.*, vol. 5, no. 10, pp. 2929–2943, 2015.

[23] A. A. Onitilo, J. M. Engel, R. T. Greenlee, and B. N. Mukesh, “Breast Cancer Subtypes Based on ER/PR and Her2 Expression: Comparison of Clinicopathologic Features and Survival,” *Clin. Med. Res.*, vol. 7, no. 1–2, pp. 4–13, Jun. 2009, doi: 10.3121/cmr.2008.825.

[24] K. Gelmon, R. Dent, J. R. Mackey, K. Laing, D. McLeod, and S. Verma, “Targeting triple-negative breast cancer: optimising therapeutic outcomes,” *Ann. Oncol.*, vol. 23, no. 9, pp. 2223–2234, Sep. 2012, doi: 10.1093/annonc/mds067.

[25] V. Guarneri, M. V. Dieci, and P. Conte, “Relapsed Triple-Negative Breast Cancer: Challenges and Treatment Strategies,” *Drugs*, vol. 73, no. 12, pp. 1257–1265, Aug. 2013, doi: 10.1007/s40265-013-0091-6.

[26] I. A. Mayer, V. G. Abramson, B. D. Lehmann, and J. A. Pietenpol, “New Strategies for Triple-Negative Breast Cancer—Deciphering the Heterogeneity,” *Clin. Cancer Res.*, vol. 20, no. 4, pp. 782–790, Feb. 2014, doi: 10.1158/1078-0432.CCR-13-0583.

[27] S. H. Giordano, G. N. Hortobagyi, S.-W. C. Kau, R. L. Theriault, and M. L. Bondy, “Breast Cancer Treatment Guidelines in Older Women,” *J. Clin. Oncol.*, vol. 23, no. 4, pp. 783–791, Feb. 2005, doi: 10.1200/JCO.2005.04.175.

[28] V. B. Pai and M. C. Nahata, “Cardiotoxicity of Chemotherapeutic Agents: Incidence, Treatment and Prevention,” *Drug Saf.*, vol. 22, no. 4, pp. 263–302, 2000, doi: 10.2165/00002018-200022040-00002.

[29] L. Tang *et al.*, “Versatile carbon nanoplatforms for cancer treatment and diagnosis: strategies, applications and future perspectives,” *Theranostics*, vol. 12, no. 5, pp. 2290–2321, 2022, doi: 10.7150/thno.69628.

[30] K. Kuche, N. Bhargavi, C. P. Dora, and S. Jain, “Drug-Phospholipid Complex—a Go Through Strategy for Enhanced Oral Bioavailability,” *AAPS PharmSciTech*, vol. 20, no. 2, p. 43, Feb. 2019, doi: 10.1208/s12249-018-1252-4.

[31] P. Mathur, S. Rawal, B. Patel, and M. M. Patel, “Oral Delivery of Anticancer Agents Using Nanoparticulate Drug Delivery System,” *Curr. Drug Metab.*, vol. 20, no. 14, pp. 1132–1140, Feb. 2020, doi: 10.2174/1389200220666191007154017.

[32] N. Aminu, I. Bello, N. M. Umar, N. Tanko, A. Aminu, and M. M. Audu, “The influence of nanoparticulate drug delivery systems in drug therapy,” *J. Drug Deliv. Sci. Technol.*, vol. 60, p. 101961, Dec. 2020, doi: 10.1016/j.jddst.2020.101961.

[33] S. Agarwal, Y. Zhang, S. Maji, and A. Greiner, “PDMAEMA based gene delivery materials,” *Mater. Today*, vol. 15, no. 9, pp. 388–393, Sep. 2012, doi: 10.1016/S1369-7021(12)70165-7.

[34] D. Iyengar, K. Tatiparti, N. S. Gavande, S. Sau, and A. K. Iyer, “Nanomedicine for overcoming therapeutic and diagnostic challenges associated with pancreatic cancer,” *Drug Discov. Today*, vol. 27, no. 6, pp. 1554–1559, Jun. 2022, doi: 10.1016/j.drudis.2022.02.026.

[35] J. Shi, P. W. Kantoff, R. Wooster, and O. C. Farokhzad, “Cancer nanomedicine: progress, challenges and opportunities,” *Nat. Rev. Cancer*, vol. 17, no. 1, pp. 20–37, Jan. 2017, doi: 10.1038/nrc.2016.108.

[36] V. S. Madamsetty, A. Mukherjee, and S. Mukherjee, “Recent Trends of the Bio-Inspired Nanoparticles in Cancer Theranostics,” *Front. Pharmacol.*, vol. 10, p. 1264, Oct. 2019, doi: 10.3389/fphar.2019.01264.

[37] G. Yan, A. Li, A. Zhang, Y. Sun, and J. Liu, “Polymer-Based Nanocarriers for Co-Delivery and Combination of Diverse Therapies against Cancers,” *Nanomaterials*, vol. 8, no. 2, p. 85, 2018, doi: 10.3390/nano8020085.

[38] O. Esim, S. Kurbanoglu, A. Savaser, S. A. Ozkan, and Y. Ozkan, “Nanomaterials for Drug Delivery Systems,” in *New Developments in Nanosensors for Pharmaceutical Analysis*, Elsevier, 2019, pp. 273–301. doi: 10.1016/B978-0-12-816144-9.00009-2.

[39] Z. P. Xu, Q. H. Zeng, G. Q. Lu, and A. B. Yu, “Inorganic nanoparticles as carriers for efficient cellular delivery,” *Chem. Eng. Sci.*, vol. 61, no. 3, pp. 1027–1040, Feb. 2006, doi: 10.1016/j.ces.2005.06.019.

[40] Z. Shi, Y. Zhou, T. Fan, Y. Lin, H. Zhang, and L. Mei, “Inorganic nano-carriers based smart drug delivery systems for tumor therapy,” *Smart Mater. Med.*, vol. 1, pp. 32–47, 2020, doi: 10.1016/j.smaim.2020.05.002.

[41] M. Mohajeri, B. Behnam, and A. Sahebkar, “Biomedical applications of carbon nanomaterials: Drug and gene delivery potentials,” *J. Cell. Physiol.*, vol. 234, no. 1, pp. 298–319, Jan. 2019, doi: 10.1002/jcp.26899.

[42] S. W. S. Young, M. Stenzel, and Y. Jia-Lin, “Nanoparticle-siRNA: A potential cancer therapy?,” *Crit. Rev. Oncol. Hematol.*, vol. 98, pp. 159–169, Feb. 2016, doi: 10.1016/j.critrevonc.2015.10.015.

[43] Q. Zhang *et al.*, “Advanced review of graphene-based nanomaterials in drug delivery systems: Synthesis, modification, toxicity and application,” *Mater. Sci. Eng. C*, 2017, doi: 10.1016/j.msec.2017.03.196.

[44] R. H. Petrucci, F. G. Herring, J. D. Madura, and C. Bissonnette, *General Chemistry: Principles and Modern Applications*, 10th ed. Pearson Prentice Hall, 2010.

[45] A. Hirsch, “The era of carbon allotropes,” *Nat. Mater.*, vol. 9, no. 11, pp. 868–871, Nov. 2010, doi: 10.1038/nmat2885.

[46] H. W. Kroto, J. R. Heath, S. C. O’Brien, R. F. Curl, and R. E. Smalley, “C60: Buckminsterfullerene,” *Nature*, vol. 318, no. 6042, pp. 162–163, Nov. 1985, doi: 10.1038/318162a0.

[47] S. Iijima, “Helical microtubules of graphitic carbon,” *Nature*, vol. 354, no. 6348, pp. 56–58, Nov. 1991, doi: 10.1038/354056a0.

[48] K. S. Novoselov *et al.*, “Electric Field Effect in Atomically Thin Carbon Films,” *Science*, vol. 306, no. 5696, pp. 666–669, 2004, doi: 10.1126/science.1102896.

[49] A. K. Geim and K. S. Novoselov, “The rise of graphene,” *Nat. Mater.*, vol. 6, no. 3, pp. 183–191, Mar. 2007, doi: 10.1038/nmat1849.

[50] M. Maruyama and S. Okada, “Magnetic Properties of Graphene Quantum Dots Embedded in h-BN Sheet,” *J. Phys. Chem. C*, vol. 120, no. 2, pp. 1293–1302, Jan. 2016, doi: 10.1021/acs.jpcc.5b09882.

[51] J. Hass, W. A. de Heer, and E. H. Conrad, “The growth and morphology of epitaxial multilayer graphene,” *J. Phys. Condens. Matter*, vol. 20, no. 32, p. 323202, Aug. 2008, doi: 10.1088/0953-8984/20/32/323202.

[52] K. S. Kim *et al.*, “Large-scale pattern growth of graphene films for stretchable transparent electrodes,” *Nature*, vol. 457, no. 7230, pp. 706–710, 2009, doi: 10.1038/nature07719.

[53] J. C. Meyer, C. Kisielowski, R. Erni, M. D. Rossell, M. F. Crommie, and A. Zettl, “Direct imaging of lattice atoms and topological defects in graphene membranes,” *Nano Lett.*, vol. 8, no. 11, pp. 3582–3586, 2008, doi: 10.1021/nl801386m.

[54] S. Chen *et al.*, “Thermal conductivity of isotopically modified graphene,” *Nat. Mater.*, vol. 11, no. 3, pp. 203–207, Jan. 2012, doi: 10.1038/nmat3207.

[55] Toshiaki. Enoki, Masatsugu. Suzuki, and Morinobu. Endo, *Graphite Intercalation Compounds and Applications.* Oxford University Press, USA, 2003.

[56] Pierre. Delhaes, *Graphite and precursors*. Gordon & Breach, 2001.

[57] Z. Xu and C. Gao, "Graphene fiber: a new trend in carbon fibers," *Mater. Today*, vol. 18, no. 9, pp. 480–492, Nov. 2015, doi: 10.1016/j.mattod.2015.06.009.

[58] K. K. H. De Silva, H.-H. Huang, R. K. Joshi, and M. Yoshimura, "Chemical reduction of graphene oxide using green reductants," *Carbon*, vol. 119, pp. 190–199, Aug. 2017, doi: 10.1016/J.CARBON.2017.04.025.

[59] Y. H. Hu, H. Wang, and B. Hu, "Thinnest two-dimensional nanomaterial-graphene for solar energy," *ChemSusChem*, vol. 3, no. 7, pp. 782–796, 2010, doi: 10.1002/cssc.201000061.

[60] K. S. Novoselov, V. I. Fal′ko, L. Colombo, P. R. Gellert, M. G. Schwab, and K. Kim, "A roadmap for graphene," *Nature*, vol. 490, no. 7419, pp. 192–200, Oct. 2012, doi: 10.1038/nature11458.

[61] R. Tarcan, O. Todor-Boer, I. Petrovai, C. Leordean, S. Astilean, and I. Botiz, "Reduced graphene oxide today," *J. Mater. Chem. C*, vol. 8, no. 4, pp. 1198–1224, 2020, doi: 10.1039/C9TC04916A.

[62] D. C. Marcano *et al.*, "Improved synthesis of graphene oxide," *ACS Nano*, vol. 4, no. 8, pp. 4806–4814, 2010, doi: 10.1021/nn1006368.

[63] N. I. Zaaba, K. L. Foo, U. Hashim, S. J. Tan, W.-W. Liu, and C. H. Voon, "Synthesis of Graphene Oxide using Modified Hummers Method: Solvent Influence," *Procedia Eng.*, vol. 184, pp. 469–477, 2017, doi: 10.1016/j.proeng.2017.04.118.

[64] W. Yu, L. Sisi, Y. Haiyan, and L. Jie, "Progress in the functional modification of graphene/graphene oxide: a review," *RSC Adv.*, vol. 10, no. 26, pp. 15328–15345, 2020, doi: 10.1039/D0RA01068E.

[65] E. Jimenez-Cervantes, J. López-Barroso, A. L. Martínez-Hernández, and C. Velasco-Santos, "Graphene-Based Materials Functionalization with Natural Polymeric Biomolecules," in *Recent Advances in Graphene Research*, P. K. Nayak, Ed. InTech, 2016. doi: 10.5772/64001.

[66] V. Agarwal and P. B. Zetterlund, "Strategies for reduction of graphene oxide – A comprehensive review," *Chem. Eng. J.*, vol. 405, p. 127018, Feb. 2021, doi: 10.1016/j.cej.2020.127018.

[67] V. B. Mohan *et al.*, "Graphene-based materials and their composites: A review on production, applications and product limitations," *Compos. Part B Eng.*, vol. 142, no. January, pp. 200–220, 2018, doi: 10.1016/j.compositesb.2018.01.013.

[68] Q. Xiang, B. Cheng, and J. Yu, "Graphene-Based Photocatalysts for Solar-Fuel Generation," *Angew. Chem. - Int. Ed.*, vol. 54, no. 39, pp. 11350–11366, 2015, doi: 10.1002/anie.201411096.

[69] B. Qiu, M. Xing, and J. Zhang, “Recent advances in three-dimensional graphene based materials for catalysis applications,” *Chem. Soc. Rev.*, vol. 47, no. 6, pp. 2165–2216, Mar. 2018, doi: 10.1039/C7CS00904F.

[70] A. E. Jakus, E. B. Secor, A. L. Rutz, S. W. Jordan, M. C. Hersam, and R. N. Shah, “Three-Dimensional Printing of High-Content Graphene Scaffolds for Electronic and Biomedical Applications,” *ACS Nano*, vol. 9, no. 4, pp. 4636–4648, Apr. 2015, doi: 10.1021/acsnano.5b01179.

[71] F. Perreault, A. Fonseca de Faria, and M. Elimelech, “Environmental applications of graphene-based nanomaterials,” *Chem Soc Rev*, vol. 44, no. 16, pp. 5861–5896, 2015, doi: 10.1039/C5CS00021A.

[72] J. Bartelmess, S. J. Quinn, and S. Giordani, “Carbon nanomaterials: multi-functional agents for biomedical fluorescence and Raman imaging,” *Chem Soc Rev*, vol. 44, no. 14, pp. 4672–4698, 2015, doi: 10.1039/C4CS00306C.

[73] M. Riley and W. Vermerris, “Recent Advances in Nanomaterials for Gene Delivery—A Review,” *Nanomaterials*, vol. 7, no. 5, p. 94, 2017, doi: 10.3390/nano7050094.

[74] X. Ding, H. Liu, and Y. Fan, “Graphene-Based Materials in Regenerative Medicine,” *Adv. Healthc. Mater.*, vol. 4, no. 10, pp. 1451–1468, 2015, doi: 10.1002/adhm.201500203.

[75] Z. Wang and Z. Dai, “Carbon nanomaterial-based electrochemical biosensors: an overview,” *Nanoscale*, vol. 7, no. 15, pp. 6420–6431, 2015, doi: 10.1039/C5NR00585J.

[76] D. Chai *et al.*, “Delivery of Oridonin and Methotrexate via PEGylated Graphene Oxide,” *ACS Appl. Mater. Interfaces*, vol. 11, no. 26, pp. 22915–22924, Jul. 2019, doi: 10.1021/acsami.9b03983.

[77] Y. Oz, A. Barras, R. Sanyal, R. Boukherroub, S. Szunerits, and A. Sanyal, “Functionalization of Reduced Graphene Oxide via Thiol–Maleimide ‘Click’ Chemistry: Facile Fabrication of Targeted Drug Delivery Vehicles,” *ACS Appl. Mater. Interfaces*, vol. 9, no. 39, pp. 34194–34203, Oct. 2017, doi: 10.1021/acsami.7b08433.

[78] K. M. Wyss, D. X. Luong, and J. M. Tour, “Large-Scale Syntheses of 2D Materials: Flash Joule Heating and Other Methods,” *Adv. Mater.*, vol. 34, no. 8, p. 2106970, Feb. 2022, doi: 10.1002/adma.202106970.

[79] S. Syama and P. V. Mohanan, “Comprehensive Application of Graphene: Emphasis on Biomedical Concerns,” *Nano-Micro Lett.*, vol. 11, no. 1, p. 6, Dec. 2019, doi: 10.1007/s40820-019-0237-5.

[80] R. Rai, S. Alwani, and I. Badea, “Polymeric Nanoparticles in Gene Therapy: New Avenues of Design and Optimization for Delivery Applications,” *Polymers*, vol. 11, no. 4, p. 745, Apr. 2019, doi: 10.3390/polym11040745.

[81] M. Teymouri, M. Mashreghi, E. Saburi, A. Hejazi, and A. R. Nikpoor, “The trip of a drug inside the body: From a lipid-based nanocarrier to a target cell,” *J. Controlled Release*, vol. 309, pp. 59–71, Sep. 2019, doi: 10.1016/j.jconrel.2019.07.027.

[82] P. R. Riley and R. J. Narayan, “Recent advances in carbon nanomaterials for biomedical applications: A review,” *Curr. Opin. Biomed. Eng.*, vol. 17, p. 100262, Mar. 2021, doi: 10.1016/j.cobme.2021.100262.

[83] C. Bharti, N. Gulati, U. Nagaich, and A. Pal, “Mesoporous silica nanoparticles in target drug delivery system: A review,” *Int. J. Pharm. Investig.*, vol. 5, no. 3, p. 124, 2015, doi: 10.4103/2230-973X.160844.

[84] S. Siddique and J. C. L. Chow, “Gold Nanoparticles for Drug Delivery and Cancer Therapy,” *Appl. Sci.*, vol. 10, no. 11, p. 3824, May 2020, doi: 10.3390/app10113824.

[85] A. V. Samrot, C. S. Sahithya, J. Selvarani A, S. K. Purayil, and P. Ponnaiah, “A review on synthesis, characterization and potential biological applications of superparamagnetic iron oxide nanoparticles,” *Curr. Res. Green Sustain. Chem.*, vol. 4, p. 100042, 2021, doi: 10.1016/j.crgsc.2020.100042.

[86] X. Zhang *et al.*, “Distribution and biocompatibility studies of graphene oxide in mice after intravenous administration,” *Carbon*, vol. 49, no. 3, pp. 986–995, Mar. 2011, doi: 10.1016/j.carbon.2010.11.005.

[87] A. Sasidharan *et al.*, “Differential nano-bio interactions and toxicity effects of pristine versus functionalized graphene,” *Nanoscale*, vol. 3, no. 6, p. 2461, 2011, doi: 10.1039/c1nr10172b.

[88] X. Zhang, W. Hu, J. Li, L. Tao, and Y. Wei, “A comparative study of cellular uptake and cytotoxicity of multi-walled carbon nanotubes, graphene oxide, and nanodiamond,” *Toxicol. Res.*, vol. 1, no. 1, p. 62, 2012, doi: 10.1039/c2tx20006f.

[89] I. S. Raja *et al.*, “Differential Toxicity of Graphene Family Nanomaterials Concerning Morphology,” in *Multifaceted Biomedical Applications of Graphene*, vol. 1351, D.-W. Han and S. W. Hong, Eds. Singapore: Springer Singapore, 2022, pp. 23–39. doi: 10.1007/978-981-16-4923-3_2.

[90] G. Duan *et al.*, “Graphene-Induced Pore Formation on Cell Membranes,” *Sci. Rep.*, vol. 7, no. 1, p. 42767, Mar. 2017, doi: 10.1038/srep42767.

[91] S. C. Reshma, S. Syama, and P. V. Mohanan, “Nano-biointeractions of PEGylated and bare reduced graphene oxide on lung alveolar epithelial cells: A comparative in vitro study,” *Colloids Surf. B Biointerfaces*, vol. 140, pp. 104–116, 2016, doi: 10.1016/j.colsurfb.2015.12.030.

[92] A. Wang *et al.*, “Role of surface charge and oxidative stress in cytotoxicity and genotoxicity of graphene oxide towards human lung fibroblast cells: Toxicity of graphene oxide to HLF cells,” *J. Appl. Toxicol.*, vol. 33, no. 10, pp. 1156–1164, Oct. 2013, doi: 10.1002/jat.2877.

[93] K. Wu, Q. Zhou, and S. Ouyang, “Direct and Indirect Genotoxicity of Graphene Family Nanomaterials on DNA—A Review,” *Nanomaterials*, vol. 11, no. 11, p. 2889, Oct. 2021, doi: 10.3390/nano11112889.

[94] W. Hu *et al.*, “Protein corona-mediated mitigation of cytotoxicity of graphene oxide,” *ACS Nano*, vol. 5, no. 5, pp. 3693–3700, May 2011, doi: 10.1021/nn200021j.

[95] B. Zhang, P. Wei, Z. Zhou, and T. Wei, “Interactions of graphene with mammalian cells: Molecular mechanisms and biomedical insights,” *Adv. Drug Deliv. Rev.*, vol. 105, pp. 145–162, 2016, doi: 10.1016/j.addr.2016.08.009.

[96] D. Chen, C. A. Dougherty, K. Zhu, and H. Hong, “Theranostic applications of carbon nanomaterials in cancer: Focus on imaging and cargo delivery,” *J. Controlled Release*, vol. 210, pp. 230–245, Jul. 2015, doi: 10.1016/j.jconrel.2015.04.021.

[97] Y. Qin *et al.*, “Graphene quantum dots induce apoptosis, autophagy, and inflammatory response via p38 mitogen-activated protein kinase and nuclear factor-κB mediated signaling pathways in activated THP-1 macrophages,” *Toxicology*, vol. 327, pp. 62–76, Jan. 2015, doi: 10.1016/j.tox.2014.10.011.

[98] X. Zhang, W. Hu, J. Li, L. Tao, and Y. Wei, “A comparative study of cellular uptake and cytotoxicity of multi-walled carbon nanotubes, graphene oxide, and nanodiamond,” *Toxicol. Res.*, vol. 1, no. 1, p. 62, Jul. 2012, doi: 10.1039/c2tx20006f.

[99] X. Zhang *et al.*, “Distribution and biocompatibility studies of graphene oxide in mice after intravenous administration,” *Carbon*, vol. 49, no. 3, pp. 986–995, Mar. 2011, doi: 10.1016/J.CARBON.2010.11.005.

[100] X. Niu *et al.*, “Electrochemical DNA biosensor based on gold nanoparticles and partially reduced graphene oxide modified electrode for the detection of Listeria monocytogenes hly gene sequence,” *J. Electroanal. Chem.*, vol. 806, pp. 116–122, Dec. 2017, doi: 10.1016/j.jelechem.2017.10.049.

[101] J. Chen and L. Li, “Effect of oxidation degree on the thermal properties of graphene oxide,” *J. Mater. Res. Technol.*, vol. 9, no. 6, pp. 13740–13748, Nov. 2020, doi: 10.1016/j.jmrt.2020.09.092.

[102] H. Kim, D. Lee, J. Kim, T. Kim, and W. J. Kim, “Photothermally Triggered Cytosolic Drug Delivery via Endosome Disruption Using a Functionalized Reduced Graphene Oxide,” *ACS Nano*, vol. 7, no. 8, pp. 6735–6746, 2013, doi: 10.1021/nn403096s.

[103] S. Das *et al.*, “Oxygenated Functional Group Density on Graphene Oxide: Its Effect on Cell Toxicity,” *Part. Part. Syst. Charact.*, vol. 30, no. 2, pp. 148–157, Feb. 2013, doi: 10.1002/ppsc.201200066.

[104] R. F. Pérez *et al.*, “No genome-wide DNA methylation changes found associated with medium-term reduced graphene oxide exposure in human lung epithelial cells,” *Epigenetics*, vol. 15, no. 3, pp. 283–293, Mar. 2020, doi: 10.1080/15592294.2019.1666650.

[105] S. Bengtson *et al.*, “Differences in inflammation and acute phase response but similar genotoxicity in mice following pulmonary exposure to graphene oxide and reduced graphene oxide,” *PLOS ONE*, vol. 12, no. 6, p. e0178355, Jun. 2017, doi: 10.1371/journal.pone.0178355.

[106] A. Palejwala *et al.*, “Biocompatibility of reduced graphene oxide nanoscaffolds following acute spinal cord injury in rats,” *Surg. Neurol. Int.*, vol. 7, no. 1, p. 75, 2016, doi: 10.4103/2152-7806.188905.

[107] Z. A. Jonoush *et al.*, “Surface Modification of Graphene and its Derivatives for Drug Delivery Systems,” *Mini-Rev. Org. Chem.*, vol. 18, no. 1, pp. 78–92, Mar. 2021, doi: 10.2174/1570193X17999200507093954.

[108] H. Y. Wen *et al.*, “Engineered Redox-Responsive PEG Detachment Mechanism in PEGylated Nano-Graphene Oxide for Intracellular Drug Delivery,” *Small*, vol. 8, no. 5, pp. 760–769, 2012, doi: 10.1002/smll.201101613.

[109] R. K. Thapa, Y. S. Youn, J. H. Jeong, H. G. Choi, C. S. Yong, and J. O. Kim, “Graphene oxide-wrapped PEGylated liquid crystalline nanoparticles for effective chemo-photothermal therapy of metastatic prostate cancer cells,” *Colloids Surf. B Biointerfaces*, vol. 143, pp. 271–277, 2016, doi: 10.1016/j.colsurfb.2016.03.045.

[110] N. G. Sahoo *et al.*, “Functionalized carbon nanomaterials as nanocarriers for loading and delivery of a poorly water-soluble anticancer drug: a comparative study,” *Chem. Commun.*, vol. 47, no. 18, p. 5235, 2011, doi: 10.1039/c1cc00075f.

[111] L. Zhang, Z. Lu, Q. Zhao, J. Huang, H. Shen, and Z. Zhang, “Enhanced chemotherapy efficacy by sequential delivery of siRNA and anticancer drugs using PEI-grafted graphene oxide,” *Small*, vol. 7, no. 4, pp. 460–464, 2011, doi: 10.1002/smll.201001522.

[112] E. Song *et al.*, “Hyaluronic acid-decorated graphene oxide nanohybirds as nanocarriers for targeted and pH-response anticancer drug delivery,” *ACS Appl Mater Interfaces*, 2014, doi: 10.1021/am502423r.

[113] H. Zhang *et al.*, “Graphene oxide-chitosan nanocomposites for intracellular delivery of immunostimulatory CpG oligodeoxynucleotides,” *Mater. Sci. Eng. C*, vol. 73, pp. 144–151, 2017, doi: 10.1016/j.msec.2016.12.072.

[114] K. Liu, Y. Wang, H. Li, and Y. Duan, “A facile one-pot synthesis of starch functionalized graphene as nano-carrier for pH sensitive and starch-mediated drug delivery,” *Colloids Surf. B Biointerfaces*, vol. 128, pp. 86–93, 2015, doi: 10.1016/j.colsurfb.2015.02.010.

[115] G. Reina, A. Ruiz, D. Murera, Y. Nishina, and A. Bianco, “‘Ultramixing’: A Simple and Effective Method To Obtain Controlled and Stable Dispersions of Graphene Oxide in Cell Culture Media,” *ACS Appl. Mater. Interfaces*, vol. 11, no. 8, pp. 7695–7702, 2019, doi: 10.1021/acsami.8b18304.

[116] X. Zhang *et al.*, “Mussel-inspired fabrication of functional materials and their environmental applications: Progress and prospects,” *Appl. Mater. Today*, vol. 7, pp. 222–238, Jun. 2017, doi: 10.1016/j.apmt.2017.04.001.

[117] X. Zhang *et al.*, “Preparation of amine functionalized carbon nanotubes via a bioinspired strategy and their application in Cu2+ removal,” *Appl. Surf. Sci.*, vol. 343, pp. 19–27, Jul. 2015, doi: 10.1016/j.apsusc.2015.03.081.

[118] M. Liu *et al.*, “Recent developments in polydopamine: an emerging soft matter for surface modification and biomedical applications,” *Nanoscale*, vol. 8, no. 38, pp. 16819–16840, 2016, doi: 10.1039/C5NR09078D.

[119] L. Huang, M. Liu, H. Huang, Y. Wen, X. Zhang, and Y. Wei, “Recent Advances and Progress on Melanin-like Materials and Their Biomedical Applications,” *Biomacromolecules*, vol. 19, no. 6, pp. 1858–1868, Jun. 2018, doi: 10.1021/acs.biomac.8b00437.

[120] Y. Liu, K. Ai, and L. Lu, “Polydopamine and Its Derivative Materials: Synthesis and Promising Applications in Energy, Environmental, and Biomedical Fields,” *Chem. Rev.*, vol. 114, no. 9, pp. 5057–5115, May 2014, doi: 10.1021/cr400407a.

[121] F. M. Veronese and G. Pasut, “PEGylation, successful approach to drug delivery,” *Drug Discov. Today*, vol. 10, no. 21, pp. 1451–1458, 2005, doi: 10.1016/S1359-6446(05)03575-0.

[122] F. Liu, Y. Sun, C. Kang, and H. Zhu, “Pegylated Drug Delivery Systems: From Design to Biomedical Applications,” *Nano LIFE*, vol. 06, no. 03n04, p. 1642002, 2016, doi: 10.1142/S1793984416420022.

[123] L. Ou *et al.*, “Toxicity of graphene-family nanoparticles: A general review of the origins and mechanisms,” *Part. Fibre Toxicol.*, vol. 13, no. 1, 2016, doi: 10.1186/s12989-016-0168-y.

[124] C. Xu *et al.*, “Long circulating reduced graphene oxide–iron oxide nanoparticles for efficient tumor targeting and multimodality imaging,” *Nanoscale*, vol. 8, no. 25, pp. 12683–12692, 2016, doi: 10.1039/C5NR09193D.

[125] S. D. Li and L. Huang, “Nanoparticles evading the reticuloendothelial system: Role of the supported bilayer,” *Biochim. Biophys. Acta - Biomembr.*, vol. 1788, no. 10, pp. 2259–2266, 2009, doi: 10.1016/j.bbamem.2009.06.022.

[126] Z. Liu, J. T. Robinson, X. Sun, and H. Dai, “PEGylated nanographene oxide for delivery of water-insoluble cancer drugs,” *J Am Chem Soc*, vol. 130, no. 33, pp. 10876–10877, 2008, doi: 10.1021/ja803688x.

[127] K. Yang, J. Wan, S. Zhang, B. Tian, Y. Zhang, and Z. Liu, “The influence of surface chemistry and size of nanoscale graphene oxide on photothermal therapy of cancer using ultra-low laser power,” *Biomaterials*, vol. 33, no. 7, pp. 2206–2214, Mar. 2012, doi: 10.1016/j.biomaterials.2011.11.064.

[128] K. Yang, J. Wan, S. Zhang, Y. Zhang, S. T. Lee, and Z. Liu, “In vivo pharmacokinetics, long-term biodistribution, and toxicology of pegylated graphene in mice,” *ACS Nano*, vol. 5, no. 1, pp. 516–522, 2011, doi: 10.1021/nn1024303.

[129] B. Li *et al.*, “Influence of polyethylene glycol coating on biodistribution and toxicity of nanoscale graphene oxide in mice after intravenous injection,” *Int. J. Nanomedicine*, vol. 9, no. 1, pp. 4697–4707, 2014, doi: 10.2147/IJN.S66591.

[130] K. Yang, S. A. Zhang, G. X. Zhang, X. M. Sun, S. T. Lee, and Z. A. Liu, “Graphene in Mice: Ultrahigh In Vivo Tumor Uptake and Efficient Photothermal Therapy,” *Nano Lett.*, vol. 10, no. 9, pp. 3318–3323, 2010, doi: 10.1021/nl100996u.

[131] A. Sasidharan *et al.*, “Comparative in vivo toxicity, organ biodistribution and immune response of pristine, carboxylated and PEGylated few-layer graphene

sheets in Swiss albino mice: A three month study," *Carbon*, vol. 95, pp. 511–524, 2015, doi: 10.1016/j.carbon.2015.08.074.

[132] S. Shi, F. Chen, E. B. Ehlerding, and W. Cai, "Surface Engineering of Graphene-Based Nanomaterials for Biomedical Applications," *Bioconjug. Chem.*, vol. 25, no. 9, pp. 1609–1619, 2014, doi: 10.1021/bc500332c.

[133] D. R. Dreyer, A. D. Todd, and C. W. Bielawski, "Harnessing the chemistry of graphene oxide," *Chem Soc Rev*, vol. 43, no. 15, pp. 5288–5301, 2014, doi: 10.1039/c4cs00060a.

[134] J. Chen, B. Yao, C. Li, and G. Shi, "An improved Hummers method for eco-friendly synthesis of graphene oxide," *Carbon*, vol. 64, no. 1, pp. 225–229, 2013, doi: 10.1016/j.carbon.2013.07.055.

[135] W. Gao, D. R. Dreyer, S. Park, C. W. Bielawski, and R. S. Ruoff, "The chemistry of graphene oxide," *Chem Soc Rev*, vol. 39, no. 1, pp. 228–240, 2010, doi: 10.1039/b917103g.

[136] Q. Ren, L. Feng, R. Fan, X. Ge, and Y. Sun, "Water-dispersible triethylenetetramine-functionalized graphene: Preparation, characterization and application as an amperometric glucose sensor," *Mater. Sci. Eng. C*, vol. 68, pp. 308–316, 2016, doi: 10.1016/j.msec.2016.05.124.

[137] J. Liu, Y. Ye, Y. Xue, X. Xie, and Y.-W. W. Mai, "Recent advances in covalent functionalization of carbon nanomaterials with polymers: Strategies and perspectives," *J. Polym. Sci. Part Polym. Chem.*, vol. 55, no. 4, pp. 622–631, 2017, doi: 10.1002/pola.28426.

[138] X. Gao, J. Jang, and S. Nagase, "Hydrazine and thermal reduction of graphene oxide: Reaction mechanisms, product structures, and reaction design," *J. Phys. Chem. C*, vol. 114, no. 2, pp. 832–842, 2010, doi: 10.1021/jp909284g.

[139] C. K. Chua and M. Pumera, "Covalent chemistry on graphene," *Chem. Soc. Rev.*, vol. 42, no. 8, p. 3222, Mar. 2013, doi: 10.1039/c2cs35474h.

[140] R. K. Singh, R. Kumar, and D. P. Singh, "Graphene oxide: strategies for synthesis, reduction and frontier applications," *RSC Adv.*, vol. 6, no. 69, pp. 64993–65011, 2016, doi: 10.1039/C6RA07626B.

[141] S. Stankovich, R. D. Piner, S. B. T. Nguyen, and R. S. Ruoff, "Synthesis and exfoliation of isocyanate-treated graphene oxide nanoplatelets," *Carbon*, vol. 44, no. 15, pp. 3342–3347, 2006, doi: 10.1016/j.carbon.2006.06.004.

[142] R. Wang, Y. Wang, C. Xu, J. Sun, and L. Gao, "Facile one-step hydrazine-assisted solvothermal synthesis of nitrogen-doped reduced graphene oxide: reduction effect and mechanisms," *RSC Adv*, vol. 3, no. 4, pp. 1194–1200, 2013, doi: 10.1039/C2RA21825A.

[143] M. J. McAllister *et al.*, "Single Sheet Functionalized Graphene by Oxidation and Thermal Expansion of Graphite," *Chem. Mater.*, vol. 19, no. 18, pp. 4396–4404, Sep. 2007, doi: 10.1021/cm0630800.

[144] J. Zhan, Z. Lei, and Y. Zhang, "Non-covalent interactions of graphene surface: Mechanisms and applications," *Chem*, vol. 8, no. 4, pp. 947–979, Apr. 2022, doi: 10.1016/j.chempr.2021.12.015.

[145] J. Liu, L. Cui, and D. Losic, “Graphene and graphene oxide as new nanocarriers for drug delivery applications,” *Acta Biomater*, vol. 9, no. 12, pp. 9243–9257, 2013, doi: 10.1016/j.actbio.2013.08.016.

[146] J. Liu, W. Yang, L. Tao, D. Li, C. Boyer, and T. P. Davis, “Thermosensitive graphene nanocomposites formed using pyrene-terminal polymers made by RAFT polymerization,” *J. Polym. Sci. Part Polym. Chem.*, vol. 48, no. 2, pp. 425–433, 2010, doi: 10.1002/pola.23802.

[147] J. Liu *et al.*, “Synthesis, characterization, and multilayer assembly of pH sensitive graphene-polymer nanocomposites,” *Langmuir*, vol. 26, no. 12, pp. 10068–10075, 2010, doi: 10.1021/la1001978.

[148] Y. Zhang, C. Liu, W. Shi, Z. Wang, L. Dai, and X. Zhang, “Direct Measurements of the Interaction between Pyrene and Graphite in Aqueous Media by Single Molecule Force Spectroscopy: Understanding the $π$−$π$ Interactions,” *Langmuir*, vol. 23, no. 15, pp. 7911–7915, 2007, doi: 10.1021/la700876d.

[149] Z. Xu, S. Wang, Y. Li, M. Wang, P. Shi, and X. Huang, “Covalent functionalization of graphene oxide with biocompatible poly(ethylene glycol) for delivery of paclitaxel,” *ACS Appl Mater Interfaces*, vol. 6, no. 19, pp. 17268–17276, 2014, doi: 10.1021/am505308f.

[150] M. Kazempour, H. Namazi, A. Akbarzadeh, and R. Kabiri, “Synthesis and characterization of PEG-functionalized graphene oxide as an effective pH-sensitive drug carrier,” *Artif. Cells Nanomedicine Biotechnol.*, vol. 47, no. 1, pp. 90–94, Dec. 2019, doi: 10.1080/21691401.2018.1543196.

[151] A. Deb and R. Vimala, “Camptothecin loaded graphene oxide nanoparticle functionalized with polyethylene glycol and folic acid for anticancer drug delivery,” *J. Drug Deliv. Sci. Technol.*, vol. 43, pp. 333–342, Feb. 2018, doi: 10.1016/j.jddst.2017.10.025.

[152] R. L. Setten, J. J. Rossi, and S. Han, “The current state and future directions of RNAi-based therapeutics,” *Nat. Rev. Drug Discov.*, vol. 18, no. 6, pp. 421–446, Jun. 2019, doi: 10.1038/s41573-019-0017-4.

[153] A. Fire, S. Xu, M. K. Montgomery, S. A. Kostas, S. E. Driver, and C. C. Mello, “Potent and specific genetic interference by double-stranded RNA in Caenorhabditis elegans,” *Nature*, vol. 391, no. 6669, pp. 806–811, Feb. 1998, doi: 10.1038/35888.

[154] R. Bernards, “[The Nobel Prize in Physiology or Medicine for 2006 for the discovery of RNA interference],” *Ned. Tijdschr. Geneeskd.*, vol. 150, no. 52, pp. 2849–2853, Dec. 2006.

[155] S. M. Elbashir, J. Harborth, W. Lendeckel, A. Yalcin, K. Weber, and T. Tuschl, “Duplexes of 21-nucleotide RNAs mediate RNA interference in cultured mammalian cells,” *Nature*, vol. 411, no. 6836, pp. 494–498, May 2001, doi: 10.1038/35078107.

[156] D. Adams *et al.*, “Patisiran, an RNAi Therapeutic, for Hereditary Transthyretin Amyloidosis,” *N. Engl. J. Med.*, vol. 379, no. 1, pp. 11–21, Jul. 2018, doi: 10.1056/NEJMoa1716153.

[157] M. Ashrafizadeh *et al.*, “Biomedical application of chitosan-based nanoscale delivery systems: Potential usefulness in siRNA delivery for cancer therapy,” *Carbohydr. Polym.*, vol. 260, p. 117809, May 2021, doi: 10.1016/j.carbpol.2021.117809.

[158] B. Hu *et al.*, “Therapeutic siRNA: state of the art,” *Signal Transduct. Target. Ther.*, vol. 5, no. 1, p. 101, Dec. 2020, doi: 10.1038/s41392-020-0207-x.

[159] W. Alshaer *et al.*, “siRNA: Mechanism of action, challenges, and therapeutic approaches,” *Eur. J. Pharmacol.*, vol. 905, p. 174178, Aug. 2021, doi: 10.1016/j.ejphar.2021.174178.

[160] S. Aghamiri *et al.*, “Nonviral siRNA delivery systems for pancreatic cancer therapy,” *Biotechnol. Bioeng.*, vol. 118, no. 10, pp. 3669–3690, Oct. 2021, doi: 10.1002/bit.27869.

[161] M. Ramamoorth, “Non Viral Vectors in Gene Therapy- An Overview,” *J. Clin. Diagn. Res.*, 2015, doi: 10.7860/JCDR/2015/10443.5394.

[162] R. Goswami *et al.*, “Gene Therapy Leaves a Vicious Cycle,” *Front. Oncol.*, vol. 9, p. 297, Apr. 2019, doi: 10.3389/fonc.2019.00297.

[163] S. K. Tripathi, R. Goyal, K. C. Gupta, and P. Kumar, “Functionalized graphene oxide mediated nucleic acid delivery,” *Carbon*, vol. 51, no. 1, pp. 224–235, 2013, doi: 10.1016/j.carbon.2012.08.047.

[164] Y.-P. Huang *et al.*, “Suppression of Breast Cancer Cell Migration by Small Interfering RNA Delivered by Polyethylenimine-Functionalized Graphene Oxide,” *Nanoscale Res. Lett.*, vol. 11, no. 1, p. 247, Dec. 2016, doi: 10.1186/s11671-016-1463-0.

[165] H. Q. Bao *et al.*, “Chitosan-Functionalized Graphene Oxide as a Nanocarrier for Drug and Gene Delivery,” *Small*, vol. 7, no. 11, pp. 1569–1578, Jun. 2011, doi: 10.1002/smll.201100191.

[166] H. Hu, C. Tang, and C. Yin, “Folate conjugated trimethyl chitosan/graphene oxide nanocomplexes as potential carriers for drug and gene delivery,” *Mater. Lett.*, vol. 125, pp. 82–85, 2014, doi: 10.1016/j.matlet.2014.03.133.

[167] X. Liu *et al.*, “Polyamidoamine dendrimer and oleic acid-functionalized graphene as biocompatible and efficient gene delivery vectors,” *ACS Appl. Mater. Interfaces*, vol. 6, no. 11, pp. 8173–8183, Jun. 2014, doi: 10.1021/am500812h.

[168] M. Teimouri, A. H. Nia, K. Abnous, H. Eshghi, and M. Ramezani, “Graphene oxide–cationic polymer conjugates: Synthesis and application as gene delivery vectors,” *Plasmid*, vol. 84–85, pp. 51–60, Mar. 2016, doi: 10.1016/j.plasmid.2016.03.002.

[169] S. Han *et al.*, “Effects of hydrophobic core components in amphiphilic PDMAEMA nanoparticles on siRNA delivery,” *Biomaterials*, vol. 48, pp. 45–55, Apr. 2015, doi: 10.1016/j.biomaterials.2015.01.026.

[170] P. van de Wetering, E. E. Moret, N. M. E. Schuurmans-Nieuwenbroek, M. J. van Steenbergen, and W. E. Hennink, “Structure−Activity Relationships of Water-Soluble Cationic Methacrylate/Methacrylamide Polymers for Nonviral Gene

Delivery," *Bioconjug. Chem.*, vol. 10, no. 4, pp. 589–597, 1999, doi: 10.1021/bc980148w.

[171] Y. Y. Durmaz, Y.-L. L. Lin, and M. E. H. H. ElSayed, "Development of Degradable, pH-Sensitive Star Vectors for Enhancing the Cytoplasmic Delivery of Nucleic Acids," *Adv. Funct. Mater.*, vol. 23, no. 31, pp. 3885–3895, 2013, doi: 10.1002/adfm.201203762.

[172] K. Bukowski, M. Kciuk, and R. Kontek, "Mechanisms of Multidrug Resistance in Cancer Chemotherapy," *Int. J. Mol. Sci.*, vol. 21, no. 9, p. 3233, May 2020, doi: 10.3390/ijms21093233.

[173] Y. Chen, S. R. Bathula, J. Li, and L. Huang, "Multifunctional Nanoparticles Delivering Small Interfering RNA and Doxorubicin Overcome Drug Resistance in Cancer," *J. Biol. Chem.*, vol. 285, no. 29, pp. 22639–22650, Jul. 2010, doi: 10.1074/jbc.M110.125906.

[174] J. Y. Yhee *et al.*, "Cancer-targeted MDR-1 siRNA delivery using self-cross-linked glycol chitosan nanoparticles to overcome drug resistance," *J. Controlled Release*, vol. 198, pp. 1–9, Jan. 2015, doi: 10.1016/j.jconrel.2014.11.019.

[175] J. Kim *et al.*, "Combination of cancer-specific prodrug nanoparticle with Bcl-2 inhibitor to overcome acquired drug resistance," *J. Controlled Release*, vol. 330, pp. 920–932, Feb. 2021, doi: 10.1016/j.jconrel.2020.10.065.

[176] G. Szakács, J. K. Paterson, J. A. Ludwig, C. Booth-Genthe, and M. M. Gottesman, "Targeting multidrug resistance in cancer," *Nat. Rev. Drug Discov.*, vol. 5, no. 3, pp. 219–234, Mar. 2006, doi: 10.1038/nrd1984.

[177] R. I. Pakunlu, Y. Wang, W. Tsao, V. Pozharov, T. J. Cook, and T. Minko, "Enhancement of the Efficacy of Chemotherapy for Lung Cancer by Simultaneous Suppression of Multidrug Resistance and Antiapoptotic Cellular Defense," *Cancer Res.*, vol. 64, no. 17, pp. 6214–6224, Sep. 2004, doi: 10.1158/0008-5472.CAN-04-0001.

[178] S. J. Zhen, T. T. Wang, Y. X. Liu, Z. L. Wu, H. Y. Zou, and C. Z. Huang, "Reduced graphene oxide coated Cu 2−x Se nanoparticles for targeted chemo-photothermal therapy," *J. Photochem. Photobiol. B*, vol. 180, pp. 9–16, Mar. 2018, doi: 10.1016/j.jphotobiol.2018.01.020.

[179] Z. Yang *et al.*, "Simultaneous Delivery of antimiR-21 and Doxorubicin by Graphene Oxide for Reducing Toxicity in Cancer Therapy," *ACS Omega*, vol. 5, no. 24, pp. 14437–14443, Jun. 2020, doi: 10.1021/acsomega.0c01010.

[180] S. Izadi *et al.*, "Codelivery of HIF-1α siRNA and Dinaciclib by Carboxylated Graphene Oxide-Trimethyl Chitosan-Hyaluronate Nanoparticles Significantly Suppresses Cancer Cell Progression," *Pharm. Res.*, vol. 37, no. 10, p. 196, Oct. 2020, doi: 10.1007/s11095-020-02892-y.

[181] K. Y. Cho *et al.*, "Ionic block copolymer doped reduced graphene oxide supports with ultra-fine Pd nanoparticles: strategic realization of ultra-accelerated nanocatalysis," *J. Mater. Chem. A*, vol. 3, no. 41, pp. 20471–20476, 2015, doi: 10.1039/C5TA06076A.

[182] P. Petrov, F. Stassin, C. Pagnoulle, and R. Jérôme*, “Noncovalent functionalization of multi-walled carbon nanotubes by pyrene containing polymers,” *Chem Commun*, vol. 0, no. 23, pp. 2904–2905, 2003, doi: 10.1039/B307751A.

[183] Z. Liu, J. T. Robinson, X. Sun, and H. Dai, “PEGylated nanographene oxide for delivery of water-insoluble cancer drugs,” *J Am Chem Soc*, vol. 130, no. 33, pp. 10876–10877, 2008, doi: 10.1021/ja803688x.

[184] X. Sun *et al.*, “Nano-Graphene Oxide for Cellular Imaging and Drug Delivery,” *Nano Res*, vol. 1, no. 3, pp. 203–212, Sep. 2008, doi: 10.1007/s12274-008-8021-8.

[185] K. Yang, L. Feng, X. Shi, and Z. Liu, “Nano-graphene in biomedicine: theranostic applications,” *Chem Soc Rev*, vol. 42, no. 2, pp. 530–547, Dec. 2013, doi: 10.1039/C2CS35342C.

[186] K. Yang, S. A. Zhang, G. X. Zhang, X. M. Sun, S. T. Lee, and Z. A. Liu, “Graphene in Mice: Ultrahigh In Vivo Tumor Uptake and Efficient Photothermal Therapy,” *Nano Lett.*, vol. 10, no. 9, pp. 3318–3323, 2010, doi: 10.1021/nl100996u.

[187] P. Y. Liyanage *et al.*, “Nanoparticle-mediated targeted drug delivery for breast cancer treatment,” *Biochim. Biophys. Acta BBA - Rev. Cancer*, vol. 1871, no. 2, pp. 419–433, Apr. 2019, doi: 10.1016/j.bbcan.2019.04.006.

[188] A. T. Stopeck *et al.*, “The role of targeted therapy and biomarkers in breast cancer treatment,” *Clin. Exp. Metastasis*, vol. 29, no. 7, pp. 807–819, Oct. 2012, doi: 10.1007/s10585-012-9496-y.

[189] V. V. Padma, “An overview of targeted cancer therapy,” *BioMedicine*, vol. 5, no. 4, p. 19, Dec. 2015, doi: 10.7603/s40681-015-0019-4.

[190] S. M. Barratt-Boyes, “Making the most of mucin: a novel target for tumor immunotherapy,” *Cancer Immunol Immunother*, vol. 43, pp. 142–151, 1996, doi: 10.1007/s002620050315.

[191] P. Thulasiraman and A. B. Johnson, “Regulation of Mucin 1 and multidrug resistance protein 1 by honokiol enhances the efficacy of doxorubicin-mediated growth suppression in mammary carcinoma cells,” *Int. J. Oncol.*, p. 8, 2016.

[192] A. Moore, Z. Medarova, A. Potthast, and G. Dai, “In Vivo Targeting of Underglycosylated MUC-1 Tumor Antigen Using a Multimodal Imaging Probe,” *Cancer Res.*, vol. 64, no. 5, pp. 1821–1827, 2004, doi: 10.1158/0008-5472.CAN-03-3230.

[193] R. Hussain, N. S. Courtenay-Luck, and G. Siligardi, “Structure-function correlation and biostability of antibody CDR-derived peptides as tumour imaging agents,” *Biomed. Pept. Proteins Nucleic Acids Struct. Synth. Biol. Act.*, vol. 2, no. 3, pp. 67–70, 1997 1996.

[194] N. Kaushal *et al.*, “Synergistic inhibition of aggressive breast cancer cell migration and invasion by cytoplasmic delivery of anti-RhoC silencing RNA and presentation of EPPT1 peptide on ‘smart’ particles,” *J. Controlled Release*, vol. 289, no. July, pp. 79–93, 2018, doi: 10.1016/j.jconrel.2018.07.042.

[195] R. C. Young, R. F. Ozols, and C. E. Myers, “The Anthracycline Antineoplastic Drugs,” *N. Engl. J. Med.*, vol. 305, no. 3, pp. 139–153, Jul. 1981, doi: 10.1056/NEJM198107163050305.

[196] P. S. Rawat, A. Jaiswal, A. Khurana, J. S. Bhatti, and U. Navik, “Doxorubicin-induced cardiotoxicity: An update on the molecular mechanism and novel therapeutic strategies for effective management,” *Biomed. Pharmacother.*, vol. 139, p. 111708, Jul. 2021, doi: 10.1016/j.biopha.2021.111708.

[197] J. J. Doyle, A. I. Neugut, J. S. Jacobson, V. R. Grann, and D. L. Hershman, “Chemotherapy and Cardiotoxicity in Older Breast Cancer Patients: A Population-Based Study,” *J. Clin. Oncol.*, vol. 23, no. 34, pp. 8597–8605, Dec. 2005, doi: 10.1200/JCO.2005.02.5841.

[198] P. K. Singal and N. Iliskovic, “Doxorubicin-Induced Cardiomyopathy,” *N. Engl. J. Med.*, vol. 339, no. 13, pp. 900–905, Sep. 1998, doi: 10.1056/NEJM199809243391307.

[199] T. Yan, S. Zhu, W. Hui, J. He, Z. Liu, and J. Cheng, “Chitosan based pH-responsive polymeric prodrug vector for enhanced tumor targeted co-delivery of doxorubicin and siRNA,” *Carbohydr. Polym.*, vol. 250, p. 116781, Dec. 2020, doi: 10.1016/j.carbpol.2020.116781.

[200] W. Sun *et al.*, “Co-Delivery of Doxorubicin and Anti-BCL-2 siRNA by pH-Responsive Polymeric Vector to Overcome Drug Resistance in In Vitro and In Vivo HepG2 Hepatoma Model,” *Biomacromolecules*, vol. 19, no. 6, pp. 2248–2256, Jun. 2018, doi: 10.1021/acs.biomac.8b00272.

[201] M. Zhou, X. Zhang, X. Xu, X. Chen, and X. Zhang, “Doxorubicin@Bcl-2 siRNA Core@Shell Nanoparticles for Synergistic Anticancer Chemotherapy,” *ACS Appl. Bio Mater.*, vol. 1, no. 2, pp. 289–297, Aug. 2018, doi: 10.1021/acsabm.8b00065.

[202] H. Liu *et al.*, “A targeted nanoplatform co-delivery of pooled siRNA and doxorubicin for reversing of multidrug resistance in breast cancer,” *Nano Res.*, vol. 15, no. 7, pp. 6306–6314, Jul. 2022, doi: 10.1007/s12274-022-4254-1.

[203] H. Durmaz, A. Dag, U. Tunca, and G. Hizal, “Synthesis and characterization of pyrene bearing amphiphilic miktoarm star polymer and its noncovalent interactions with multiwalled carbon nanotubes,” *J. Polym. Sci. Part Polym. Chem.*, vol. 50, no. 12, pp. 2406–2414, 2012, doi: 10.1002/pola.26016.

[204] M. Erdogan, Y. Hepuzer, I. Cianga, Y. Yagcı, and O. Pekcan, “Diffusion of Pyrene End-Capped Polystyrene Prepared via Atom Transfer Radical Polymerization into Polystyrene Gels in the Presence of Toluene,” *J. Phys. Chem. A*, vol. 107, no. 40, pp. 8363–8370, Oct. 2003, doi: 10.1021/jp030036o.

[205] X. M. Liu, H. T. Lee, R. A. Reinhardt, L. A. Marky, and D. Wang, “Novel biomineral-binding cyclodextrins for controlled drug delivery in the oral cavity,” *J. Controlled Release*, vol. 122, no. 1, pp. 54–62, Sep. 2007, doi: 10.1016/j.jconrel.2007.06.021.

[206] T. L. Gilchrist, R. C. Wasson, F. D. King, and G. Wootton, “Intramolecular cycloaddition of azoalkenes derived from terminal alkenoic and alkynoic acids,” *J. Chem. Soc. Perkin 1*, pp. 2511–2516, 1987, doi: 10.1039/p19870002511.

[207] J. Soubhye *et al.*, “From Dynamic Combinatorial Chemistry to in Vivo Evaluation of Reversible and Irreversible Myeloperoxidase Inhibitors,” *ACS Med Chem Lett*, vol. 8, pp. 206–210, 2017, doi: 10.1021/acsmedchemlett.6b00417.

[208] D. Neugebauer, Y. Zhang, T. Pakula, S. S. Sheiko, and K. Matyjaszewski, “Densely-Grafted and Double-Grafted PEO Brushes via ATRP. A Route to Soft Elastomers,” *Macromolecules*, vol. 36, no. 18, pp. 6746–6755, Sep. 2003, doi: 10.1021/ma0345347.

[209] D. Neugebauer, Y. Zhang, T. Pakula, and K. Matyjaszewski, “Heterografted PEO-Pn BA brush copolymers,” *Polymer*, vol. 44, no. 22, pp. 6863–6871, 2003, doi: 10.1016/j.polymer.2003.08.028.

[210] E. Demirel, E. Karaca, and Y. Yuksel Durmaz, “Effective PEGylation method to improve biocompatibility of graphene derivatives,” *Eur. Polym. J.*, vol. 124, no. January, p. 109504, Feb. 2020, doi: 10.1016/j.eurpolymj.2020.109504.

[211] M. J. E. Fischer, “Amine Coupling Through EDC/NHS: A Practical Approach,” in *Surface Plasmon Resonance*, vol. 627, N. J. Mol and M. J. E. Fischer, Eds. Totowa, NJ: Humana Press, 2010, pp. 55–73. doi: 10.1007/978-1-60761-670-2_3.

[212] M. L. Bruschi, Ed., “Mathematical models of drug release,” in *Strategies to Modify the Drug Release from Pharmaceutical Systems*, Woodhead Publishing, 2015, pp. 63–86. doi: 10.1016/B978-0-08-100092-2.00005-9.

[213] Z. Ma, J. Bai, Y. Wang, and X. Jiang, “Impact of shape and pore size of mesoporous silica nanoparticles on serum protein adsorption and RBCS hemolysis,” *ACS Appl. Mater. Interfaces*, vol. 6, no. 4, pp. 2431–2438, Feb. 2014, doi: 10.1021/am404860q.

[214] X. Q. Wei *et al.*, “Insight into the Interaction of Graphene Oxide with Serum Proteins and the Impact of the Degree of Reduction and Concentration,” *ACS Appl. Mater. Interfaces*, vol. 7, no. 24, pp. 13367–13374, 2015, doi: 10.1021/acsami.5b01874.

[215] M. A. Dobrovolskaia, J. D. Clogston, B. W. Neun, J. B. Hall, A. K. Patri, and S. E. McNeil, “Method for Analysis of Nanoparticle Hemolytic Properties in Vitro,” *Nano Lett.*, vol. 8, no. 8, pp. 2180–2187, Aug. 2008, doi: 10.1021/nl0805615.

[216] K. Lu, S. Dong, T. Xia, and L. Mao, “Kupffer Cells Degrade ^{14} C-Labeled Few-Layer Graphene to ^{14} CO_2 in Liver through Erythrophagocytosis,” *ACS Nano*, vol. 15, no. 1, pp. 396–409, Jan. 2021, doi: 10.1021/acsnano.0c07452.

[217] K. H. Liao, Y. S. Lin, C. W. MacOsko, and C. L. Haynes, “Cytotoxicity of graphene oxide and graphene in human erythrocytes and skin fibroblasts,” *ACS Appl. Mater. Interfaces*, vol. 3, no. 7, pp. 2607–2615, 2011, doi: 10.1021/am200428v.

[218] S. S. Park, M. A. Kim, Y. W. Eom, and K. S. Choi, “Bcl-xL blocks high dose doxorubicin-induced apoptosis but not low dose doxorubicin-induced cell death through mitotic catastrophe,” *Biochem. Biophys. Res. Commun.*, vol. 363, no. 4, pp. 1044–1049, Nov. 2007, doi: 10.1016/J.BBRC.2007.09.037.

[219] N. A. P. Franken, H. M. Rodermond, J. Stap, J. Haveman, and C. van Bree, "Clonogenic assay of cells in vitro," *Nat. Protoc.*, vol. 1, no. 5, pp. 2315–2319, 2006, doi: 10.1038/nprot.2006.339.

[220] H. Rafehi, C. Orlowski, G. T. Georgiadis, K. Ververis, A. El-Osta, and T. C. Karagiannis, "Clonogenic Assay: Adherent Cells," *J. Vis. Exp. JoVE*, no. 49, p. 49, 2011, doi: 10.3791/2573.

[221] B. Qin and K. Cheng, "Silencing of the IKKε gene by siRNA inhibits invasiveness and growth of breast cancer cells," *Breast Cancer Res.*, vol. 12, no. 5, p. R74, Oct. 2010, doi: 10.1186/bcr2644.

[222] K. J. Livak and T. D. Schmittgen, "Analysis of Relative Gene Expression Data Using Real-Time Quantitative PCR and the 2−ΔΔCT Method," *Methods*, vol. 25, no. 4, pp. 402–408, Dec. 2001, doi: 10.1006/meth.2001.1262.

[223] R. Fridman, G. Benton, I. Aranoutova, H. K. Kleinman, and R. D. Bonfil, "Increased initiation and growth of tumor cell lines, cancer stem cells and biopsy material in mice using basement membrane matrix protein (Cultrex or Matrigel) co-injection," *Nat. Protoc.*, vol. 7, no. 6, pp. 1138–1144, Jun. 2012, doi: 10.1038/nprot.2012.053.

[224] B. L. Carlson, J. L. Pokorny, M. A. Schroeder, and J. N. Sarkaria, "Establishment, Maintenance, and In Vitro and In Vivo Applications of Primary Human Glioblastoma Multiforme (GBM) Xenograft Models for Translational Biology Studies and Drug Discovery," *Curr. Protoc. Pharmacol.*, vol. 52, no. 1, Mar. 2011, doi: 10.1002/0471141755.ph1416s52.

[225] R. Y. S. Cheng *et al.*, "Studying Triple Negative Breast Cancer Using Orthotopic Breast Cancer Model," *J. Vis. Exp.*, no. 157, p. 60316, Mar. 2020, doi: 10.3791/60316.

[226] M. M. Baris *et al.*, "Xenograft Tumor Volume Measurement in Nude Mice: Estimation of 3D Ultrasound Volume Measurements Based on Manual Caliper Measurements," *J. Basic Clin. Health Sci.*, vol. M, pp. 90–95, 2020, doi: 10.30621/jbachs.2020.902.

[227] A. M. Y. Cheung *et al.*, "Three-dimensional ultrasound biomicroscopy for xenograft growth analysis," *Ultrasound Med. Biol.*, vol. 31, no. 6, pp. 865–870, Jun. 2005, doi: 10.1016/j.ultrasmedbio.2005.03.003.

[228] M. Emi, R. Kim, K. Tanabe, Y. Uchida, and T. Toge, "Targeted therapy against Bcl-2-related proteins in breast cancer cells," *Breast Cancer Res.*, vol. 7, no. 6, p. R940, Dec. 2005, doi: 10.1186/bcr1323.

[229] J. Fang, Y. Liu, Y. Chen, D. Ouyang, G. Yang, and T. Yu, "Graphene quantum dots-gated hollow mesoporous carbon nanoplatform for targeting drug delivery and synergistic chemo-photothermal therapy," *Int. J. Nanomedicine*, vol. Volume 13, pp. 5991–6007, Oct. 2018, doi: 10.2147/IJN.S175934.

[230] Z. Tu *et al.*, "Graphene Oxide-Cyclic R10 Peptide Nuclear Translocation Nanoplatforms for the Surmounting of Multiple-Drug Resistance," *Adv. Funct. Mater.*, vol. 30, no. 35, p. 2000933, Aug. 2020, doi: 10.1002/adfm.202000933.

[231] K. Maruyama-Takahashi *et al.*, “A neutralizing anti-fibroblast growth factor (FGF) 8 monoclonal antibody shows anti-tumor activity against FGF8b-expressing LNCaP xenografts in androgen-dependent and -independent conditions,” *The Prostate*, vol. 68, no. 6, pp. 640–650, May 2008, doi: 10.1002/pros.20728.

[232] G. Yang *et al.*, “Mesoporous silica nanorods intrinsically doped with photosensitizers as a multifunctional drug carrier for combination therapy of cancer,” *Nano Res.*, vol. 8, no. 3, pp. 751–764, Mar. 2015, doi: 10.1007/s12274-014-0558-0.

[233] Y. Yu *et al.*, “Animal heat activated cancer therapy by a traditional catalyst TiO2-Pd/graphene composites,” *Sci. Rep.*, vol. 10, no. 1, p. 15823, Dec. 2020, doi: 10.1038/s41598-020-72682-4.

[234] O. Akhavan and E. Ghaderi, “Graphene Nanomesh Promises Extremely Efficient In Vivo Photothermal Therapy,” *Small*, vol. 9, no. 21, pp. 3593–3601, Nov. 2013, doi: 10.1002/smll.201203106.

[235] J. Bai, Y. Liu, and X. Jiang, “Multifunctional PEG-GO/CuS nanocomposites for near-infrared chemo-photothermal therapy,” *Biomaterials*, vol. 35, no. 22, pp. 5805–5813, 2014, doi: 10.1016/j.biomaterials.2014.04.008.

[236] J. Schindelin *et al.*, “Fiji: an open-source platform for biological-image analysis,” *Nat. Methods*, vol. 9, no. 7, pp. 676–682, Jul. 2012, doi: 10.1038/nmeth.2019.

[237] Y.-R. Yoon, Y. Lim, E. Lee, and M. Lee, “Self-assembly of a peptide rod–coil: a polyproline rod and a cell-penetrating peptide Tat coil,” *Chem. Commun.*, vol. 0, no. 16, p. 1892, 2008, doi: 10.1039/b719868j.

[238] W. Zhang *et al.*, “Preparation of amino-functionalized graphene oxide by Hoffman rearrangement and its performances on polyacrylate coating latex,” *Prog. Org. Coat.*, vol. 94, pp. 9–17, May 2016, doi: 10.1016/j.porgcoat.2016.01.013.

[239] P. Gangwar, S. Singh, and N. Khare, “Study of optical properties of graphene oxide and its derivatives using spectroscopic ellipsometry,” *Appl. Phys. A*, vol. 124, no. 9, p. 620, Sep. 2018, doi: 10.1007/s00339-018-1999-1.

[240] J. I. Paredes, S. Villar-Rodil, A. Martínez-Alonso, J. M. D. Tascón, A. Martinez-Alonso, and J. M. Tascon, “Graphene oxide dispersions in organic solvents,” *Langmuir*, vol. 24, no. 19, pp. 10560–10564, 2008, doi: 10.1021/la801744a.

[241] S. Park *et al.*, “Aqueous Suspension and Characterization of Chemically Modified Graphene Sheets,” *Communications*, vol. 20, no. 14, pp. 6592–6594, 2008, doi: 10.1021/cm801932u.

[242] J. Zhang *et al.*, “Unraveling the molecular interaction mechanism between graphene oxide and aromatic organic compounds with implications on wastewater treatment,” *Chem. Eng. J.*, vol. 358, no. July 2018, pp. 842–849, 2019, doi: 10.1016/j.cej.2018.10.064.

[243] E. Tatarova *et al.*, “Towards large-scale in free-standing graphene and N-graphene sheets,” *Sci. Rep.*, vol. 7, no. 1, p. 10175, 2017, doi: 10.1038/s41598-017-10810-3.

[244] N. Díez, A. Śliwak, S. Gryglewicz, B. Grzyb, and G. Gryglewicz, “Enhanced reduction of graphene oxide by high-pressure hydrothermal treatment,” *RSC Adv.*, vol. 5, no. 100, pp. 81831–81837, 2015, doi: 10.1039/C5RA14461B.

[245] M. Eredia *et al.*, “Morphology and Electronic Properties of Electrochemically Exfoliated Graphene,” *J. Phys. Chem. Lett.*, vol. 8, no. 14, pp. 3347–3355, 2017, doi: 10.1021/acs.jpclett.7b01301.

[246] Z. Baig, O. Mamat, M. Mustapha, A. Mumtaz, K. S. Munir, and M. Sarfraz, “Investigation of tip sonication effects on structural quality of graphene nanoplatelets (GNPs) for superior solvent dispersion,” *Ultrason. Sonochem.*, vol. 45, pp. 133–149, 2018, doi: 10.1016/J.ULTSONCH.2018.03.007.

[247] H. Wang *et al.*, “Thermo-sensitive graphene oxide–polymer nanoparticle hybrids: synthesis, characterization, biocompatibility and drug delivery,” *J. Mater. Chem. B*, vol. 2, no. 10, p. 1362, 2014, doi: 10.1039/c3tb21538e.

[248] Z. Xu, S. Wang, Y. Li, M. Wang, P. Shi, and X. Huang, “Covalent functionalization of graphene oxide with biocompatible poly(ethylene glycol) for delivery of paclitaxel,” *ACS Appl Mater Interfaces*, vol. 6, no. 19, pp. 17268–17276, 2014, doi: 10.1021/am505308f.

[249] G. Gonçalves *et al.*, “Breakdown into nanoscale of graphene oxide: Confined hot spot atomic reduction and fragmentation,” *Sci. Rep.*, vol. 4, pp. 1–8, 2014, doi: 10.1038/srep06735.

[250] S. F. Kiew, L. V. Kiew, H. B. Lee, T. Imae, and L. Y. Chung, “Assessing biocompatibility of graphene oxide-based nanocarriers: A review,” *J. Controlled Release*, vol. 226, pp. 217–228, Mar. 2016, doi: 10.1016/j.jconrel.2016.02.015.

[251] J.-H. Liu, S.-T. Yang, H. Wang, Y. Chang, A. Cao, and Y. Liu, “Effect of size and dose on the biodistribution of graphene oxide in mice,” *Nanomed.*, vol. 7, no. 12, pp. 1801–1812, 2012, doi: 10.2217/nnm.12.60.

[252] X. Guo and N. Mei, “Assessment of the toxic potential of graphene family nanomaterials,” *J. Food Drug Anal.*, vol. 22, no. 1, pp. 105–115, Mar. 2014, doi: 10.1016/J.JFDA.2014.01.009.

[253] A. Bianco, “Graphene: Safe or toxic? the two faces of the medal,” *Angew. Chem. - Int. Ed.*, vol. 52, no. 19, pp. 4986–4997, 2013, doi: 10.1002/anie.201209099.

[254] J. R. Roberts *et al.*, “Evaluation of pulmonary and systemic toxicity following lung exposure to graphite nanoplates: a member of the graphene-based nanomaterial family.,” *Part. Fibre Toxicol.*, vol. 13, no. 1, p. 34, 2016, doi: 10.1186/s12989-016-0145-5.

[255] L. Ma-Hock *et al.*, “Comparative inhalation toxicity of multi-wall carbon nanotubes, graphene, graphite nanoplatelets and low surface carbon black,” *Part. Fibre Toxicol.*, vol. 10, no. 1, p. 23, 2013, doi: 10.1186/1743-8977-10-23.

[256] S. K. Singh *et al.*, “Thrombus Inducing Property of Atomically Thin Graphene Oxide Sheets,” *ACS Nano*, vol. 5, no. 6, pp. 4987–4996, 2011, doi: 10.1021/nn201092p.

[257] D. de Melo-Diogo, R. Lima-Sousa, C. G. Alves, E. C. Costa, R. O. Louro, and I. J. Correia, “Functionalization of graphene family nanomaterials for application in cancer therapy,” *Colloids Surf. B Biointerfaces*, vol. 171, no. July, pp. 260–275, 2018, doi: 10.1016/j.colsurfb.2018.07.030.

[258] C. V. Synatschke, A. Schallon, V. Jérôme, R. Freitag, and A. H. E. Müller, “Influence of Polymer Architecture and Molecular Weight of Poly(2-(dimethylamino)ethyl methacrylate) Polycations on Transfection Efficiency and Cell Viability in Gene Delivery,” *Biomacromolecules*, vol. 12, no. 12, pp. 4247–4255, Dec. 2011, doi: 10.1021/bm201111d.

[259] S. Wu *et al.*, “Adsorption properties of doxorubicin hydrochloride onto graphene oxide: Equilibrium, kinetic and thermodynamic studies,” *Materials*, vol. 6, no. 5, pp. 2026–2042, 2013, doi: 10.3390/ma6052026.

[260] M. J. Hortigüela, D. Machado, I. Bdikin, V. Neto, and G. Otero-Irurueta, “Chemical Changes of Graphene Oxide Thin Films Induced by Thermal Treatment under Vacuum Conditions,” *Coatings*, vol. 10, no. 2, p. 113, Jan. 2020, doi: 10.3390/coatings10020113.

[261] M. Niu *et al.*, “Polyethylene glycol grafted with carboxylated graphene oxide as a novel interface modifier for polylactic acid/graphene nanocomposites,” *R. Soc. Open Sci.*, vol. 7, no. 7, p. 192154, Jul. 2020, doi: 10.1098/rsos.192154.

[262] K. Taylor, T. A. Tabish, and R. J. Narayan, “Drug Release Kinetics of DOX-Loaded Graphene-Based Nanocarriers for Ovarian and Breast Cancer Therapeutics,” *Appl. Sci.*, vol. 11, no. 23, p. 11151, Nov. 2021, doi: 10.3390/app112311151.

[263] L. Pourtalebi Jahromi, M. Ghazali, H. Ashrafi, and A. Azadi, “A comparison of models for the analysis of the kinetics of drug release from PLGA-based nanoparticles,” *Heliyon*, vol. 6, no. 2, p. e03451, Feb. 2020, doi: 10.1016/j.heliyon.2020.e03451.

[264] M. P. Paarakh, P. A. Jose, C. M. Setty, and G. V. P. Christoper, “Release Kinetics – Concepts and Applications,” *Int. J. Pharm. Res. Technol.*, vol. 8, no. 1, Jan. 2019, doi: 10.31838/ijprt/08.01.02.

[265] N. S. Heredia *et al.*, “Comparative statistical analysis of the release kinetics models for nanoprecipitated drug delivery systems based on poly(lactic-co-glycolic acid),” *PLOS ONE*, vol. 17, no. 3, p. e0264825, Mar. 2022, doi: 10.1371/journal.pone.0264825.

[266] D. Y. Arifin, L. Y. Lee, and C.-H. Wang, “Mathematical modeling and simulation of drug release from microspheres: Implications to drug delivery systems,” *Adv. Drug Deliv. Rev.*, vol. 58, no. 12–13, pp. 1274–1325, Nov. 2006, doi: 10.1016/j.addr.2006.09.007.

[267] N. C. Stellwagen, “Electrophoresis of DNA in agarose gels, polyacrylamide gels and in free solution,” *Electrophoresis*, vol. 30, no. S1, pp. S188–S195, Jun. 2009, doi: 10.1002/elps.200900052.

[268] Y. Gu *et al.*, “A polyamidoamne dendrimer functionalized graphene oxide for DOX and MMP-9 shRNA plasmid co-delivery,” *Mater. Sci. Eng. C*, vol. 70, pp. 572–585, Jan. 2017, doi: 10.1016/j.msec.2016.09.035.

[269] P. Arenas-Guerrero *et al.*, “Determination of the size distribution of non-spherical nanoparticles by electric birefringence-based methods,” *Sci. Rep.*, vol. 8, no. 1, p. 9502, Dec. 2018, doi: 10.1038/s41598-018-27840-0.

[270] M. Lotya, A. Rakovich, J. F. Donegan, and J. N. Coleman, “Measuring the lateral size of liquid-exfoliated nanosheets with dynamic light scattering,” *Nanotechnology*, vol. 24, no. 26, p. 265703, Jul. 2013, doi: 10.1088/0957-4484/24/26/265703.

[271] M. Danaei *et al.*, “Impact of Particle Size and Polydispersity Index on the Clinical Applications of Lipidic Nanocarrier Systems,” *Pharmaceutics*, vol. 10, no. 2, p. 57, May 2018, doi: 10.3390/pharmaceutics10020057.

[272] C. Gest *et al.*, “Rac3 induces a molecular pathway triggering breast cancer cell aggressiveness: differences in MDA-MB-231 and MCF-7 breast cancer cell lines,” *BMC Cancer*, vol. 13, no. 1, p. 63, Dec. 2013, doi: 10.1186/1471-2407-13-63.

[273] H. Liu, C. Zang, M. H. Fenner, K. Possinger, and E. Elstner, “PPARγ Ligands and ATRA Inhibit the Invasion of Human Breast Cancer Cells in vitro,” *Breast Cancer Res. Treat.*, vol. 79, no. 1, pp. 63–74, May 2003, doi: 10.1023/A:1023366117157.

[274] M. D. Walsh, S. M. Luckie, M. C. Cummings, T. M. Antalis, and M. A. McGuckin, “Heterogeneity of MUC1 expression by human breast carcinoma cell lines in vivo and in vitro,” *Breast Cancer Res. Treat.*, vol. 58, no. 3, pp. 255–266, 1999, doi: 10.1023/a:1006345301364.

[275] O. Tacar, P. Sriamornsak, and C. R. Dass, “Doxorubicin: an update on anticancer molecular action, toxicity and novel drug delivery systems,” *J. Pharm. Pharmacol.*, vol. 65, no. 2, pp. 157–170, Dec. 2012, doi: 10.1111/j.2042-7158.2012.01567.x.

[276] L. Fan, Y.-J. Fu, Q.-L. Liu, D.-T. Lu, C. Dong, and S.-M. Shuang, “Novel far-visible and near-infrared pH probes based on styrylcyanine for imaging intracellular pH in live cells,” *Chem. Commun.*, vol. 48, no. 91, p. 11202, 2012, doi: 10.1039/c2cc35363f.

[277] D. Ding, K.-Y. Pu, K. Li, and B. Liu, “Conjugated oligoelectrolyte-polyhedral oligomeric silsesquioxane loaded pH-responsive nanoparticles for targeted fluorescence imaging of cancer cell nucleus,” *Chem. Commun.*, vol. 47, no. 35, p. 9837, 2011, doi: 10.1039/c1cc13237g.

[278] B. Fadeel and D. Xue, “The ins and outs of phospholipid asymmetry in the plasma membrane: roles in health and disease,” *Crit. Rev. Biochem. Mol. Biol.*, vol. 44, no. 5, pp. 264–277, Oct. 2009, doi: 10.1080/10409230903193307.

[279] Y.-H. Ma, B. Li, J. Yang, X. Han, Z. Chen, and X. Lu, “Calcium-dependent and -independent annexin V binding: distinct molecular behaviours at cell membrane interfaces,” *Chem. Commun.*, vol. 56, no. 11, pp. 1653–1656, 2020, doi: 10.1039/C9CC09184J.

[280] A. M. Rieger, K. L. Nelson, J. D. Konowalchuk, and D. R. Barreda, “Modified Annexin V/Propidium Iodide Apoptosis Assay For Accurate Assessment of Cell Death,” *J. Vis. Exp.*, no. 50, p. 2597, Apr. 2011, doi: 10.3791/2597.

[281] J. Fu *et al.*, “Synergistic Therapy Using Doxorubicin-Loading and Nitric Oxide-Generating Hollow Prussian Blue Nanoparticles with Photoacoustic Imaging Potential Against Breast Cancer,” *Int. J. Nanomedicine*, vol. Volume 16, pp. 6003–6016, Aug. 2021, doi: 10.2147/IJN.S327598.

[282] M. A. Sirover, “New nuclear functions of the glycolytic protein, glyceraldehyde-3-phosphate dehydrogenase, in mammalian cells,” *J. Cell. Biochem.*, vol. 95, no. 1, pp. 45–52, May 2005, doi: 10.1002/jcb.20399.

[283] R. E. Ferguson, H. P. Carroll, A. Harris, E. R. Maher, P. J. Selby, and R. E. Banks, “Housekeeping proteins: A preliminary study illustrating some limitations as useful references in protein expression studies,” *PROTEOMICS*, vol. 5, no. 2, pp. 566–571, Feb. 2005, doi: 10.1002/pmic.200400941.

[284] R. Pan, W. Xu, M. Jafari, B. Chen, T. Sheinin, and P. Chen, “DEGylation Enhanced the Stability of Peptide-siRNA Complexes in Serum,” *J. Nanosci. Nanotechnol.*, vol. 15, no. 12, pp. 9982–9990, Dec. 2015, doi: 10.1166/jnn.2015.12074.

[285] H. Lv, S. Zhang, B. Wang, S. Cui, and J. Yan, “Toxicity of cationic lipids and cationic polymers in gene delivery,” *J. Controlled Release*, vol. 114, no. 1, pp. 100–109, Aug. 2006, doi: 10.1016/j.jconrel.2006.04.014.

[286] H. Yan *et al.*, “Facile synthesis of semi-library of low charge density cationic polyesters from poly(alkylene maleate)s for efficient local gene delivery,” *Biomaterials*, vol. 178, pp. 559–569, Sep. 2018, doi: 10.1016/j.biomaterials.2018.03.050.

[287] K. Nohara, F. Wang, and S. Spiegel, “Glycosphingolipid composition of MDA-MB-231 and MCF-7 human breast cancer cell lines,” *Breast Cancer Res. Treat.*, vol. 48, no. 2, pp. 149–157, Mar. 1998, doi: 10.1023/A:1005986606010.

[288] M. İ. Han *et al.*, “Design, synthesis, and *in vitro* and in vivo anticancer activity studies of new (S)-Naproxen thiosemicarbazide/1,2,4-triazole derivatives,” *New J. Chem.*, vol. 46, no. 13, pp. 6046–6059, 2022, doi: 10.1039/D1NJ05899A.

[289] N. Pilco-Ferreto and G. M. Calaf, “Influence of doxorubicin on apoptosis and oxidative stress in breast cancer cell lines,” *Int. J. Oncol.*, vol. 49, no. 2, pp. 753–762, Aug. 2016, doi: 10.3892/ijo.2016.3558.

[290] N. Ghasemimehr, A. Farsinejad, R. Mirzaee Khalilabadi, Z. Yazdani, and A. Fatemi, “The telomerase inhibitor MST-312 synergistically enhances the apoptotic effect of doxorubicin in pre-B acute lymphoblastic leukemia cells,” *Biomed. Pharmacother.*, vol. 106, pp. 1742–1750, Oct. 2018, doi: 10.1016/j.biopha.2018.07.140.

[291] K. Nikiforos and G. Kontogeorgos, “Bcl-2 Gene Family in Endocrine Pathology: A Review,” *Endocr. Pathol.*, vol. 11, no. 3, pp. 205–214, 2000, doi: 10.1385/EP:11:3:205.

[292] S. Staubach, H. Razawi, and F.-G. Hanisch, “Proteomics of MUC1-containing lipid rafts from plasma membranes and exosomes of human breast carcinoma cells MCF-7,” *PROTEOMICS*, vol. 9, no. 10, pp. 2820–2835, May 2009, doi: 10.1002/pmic.200800793.

[293] S. Luanpitpong *et al.*, “Mitochondrial superoxide mediates doxorubicin-induced keratinocyte apoptosis through oxidative modification of ERK and Bcl-2 ubiquitination,” *Biochem. Pharmacol.*, vol. 83, no. 12, pp. 1643–1654, 2012, doi: 10.1016/j.bcp.2012.03.010.

[294] H. Bavorova, T. Svadlakova, Z. Fiala, R. Pisal, and J. Mokry, “The Dose- and Time-Dependent Cytotoxic Effect of Graphene Nanoplatelets: In Vitro and In Vivo Study,” *Nanomaterials*, vol. 12, no. 12, p. 1978, Jun. 2022, doi: 10.3390/nano12121978.

[295] A. K. Barui, J. Y. Oh, B. Jana, C. Kim, and J. Ryu, “Cancer-Targeted Nanomedicine: Overcoming the Barrier of the Protein Corona,” *Adv. Ther.*, vol. 3, no. 1, p. 1900124, Jan. 2020, doi: 10.1002/adtp.201900124.

[296] S. Chen, S. Zhang, Y. Wang, X. Yang, H. Yang, and C. Cui, “Anti-EpCAM functionalized graphene oxide vector for tumor targeted siRNA delivery and cancer therapy,” *Asian J. Pharm. Sci.*, vol. 16, no. 5, pp. 598–611, Sep. 2021, doi: 10.1016/j.ajps.2021.04.002.

[297] Y. Qu *et al.*, “Glycyrrhetinic acid-modified graphene oxide mediated siRNA delivery for enhanced liver-cancer targeting therapy,” *Eur. J. Pharm. Sci.*, vol. 139, p. 105036, Nov. 2019, doi: 10.1016/j.ejps.2019.105036.

[298] N. D. Q. Chau *et al.*, “Elucidation of siRNA complexation efficiency by graphene oxide and reduced graphene oxide,” *Carbon*, vol. 122, pp. 643–652, 2017, doi: 10.1016/j.carbon.2017.07.016.

[299] R. K. Thapa, J. H. Byeon, S. K. Ku, C. S. Yong, and J. O. Kim, “Easy on-demand self-assembly of lateral nanodimensional hybrid graphene oxide flakes for near-infrared-induced chemothermal therapy,” *NPG Asia Mater.*, vol. 9, no. 8, pp. e416–e416, Aug. 2017, doi: 10.1038/am.2017.141.

[300] N. Cao, D. Cheng, S. Zou, H. Ai, J. Gao, and X. Shuai, “The synergistic effect of hierarchical assemblies of siRNA and chemotherapeutic drugs co-delivered into hepatic cancer cells,” *Biomaterials*, vol. 32, no. 8, pp. 2222–2232, Mar. 2011, doi: 10.1016/j.biomaterials.2010.11.061.

[301] M. Guo *et al.*, “Magnetic and pH-responsive nanocarriers with multilayer core–shell architecture for anticancer drug delivery,” *J. Mater. Chem.*, vol. 18, no. 42, p. 5104, 2008, doi: 10.1039/b810061f.

[302] U. Akar *et al.*, “Silencing of Bcl-2 expression by small interfering RNA induces autophagic cell death in MCF-7 breast cancer cells,” *Autophagy*, vol. 4, no. 5, pp. 669–679, Jul. 2008, doi: 10.4161/auto.6083.

[303] F. Jokar *et al.*, “Differential Expression of HSP90 β in MDA-MB-231 and MCF-7 Cell Lines after Treatment with Doxorubicin,” *J. Pharmacopuncture*, vol. 22, no. 1, pp. 28–34, Mar. 2019, doi: 10.3831/KPI.2019.22.003.

[304] A. Taherian and T. Mazoochi, “Different Expression of Extracellular Signal-Regulated Kinases (ERK) 1/2 and Phospho-Erk Proteins in MBA-MB-231 and MCF-7 Cells after Chemotherapy with Doxorubicin or Docetaxel,” *Iran. J. Basic Med. Sci.*, vol. 15, no. 1, pp. 669–677, Jan. 2012.

[305] E. Elstner *et al.*, “Novel Therapeutic Approach: Ligands for PPARγ and Retinoid Receptors Induce Apoptosis in bcl-2-positive Human Breast Cancer Cells,” *Breast Cancer Res. Treat.*, vol. 74, no. 2, pp. 155–165, Jul. 2002, doi: 10.1023/A:1016114026769.

[306] B. Majumder *et al.*, “Conjugated linoleic acids (CLAs) regulate the expression of key apoptotic genes in human breast cancer cells,” *FASEB J.*, vol. 16, no. 11, pp. 1447–1449, Sep. 2002, doi: 10.1096/fj.01-0720fje.

[307] C. Yde and O.-G. Issinger, “Enhancing cisplatin sensitivity in MCF-7 human breast cancer cells by down-regulation of Bcl-2 and cyclin D1,” *Int. J. Oncol.*, Dec. 2006, doi: 10.3892/ijo.29.6.1397.

CURRICULUM VITAE

Name Surname :Erhan Demirel

Place and Date of Birth :

E-Mail :

EDUCATION:

B.Sc. :2013, Istanbul Technical University, Faculty of Science and Letters, Chemistry

M.Sc. :2015, Istanbul Technical University, Graduate School of Science, Engineering and Technology, Chemistry

PROFESSIONAL EXPERIENCE AND REWARDS:

- 2017, Istanbul Medipol University, School of Engineering and Natural Sciences, Biomedical Engineering, Research & Teaching Assistant.
- 2017-2020, Istanbul Medipol University, Prof. Dr. Yasemin YÜKSEL DURMAZ Research Group, Researcher, "Development of Targeted, Dual-Drug Delivery System and Investigation of Anticancer Activity" Funded by TÜBİTAK 1001.
- 2016-2017, Istanbul Medipol University, Prof. Dr. Yasemin YÜKSEL DURMAZ Research Group, Researcher, "Development of Biocompatible Graphene Platform for Biomedical Applications and Investigation of Cytotoxicity" Funded by TÜBİTAK 3001.
- 2014-2015, Istanbul Technical University, Prof. Dr. HIZAL, and Prof. Dr. TUNCA Research Group, "Carbon Nanotube-Based Breath Analyzer", Funded by Istanbul Development Agency.
- 2013, Best oral presentation prize at 4th National Chemistry Student Congress, May 18-20, Manisa, Turkey.

PUBLICATIONS, PRESENTATIONS, AND PATENTS ON THE THESIS:

- Y. Yuksel Durmaz and E. Demirel, "Reduced Graphene Oxide (rGO) Based Drug Carrier Systems," WO2022146360A2, Jul. 07, 2022 [Online]. Available: https://patents.google.com/patent/WO2022146360A2.
- E. Demirel, E. Karaca, and Y. Yuksel Durmaz, "Effective PEGylation method to improve biocompatibility of graphene derivatives," *European Polymer Journal*, vol. 124, p. 109504, Feb. 2020, doi: 10.1016/j.eurpolymj.2020.109504.
- E. Demirel, E. Karaca, and Y. Yuksel Durmaz, "Hedefli, İkili İlaç Taşıma Sistemi Geliştirilmesi ve Anti-kanser Etkisinin İncelenmesi," poster presented at 31st National Chemistry Congress, Yıldız Technical University, Istanbul, Turkey Sep. 10-13, 2019.

- E. Demirel, E. Karaca, and Y. Yuksel Durmaz, "Development of Targeted, Dual Drug Delivery System and Examination of Anticancer Effect," presented at International Natural Science, Engineering and Materials Technology Conference (NEM 2019), Istanbul, Turkey, Sep. 9-10, 2019.
- E. Demirel and Y. Yuksel Durmaz, "Development of a Biocompatible Graphene Nano-platform," poster presented at VII. Polymer Science and Technology Congress with International Participation (Poli(mer) 2018), Eskişehir Osmangazi University, Eskişehir, Turkey, Sep. 09-12, 2018.
- Y. Yuksel Durmaz and E. Demirel, "A Method for Coating Graphene Oxide and Biocompatible Graphene Oxide Obtained from Thereof," WO2018088978A1, May 17, 2018 [Online]. Available: https://patents.google.com/patent/WO2018088978A1.
- E. Demirel and Y. Yuksel Durmaz, "Development of Biocompatible Graphene Platform for Biomedical Applications," poster presented at 22nd International Biomedical Science and Technology Symposium (BIOMED 2017), Ankara, Turkey, May 12-14, 2017.

OTHER PUBLICATIONS, PRESENTATIONS, AND PATENTS:

- T. U. Rehman, J. Khirallah, E. Demirel, J. Howell, E. Vlaisavljevich, and Y. Yuksel Durmaz, "Development of Acoustically Active Nanocones Using the Host–Guest Interaction as a New Histotripsy Agent," *ACS Omega*, vol. 4, no. 2, pp. 4176–4184, Feb. 2019, doi: 10.1021/acsomega.8b02922.
- J. Khirallah *et al.*, "Nanoparticle-mediated histotripsy (NMH) using perfluorohexane 'nanocones,'" *Physics in Medicine & Biology*, vol. 64, no. 12, p. 125018, Jun. 2019, doi: 10.1088/1361-6560/ab207e.
- E. Demirel, H. Durmaz, G. Hizal, and U. Tunca, "A route toward multifunctional polyurethanes using triple click reactions," *Journal of Polymer Science Part A: Polymer Chemistry*, vol. 54, no. 4, pp. 480–486, Feb. 2016, doi: 10.1002/pola.27796.
- U. S. Gunay, E. Demirel, G. Hizal, U. Tunca, and H. Durmaz, "Ring-opening reactions of backbone epoxidized polyoxanorbornene," *Reactive and Functional Polymers*, vol. 94, pp. 35–42, Sep. 2015, doi: 10.1016/j.reactfunctpolym.2015.07.004.
- L. N. Atici, E. Demirel, U. Tunca, G. Hizal, and H. Durmaz, "Postfunctionalization of polyoxanorbornene backbone through the combination of bromination and nitroxide radical coupling reactions," *Journal of Polymer Science, Part A: Polymer Chemistry*, vol. 53, no. 20, pp. 2381–2389, Oct. 2015, doi: 10.1002/pola.27697.

THE DEVELOPMENT OF MULTIFUNCTIONAL NANOPLATFORMS FOR TARGETED DUAL DRUG DELIVERY

ORIGINALITY REPORT

15%	11%	8%	2%
SIMILARITY INDEX	INTERNET SOURCES	PUBLICATIONS	STUDENT PAPERS

PRIMARY SOURCES

1	hdl.handle.net Internet Source	1%
2	sens.medipol.edu.tr Internet Source	<1%
3	www.freepatentsonline.com Internet Source	<1%
4	www.mdpi.com Internet Source	<1%
5	www.researchgate.net Internet Source	<1%
6	centlab.bme.umich.edu Internet Source	<1%
7	dr.ntu.edu.sg Internet Source	<1%
8	www.frontiersin.org Internet Source	<1%
9	research.sabanciuniv.edu Internet Source	<1%